

A Thesis Submitted for the Degree of PhD at the University of Warwick

Permanent WRAP URL:

<http://wrap.warwick.ac.uk/129862>

Copyright and reuse:

This thesis is made available online and is protected by original copyright.

Please scroll down to view the document itself.

Please refer to the repository record for this item for information to help you to cite it.

Our policy information is available from the repository home page.

For more information, please contact the WRAP Team at: wrap@warwick.ac.uk

Brain iron trafficking in health and disease: a systems approach

by

Vindy Tjendana Tjhin

A thesis submitted in partial fulfilment of the requirement for the degree
of
Doctor of Philosophy in Engineering

University of Warwick, Department of Engineering

February 2019



Contents

Contents	ii
List of Figures.....	vi
List of Tables	xii
Declaration.....	xiii
Ethics	xiv
Acknowledgements	xv
List of abbreviations	xvi
Abstract.....	xviii
Chapter 1 Introduction	1
1.1 Motivation	1
1.2 Aims	2
Chapter 2 Background.....	4
2.1 Iron and oxidative stress in Parkinson's disease	4
2.2 Brain iron metabolism	6
2.2.1 Brain iron uptake	6
2.2.2 Cellular regulation: iron response protein and iron response elements	7
2.2.3 Transferrin and transferrin receptors.....	7
2.2.4 Divalent metal transporter 1	8
2.2.5 Ferritin.....	9
2.2.6 Neuromelanin	9
2.2.7 Alpha-synuclein	10
2.2.8 Ferroportin	10
2.2.9 Hepcidin	10

2.2.10	Blood brain barrier.....	11
2.2.11	Blood cerebrospinal fluid barrier.....	11
2.2.12	Dopaminergic neurone.....	12
2.3	<i>Synchrotron-based technique</i>	13
2.3.1	Synchrotron X-ray fluorescence (SXRF).....	13
2.3.1.1	X-ray fluorescence	13
2.3.2	Scanning transmission X-ray microscopy (STXM).....	14
2.3.2.1	X-ray absorption spectral	14
2.4	<i>Modelling technique and tools</i>	16
2.4.1	Ordinary Differential Equations Based Modelling	16
2.4.2	COPASI	17
2.4.3	Sensitivity analysis.....	17
Chapter 3	Brain iron imaging using synchrotron X-ray mapping	19
3.1	<i>Tissue sample preparation</i>	19
3.1.1	Preventing iron contamination of tissue samples.....	20
3.1.2	SXRF tissue sample preparation	20
3.1.2.1	Sample sectioning: Cryomicrotome	21
3.1.3	STXM tissue sample preparation	23
3.1.3.1	Sample sectioning: Ultramicrotome	25
3.2	<i>Mapping methods</i>	26
3.2.1	SXRF mapping.....	26
3.2.1.1	SXRF Experimental setup	27
3.2.1.2	Data acquisition: Creating an SXRF map	28
3.2.2	STXM mapping.....	28
3.2.2.1	STXM Experimental Setup	29
3.2.2.2	Data acquisition: STXM map.....	30
3.2.2.2.1	Neuromelanin absorption spectroscopy	31
3.3	<i>Data processing</i>	32
3.3.1	SXRF data processing	32
3.3.1.1	SXRF spectral fitting.....	33
3.3.1.2	Data normalisation	34
3.3.1.3	Region of Interest (ROI) analysis in ImageJ.....	34
3.3.1.4	Background subtraction.....	35
3.3.1.5	Signal threshold	35
3.3.1.6	Sources of measurement uncertainty.....	35

3.3.1.7	Segmentation of SXRF images	36
3.3.2	STXM data processing	39
3.3.2.1	Background subtraction	39
3.3.2.2	Energy map alignment	39
3.3.2.3	Composite map	40
3.3.2.4	Spectral smoothing	40
3.4	<i>Results</i>	41
3.4.1	SXRF results: quantitative analysis from the SXRF map	41
3.4.2	STXM results: identifying a neuromelanin signature	41
3.4.3	Iron chemistry in control tissue	44
3.4.4	Iron chemistry in the PD tissue	46
3.5	<i>Discussion</i>	50
3.5.1	SXRF iron quantification	50
3.5.2	STXM tissue mapping spectra from iron deposits	50
Chapter 4	Modelling brain iron metabolism in the barrier systems	53
4.1	<i>Iron uptake in the brain background</i>	54
4.2	<i>Materials and methods</i>	57
4.3	<i>Model simulation results</i>	73
4.3.1	Transferrin-transferrin receptor binding	73
4.3.2	Iron uptake across the blood brain barrier	75
4.3.3	Sensitivity analysis	79
4.3.4	Metabolite expression rates	84
4.3.5	Iron uptake in response to varying iron usage in the brain	89
4.4	<i>Discussion</i>	91
Chapter 5	Modelling iron metabolism in dopaminergic neurone of the Substantia nigra	97
5.1	<i>Materials and methods</i>	100
5.2	<i>Results</i>	108
5.2.1	Iron concentrations in the DA neurone	108
5.2.2	Iron concentration in DA neurone in the PD/NBIA simulation	110
5.2.3	Metabolic control analysis	112
5.3	<i>Discussion</i>	116
Chapter 6	Conclusions and future work	118

6.1	<i>Cell to neuropil iron concentration ratio determined by SXRF</i>	<i>118</i>
6.2	<i>Neuromelanin in the DA neurone</i>	<i>119</i>
6.3	<i>Ferrous and zero valent iron in the SNpc in PD</i>	<i>120</i>
6.4	<i>Synchrotron imaging: challenges faced and future opportunities</i>	<i>122</i>
6.5	<i>Evaluating the computational model of brain iron metabolism in health</i>	<i>123</i>
6.6	<i>Evaluating the computational model of SNpc DA neurone iron metabolism in health and neurodegenerative condition</i>	<i>126</i>
6.7	<i>Computational model limitations and future opportunities</i>	<i>128</i>
6.7.1	<i>Future modelling experiment opportunities</i>	<i>131</i>
References		134
Appendix A		a
Appendix B		l
Appendix C		o
Appendix D		r
Appendix E		t
Appendix F		kk

List of Figures

Figure 2.1 The iron L2 and L3 X-ray absorption edge spectra displaying the effect of varying the Fe^{3+} and Fe^{2+} ratios on the absorption features. The iron ratios are displayed above each spectrum. Reproduced with permission from Dr J. Everett (Everett 2015) [90].	15
Figure 3.1 The set-up for tissue sectioning. The sample was not embedded in the mounting medium. There was only enough mounting medium to attach the sample on to the chuck. A sapphire blade was used for sectioning to prevent metal contamination. The paintbrush was used to control the section and prevent the tissue from curling after sectioning. (reproduced with permission from Dr M.E. Finnegan (Finnegan 2013) [100]).	22
Figure 3.2 SXRF mapping set-up reproduced with permission from Dr M.E. Finnegan (Finnegan 2013) [100]. a) a photograph of the configuration of the experimental set up taken by Dr M.E. Finnegan at I18, b) the photograph of the sample fixed on the slide holder. The slide is covered by kapton film, c) the schematic of the experimental set-up corresponding to a).	27
Figure 3.3 Subtraction process performed in Axis2000. (a) image at the protein peak carbon <i>K</i> -edge absorption energy, 288.3 eV. (b) image at the resin peak carbon <i>K</i> -edge absorption energy, 290 eV. (c) image created by subtracting image (b) from (a). The subtraction also removes artefact from the image.	30
Figure 3.4 Images of the carbon <i>K</i> -edge STXM protein map selected from the carbon stacks performed over the carbon <i>K</i> -edge. The selected energy map are: (a) 278 eV, off peak energy, (b) 286 eV, the proposed energy for the neuromelanin-like granular structure, (c) 288.3 eV, peak energy for tissue protein structure, and (d) 290 eV peak energy for the embedding resin. Mapping at 286 eV shows the most granular features without the tissue protein structure.	32
Figure 3.5 Calibration of the energy of the detector channels in PyMCA software. The element for the fluorescence peaks are identified and saved. The peak energy for $\text{Fe } K\alpha$ is 6.4039KeV.	33
Figure 3.6 Images of the step to step process performed to determine the area of the optical image that corresponds to the high resolution map 1 and 2. (a) optical image of the whole tissue section. (b) the corresponding iron fluorescence map of the whole section. (c) the area where the high resolution scan were performed. The areas are	

labelled 1 and 2. (d) overlapped image of the optical image over the fluorescence map to determine the optical image that corresponds to the high resolution fluorescence map.....36

Figure 3.7 The segmenting process of tissue C2 with the guidance of fluorescence image from PyMCA. (a) fluorescence image of tissue section C2. (b) image of the fluorescence map with the cell areas circled in yellow and filled in red. (c) image of the fluorescence map with the rest of the areas filled in red.....38

Figure 3.8 Carbon K-edge STXM protein map from a control (C1) tissue section. Neuromelanin-like granular structure within the tissue morphology. (a) Image of the tissue structure taken at the protein peak, 288.3 eV. (b) Image of the neuromelanin-like granular structure taken at the carbon K-edge energy of 286 eV. At this energy, the tissue structures are not visible. (c) Composite image of the area for the two energy map showing the neuromelanin-like granular structure localised within the protein structure. The protein structures are in cyan and the neuromelanin-like granular structures are in green.42

Figure 3.9 Images to determine the nature of the neuromelanin-like granular structure (a) transmission optical image of the tissue embedded resin on a 100 mesh copper electro-microscope grid (black squares surrounding the area). The red arrows point at the dust on the microscope and not on the sample. The structures in the blue box is possibly a neuromelanin. (b) The carbon K-edge STXM protein map taken at 288.3 eV showing the protein structure inside the electron grid square. (c) The carbon K-edge STXM protein map taken at 288.3 eV of the area in the blue box in (a) and (b). This image is taken at a higher resolution at 125nm. (d) The carbon K-edge STXM protein map taken at 286 eV showing the neuromelanin-like granular structure in the same area as (c). The shape of the neuromelanin-like granules corresponds to the neuromelanin structure in the optical image. (c) and (d) are the same images presented in figure 3.8 (a) and (b), respectively.....43

Figure 3.10 Iron deposits found within and out of the tissue structures of the control (C1) tissue section. (a) Composite map of STXM images of the tissue section at the resolution of 175 nm. The protein structures taken at carbon *K*-edge energy 288.3 eV are in cyan, the neuromelanin-like granular structures taken at carbon *K*-edge energy 286 eV are in green, and the iron deposits taken at iron *L*-edge energy 710 eV are in red. The three iron deposits are shown in a higher resolution map 50 nm labelled A, B and C. (A-C) background subtracted image of the iron deposit. (b) Iron *L*-edge X-ray absorption spectra of the three iron deposits comparable to Fe^{3+} ($\text{FeO}(\text{OH})$) reference spectra. Spectra for iron deposits B and C are cut short due to time constraint and they show obvious features of Fe^{3+} peak. The reference spectrum $\text{FeO}(\text{OH})$ was reproduced with permission from Dr J. Everett (Everett 2015) [90].....45

Figure 3.11 Iron deposits found within and out of the tissue structures of the Parkinson's disease (PD2) tissue section. (a) Composite map of STXM images of the section taken at different energy with a resolution of 125 nm. The protein structures taken at carbon K-edge energy 288.3 eV are in cyan and the iron deposits taken at iron L-edge energy 710 eV are in red. The neuromelanin is not present in this PD tissue. The two iron deposits are shown in a higher resolution map 50 nm labelled D and E.

(D-E) background subtracted image of the iron deposit. (b) Iron L-edge X-ray absorption spectra of the two iron deposits. The iron deposit spectra are compared to Fe^{3+} ($\text{FeO}(\text{OH})$) and Fe^{2+} (FeCl_2) reference spectra. Spectra for iron regions D and E demonstrate an increase intensity of the Fe^{2+} feature at 708 eV (L_3 edge) and 721 eV (L_2 edge), compared to the Fe^{3+} reference feature at 710 eV (L_3 edge) and 723 eV (L_2 edge). The reference spectra were reproduced with permission from Dr J. Everett (Everett 2015) [90].....47

Figure 3.12 Iron deposits found within and out of the tissue structures of the Parkinson's disease (PD2) tissue section. (a) Composite map of STXM images of the section taken at different energy with a resolution of 125 nm. The protein structures taken at carbon K-edge energy 288.3 eV are in cyan and the iron deposits taken at iron L-edge energy 710 eV are in red. The neuromelanin is not present in this PD tissue. The two iron deposits are shown in a higher resolution map 50 nm labelled F and G. (F-G) background subtracted image of the iron deposit showing complex. The reference spectrum was reproduced with permission from Dr J. Everett (Everett 2015) [90].....48

Figure 3.13 Iron L-edge X-ray absorption spectra of the two iron deposits. The iron deposit spectra are compared to zero valent iron (Fe^0) reference spectra. Spectra for iron regions D and E demonstrate a resemblance to spectra feature that is close to Fe^0 spectra. The reference spectrum was reproduced with permission from Dr J. Everett (Everett 2015) [90].....49

Figure 4.1 (A) Illustration of the flow of iron between the blood and the brain. The fenestrated cells between the ISF and the CSF allow free exchange of iron, but the direction of the fluid bulk flow is principally from the ISF into the CSF. The arrow represents the direction of the iron transport and the dotted arrow represents the weaker flow of Tf-Fe from ISF to CSF. (B) Conceptual biological diagram for iron uptake in the brain that the model in this chapter derived from. Abbreviations: BBB: blood brain barrier, BCB: blood cerebrospinal fluid, BCEC: brain capillary endothelial cell (comprises the BBB), CPEC: choroid plexus epithelial cell (comprises the BCB), CSF: cerebrospinal fluid, DMT1: divalent metal transporter 1, Fe: iron, Fpn: ferroportin, Ft: ferritin, Hpc: hepcidin, IRP: iron response protein, ISF: interstitial fluid, LIP: labile iron pool, Tf: transferrin, Tf-Fe: transferrin bound iron, TfR: transferrin receptor...56

Figure 4.2 Systems Biology Graphical Notation (SBGN) process diagram of iron trafficking in the human brain barrier system model based on the mechanistic representation of the biological system shown in figure 4.1. Complexes are represented in boxes with component species. In the special case of the ferritin-iron complex symbol, the amounts of each species are not in stoichiometric amounts (there are thousands of iron ions per ferritin). Species overlaid on the compartment boundaries represent membrane-associated species. Abbreviation: BBB: blood brain barrier, BCB: blood cerebrospinal fluid, CSF: cerebrospinal fluid, DMT1: divalent metal transporter 1, Fe: iron, Fpn: ferroportin, Ft: ferritin, IRP: iron response protein, LIP: labile iron pool, Tf-Fe Serum: transferrin bound iron in the blood plasma, TfR: transferrin receptor.....57

Figure 4.3 Transferrin – Transferrin Receptor binding curve, showing saturating of iron binding to BBB cells as seen in the experimental data with rat brain slices from Hill et al. (1985) [130]. Both simulation and experimental data share the same y-axis. The top axis is for the simulation data and the bottom axis is for the experimental data. The model was not fitted to these data.....	74
Figure 4.4 Semi-log plot of the time course of Tf-Fe Uptake across the BBB following an iron injection event. The simulation result shows similar dynamics for iron influx and subsequent outflow following radio-labelled iron injection compared to the study undertaken by Taylor and Morgan 1990 [131] on rat brains. The model was not fitted to these data. To confirm the model appropriateness we compared uptake dynamics with a simulation representing iron injection.....	76
Figure 4.5 Metabolites in the model responding to various levels of increased iron load. (A) The rate of the iron uptake into the brain ISF. (B) The concentration of labile iron pool (LIP) in the BBB and BCB. (C) The concentration of Tf-Fe in the ISF. ...	78
Figure 4.6 The effect of system-wide expression changes in TfR and IRP on the concentration of Tf-Fe in ISF and labile iron pool in both BBB and BCB under 3 conditions: normal iron serum 20 μM , iron deficiency 0.2 μM and iron overload 200 μM . This shows that system-wide changes in the expression rate of TfR and IRP decrease the concentration of iron in the brain ISF under normal and overload condition, but do not significantly change the amount of iron reaching the ISF under iron deficiency condition. There appears to be a shift on the effect of TfR or IRP expression with insufficient iron in the serum.....	86
Figure 4.7 The consequences of perturbations of IRP and TfR expression only in BBB under 3 conditions: normal iron serum 20 μM , iron deficiency 0.2 μM and iron overload 200 μM . This shows that changes in BBB expression rate of TfR and IRP do not affect the concentration of iron in the brain ISF, as well as LIP in BBB and BCB, under normal and overload condition, but significantly change the amount of iron reaching the ISF and LIP under iron deficiency condition. There appears to be a shift on the effect of TfR or IRP expression with insufficient iron in the serum.....	87
Figure 4.8 The consequences of perturbations of IRP and TfR expression only in BCB under 3 conditions: normal iron serum 20 μM , iron deficiency 0.2 μM and iron overload 200 μM . This shows that under all three conditions the changes in BBB expression rate of TfR and IRP decrease the concentration of iron in the brain ISF, but has no/ slight effect on the LIP in BBB and BCB.	88
Figure 4.9 Iron uptake across the BBB in response to a temporary increase in the rate of Tf-Fe ISF usage. (A) The signal triggered to simulate an increase in Tf-FE ISF usage for one day period. The set peak rate of Tf-Fe usage in the ISF is 0.20 $\mu\text{M s}^{-1}$. (B) The concentration of the LIP in the BBB and (C) Tf-Fe in ISF in response to an increase in the ISF Tf-Fe consumption signal in A. (D) The signal triggered to simulate an increase in Tf-FE ISF usage for a long period of time (more than 200 days). (E) The concentration of the LIP in the BBB and (C) Tf-Fe in the ISF in response to an increase in the ISF Tf-Fe consumption signal in D.	90

Figure 5.1 Illustration of the flow of iron between the blood and the brain including the DA neurone. The fenestrated cells between the ISF and the CSF allow free exchange of iron, but the direction of the fluid bulk flow is principally from the ISF into the CSF. The arrows represent the direction of the iron transport and the dotted arrow represents the weaker flow of Tf-Fe from ISF to CSF.98

Figure 5.2 Conceptual biological diagram for iron uptake in the brain from which the model in this chapter derived. The direction of the flow of iron is shown in figure 5.1. Abbreviations: BBB: blood brain barrier, BCB: blood cerebrospinal fluid, BCEC: brain capillary endothelial cell (comprises the BBB), CPEC: choroid plexus epithelial cell (comprises the BCB), CSF: cerebrospinal fluid, DA neurone: dopaminergic neurone, DMT1: divalent metal transporter 1, Fe: iron, Fpn: ferroportin, Ft: ferritin, Hpc: hepcidin, IRP: iron response protein, ISF: interstitial fluid, LIP: labile iron pool, Tf: transferrin, Tf-Fe: transferrin bound iron, TfR: transferrin receptor.99

Figure 5.3 System Biology Graphical Notation (SBGN) process diagram of iron trafficking in the human brain barrier system and dopaminergic neurone model based on the mechanistic representation of the biological system shown in figure 5.2. Complexes are represented in boxes with component species. In the special case of the ferritin-iron complex, the amount for each species are not depicted in stoichiometric quantities (there are thousands of iron ions per ferritin). Species overlaid on the compartment boundaries represent membrane-associated species. Abbreviation: AS: ascorbate, BBB: blood brain barrier, BCB: blood cerebrospinal fluid, CSF: cerebrospinal fluid, DA neurone: dopaminergic neurone, DMT1: divalent metal transporter 1, Fe: iron, Fpn: ferroportin, Ft: ferritin, IRP: iron response protein, LIP: labile iron pool, NM: neuromelanin, Tf-Fe Serum: transferrin bound iron in the blood plasma, TfR: transferrin receptor. 101

Figure 5.4 Time course simulations of the concentration of the metabolites in the DA neurone model responding to various levels of increased iron load. (A) The concentration of LIP in the DA neurone. (B) The concentration of iron in the ferritin in the DA neurone. (C) The concentration of iron at the high affinity binding sites of the neuromelanin in the DA neurone. (D) The concentration of iron at the low affinity binding sites of the neuromelanin in the DA neurone. The simulation was performed under normal conditions, Tf-Fe serum 20 μM , and is represented in bright blue. The curves representing Tf-Fe serum over than 30 μM overlaps. 108

Figure 5.5 (A) Simulated time course of the accumulation of the total iron concentration in the DA neurone (red curve) and the total iron in the neurone without the iron in neuromelanin. Most of the iron in the DA neurone is sequestered to the neuromelanin. (B) The Simulated iron concentration in neuromelanin, ($\text{Fe}/\text{NM} = 4500$ ng/mg neuromelanin), compared to the concentration determined experimentally in post-mortem LC (Locus Coeruleus) and SN (Substantia Nigra) tissue extracted from Zecca et al. (2006) [1]. 109

Figure 5.6 Time course simulations of the concentration of the metabolites in the DA neurone model responding to various levels of increased iron load in the PD/NBIA simulation. (A) The concentration of LIP in the DA neurone. (B) The concentration of iron in ferritin in the DA neurone. (C) The concentration of iron at the high affinity

binding sites of neuromelanin in the DA neurone. (D) The concentration of iron at the low affinity binding sites of neuromelanin in the DA neurone. The simulations performed under normal conditions, where Tf-Fe serum of 20 μ M, is represented in bright blue. 111

Figure 6.1 (A) Tissue structures of human putamen (left) and amygdala (right) taken at oxygen K-edge energy 532.1 eV. (B) Speciation maps of a protein deposit in human amygdala tissue with Alzheimer's disease. Acquisition energies: carbon K-edge (285.2 eV; protein), calcium L-edge (352.6 eV), oxygen K-edge (533.8 eV; carbonate (CO)), potassium L-edge (300 eV) and iron L-edge (710 eV). Composite image created using colours indicated in the individual map panels. Scale bars 2 μ m. (C) Iron L-edge X-ray absorption spectra of the two iron deposits identified in the iron panel map in (B). [151]..... 121

List of Tables

Table 3-1 The details of the samples studied using SXRF mapping. C is control and PD is Parkinson's disease.	21
Table 3-2 The details of the samples studied STXM mapping. C is control and PD is Parkinson's disease	23
Table 3-3 List of all the Diamond Light Source (DLS) experiments and the samples presented in this thesis. C represents control cases and PD represents the Parkinson's disease cases. JFC: Dr J.F. Collingwood and MEF: Dr M.E. Finnegan	26
Table 4-1 Volume of model compartments	58
Table 4-2 Initial concentration of all metabolites	59
Table 4-3 Reactions involved in the iron transport in the barriers and their parameters	65
Table 4-4 Generic sensitivity analysis (sensitivity coefficient (SC)) and metabolic control analysis (concentration control coefficient (CCC)) for LIP in BBB	80
Table 4-5 Generic sensitivity analysis (sensitivity coefficient (SC)) and metabolic control analysis (concentration control coefficient (CCC)) for LIP in BCB	81
Table 4-6 Generic sensitivity analysis (sensitivity coefficient (SC)) and metabolic control analysis (concentration control coefficient (CCC)) for Tf-Fe in ISF	82
Table 5-1 List of the reactions and their parameters for the DA neurone compartment in the extended model.	104
Table 5-2 MCA concentration control coefficient (CCC) for LIP in the DA neurone	113
Table 5-3 MCA concentration control coefficient (CCC) for the concentration of iron at the high affinity binding sites of neuromelanin in the DA neurone.....	114
Table 5-4 MCA concentration control coefficient (CCC) for the concentration of iron at the low affinity binding sites of neuromelanin in the DA neurone.....	115

Declaration

I hereby declare that the work presented in this thesis is my own work except where stated otherwise, and was carried out entirely at the University of Warwick, from October 2014 to September 2018, under the supervision of Dr Joanna Collingwood, Professor Michael Chappell and Professor Charles Hutchinson. The research reported here has not been submitted, either wholly or in part, in this or any other academic institution for admission to a higher degree.

The work presented was carried out by the author except in the cases outlined below:

- The SXRF data reported in Chapter 3, were acquired before the work performed in this thesis and not by the author, the work focused on method development and not on data acquisition.

Tjendana Tjhin

2019

Ethics

The tissue used in this study were obtained and analysed under the multi-centre research ethics committee (MREC) approval 07/MRE08/12, held by Dr J.F. Collingwood valid until 2020. The analysis in chapter 3 was performed under biomedical and scientific research ethics committee (BSREC) approval (REGO – 2018-2222). The approval letter is in appendix B.

Acknowledgements

I would like to express my very great appreciation for my first supervisor, Dr. Joanna Collingwood, for her patient guidance, enthusiastic encouragement, and constant support throughout this project. I am very grateful for all the insights and the countless discussion that is fundamental, not only for my project but also for my growth as a researcher. I would also like to offer my special thanks to Prof. Michael Chappell for all the advice and supports he has provided throughout the project.

I would like to express my sincere gratitude to the EPSRC [EP/K035193/1], the Arden center (University Hospital of Coventry and Warwickshire), the Warwick Alumni and the University of Warwick, School of Engineering for the funding this research. And, I would like to offer my deepest gratitude to Prof Charles Hutchinson for securing fundings that enabled me to do this research.

My grateful thanks are also extended to Dr. Simon Mitchell and Dr. Elizabeth Milward for their collaboration. Their input to the ideas has helped shaped the thinking of the thesis. Additional thank you to Dr. Simon Mitchell for hosting visits at the UCLA to work on the computational models. His guidance with the computational model has aided the progress of this project.

I would like to thank everyone in the office for creating a warm and supportive environment, making my Ph.D. journey a great experience.

List of abbreviations

ALS	Advanced Light Source
BBB	Blood brain barrier
BCB	Blood cerebrospinal fluid barrier
BCECs	Brain capillary endothelial cells
iPLA2 β	Calcium-independent phospholipase A2 β
CSF	Cerebrospinal fluid
DA	Dopaminergic
DFP	Deferiprone
DLS	Diamond Light Source
DMT1	Divalent metal transporter 1
Fe ²⁺	Ferrous iron
Fe ³⁺	Ferric iron
HIF	Hypoxia inducible factor
IRE	Iron regulatory element
IRP	Iron regulatory protein
ISF	Interstitial fluid
LC	Locus Coeruleus
LIP	Labile iron pool

MCA	Metabolic control analysis
MREC	Multi-centre research ethics committee
NBIA	Neurodegeneration with brain accumulation
NBTR	Newcastle Brain Tissue Resource
ODE	Ordinary differential equation
PD	Parkinson's disease
PLAN	PLA2G6-associated neurodegeneration
ROS	Reactive oxygen species
SBGN	Systems biology graphical notation
SNpc	Substantia nigra pars compacta
STXM	Scanning transmission X-ray microscopy
SXRF	Synchrotron X-ray fluorescence
TEER	Trans-endothelial electrical resistance
Tf	Transferrin
Tf-Fe ³⁺	Transferrin bound iron
TfR	Transferrin receptor
UTR	Untranslated region

Abstract

The study in this thesis sets to explore the techniques to study the iron trafficking into the brain, and more closely in the substantia nigra par compacta (SNpc) region, and also, the altered iron loading mechanism, with particular application in disorders where specific compartments show elevated iron concentration, such as Parkinson's disease (PD). Iron is essential for numerous biochemical reactions in the brain, but excess iron may produce reactive oxygen species that can induce cell death. The increase in iron concentration in this area has been shown repeatedly over the years, and it has been accepted as one of the main characteristics of PD. Another main characteristic of PD is the loss of neuromelanin-containing dopaminergic (DA) neurone in the SNpc. Neuromelanin binds to and stores iron. The disappearance of neuromelanin in the SNpc is another indication that iron is involved in the progression of PD. The detail of iron involvement in PD, however, is still unknown. Attempts have been made in this thesis to create tools to answer some of the questions by image analysis to examine post-mortem human brain tissue; and building a novel computational model of iron transport into the brain.

Synchrotron-based experiments, scanning transmission X-ray microscopy (STXM) and synchrotron X-ray fluorescence (SXRF), on post-mortem tissue are described in this thesis to investigate the spatial distribution and relative concentration of iron in the DA neurone and the redox state of the iron. These methods do not require dyes or fixing of the sample, thus allowing the native chemistry of the tissue samples to be better preserved. The investigation of the chemical state of iron using STXM method is of interest because it shows the region-specific toxicity state of the iron in the tissue and the neuromelanin. SXRF mapping can produce a high-resolution map of iron distribution in the tissue, and also calculate the relative concentration of iron in the DA neurone compared to the extracellular concentration. SXRF mapping and processing are described in detail in this thesis to inform how SXRF could be an excellent tool to study the involvement of iron in the PD. SXRF maps from experiments performed before this project are analysed and presented here.

The iron absorption spectra from STXM mapping of 200 nm resin-embedded tissues revealed the presence of redox-active iron in the PD case but not in the control. This result supports the hypothesis that the cell death in PD is induced by oxidative stress. Carbon K-edge examination of the neuromelanin in the tissue reveals a feature in the energy

spectrum that is possibly unique to neuromelanin. However, further study needs to be done to confirm this finding. The result of such a study would allow label-free direct analysis of the chemical state of iron in the neuromelanin and to determine if the state changes in PD.

Two computational models were built to create *in silico* representations of (1) iron transport into the interstitial fluid of the brain, and (2) iron transport into the DA neurones, using the modelling software COPASI. Model 1, the barrier systems model, was based on an existing well-developed concept from Drs Mitchell and Collingwood, and the original work in this thesis arose from testing and refining the model. Model 2, the DA neurone model, is completely original work, and designed so that it can be integrated with the barrier systems model in the longer term. The models are comprised from nonlinear ordinary differential equations which are used to characterise the kinetics of each chemical species incorporated. Model parameters values for compartmental volumes, and initial concentrations and rate constants for each species, were derived from experimental results from the literature. The simulations show that the regulatory activity of the brain barrier systems protects the brain against excessive iron loading, and a sensing mechanism may be required to prevent low brain iron concentration. Metabolic control analysis identified TfR as the key regulatory factor of iron concentration in the dopaminergic neurones and also the brain barrier systems. These new models are, to the best of our knowledge, the most comprehensive computational models of brain iron transport that have been developed to date. It is intended that they will provide *in silico* resources to explore the dysregulation of iron transport in PD and related disorders.

The synchrotron-based mapping techniques and computational modelling presented in this thesis are excellent tools to study the implication of iron in PD. The SXRF mapping has the potential to produce a cell-specific concentration of iron as an input to the computational model, and the STXM mapping has the potential to reveal the basic knowledge for building the models, such as the compartmentalisation of the iron deposits in the neuromelanin. The synchrotron-based analyses produce results that are useful in the building of the computational model, and the computational models reveal the dynamic processes involved that cannot be observed from post-mortem analysis, so they are both critical. In combination, they offer a new approach to study unresolved questions in the field.

Chapter 1 Introduction

1.1 Motivation

Parkinson's disease (PD), named after the English doctor Dr James Parkinson who described the illness in 1987, is a slow-progressing neurodegenerative disease. The disease affects the basal ganglia, which are involved in the control of arbitrary and spontaneous movement. Patients are not only affected by the motoric manifestation but also suffer from depression and anxiety, cognition difficulties, sleeping disorders and autonomic dysfunction such as digestive problems [2-4].

A hallmark feature of PD is the loss of dopaminergic neurones in substantia nigra par compacta (SNpc). In the brain, iron is important for reactions such as myelin formation and energy production via changes in its valence states [5-7]. Iron's ability to change between valence states, however, can lead to the production of toxic reactive oxygen species in overload circumstances. Iron readily participates in the oxidation and reduction reactions switching between ferric and ferrous states. An increase in iron concentration has been found in these neurones, and the overload of iron here has been implicated to be a likely cause of the neuronal damage in PD. The detailed mechanism of iron metabolism in the brain and how it is related to the unknown aspects of pathogenesis in PD remains unclear.

Determining the pathogenesis of PD is a major area of interest. Key questions regarding PD pathogenesis that still need to be answered include [4]: (1) why are

dopaminergic (DA) neurones in the SNpc especially vulnerable; (2) which mechanisms underlie progressive cell loss of DA neurone in SNpc; and (3) what do Lewy bodies or α -synuclein reveal about disease progression.

The full reasons for the death of neuronal cells in the Parkinson's disease brain, including the DA neurons, are still unknown. The suggestion that excessive free radical formation and oxidative stress is a cause of the damage, indicates a link between iron accumulation and the PD pathogenesis [8].

1.2 Aims

This study aims to develop ways to study the roles of iron in connection to the specific vulnerability of certain types of neuronal cell, including DA neurones in the SNpc and the underlying mechanism of the disease progression. The areas that are investigated in this thesis are:

1. Using synchrotron based hard X-ray fluorescence (SXRF) to calculate the relative concentration of iron in the DA neurone compared to the surrounding cells. This is to study a possible reason that the DA neurones are more prone to dying compared to other surrounding cells in PD. The semi-quantitative result from this study may be used to validate the computational model built in this thesis.
2. Using scanning transmission X-ray microscopy (STXM) to study the compartmentalisation of iron deposits in the SNpc tissue. The STXM uses soft x-rays that allow the observation of the iron deposits within the biological materials. The findings of this study may inform how the iron uptake into the DA neurone is modelled using the computational model.
3. Building a model to describe iron uptake with the brain across the blood brain barrier (BBB) to create a new way of investigating the dynamics of brain iron trafficking.

4. Building a computational model of the iron transport into the DA neurone of SNpc that allows for investigation of the iron dysregulation in health and PD, and to create simulations to test theories about why DA neurone cells in the SNpc are affected in PD.

Chapter 2 Background

2.1 Iron and oxidative stress in Parkinson's disease

Parkinson's disease (PD) is one of the most common movement disorders and neurodegenerative diseases [3]. Meta-analysis studies show an increase in the global incidence rate of PD. The overall incidence rate of PD is estimated to be 100 to 200 per 100,000 people, and the annual incidence is estimated to be 15 per 100,000 [3]. In the UK, the estimated prevalence of PD in 2018 is around 66 million [9]. Genetic factors were identified in 5-10% of the patients [3], but the cause of PD in most cases is still unknown.

The three major motor signs that are considered as the hallmarks of PD are bradykinesia, rigidity and tremor. PD is characterised by the loss of certain types of brain cell, including the dopaminergic (DA) neurones, and the presence of α -synuclein-containing Lewy bodies in the substantia nigra par compacta (SNpc) [2]. It is this loss of DA neurone in the SNpc that leads to the reduced facilitation of voluntary movement [3]. The increase in the concentration of iron in SNpc in PD has led to the speculation that the cell death in this region was induced by iron-related oxidative stress.

Iron in living cells dominantly exist in the forms of ferrous (Fe^{2+}) and ferric (Fe^{3+}) iron whose complexes readily undergo cyclic oxidation and reduction [10, 11]. This characteristic explains iron involvement in oxygen transport and other metabolic

processes, such as DNA synthesis [12]. This activity, however, can generate oxygen-derived free radicals called reactive oxygen species (ROS), which may cause biological damage. ROS are rapidly detoxified by the body defence mechanism under normal condition. Also, the body homeostatic mechanisms maintain the ideal iron level between optimum cell function and minimal ROS production due to excessive free iron concentration. However, when the iron homeostatic mechanism is disturbed, excessive amount of ROS are produced and end up overwhelming the cellular defence mechanism [13].

Iron in healthy human serum ($\sim 20 \mu\text{M}$) is primarily in the Fe^{3+} form and safely bound to proteins such as transferrin, so they are not readily reduced to produce ROS [14]. Intracellularly, iron is in its reduced, soluble Fe^{2+} form which constitutes the labile iron pool (LIP). In typical cells, the LIP concentration is $\sim 2\text{-}3 \mu\text{M}$. The LIP may be utilised in various cellular processes or oxidised and stored in a storage protein called ferritin to prevent the occurrence of unwanted oxidative reactions that generate ROS and subsequent cell damage.

The concentration of iron in the SNpc in PD was reported by multiple studies to increase compared to control concentration [15-17]. The increased iron concentration has been linked to the severity of PD. The concentration of ferritin protein in this area does not increase in parallel with the increased iron concentration [17], suggesting a disruption in iron metabolism.

One of the therapeutic methods that has been implemented to treat systemic iron overload is iron chelation [18]. Iron chelators are able to bind with excess iron and remove it from the system [19]. Recently, Devos et al. (2014) [20] published their observations from a clinical trial using an iron chelating drug in PD patients. According to their result, patients treated with Deferiprone (DFP), the chelating drug used in the clinical trial, show better motor performance and a reduction of the R2^* value in the Substantia nigra which is consistent with a lowered iron concentration [20].

2.2 Brain iron metabolism

2.2.1 Brain iron uptake

Non-heme iron that is carried by the blood around the body is mostly in the form of Fe^{3+} and bound to a transport protein called transferrin (Tf). For transferrin bound iron (Tf-Fe^{3+}) to be transported into the brain, it has to cross the blood capillary. The endothelial cells of the blood capillary in the brain are connected by tight junctions, creating the blood brain barrier (BBB), which makes passive transport of iron impossible. Tf-Fe^{3+} binds to a transferrin receptor (TfR) that is located on the surface of the luminal side of the BBB. The binding of two Tf-Fe^{3+} to the TfR initiates the receptor mediated transport, invaginating the TfR Tf-Fe^{3+} complex into clathrin-coated pits which fuse the targeted membrane to form an endosome vesicle inside the BBB [21].

In the endosome, a proton pump increases the pH inside which results in iron being released from the transferrin. A ferric reductase enzyme converts Fe^{3+} into Fe^{2+} and subsequently, free Fe^{2+} is transported out of the endosome into the cytosol by divalent metal transporter 1 (DMT1) [22, 23]. The apo-Tf (empty transferrin) still bound to the TfR is recycled back to the luminal side of BBB. Systemic apo-Tf does not enter the brain interstitial fluid (ISF) [24].

In the cytosol of the BBB, the released Fe^{2+} joins the LIP and can be stored inside ferritin, an iron storage protein [25, 26], or transported out of BBB via an iron transporter protein called ferroportin. After Fe^{2+} is transported out by ferroportin, it is oxidised by iron oxidising protein. Then the Fe^{2+} that enters the interstitial fluid (ISF) of the brain binds to Tf expressed by the oligodendrocytes in the brain [27]. The presence of DMT1 in the BBB has been the subject of debate in the recent literature [28-31].

Tf-Fe molecules in the ISF are taken up by cells in the brain or constantly moving towards the cerebrospinal fluid (CSF) by bulk flow. It is postulated that CSF composition reflects that of ISF because the ISF and CSF are separated by highly permeable cellular layers that allow molecules up to the size of ferritin to pass through [32]. Tf-Fe in the CSF is transported back to the blood by a similar mechanism to the TfR mediated transport at the epithelial cells of the choroid plexus [7].

2.2.2 Cellular regulation: iron response protein and iron response elements

Iron response proteins 1 and 2 (IRP1 and IRP2) are proteins that post-transcriptionally control the expression of several mRNAs encoding proteins involved in the metabolism of iron. The mechanism involved is the binding of IRP to the corresponding iron response elements (IREs), a stem-loop structure in the untranslated region (UTR) of the target mRNAs [33]. This binding stabilises the mRNAs and initiates or inhibits the expression of the target mRNAs depending on the position of the IRE in the target mRNAs [34]. Examples of proteins that have IRE in their mRNAs are TfR [35], DMT1, ferritin [36] and ferroportin [37].

IRP binding inhibits the translation of the target mRNAs if the IRE is located in the 5'UTR of the target mRNAs, as in ferritin and ferroportin. The binding initiates the translation of the target mRNAs if the IRE is located in the 3'UTR of the target mRNAs, as in TfR and DMT1 [33, 37].

2.2.3 Transferrin and transferrin receptors

Tf is an iron transport protein that has two iron binding site domains of equal size and affinity. The affinity of Tf for iron is very high at pH 7.4 so that Tf-Fe³⁺ is stable and not likely to be involved in the chemical reactions that create ROS. Tf is expressed in the brain, in the oligodendrocytes and the choroid plexus [36, 38]. In the plasma and other extracellular fluid, Tfs are found in the form of apo-Tf (free, no iron bound to

the Tf), mono-Tf (one Fe^{3+} bound to the Tf) and holo-Tf (two Fe^{3+} bound to the Tf) [39, 40].

TfR is the main iron importer protein in cells. It consists of a disulphide-linked transmembrane glycoprotein homodimer having a molecular mass of 180 kDa [41]. Each subunit of TfR has a molecular mass of 90 kDa that binds to one molecule of Tf, hence a TfR can bind to two molecules of holo-Tf [40, 42]. The binding of TfR to Tf is also influenced by the pH of the environment. At lower pH, the binding affinity of TfR for Tf increases, thus during the receptor-mediated endocytosis the Tfs stay bound to TfR and are released back to the plasma or extracellular fluid [39].

2.2.4 Divalent metal transporter 1

Divalent metal transporter 1 (DMT1), also known as SLC11A2, Nramp2, and DCT1, is a proton-coupled metal transporter protein that has a broad substrate range that includes Fe^{2+} , Mn^{2+} , and Cu^{2+} [43-45]. It facilitates the direct transport of Fe^{2+} into a cell across the cell membrane and also the transport of Fe^{2+} across the endosomal membrane into the cell cytoplasm in the endosomal uptake pathway [46, 47]. The analysis of the mRNA expression indicates that the protein is present in many tissues including the brain. Gene expression of the DMT1 reveals four different types of DMT1 isoform: 1A/(+IRE), 1A/(-IRE), 1B/(+IRE) and 1B/(-IRE). 1A and 1B indicate the exon where the mRNA transcript starts, and in the brain, it is presumed that the DMT1 gene expression is exclusively on the 1B isoforms [48]. (+IRE) and (-IRE) signify the presence of the iron response element at the three prime untranslated region (3' UTR) of the mRNA [49]. The (+IRE) isoforms are localised to the cell membrane, and the (-IRE) isoforms are not [50]. The four isoforms have the same turnover rate, functional properties and rate limiting steps.

2.2.5 Ferritin

Ferritin is an iron storage protein that stores intracellular iron that is not needed for immediate use. Ferritin is ubiquitous and present in almost all organisms. A single ferritin protein could store up to 4500 atoms of iron within its core shell in the form of chemically less active ferrihydrite [51]. Most ferritin proteins consist of 24 subunits. There are two different types of ferritin subunit, heavy (H) and light (L) subunit. The predominant subunit in the brain is H, and the isoform distribution is cell specific. The ferritin in the neurone is predominantly H- ferritin [52]. The two subunit types have specific functions; the H subunit role is to perform oxidation of the cellular iron before it is stored, and the L subunits form the site for nucleation of the mineral core [53]. The ratio between the H and L subunits defines the dominant function of the ferritin in the cell and may change depending on a variety of extracellular stimuli such as inflammation [54].

2.2.6 Neuromelanin

Neuromelanin is a dark insoluble pigment localised to several types of neurone in the brain, particularly the DA neurones in the SNpc. In these cells, the neuromelanin pigment is located within cytoplasmic organelles with varying sizes ranging from 0.5 – 3.0 μm . The granular aggregates of neuromelanin are 200-600 nm in size [55-57].

Mossbauer analysis of the neuromelanin reveals that its binding sites have similar features to human ferritin and that it binds to Fe^{3+} [58], however, there has been no mention of neuromelanin oxidizing Fe^{2+} as an equivalent process to that in ferritin. There are two different binding sites in the neuromelanin: the high affinity and low affinity binding sites. Iron bound to the high affinity sites is safely bound and stable, creating an anti-oxidant effect. However, in the iron overload condition, more iron starts to bind with the low affinity sites of neuromelanin, and iron binds to the low affinity sites might remain redox-active [59].

2.2.7 Alpha-synuclein

Alpha-synuclein (α -synuclein) is a protein mainly found in the brain tissue that has been proposed to play an important role in the modulation of dopamine release, by regulating the rate-limiting enzyme in the biosynthesis of dopamine in the SNpc [2, 60]. The DA neurone appears to be selectively vulnerable to the toxicity of α -synuclein [61]. Studies have shown that α -synuclein may be the building blocks of Lewy bodies, which are abnormal intracellular inclusions found in PD. α -synuclein binds with Fe^{3+} and Fe^{2+} with a binding constant of $1.2 \times 10^{13} \text{ M}^{-1}$ [62] and $5.8 \times 10^3 \text{ M}^{-1}$ [63], respectively. The relationship between iron and the toxicity of α -synuclein has been observed *in vitro*. In numerous *in vitro* studies, iron was found to enhance the intracellular aggregation of α -synuclein [63, 64] and the incubation of α -synuclein with Fe^{2+} leads to the formation of ROS [65].

2.2.8 Ferroportin

Ferroportin is the only known mammalian cellular iron exporter that together with a ferrireductase is responsible for the cellular efflux of ferrous iron [66-68]. It is regulated post-transcriptionally by the regulatory hormone hepcidin. In the BBB, the expression of ferroportin has been documented in recent years [67, 69].

2.2.9 Hepcidin

Hepcidin regulates the degradation of ferroportin. The binding of hepcidin on to its receptor site in ferroportin initiates the internalisation and subsequent lysosomal degradation of both ferroportin and hepcidin [68, 70]. The hepcidin protein responds to stimuli by the increased expression during iron overload and decreased expression during iron deficiency. Systemic hepcidin does not regulate brain iron uptake due to the lack of BBB permeability [68], so the expression of hepcidin in the brain has been studied by several groups. There is evidence that the hepcidin mRNA is found in the mouse brain and animal studies of hepcidin in the brain have shown rapid depletion

of overall brain ferroportin [71, 72]. However, there was no many evidence that the hepcidin mRNA is expressed in the human brain [73, 74].

2.2.10 Blood brain barrier

The discovery of a barrier separating the brain and blood arose from the observation that certain compounds did not show pharmacological activity when injected into the blood of experimental animals, but presented visible effects when injected into the CSF. This hypothesis was further supported by whole body staining that shows Trypan Blue stained all tissues except the brain and the spinal cord when injected into the blood, and stained the brain tissues and spinal cord when injected directly into the CSF [75].

The blood brain barrier (BBB) describes the property of the brain microvasculature which is made up of brain capillary endothelial cells (BCECs) [76, 77]. The surface area of the BBB is between 150 and 200 cm² g⁻¹ tissue constituting the largest interface for blood-brain exchange [77]. One of the morphological features that differentiates BCECs from non-neural vessels is the presence of tight junctions at the apical end of the inter-endothelial space. The tight junction consists of complex of proteins called occludin and claudins, and junctional adhesion molecules [77]. Together, these proteins create a membrane with high values of trans-endothelial electrical resistance (TEER) of 1800 Ω cm², which significantly limits the permeation of molecules larger than 400 Da between the BCECs [78].

The expression of TfR in the BBB has been found to be 6-10x the expression in the brain parenchyma [79]. Its distribution is specific to the brain with 10% of the TfR protein available at the surface and the rest located in the cytoplasm [78].

2.2.11 Blood cerebrospinal fluid barrier

The blood cerebrospinal fluid barrier (BCB) is made of the epithelial cells of the choroid plexus. The choroid plexus lines the brain ventricles, which are filled with

CSF. As the name suggests, the cells divide the CSF from the blood. The endothelial cells of the blood vessel in this region are not tightly bound, so it allows the particles to pass freely. It is the epithelial cells of the choroid plexus that have tight junctions between the cells, regulating the transport of iron across the barrier [80, 81].

The BCB also possesses proteins that are involved in the iron upregulation across the barrier, similar to the BBB. The presence of transferrin, transferrin receptors, ferritin, DMT1 and other iron transporters in the choroid plexus (i.e. BCB) have been demonstrated in the literature [7, 82, 83]. In the BCB, the TfR clusters around the nuclei and the ferroportin diffuses in the cytoplasm indicating the possibility of a two direction transport, but the DMT1 only exists on the side facing the CSF; this may indicate the direction of the iron flow across this barrier, from the CSF to the blood [7]. The DMT1 mediated efflux of iron in the BCB may constitute a clearance mechanism maintaining the iron concentration in brain extracellular fluid at a relatively stable level [7].

2.2.12 Dopaminergic neurone

Dopaminergic (DA) neurones are the neurone cells producing dopamine found in the SNpc and the LC, characterised by the dark brown pigment, neuromelanin. The measurement of iron in the SNpc using isothermal remanent magnetisation suggests an almost two fold increase in the concentration of iron for PD compared to healthy controls [17]. The concentration of the iron in the individual DA neurone was also shown to increase compared to the extracellular concentration by $\sim 1.5\times$ in PD [84]. The death of DA neurone has been linked to the aggregation of α -synuclein, however, it is still not known why the DA neurone is particularly sensitive to this mutation since α -synuclein is found in other areas in the brain. The presence of TfR, DMT1 and ferroportin has been found in DA neurone [85]. The TfR concentration in the DA neurone of SNpc was found to be lower than in other brain areas [86], and some studies showed that the level is almost undetectable [87].

2.3 Synchrotron-based technique

Synchrotron facilities are particle accelerators that produce an intense beam of light primarily in the X-ray region of the electromagnetic spectrum [88]. The light can be further focused and tuned to produce the desired properties for specific requirement. This section will describe the principles of the two synchrotron-based techniques that are employed in this thesis.

2.3.1 Synchrotron X-ray fluorescence (SXRF)

Synchrotron X-ray fluorescence (SXRF) is a high-resolution mapping technique that captures the spectra of the sample. The high beam intensity and fine optics provided by the synchrotron facilities, enable the measurement of peak intensity for specific elements, or the full fluorescence spectrum in each pixel of the sample [88]. The intensity of the SXRF emission is proportional to the atomic abundance of the elements in the sample, which allows the quantitative measurement of the elements.

2.3.1.1 X-ray fluorescence

The X-ray fluorescence (XRF) principle is based on the interaction of the X-ray beam with the samples [88]. When the X-ray beam hits the sample, the electron absorbs the energy and is ejected from the atom. The hole left behind by the ejected electron is filled by an outer shell electron, which emits an X-ray during the ‘falling’ to the inner shell. The X-ray energy emitted is equal to the difference between the two energy levels. Therefore, the material emits radiation specific to the element of the atom present. The composition of the sample can be determined by using this characteristic fluorescence spectrum and the XRF spectrum of the sample [89].

Fluorescence lines are first named according to which shell the electron falls into, for example, if the electron falls into the K shell, then it produces K lines. The second

name depends on from which shell the electron falls, α is for the lowest energy transition, then β and γ [89].

2.3.2 Scanning transmission X-ray microscopy (STXM)

Scanning transmission x-ray microscopy (STXM) is a synchrotron-based technique that combines the principles of transmission electron microscopy and scanning electron microscopy. It allows the imaging of structures while simultaneously producing spectral information of the chemical composition of the material present. This technique has a spatial resolution of approximately 20 nm, and its X-ray beam exposure does not induce chemical changes in the iron material compositions [90].

STXM is a soft X-ray microscopy with typical energy ranging between 100-1600 eV. Soft X-rays in the energy range between the C and O *K*-edge (284.2 eV and 543.1 eV), termed the 'water window' allows the investigation of hydrated, intact and unstained biological samples to be investigated [89]. In this thesis, the samples used are human brain tissue, and although, they are not hydrated, the application of this technique allows the imaging of the biological materials (protein structure) in the sample. Raster scanning the sample at an energy creates an energy specific image map across the sample. The absorbance spectra of the sample are generated by recording the level of x-ray transmission across multiple energies through the desired energy range, for example, an energy range used in this thesis is iron *L*-edge 700 – 740 eV. The result is that each pixel in the image of a structure has an individual X-ray absorption spectrum. STXM allows the examination of the materials within the 'water window' and the metals found in a single structure, making STXM a powerful tool for characterising the metal content of a biological system and their interactions [90].

2.3.2.1 X-ray absorption spectral

When an energy from an incident X-ray beam generated by the synchrotron source hits the electron in the inner shell of the atom, the electron absorbs the energy and

excites to a higher energy shell. The photon energy of the X-ray beam is set to an energy range or ‘edge’ that excites the core electron of the material of interest. The absorption energy spectrum is sensitive to the oxidation state of the cation that absorb the X-ray. Thus, in this case, the recording the x-ray absorption spectrum across the iron L-edge produces the absorption spectrum of the oxidation state of the iron in the tissue material [90, 91].

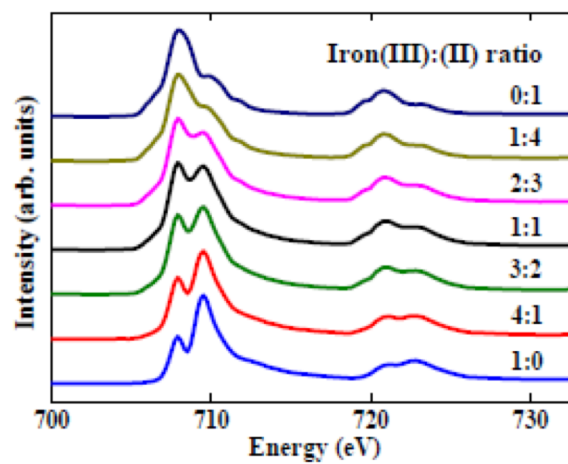


Figure 2.1 The iron L2 and L3 X-ray absorption edge spectra displaying the effect of varying the Fe^{3+} and Fe^{2+} ratios on the absorption features. The iron ratios are displayed above each spectrum. Reproduced with permission from Dr J. Everett (Everett 2015) [90].

The bright blue absorption spectra ($\text{Fe}^{3+}:\text{Fe}^{2+}$, 1:0), shown in figure 2.1, is the reference spectrum for pure Fe^{3+} minerals, which is characterised by the L_3 edge absorption peak that is dominant at the 709.5eV and a shoulder peak at the 708 eV and the two lower intensity L_2 edge absorption peaks at the 721 eV and 723eV. All the peaks arise from the X-ray absorption by the Fe^{3+} cations. The Fe^{3+} L_3 edge shoulder peak at 708 eV and the L_2 edge peak at 721 eV reside at the same energy as the Fe^{2+} L_3 and L_2 edge absorption peaks, respectively, that arise from the Fe^{2+} cations. The increase in the Fe^{2+} content of the iron material investigated will enhance these features, as shown in figure

2.1. The sensitivity of the technique allows the identification of different phases of iron found in the biomaterial [90].

2.4 Modelling technique and tools

Biochemical networks, such as brain iron metabolism, are intrinsically complex because of the large number of interacting components and their nonlinearity. The behaviour of these systems is not intuitive, and so a quantitative model is required to describe and understand better their functions [92]. Computational modelling systems biology provides a comprehensive and quantitative analysis, through computational modelling, for understanding the complex manner in which all of the components of a biological system interact. This approach allows for a comprehensive examination of the effect of the various components of the iron metabolic network over time. The model has the potential to be applied in a predictive capacity to analyse the behaviour of the iron metabolic system for simulated conditions and events [93, 94].

2.4.1 Ordinary Differential Equations Based Modelling

The biochemical networks are a set of chemical metabolites that undergo chemical reactions to convert into each other. The velocities of the chemical reactions are usually represented explicitly using mathematical expressions, such as ordinary differential equations (ODEs). Another representation available is probability distribution functions, but this method is not used in this thesis because it prefers a small number of metabolites. ODEs describe the dynamics of the concentrations of the chemical metabolites over time. An ODE is composed of the algebraic sum of the terms representing the rates of the reactions that affect the chemical metabolites, which is given by [92]:

$$\frac{dX}{dt} = \sum_{\text{all reactions } i} s_i \cdot v_i \quad \text{Eq. 2.1}$$

where s_i is a stoichiometry coefficient representing the number of molecules of metabolite X consumed or produced in one cycle of reaction i , and v_i is the velocity of the reaction i . A positive or negative sign indicates if the metabolite is produced or consumed, respectively. ODE models have been successfully applied to a variety of biological systems [95, 96], including liver iron metabolism [94].

2.4.2 COPASI

COPASI is a non-expert user friendly stand-alone software for systems biology modelling that provides a framework for deterministic and stochastic modelling [97]. COPASI offers the time course and steady state simulations. The steady state calculation in COPASI is carried out using a damped Newton method and forward or backward integration, depending on the user's preference. The time course simulations are useful for model validation from experimental time course results and also provide the simulated/predicted time course. Another tool provided by COPASI is the sensitivity analyses. In COPASI, there are two frameworks for doing sensitivity analyses, metabolic control analysis (MCA) and generic sensitivities [92].

2.4.3 Sensitivity analysis

Sensitivity analysis describes how much a specific parameter affects the behaviour of the model. The sensitivity analysis is used to identify the important parameters that require accurate values. Less accurate values are sufficient for parameters that are identified as less important. Sensitivity analysis can also give hints on the parameter that has to change to create a specific effect. The local sensitivity analysis measures the effect of varying a single parameter on the model.

MCA quantifies how much the rates of the various reactions in the model affect the concentration of the metabolites or the flux of the reactions at the steady state. It measures the distribution of control across the biochemical network [98, 99]. The results of MCA obtained by MCA measurement are concentration and flux control

coefficient. The values can be considered as the percentage change of the metabolite given a 1% change in the reaction rate [92].

Chapter 3 Brain iron imaging using synchrotron X-ray mapping

In this chapter, synchrotron based imaging techniques, synchrotron X-ray fluorescence (SXRF) and scanning transmission X-ray microscopy (STXM), are presented as strong quantitative and semi-quantitative methods to investigate the iron in the substantia nigra par compacta (SNpc) in control and Parkinson's disease (PD). The SNpc is of interest because it is one of the main regions that is affected by PD. The concentration of iron in this region increases in PD and there are losses in dopaminergic neurones, which contain of the pigment neuromelanin. The observed loss of these neurones, which leads to the resting tremor typically seen in PD patients, has been postulated to be caused by iron-induced oxidative stress. In this thesis, sensitive synchrotron imaging techniques were used to investigate the distribution of iron in tissue and cell level, as well as the state of the iron found.

3.1 Tissue sample preparation

The tissue samples were received from Newcastle Brain Tissue Resource and the Canadian Brain Tissue Bank. This project was done under the multi-centre research ethics committee (MREC) approval for the project 'Analysis and imaging of metal-ion accumulation in neurodegenerative disease' (REC reference number: 07/MRE08/12) held by Dr Joanna Collingwood, valid until 2020.

3.1.1 Preventing iron contamination of tissue samples

SXRF and STXM are highly sensitive spectroscopic mapping techniques. Any contamination in the sample could lead to false results, i.e. a signal that should not exist, or create a very strong signal that overshadows the neighbouring area. As iron is the main element of interest in this study, efforts were made to prevent iron contamination. This was done by not using metal tools in direct contact with the tissue samples, by using spectroscopically clean materials, and the highest purity chemicals during tissue processing.

3.1.2 SXRF tissue sample preparation

All of the sample preparation and data acquisition for the SXRF study were performed by Dr Joanna Collingwood and Dr Mary Finnegan before the start of this project. Details of how the samples were prepared have been published in their paper [17] and Dr Finnegan's PhD thesis [100]. The protocol implemented was similar to the one described by Antharam et al.(2012) [101]. All human tissue described in this thesis were either from the Newcastle Brain Tissue Resource (NBTR) at the University of Newcastle, UK, or the Canadian Brain Tissue Bank, Toronto, Canada. Full details are given elsewhere [100].

Three SNpc tissues from three different cases were examined using SXRF: one PD case and two controls. The reason for analysing this small set of cases was to test the feasibility of analysing human brain tissue by this method, in order to extract data for future use in computational modelling (chapter 4 and 5). The tissues used in this study are fresh frozen tissues, so they were not chemically fixed. Fixing tissue with a fixative solution has been shown to leach metals from tissue and potentially change the distribution, concentration and the state of metal in the sample. All tissues were stored in -80°C freezer at the metal trace lab at the School of Engineering, University of Warwick. They were received with case numbers assigned by the source brain bank. They were renamed to ensure anonymity with letter C or PD to represent the disease

state and a number (1, 2,...). The details of the tissue analysed in this study are listed in table 3-1.

Table 3-1 The details of the samples studied using SXRF mapping. C is control and PD is Parkinson's disease.

Case Number	Sex	Age
C1	M	85
C2	F	90
PD1	M	90

Before the tissue could be processed, it was kept overnight at a temperature of -25°C . Just before the dissection, the temperature of the tissue was increased to just below 0°C so it was soft enough to cut without fracturing the block. The cutting was performed in a low temperature environment, inside a cryostat or a biohazard hood cooled with dry ice. This was done to prevent the tissue from uncontrolled defrosting. The tissue was cut using a ceramic blade to prevent metal contamination. The tissue was then stored frozen in an airtight container.

3.1.2.1 Sample sectioning: Cryomicrotome

The tissue samples containing the region of interest were sectioned to a thickness of $30\text{ }\mu\text{m}$ using a cryomicrotome. Figure 3.1 shows the placement of the tissue sample and the blade on the microtome. A Leica Jung CM3000 cryomicrotome was used. A sapphire (non-metal) blade was installed to the cryomicrotome for the sectioning to prevent metal contamination. The prepared sample was mounted on the sectioning block of the cryomicrotome using Tissue-Tek mounting medium, but the sample was not embedded in the mounting medium to avoid introducing potential sources of metal contaminations.

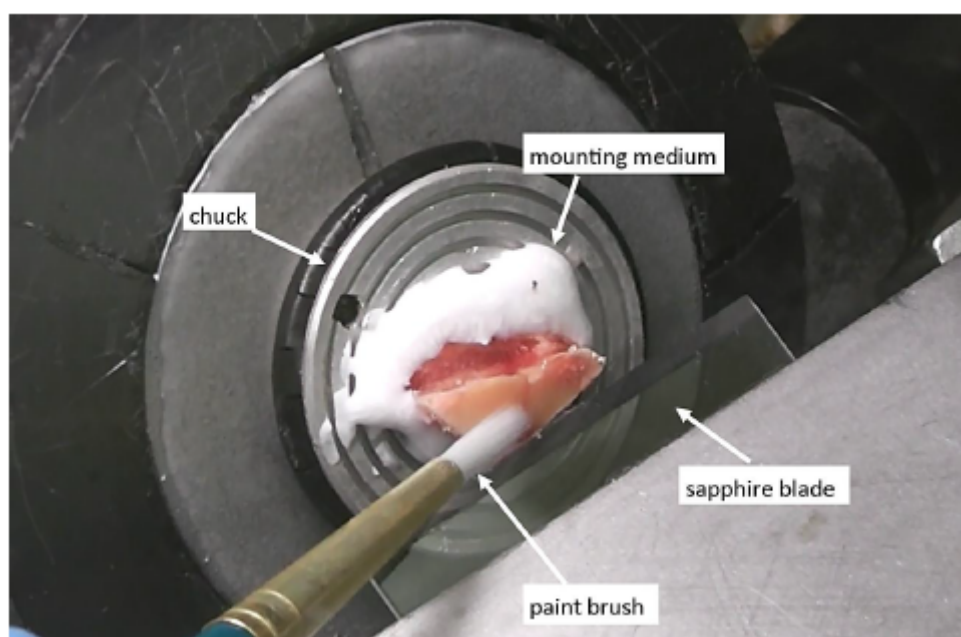


Figure 3.1 The set-up for tissue sectioning. The sample was not embedded in the mounting medium. There was only enough mounting medium to attach the sample on to the chuck. A sapphire blade was used for sectioning to prevent metal contamination. The paintbrush was used to control the section and prevent the tissue from curling after sectioning. (reproduced with permission from Dr M.E. Finnegan (Finnegan 2013) [100])

The sample was left covered in the cryomicrotome for at least an hour to bring the temperature to $\sim -17^{\circ}\text{C}$. Other instruments used during the sectioning, such as the sapphire blade and paintbrush, were also brought to the same temperature. The sapphire sectioning blade was set in the metal blade holder at a 10° angle and with approximately 15 mm of the blade protruding from the clamp. This was done so that the cut sections fell onto the blade and not the metal surface to avoid metal contamination. During the sectioning, the tip of a paintbrush was used to control and transfer the sections onto a quartz slide and to prevent the sections from curling. The sections were cut at $30\text{ }\mu\text{m}$ based on previous SXRF experiment experience by our group. A strong SXRF signal (above background) was obtained from $30\text{ }\mu\text{m}$ thick sections, using a dwell time of 1 second.

The sections on the quart slides were left to air dry inside a biohazard hood for at least 4 hours. The hood minimised the probability of particulate contaminants landing on the samples. After drying, the slides were subsequently covered with X-ray transparent Kapton film, to shield the samples from contamination outside the hood. PAP pen was used to fix the slides and the films around the edge and then they were sealed with epoxy resin. This step satisfied mandatory the health and safety requirements of the Diamond Light Source.

3.1.3 STXM tissue sample preparation

The STXM experiment is from a collaborative study including Dr Neil Telling and Dr James Everett from the University of Keele. The sample selection and the initial sample dehydration process for the samples selected for analysis in this thesis were performed by Dr Joanna Collingwood. The subsequent dehydration and embedding process was performed by Dr James Everett, assisted by the author. The tissues examined in the STXM study were fresh frozen tissue received from brain banks (as in section 3.1.2). They were stored under ethical approval in the -80°C freezer in the Trace Metals in Medicine laboratory in the School of Engineering, University of Warwick.

Two SN tissues from two different cases were prepared and measured using STXM (table 3-2): one PD case and one control. The control case investigated using STXM is the same case analysed using the SXRF, C1. The PD case (PD2) is independent of PD1 analysed by SXRF.

Table 3-2 The details of the samples studied STXM mapping. C is control and PD is Parkinson's disease

Case Number	Sex	Age
C1	M	85
PD2	M	85

During the STXM sample preparation, the tissue blocks were brought to room temperature, but the initial sample selection and excision were performed inside a cryostat to keep the remaining tissue block frozen. Inside the cryostat, several cubes of $\sim 1\text{mm}^3$ of substantia nigra tissue were cut from the rest of the tissue block. A ceramic blade was used to cut the tissue to avoid iron contamination. The tissue blocks were placed on a clean weighing boat for the dehydration process. The dehydration process was executed in a biosafety cabinet.

Inside the biosafety cabinet, the tissue blocks were immersed in an alcohol solution to remove the water content from the tissues slowly. The solution was changed every 2 hours (5 times in total) and with each change, the concentration of the alcohol solution was increased: 25% (75% pure water), 50% (50% pure water), 75% (25% pure water), and 100% to anhydrous ethanol (twice). Anhydrous ethanol is ethanol after trace water content has been removed using zeolite. Failure to fully dehydrate tissue samples would result in poor section integrity. After the last alcohol immersion step, the tissue blocks were moved into a glass vial for the embedding process.

The resin used for the tissue embedding was comprised of a 1:1 molar ratio of trimethylolpropane triglycidyl ether and 4,4'-methylenebis (2-methylcyclohexylamine). This resin was chosen because it is STXM compatible, containing no carbonyl or aromatic groups, which means it does not have a strong carbon K-absorption edge spectral feature. Chemistry of the iron in the tissue is also unaffected by the resin [102, 103].

To allow the resin to penetrate the tissue sections completely, the tissue sections were not directly embedded in 100% resin solution. Like the dehydration process, the embedding process started with the immersion of the tissue sections in a solution with 25% resin (75% ethanol). The solution was replaced a total of seven times with higher resin concentration solution every 2 hours. The resin concentrations used were 25%, 50%, 75% and 100% (4 times). A fresh resin was made for every resin change. The resin was made inside a fume hood and was stored inside a glass vial because plastic

is not a compatible container for this resin. Once it was in a closed glass vial, it was safe to move the resin into the biosafety cabinet where the embedding process was carried out. Inside the biosafety cabinet, the resin solution was transferred into the glass vial containing the tissue sections using a disposable pipette. The glass vial was then placed on a slowly moving rotating mixer to keep the resin from setting.

After the fourth 100% resin immersion, all tissue sections in the glass were transferred into individual 0.5 ml Eppendorf tubes. A fresh resin was transferred into the tubes. The tubes were then put inside a 60°C oven for 6 hours to let the resin to set. If the resin did not start to set after 4 hours, the resin would not set. The reason for the resin not setting might be because of the mixing of a slightly different molar ratio of the two resin solutions and the resin not being well mixed. Great care was taken to ensure that the embedding was successful.

3.1.3.1 Sample sectioning: Ultramicrotome

Once the resin had set, the resin embedded tissue was sectioned into thin sections (100 – 200 nm) using an ultramicrotome. The resin embedded tissue was removed from the Eppendorf tube and fixed on the sample holder of the ultramicrotome. Depending on where the tissue sample was located in the resin block, excess resin was trimmed away using a clean room standard razor blade. The razor blade contains iron, so the cutting was stopped when there was ~1 mm of resin left between the razor and the tissue sample, to ensure that the razor never came into contact with the tissue sample. The sample was then placed on the ultramicrotome.

The trimming was continued using a glass knife on the ultra-microtome. Glass knife is used for trimming because it is relatively cheaper than the diamond or sapphire knife. Once the knife reached the tissue block, the resin block was trimmed to create a square section of 1 - 1.5 mm².

The glass knife was exchanged for a diamond knife to section the tissue sections to be collected for the STXM analysis. The diamond knife had a boat that was filled with a

10% ethanol solution in 18M Ω ultrapure water. When a section of the sample was cut, it would float on the ethanol solution in the boat. The section was then transferred on to a copper microscopy grid (100 mesh) by using the grid held between a pair of tweezers to scoop the sample or using a loop to transfer the section on to the grid. A bright field picture and transmission image of the sections on the grid was taken and then the grids were stored in a grid box for transport to the synchrotron facility.

3.2 Mapping methods

3.2.1 SXRF mapping

SXRF mapping was performed on the 30 μ m thick tissue sections at the microfocus spectroscopy beamline (I18) at the Diamond Light Source (DLS), in Oxford, UK. Data were collected during three separate visits to the DLS over a period of 3 years (2008 – 2010). Table 3-3 lists all the samples analysed. Experiments A and B were performed by Dr Joanna Collingwood and experiment C was performed by Dr Mary Finnegan before the start of this PhD. The data collected from these experiments were processed by the author to produce metal maps illustrating the distribution and relative concentration of iron in the sample.

Table 3-3 List of all the Diamond Light Source (DLS) experiments and the samples presented in this thesis. C represents control cases and PD represents the Parkinson's disease cases. JFC: Dr J.F. Collingwood and MEF: Dr M.E. Finnegan

Main experiment investigator	Experiment	Date	Case number
JFC	A	Oct 2008	PD1
JFC	B	Sep 2009	C1
MEF	C	Aug 2010	C2

3.2.1.1 SXRF Experimental setup

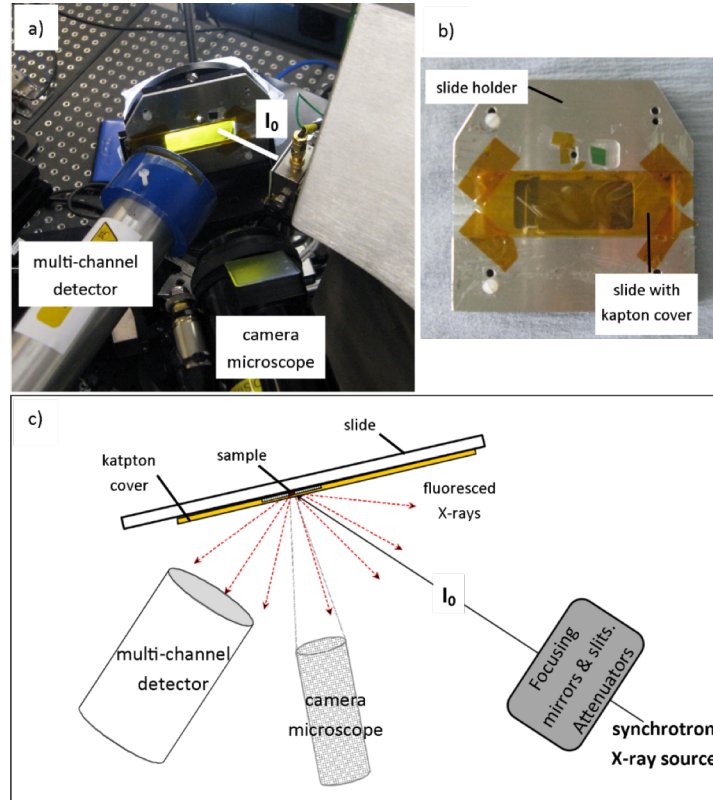


Figure 3.2 SXRF mapping set-up reproduced with permission from Dr M.E. Finnegan (Finnegan 2013) [100]. a) a photograph of the configuration of the experimental set up taken by Dr M.E. Finnegan at I18, b) the photograph of the sample fixed on the slide holder. The slide is covered by kapton film, c) the schematic of the experimental set-up corresponding to a).

The setup of the SXRF experiment is shown in figure 3.2. The quartz slide containing the tissue sections covered with the Kapton film was mounted on to the slide holder. The sample holder then was fixed on the sample stage, which was positioned at a 45° angle to the incident X-ray beam (I_0). The multi-channel detector was positioned perpendicular to the I_0 . A microscope camera was set focusing on the focal point of the beam. This camera allows the experimenter to view the sample position while moving the sample back and forth along the z-direction to bring the sample to the focal point of the beam. Once the sample was in the focal plane, the z-axis position was kept

constant. When the sample is in focus, the X-ray beam is at or near the centre of the beam. To create a map, the sample stage can also be moved horizontally (x-axis direction) and vertically (y-axis direction).

Once the slide holder with the sample slide was mounted on the sample stage, the coordinate of the map was set. Optical microscopy and staining of adjacent sections were used to locate regions of interest for mapping. Due to time consuming mapping and limited experiment time, it was important to select carefully the area to be mapped at high resolution. When mapping is not in progress, e.g. when the mapping coordinate is being selected, one of the beam shutters was closed to prevent the beam from reaching the samples. This stops the samples from being damaged by unnecessary prolonged exposure of high intensity x-rays. The signal from the slide (excluding tissue) was also measured so later it could be subtracted during data processing.

3.2.1.2 Data acquisition: Creating an SXRF map

The samples were mapped using the step mode. In this mode, the sample was moved by one step at a time. The detector collected the signal for a specified dwell time, one second per point, before the sample was moved to the next point in the map. It took approximately 0.5 seconds for the sample stage to move from one point to the next. The step size was matched to the beam spot size, which was 60 x 60 μm for the main map. Thus each pixel in the main map contains compositional information from a volume of 60 x 60 x 30 μm (section thickness) of wet tissue.

3.2.2 STXM mapping

The STXM mapping was performed on the Molecular Environmental Science (11.0.2) beamline at the Advanced Light Source (ALS) (Berkeley, USA). The data were collected during one visit to the ALS in 2015. Dr Neil Telling was the head investigator of the experiment. The aim of the experiment was to obtain images of the

iron distribution and the X-ray absorption spectroscopy data to indicate the redox state of the iron in the SNpc tissue.

3.2.2.1 STXM Experimental Setup

Before the start of the experiment, the samples to be imaged were selected based on images of the resin sections on the copper grid taken with a light microscope. Optimal sections (i.e. sections with the flattest area on the grid holes) were mounted onto stainless steel microscopy plates for the STXM imaging. The plates were then inserted onto the sample holder in the STXM chamber. Unlike the SXRF beamline at DLS, there is no camera overlooking the set up to view the sample position in this beamline. However, there is a window on the STXM chamber that the experimenter can look into to check that the zone plate does not collide with the sample during focusing.

Images of the sections of the slide were used to determine the region of interest on the tissue section. Due to time consuming mapping and limited experiment time, it was important to select carefully the area to be mapped at high resolution. When mapping is not in progress, the beam shutters automatically close to prevent the beam from reaching the samples. This stopped the samples from being damaged by unnecessary prolonged exposure of high intensity x-rays.

3.2.2.2 Data acquisition: STXM map

A large coarse scan of the sample, typically 2mm^2 , was performed to obtain the full image of the section at the peak carbon K-edge absorption energy for the tissue protein structure (288.3 eV). This large map was used to identify the area of interest. The region of interest was raster scanned at 288.3 eV to show the biological structure at a resolution of 100 – 600 nm. Another scan of the same area was taken at 290 eV, which is the peak carbon K-edge absorption energy for the epoxy resin used in the embedding process. Subtracting images obtained at 290 eV from images obtained at 288.3 eV removes the carbon artefacts from the resin material, as shown in figure 3.3. This subtraction process is done using the aXis2000 software [104].

The carbon K-edge absorption spectra for the region of interest in the biological

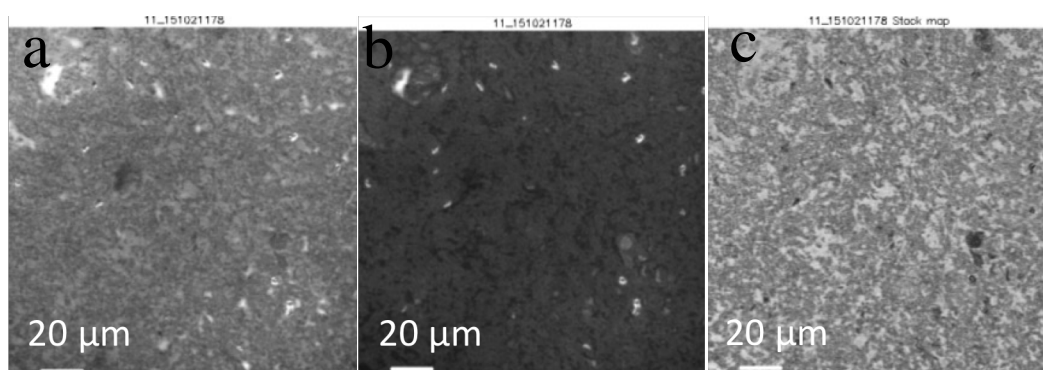


Figure 3.3 Subtraction process performed in Axis2000. (a) image at the protein peak carbon *K*-edge absorption energy, 288.3 eV. (b) image at the resin peak carbon *K*-edge absorption energy, 290 eV. (c) image created by subtracting image (b) from (a). The subtraction also removes artefact from the image.

sample was performed by doing multiple raster scans at different energies over the same area, known as carbon ‘stacks’. These stacks were performed at an energy resolution of 0.1 eV. The carbon stacks maps are performed at a lower spatial resolution than the single raster map due to time constraints.

To reveal the iron content within the tissue, another raster scan of the same area was performed at the iron L_3 -edge, similar to the raster scan at the carbon K -edge energy. The iron peak scan is performed at the energy of 710 eV and the off peak scan at the energy of 705 eV. The difference map of these two scans creates an artefact-free map that shows the location of the iron deposit. Further scans with higher spatial resolution, approximately 30 nm at the iron L_3 -edge, were made to confirm the presence of the iron deposit. Iron stack scans were performed at the iron L -edge absorption energy to obtain detailed x-ray absorption spectra of the iron deposit. The iron absorption spectra are compared to the reference iron absorption spectra to determine the oxidation state of the iron deposits.

3.2.2.2.1 Neuromelanin absorption spectroscopy

During the experiment, a carbon stack map of a tissue area that was suspected to contain neuromelanin was observed. By going through the stack images at different energies, an energy that reveals only neuromelanin-like granular structure within the protein tissue structure was determined. The images at different energies are shown in figure 3.4. The image at the carbon K -edge energy 286 eV shows a very clear picture of the granular structure but not the surrounding protein. This energy was used during the experiment to image different areas that might include neuromelanin. Carbon K -edge energy 278 eV was chosen as the off peak energy for the candidate neuromelanin image mapping because less features are shown at this energy. The final candidate neuromelanin parametric image is created by subtracting the image at 278 eV from that at 286 eV.

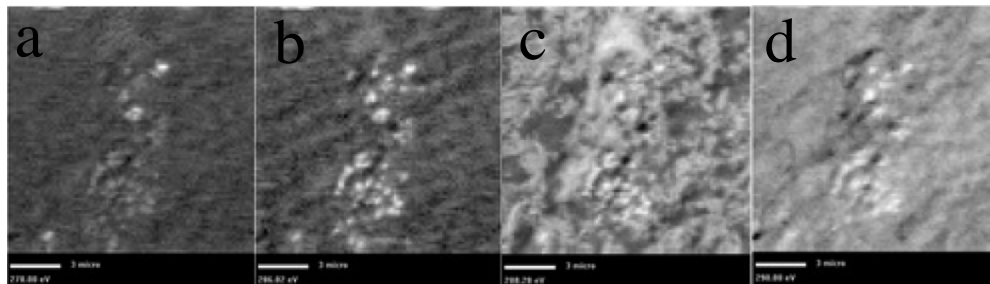


Figure 3.4 Images of the carbon K-edge STXM protein map selected from the carbon stacks performed over the carbon K-edge. The selected energy map are: (a) 278 eV, off peak energy, (b) 286 eV, the proposed energy for the neuromelanin-like granular structure, (c) 288.3 eV, peak energy for tissue protein structure, and (d) 290 eV peak energy for the embedding resin. Mapping at 286 eV shows the most granular features without the tissue protein structure.

3.3 Data processing

3.3.1 SXRF data processing

Each SXRF map file collected consists of the fluorescence spectrum for each data point. This section describes how comparison maps of the relative iron were created: fitting of the fluorescence peaks, calculating the area under the peaks, data normalisation and background subtraction. PyMCA and ImageJ, an open source software, were used to process the data.

Each set of SXRF map file is accompanied by an RGB file. The RGB file comprises the distribution and signal intensity of the key metals that are expected in biological tissues. The signal intensity data are not fitted to the fluorescence peak at this stage, and are not corrected for overlapping peaks or background signal. To obtain the relative metal concentration of the metal peaks, the peaks of the SXRF signal from these files, therefore, have to be fitted.

3.3.1.1 SXRF spectral fitting

The fluorescence spectra of the SXRF map were fitted using PyMCA. The fitting process starts with calibrating the energy of the detector channels. Known characteristic peaks of fluorescence spectra were used to set the detector channels to the correct energy, as shown in figure 3.5. Next, the peaks and background signal and the edge of the scatter peak were fitted using the ‘Advanced Fit’ tool. This fitted the average fluorescence spectra of the whole map. Once the best fit for the average spectra was obtained, this was then used to fit individual spectra at each pixel on the map. This fitting setting was saved and then reused to fit spectra of new maps with adjustments, if necessary. The fitted output file was then opened using the RGB correlator tool in PyMCA. In this tool, a distribution map for each of the individual

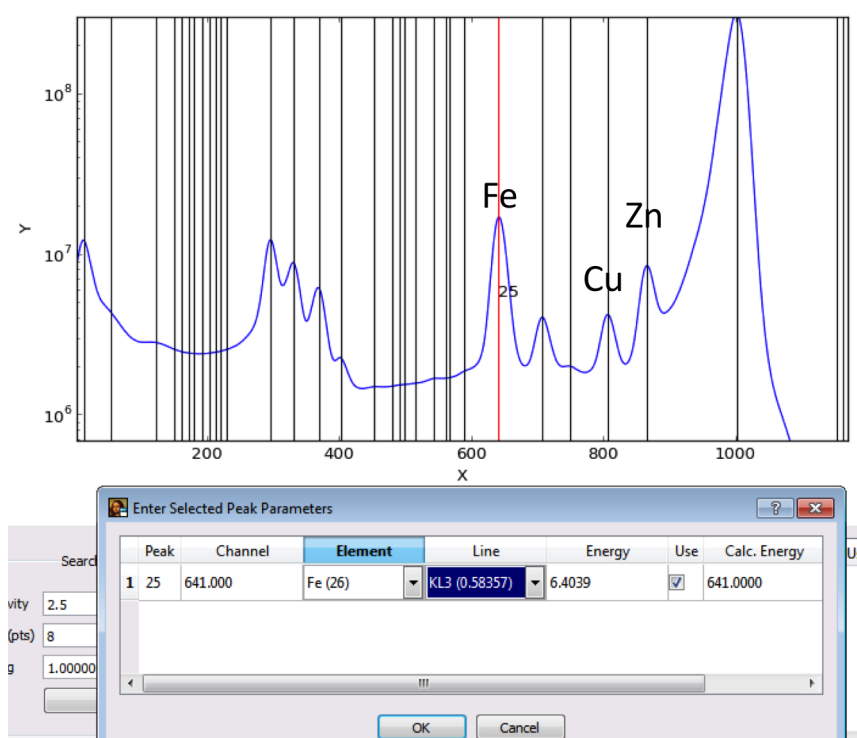


Figure 3.5 Calibration of the energy of the detector channels in PyMCA software. The element for the fluorescence peaks are identified and saved. The peak energy for Fe $K\alpha$ is 6.4039KeV.

metals fitted could be viewed and the relative concentration of the metals could be normalised as described in the next subsection.

3.3.1.2 Data normalisation

To produce a relative concentration metal map that is comparable across the sample and between different samples, the spectra must be corrected to account for possible experimental errors. These errors are: varying electron beam intensity, attenuator used in the experiments, and a shift in the detector position. This section will explain how these errors were corrected.

Although the energy of the beam at DLS is stable the intensity of the electron beams could vary depending on the time of data collection and also between experiments. The electron beam intensity has a step profile due to the difference in the intensity of the beam as the beam decays over time and is periodically topped up. The solution is to normalise the spectra in each pixel in the map to incident flux, I_0 , for that pixel. Normalisation to I_0 also corrected for changes in the intensity of I_0 due to the insertion of attenuators into the x-ray beam. This process was done using the RGB correlator tool in PyMCA, following the spectral fitting described in the previous subsection. The I_0 map from the corresponding RGB file was opened in RGB correlator tool. Then, using the image calculator tool in the software, each metal map was normalised to the I_0 and saved into Tiff format.

3.3.1.3 Region of Interest (ROI) analysis in ImageJ.

ImageJ is a free open-source software. It allows the measurement of signal intensity in the ROI in the normalised metal maps. Each pixel in the saved Tiff file contains the fitted and normalised area under the fluorescence peak for the chosen metal (e.g. iron, copper and zinc). By drawing ROIs around different tissue structures, the normalised SXRF signal intensity of these structures could be measured.

3.3.1.4 Background subtraction

The amount of fluoresced x-ray beam received by the detector is affected by the distance and angle of the detector relative to the sample. However, the position and angle could vary considerably between experiments and even over a single experiment due to detector movement during sample changes. A marker was placed to minimise such changes but slight variation was still possible. To correct for this error, the average background signal from the quartz slide was subtracted from each pixel of the metal map with ImageJ.

3.3.1.5 Signal threshold

Subtracting the average background signal from the slide for each pixel produced a pixel intensity value approximately close to zero. This value was set as the lower threshold limit for the map signal by setting the value to 'NaN' in the 'adjust threshold' function in ImageJ. This will automatically exclude areas with signal intensity falling below this threshold, such as areas of tears or cracks in the tissue. An upper threshold was set to cut out high intensity signals from contamination such as dust and folded or curled area. The threshold was set with caution as not to remove true variation in metal signal in the tissue.

3.3.1.6 Sources of measurement uncertainty

When comparing the metal concentration between different tissues, the thickness of all the tissue sections were assumed to be consistent. Non-uniform thickness may be one potential source of error. This error was minimised by using, at the time, a recently serviced and calibrated cryo-microtome. SXRF spectra fitting and background normalisation may also provide a source of error.

3.3.1.7 Segmentation of SXRF images

The samples here were segmented and analysed as a feasibility exercise to show that the analytical methods included in this chapter could be used in the future to fully

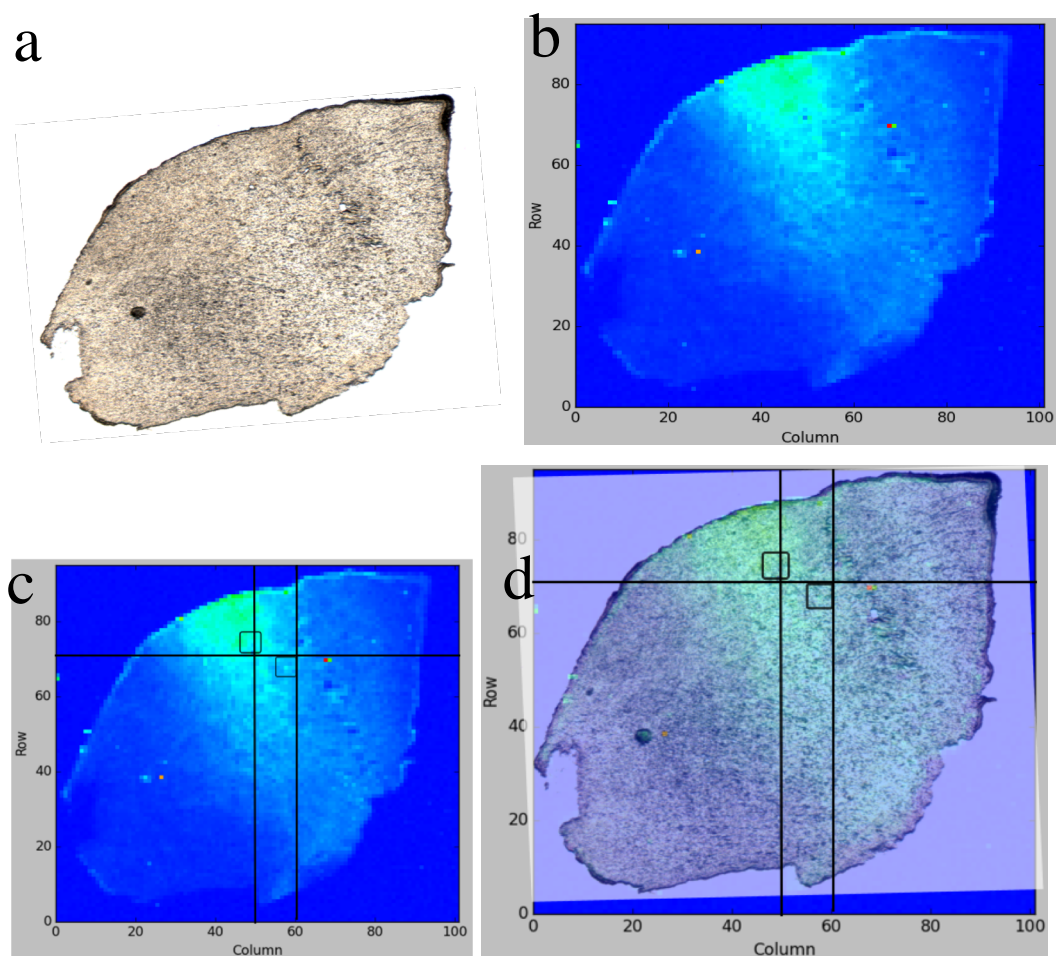


Figure 3.6 Images of the step to step process performed to determine the area of the optical image that corresponds to the high resolution map 1 and 2. (a) optical image of the whole tissue section. (b) the corresponding iron fluorescence map of the whole section. (c) the area where the high resolution scan were performed. The areas are labelled 1 and 2. (d) overlapped image of the optical image over the fluorescence map to determine the optical image that corresponds to the high resolution fluorescence map.

quantify the parameters of interest using SXRF, and that the quantified result could support computational modelling.

After the background subtraction and the threshold setting, relative fluorescence signal intensity can now be measured. To obtain the concentration of the iron in the cells and in the neuropil (area of the tissue that immediately surrounding the cells), the map has to be segmented by comparing the map to the corresponding optical image. From the optical image, cells can be identified and segmented from the rest of the area. The ‘freehand selection’ tool in ImageJ can be used to draw around the area of interest, in this case, the cells and measure the mean intensity of the selected area. This section describes the process of finding the right area in the optical image that corresponds to the high resolution fluorescence map and the segmentation process.

The optical image and the whole area map for PD1 tissue map are shown in figure 3.6a. By comparing the coordinate value for the higher resolution with the coordinate value from the whole fluorescence map the approximate area with the higher resolution can be found. The process is shown in figure 3.6b. Next, by overlapping the two maps, the optical image and the fluorescence image, together, the approximate area where the high resolution maps were taken could be determined, shown in figure 3.6. Once the area of the corresponding optical image for the highest resolution map is found, the cells are segmented from the area.

In ImageJ, the cell areas, determined by comparing to the optical image, are selected using the ‘freehand selection’ tool. Holding the shift button while selecting, allows multiple areas to be measured at the same time. Once all the cell areas are selected, the ‘measure’ function in ImageJ calculates the mean intensity in the pixels selected. This gives the mean intensity of the iron peak in the cells. The intensities of the neuropil area are calculated by first creating a mask (‘create a mask’ function) of the measured cells area, then by using the ‘threshold’ function on the mask area, the neuropil areas can be selected. The ‘analyse particle’ function saves the area, which

then can be applied to the original map to calculate the neuropil area, using the same measure function.

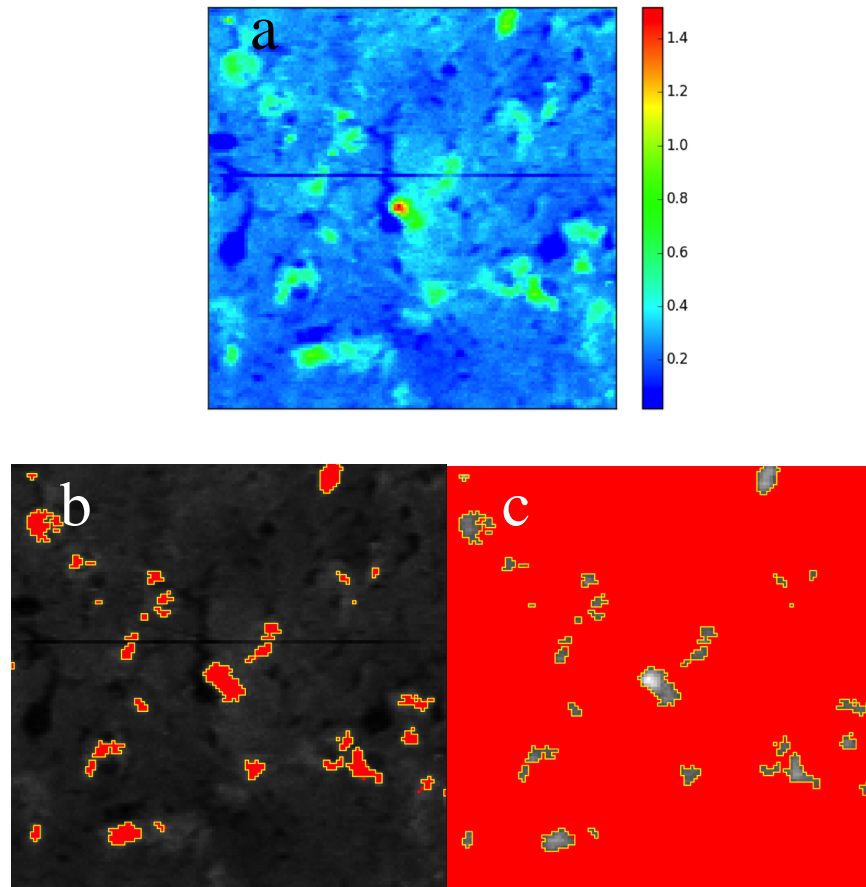


Figure 3.7 The segmenting process of tissue C2 with the guidance of fluorescence image from PyMCA. (a) fluorescence image of tissue section C2. (b) image of the fluorescence map with the cell areas circled in yellow and filled in red. (c) image of the fluorescence map with the rest of the areas filled in red.

Because the iron concentration in DA neurones is significantly above background, it may be feasible to perform segmentation even when limited optical information is available using the threshold function in ImageJ. The process begins using the threshold function to select areas with high iron signal intensities. The areas are selected by comparing to the fluorescence map from PyMCA. Then the process is similar to the one described above but without the need of using a mask. The ‘analyse

particle' function saves the area selected by the threshold then the areas are calculated by using the 'measure' function. Setting the threshold on the other end selects the areas that were not selected as the cells. The process is shown in figure 3.7.

3.3.2 STXM data processing

3.3.2.1 Background subtraction

aXis2000 (Analysis of X-ray Images and Spectra 2000) is a free imaging software program that was developed to process STXM data. In 'stack process' in aXis2000, the background signal attributed to the beamline signal is removed from the carbon or iron stacks images by converting the transmitted x-ray into optical density (OD). OD is given by [90]:

$$OD = \ln (I_0/I) \quad \text{Eq. 3.1}$$

where I_0 is the incident x-ray beam flux and I is the x-ray beam flux transmitted through the sample. In the 'stack process' window, the I_0 is obtained by selecting the area that does not contain tissue material (resin only area). The '→OD' function allows the OD conversion to be done automatically on the stacks map.

3.3.2.2 Energy map alignment

X-ray beam drift may occur during the long scanning time, up to 2 hours, for the carbon or iron stacks imaging. The zimba function in aXis2000 corrects this shift by aligning the multiple images taken at different energies to a common feature. Once the background has been subtracted from the images and the multiple images in the stack maps have been aligned, the spectra for a specific region of interest can be selected and saved in the 'stack process' window in aXis2000. The spectra are saved in the form of .txt file, which can be opened in Microsoft Excel or OriginPro 9.1 for plotting and further processing.

3.3.2.3 Composite map

The composite map in this chapter is created using ImageJ. The subtracted images to be overlaid, protein structure (288.3 eV and 290 eV), iron deposit (705 eV and 710 eV) and neuromelanin-like granular structure (278 eV and 286 eV), are opened in ImageJ. These images have to have the same pixels and bits for the composite map, and these maps usually do because they are taken at the same size and resolution. In the 'image tool', in ImageJ, the 'make composite' function can be used to overlay up to seven images using seven different colours, red, green, blue, grey, cyan, magenta and yellow. For the composite maps in this chapter, red is chosen to represent the iron deposit, green to represent the neuromelanin-like granular structure and cyan to represent the tissue protein structure. The brightness level for each image is adjusted to provide the best contrast. Then, the images are combined into a single RGB image by selecting the 'stack to RGB' function.

3.3.2.4 Spectral smoothing

Spectra smoothing is generally avoided in this chapter to preserve the peak feature of the spectra, except for the iron deposit G in figure 3.15. Iron deposit G spectrum was noisier than the rest, so spectral smoothing was performed to enable better peak identification. The smoothing is performed using the software, OriginPro 9.1, using the 'smoothing' function under analysis and signal processing. The Adjacent-Averaging method was chosen with point of windows of 5. The smoothing calculation was only performed on the off peak region of the spectra to preserve the peak feature. The rest of the iron spectra shown in this chapter are not processed.

3.4 Results

3.4.1 SXRF results: quantitative analysis from the SXRF map

The result of the quantification shows that on average the concentration of iron inside the cells of SNpc is higher by approximately 3x in control and 1.32x in PD. This result in isolation does not match the published result by Oakley et al. (2007) [84]. Although the method applied in the paper is not SXRF, the authors also measured the iron counts in the cells and the extracellular area/ neuropil in control and PD. Calculating the ratio from the results of Oakley et al. (2007) gives the ratio of the average iron counts in the cells compared to the extracellular region as 1.5x in control and 1.56x in PD.

The SXRF analysis shown here does not include sufficient cases to permit a statistical analysis, but this approach might be extended to evaluate well-matched sets of cases to describe tissue iron distribution at cellular resolution.

3.4.2 STXM results: identifying a neuromelanin signature

Figure 3.8a shows the image of the control human brain tissue at the carbon K-edge showing the protein tissue structure. The tissue map shows extensive tissue damage that is unlikely to be pathological, because this is a control tissue with no known neurodegenerative pathology. The likely cause of the extensive tissue damage is the sample archiving post-mortem, where large blocks were frozen more slowly than by plunge freezing.

Figure 3.8b shows neuromelanin-like granular structure found in the protein tissue shown in figure 3.8a. The process to obtain the granular structure image is described in section 3.2.2.2.1. The length of single granules in the structure shown is in the range of 200 to 700 nm, which is close to the published value (200- 600 nm) of neuromelanin

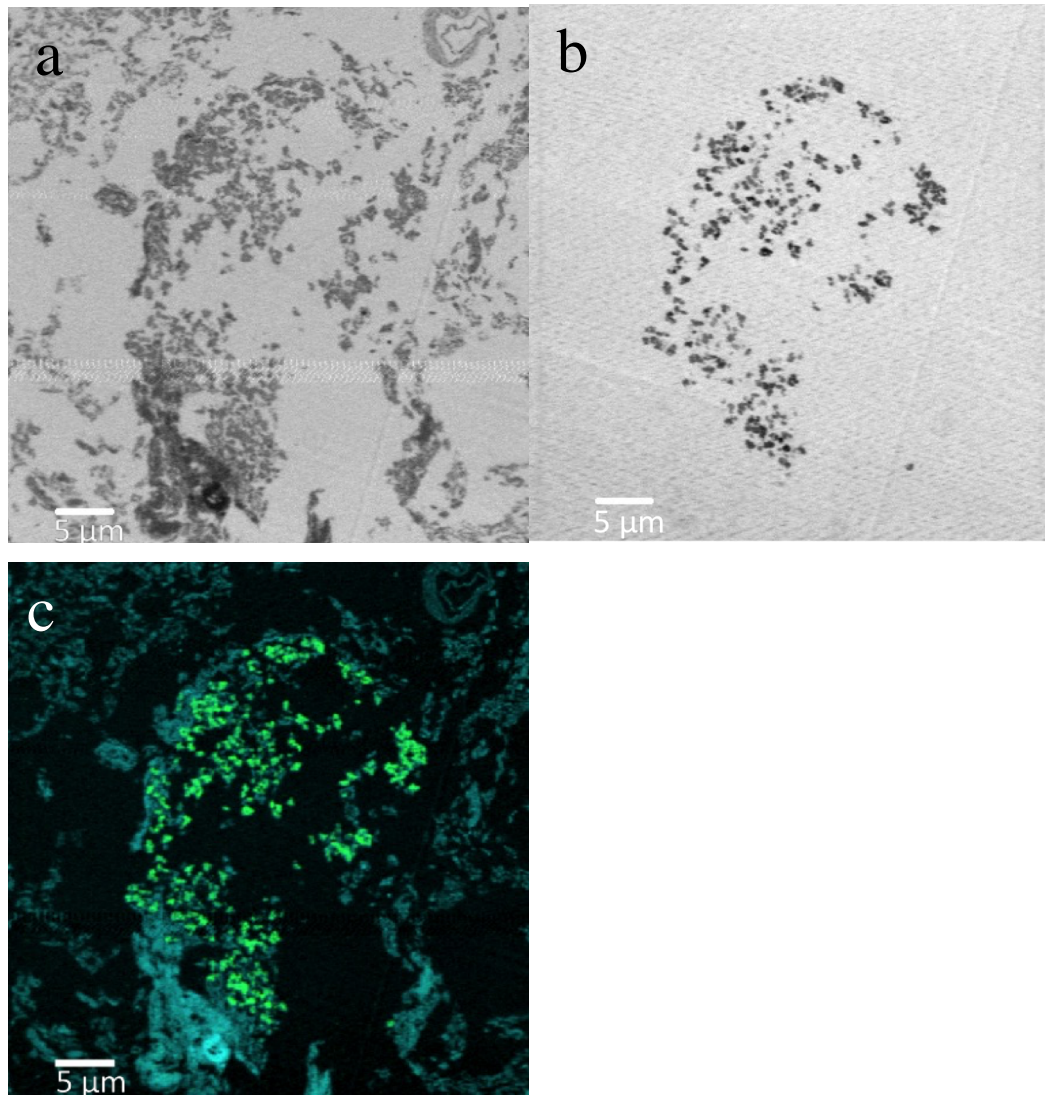


Figure 3.8 Carbon K-edge STXM protein map from a control (C1) tissue section. Neuromelanin-like granular structure within the tissue morphology. (a) Image of the tissue structure taken at the protein peak, 288.3 eV. (b) Image of the neuromelanin-like granular structure taken at the carbon K-edge energy of 286 eV. At this energy, the tissue structures are not visible. (c) Composite image of the area for the two energy map showing the neuromelanin-like granular structure localised within the protein structure. The protein structures are in cyan and the neuromelanin-like granular structures are in green.

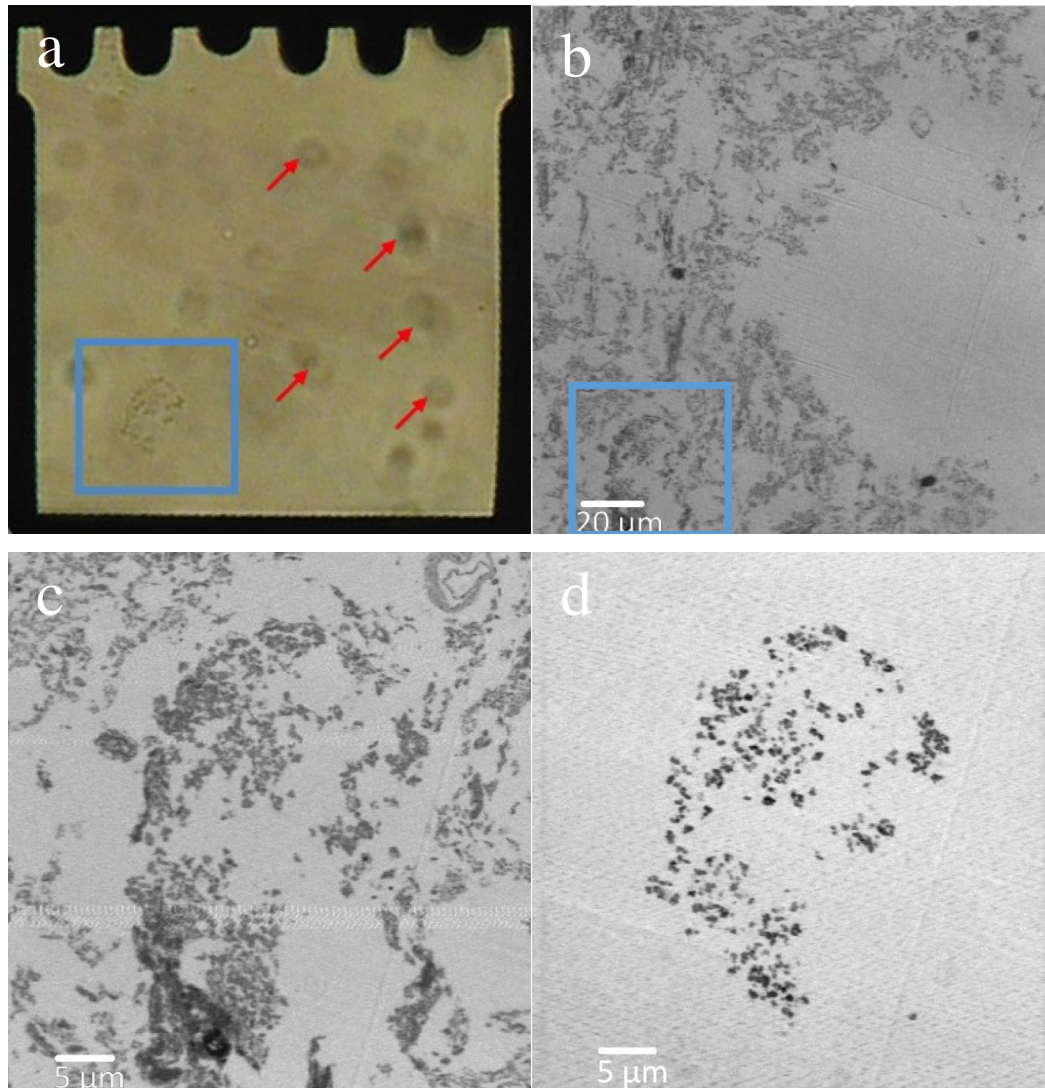


Figure 3.9 Images to determine the nature of the neuromelanin-like granular structure (a) transmission optical image of the tissue embedded resin on a 100 mesh copper electron-microscope grid (black squares surrounding the area). The red arrows point at the dust on the microscope and not on the sample. The structures in the blue box is possibly a neuromelanin. (b) The carbon K-edge STXM protein map taken at 288.3 eV showing the protein structure inside the electron grid square. (c) The carbon K-edge STXM protein map taken at 288.3 eV of the area in the blue box in (a) and (b). This image is taken at a higher resolution at 125nm. (d) The carbon K-edge STXM protein map taken at 286 eV showing the neuromelanin-like granular structure in the same area as (c). The shape of the neuromelanin-like granules corresponds to the neuromelanin structure in the optical image. (c) and (d) are the same images presented in figure 3.8 (a) and (b), respectively.

granules [57]. The composite map composed of the carbon K-edge image mapped at 288.3 eV (figure 1.10a) and 286 eV (figure 3.8), shows that the neuromelanin -like granular structure localised with the protein tissue structure, which may suggest that the granules were part of the tissue structure before it disintegrated. This matched with the profile of neuromelanin, as it is mainly contained in an organelle in dopaminergic cells.

To further determine if the structure mapped at the carbon K-edge energy 286 eV is truly neuromelanin, the carbon image is compared to an optical image of the tissue embedded resin of the same section of the same area. Figure 3.9a shows the optical image of the tissue embedded resin with a blue box indicating the area with the visible neuromelanin structure. Carbon K-edge protein map of the area inside the electron microscopy grid is shown in Figure 3.9b. From figure 3.9c and 3.9d, it can be determined that area enclosed the blue box in the figure 1.11b is the area where the neuromelanin-like granular structure is found at the carbon K-edge energy 286 eV. The size of the hole of the (100 mesh) electron microscopy is $\sim 200\mu\text{m}^2$. From this information, it can be deduced that the two blue boxes are indicating the same area. Moreover, the structure of the neuromelanin and the proposed neuromelanin-like structure are unique, such that it is extremely likely that they are the same structure. However, currently this is the only image of the neuromelanin-like structure mapped with STXM that can be compared to an optical image, so a definite conclusion on whether the carbon K-edge energy 286 eV is specific to neuromelanin structure cannot be drawn yet.

3.4.3 Iron chemistry in control tissue

The carbon K-edge map at the energy of 288.3 eV in the composite map, shown in figure 3.10a is of a different area of the same tissue section as figure 3.8a. The map reveals a similar extent of tissue damage that may affect the interpretation of the iron deposit location. As in figure 3.8, the composite map also shows neuromelanin-like structures localising in the tissue. More images of neuromelanin localising in the

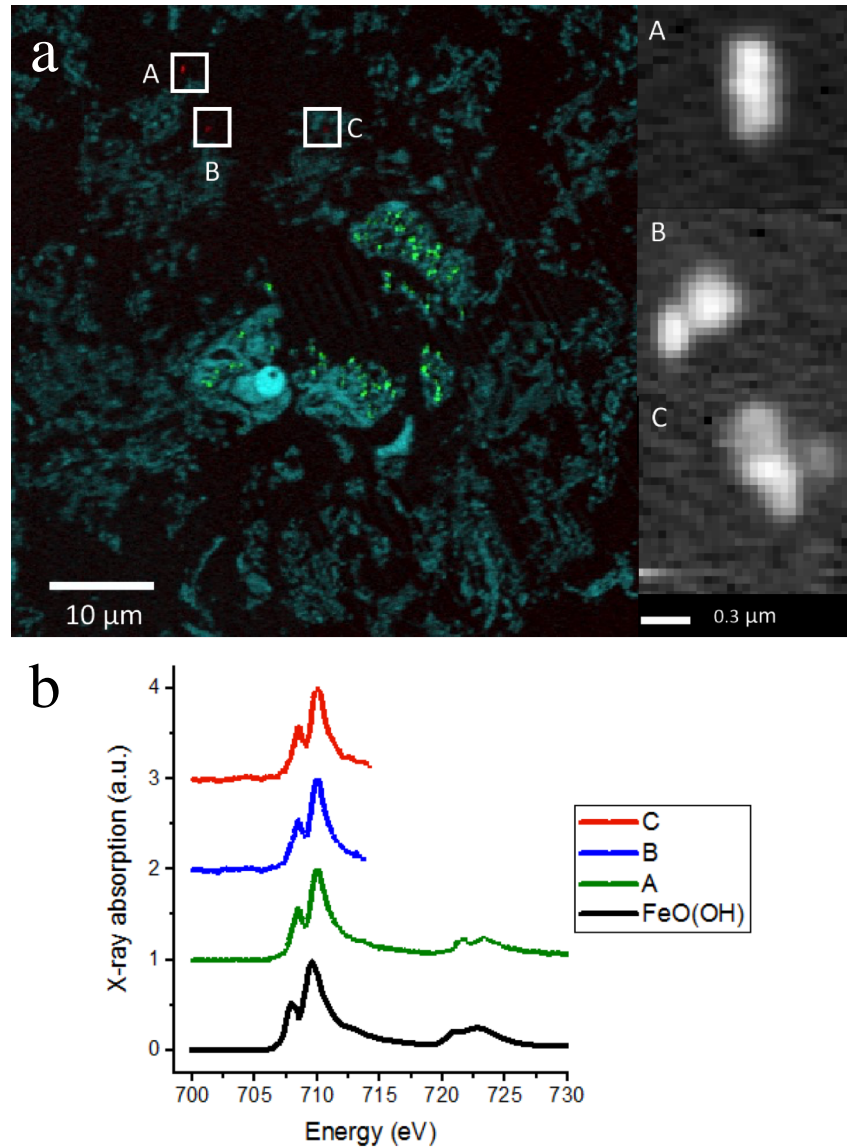


Figure 3.10 Iron deposits found within and out of the tissue structures of the control (C1) tissue section. (a) Composite map of STXM images of the tissue section at the resolution of 175 nm. The protein structures taken at carbon *K*-edge energy 288.3 eV are in cyan, the neuromelanin-like granular structures taken at carbon *K*-edge energy 286 eV are in green, and the iron deposits taken at iron *L*-edge energy 710 eV are in red. The three iron deposits are shown in a higher resolution map 50 nm labelled A, B and C. (A-C) background subtracted image of the iron deposit. (b) Iron *L*-edge X-ray absorption spectra of the three iron deposits comparable to Fe^{3+} ($\text{FeO}(\text{OH})$) reference spectra. Spectra for iron deposits B and C are cut short due to time constraint and they show obvious features of Fe^{3+} peak. The reference spectrum $\text{FeO}(\text{OH})$ was reproduced with permission from Dr J. Everett (Everett 2015) [90].

protein tissue structure were found but not shown in this thesis. No iron deposit was found in the neuromelanin structure in this tissue, but investigation on the SNpc of Alzheimer's disease brain tissue in parallel work from the group reveals iron deposits inside the neuromelanin.

Multiple areas of iron deposits (red spots) were observed inside and outside the protein tissue structure, as shown in figure 3.10a. The iron deposits observed in the control human brain tissue are approximately 300 nm in diameter and it does not exhibit any complex structure that is observed in the iron deposit of the brain tissue of AD mouse brain [103]. The comparison of the iron deposits spectra across the iron L_2 and L_3 -edge to the Fe^{3+} reference spectra demonstrate that they are present in a pure ferric form.

3.4.4 Iron chemistry in the PD tissue

The PD brain tissue investigated here has lost the neuromelanin pigment, so the neuromelanin structure observed in the control case cannot be considered directly equivalent compared to the neuromelanin measured in the PD case in this thesis. Tissue damage is also observed in this tissue, although to a lesser extent than in control tissue. It may be caused by the disease pathology or the preservation condition, and because of the fragmentation of the tissue, care should still be taken when interpreting the location of the iron deposits.

Carbon K-edge examination of the PD SNpc tissue shows that the iron deposits either co-localise directly with protein rich regions in the tissue section, or are adjacent to them. The carbon K-edge image is usually insufficient to prove if the iron deposits are intra- or extracellular except where cell membranes can be observed. The iron L-edge spectra of the iron deposits D and E in figure 3.11b demonstrate an increase in the

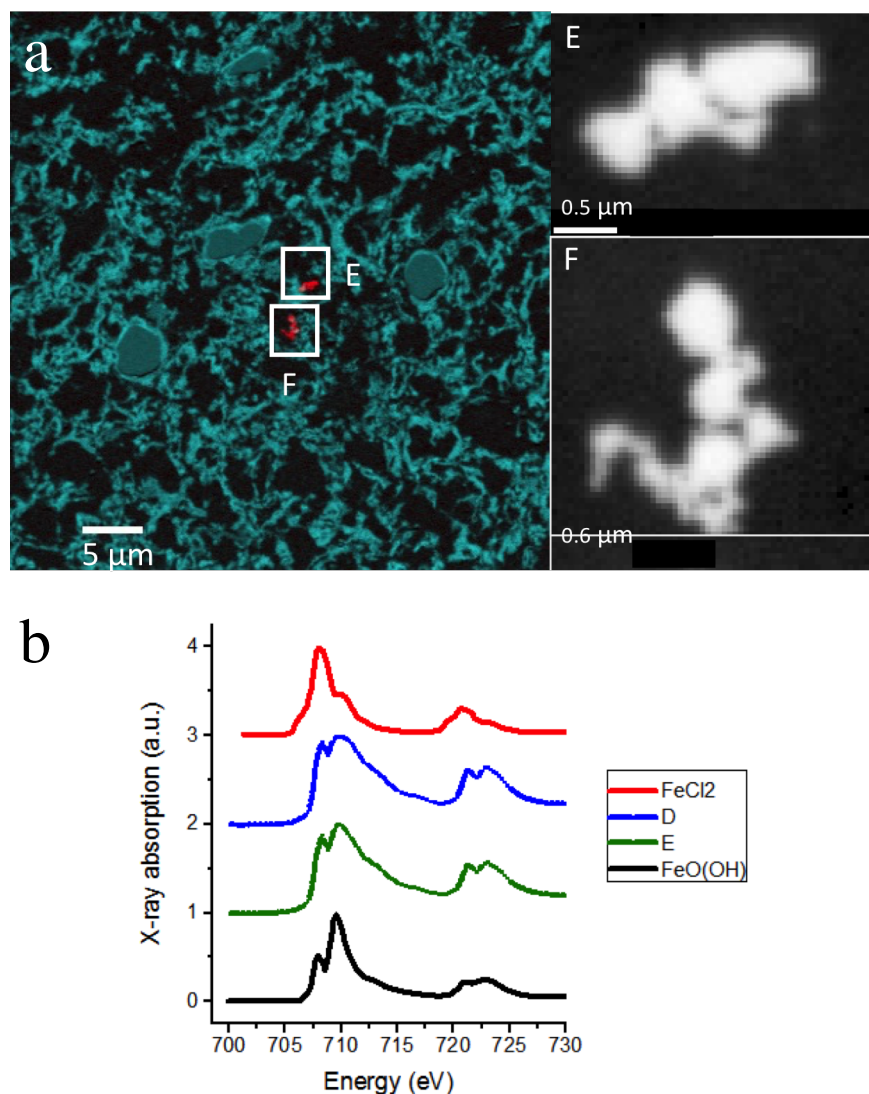


Figure 3.11 Iron deposits found within and out of the tissue structures of the Parkinson's disease (PD2) tissue section. (a) Composite map of STXM images of the section taken at different energy with a resolution of 125 nm. The protein structures taken at carbon K-edge energy 288.3 eV are in cyan and the iron deposits taken at iron L-edge energy 710 eV are in red. The neuromelanin is not present in this PD tissue. The two iron deposits are shown in a higher resolution map 50 nm labelled D and E. (D-E) background subtracted image of the iron deposit. (b) Iron L-edge X-ray absorption spectra of the two iron deposits. The iron deposit spectra are compared to Fe³⁺ (FeO(OH)) and Fe²⁺ (FeCl₂) reference spectra. Spectra for iron regions D and E demonstrate an increase intensity of the Fe²⁺ feature at 708 eV (L_3 edge) and 721 eV (L_2 edge), compared to the Fe³⁺ reference feature at 710 eV (L_3 edge) and 723 eV (L_2 edge). The reference spectra were reproduced with permission from Dr J. Everett (Everett 2015) [90].

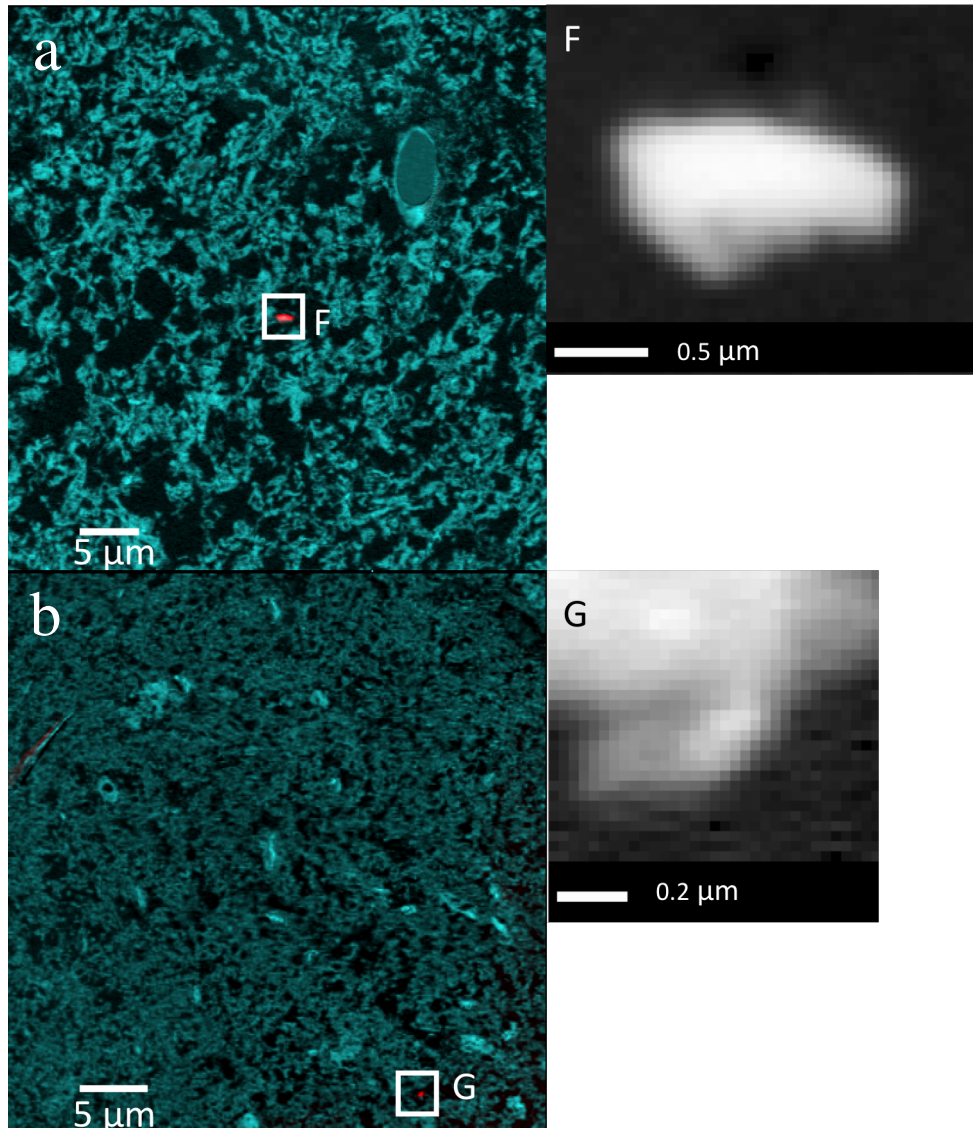


Figure 3.12 Iron deposits found within and out of the tissue structures of the Parkinson's disease (PD2) tissue section. (a) Composite map of STXM images of the section taken at different energy with a resolution of 125 nm. The protein structures taken at carbon K-edge energy 288.3 eV are in cyan and the iron deposits taken at iron L-edge energy 710 eV are in red. The neuromelanin is not present in this PD tissue. The two iron deposits are shown in a higher resolution map 50 nm labelled F and G. (F-G) background subtracted image of the iron deposit showing complex. The reference spectrum was reproduced with permission from Dr J. Everett (Everett 2015) [90].

intensities at the Fe^{2+} peak features compared to the reference Fe^{3+} peak. The iron L-edge spectra of the iron deposits F and G in figure 3.13 has lost the characteristic Fe^{3+} peak at the 710 eV and greatly resembles the zero valent (Fe^0) iron reference spectra. The zero valent form of iron is not commonly found in the measurement of biological materials, and its finding in amyloid plaque cores has only been recently reported by our group [105]. Ferrous and zero valent spectral contribution were not observed in the iron deposits sampled in the control.

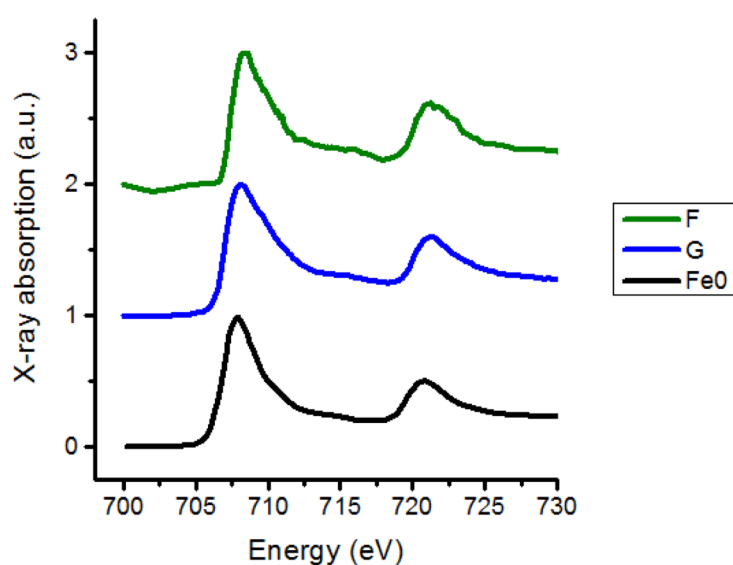


Figure 3.13 Iron L-edge X-ray absorption spectra of the two iron deposits. The iron deposit spectra are compared to zero valent iron (Fe^0) reference spectra. Spectra for iron regions D and E demonstrate a resemblance to spectra feature that is close to Fe^0 spectra. The reference spectrum was reproduced with permission from Dr J. Everett (Everett 2015) [90].

3.5 Discussion

3.5.1 SXRF iron quantification

SXRF mapping has been widely used in the quantification of metal contents in tissue sections, however, few studies have been published on its application on quantifying the iron content in cells and comparing it to the neuropil [106, 107]. Therefore, the purpose of the SXRF measurement in this chapter is to show the use of cutting edge techniques to investigate the relation of iron in disease. In the future, the result from these measurements can be applied to fit a computational model that represents the disease condition better or to validate the computational model in chapter 5.

The SXRF mapping in this thesis is for illustration purposes only, and the number of samples required for a detailed comparison might be estimated from prior single point microprobe studies, for example Oakley et al. (2007) [84].

3.5.2 STXM tissue mapping spectra from iron deposits

This thesis is the first to report possible energy at the carbon K-edge that is specific to neuromelanin.

The neuromelanin structure observed in the optical image of the resin, and the candidate neuromelanin granular structure that is mapped at 286 eV, strongly resemble each other. The size of the two structures is also similar. The finding of an energy peak that is specific to neuromelanin that can be applied to STXM would improve the way the compartmentalisation of the iron deposits in the neuromelanin and its oxidation state, can be studied. The methods that have currently been applied to study the iron deposits in the neuromelanin only allow the measurement or observation of the iron in the neuromelanin containing dopaminergic neurones, not specifically the neuromelanin granules. Using this energy, 286 eV, at the carbon K-edge to determine the neuromelanin, will allow the determination of the spatial distribution of the iron in

the neuromelanin and the oxidative states of the iron deposits. Detailed investigation of iron-neuromelanin relationships by STXM was beyond the scope of this thesis.

The iron L-edge x-ray absorption spectra of the iron deposits reveal ferrous iron deposits found in PD tissue that is not apparent in the control tissue. The iron deposits found in control tissues are in the form of pure ferric iron. Ferric iron in biological systems is mostly bound to the iron transporter, transferrin, or stored in the core of iron storage protein, ferritin. This bound ferric iron is stable and does not usually become involved in the production of reactive oxygen species (ROS). Therefore, this is consistent with iron being stored in the expected form.

The iron L-edge x-ray absorption spectra of the iron deposits F and G demonstrate the presence of zero valent iron (Fe⁰) in the PD tissue. The finding of zero valent iron state is not common. Everett et al. (2018) was the first to report the evidence of its presence in human amyloid plaque cores [105], and to the best of our knowledge this is the first observation of zero valent iron in PD tissue. The spectrum for Fe⁰ is easily distinguishable by the broader peak and the lacks of multiple fine structures. The zero valent iron findings are less likely to result from artefacts or contaminations during sample preparation, because no iron containing instruments were used in the process. The effect of prolonged exposure of x-ray on the iron has also been studied extensively and found that the x-ray beam does not chemically reduce the iron deposits in unstable aggregates even after repeated scans [90, 108].

While these findings show the power of STXM to reveal important information about iron in on PD, STXM only allows measurement of postmortem subjects (human/ animal models). The results from these methods will not reveal the dynamics of the disease progression, for example, the time it takes for iron to accumulate in the disease state. To address this, chapter 4 and 5 present the development of a computational model to be used as another effective tool to explore the role of iron in the brain, and to study dynamics of the iron uptake into the brain and dopaminergic neurone in health and disease (PD).

The published paper coming from collaborative work referred to in this chapter are included in Appendix E and F, and are as follows:

J. Everett, V. T. Tjhin, J. Brooks, F. Lermyte, I. Hands-Portman, J. Dobson, J. Collingwood, and N. Telling, "Nanoscale Examination of Biological Tissues Using X-ray Spectromicroscopy," *Microscopy and Microanalysis*, vol. 24, no. S2, pp. 490–491, 2018.

Everett, James, Joanna F. Collingwood, Vindy Tjendana-Tjhin, Jake Brooks, Frederik Lermyte, Germán Plascencia-Villa, Ian Hands-Portman, Jon Dobson, George Perry, and Neil D. Telling. "Nanoscale synchrotron X-ray speciation of iron and calcium compounds in amyloid plaque cores from Alzheimer's disease subjects." *Nanoscale* (2018).

Chapter 4 Modelling brain iron metabolism in the barrier systems

In chapter 3, we observed the capability of the synchrotron X-ray fluorescence to calculate the relative concentration of iron in the cell to the neuropil, and also the duality of scanning transmission X-ray microscopy, being capable of producing a high spatial resolution image of iron localisation in the tissue and determining the oxidative state of the iron. These are powerful techniques, however, they allow only to the investigation of iron in the post-mortem brain tissue. These data are the concentration of iron at one time point. The dysregulation of iron in Parkinson's disease (PD) has been observed for decades [2, 16, 109]. The accumulation of iron in this area has been linked to the death of cells in the tissue, but how this accumulation occurs and affect the disease progression is still not well understood [110, 111]. In this chapter, a computational model of the iron uptake in the brain is presented, which would provide an *in silico* qualitative and quantitative tool to explore the complex network of brain iron metabolism.

This chapter presents a computational model that has been developed from an initial concept by Drs J.F. Collingwood and S. Mitchell [112], which attempts to characterise iron transport in and out of the brain. The model concept was already well-developed with the majority of the reactions included at the outset of this PhD research. The initial work done was to fully understand and test the model, and to simulate alternative pathways, and determine if additional reactions were needed. The original contribution described in this chapter arises from this development and testing work,

and this unique model is the subject of a manuscript intended for joint publication including Drs J.F. Collingwood and S. Mitchell¹.

The iron in the blood and the brain is separated by the brain barrier system, the blood brain barrier (BBB) and the blood-cerebrospinal fluid barrier (BCB). Figure 4.1 illustrates the direction of flow of iron across these barriers and the full schematics of the uptake of iron into the brain adapted in the model. The additional complexity of the transport of iron into the dopaminergic (DA) neurone, one of the main cell affected in PD, is explored in chapter 5.

4.1 Iron uptake in the brain background

The brain receives iron from the blood circulation, but this uptake is not unrestricted [75]. The content of the brain is separated from the body by two barriers: the blood brain barrier (BBB) and the blood cerebrospinal fluid barrier (BCB). The BBB is formed by the brain capillary endothelial cells (BCECs) and separates the blood and the interstitial fluid (ISF) in the brain. The BCB is comprised of the epithelial cells of the choroid plexus in the brain ventricles and separates the blood from the cerebrospinal fluid (CSF) in the brain ventricles. The major flow of iron across these barriers is shown conceptually in figure 4.1. The cells in the BBB and the BCB are connected by tight junctions that prohibit the free exchange of iron between the brain and the body, thus iron has to be transported by a receptor mediated transport mechanism [113]. Transferrin receptors (TfRs) are on the luminal side of the BBB and the apical and abluminal side of BCB. TfRs bind with available transferrin-bound iron (Tf-Fe) and this initiates its endocytosis into the cells. Ferrireductase, such as six-transmembrane epithelial antigen of the prostate 3 (STEAP3) and divalent metal transporter 1 (DMT1), release the iron from the endosome into cell cytosol, creating the labile iron pool (LIP). The presence of DMT1 at the surface of the BBB recently

¹ Intended for submission to: Journal of Cerebral Blood Flow and Metabolism

started to be recognised [49]. In BCB, DMT1 is predominantly distributed on the apical surface of the BCB. The polarised distribution of DMT1 may indicate the dominant direction of iron flow in the BCB. Iron in the LIP is in a Ferrous (Fe^{2+}) state and is available to be taken up by and stored in ferritin, an iron storage protein, or to be transported out of the cell by ferroportin. Iron response proteins (IRPs) in the BBB post-transcriptionally regulate the expression of the TfR, DMT1, ferritin and ferroportin in the cells. In the liver, hepcidin regulates the degradation of ferroportin. The presence of hepcidin protein in this region has also been shown by several authors [73], but the translation of hepcidin in the brain is well known [74]. The model in this chapter disregards another hypothesis that states that systemic Tf-Fe^{3+} crosses the BBB and enters the ISF, as well as non-Tf-Fe transport, because it is commonly accepted that Tf-Fe is the primary species transported into the brain, where less than 1% of iron is in blood is unbound [7].

Once iron has crossed the BBB into the ISF, most of the iron is carried by brain transferrin (Tf) for neuronal activities. Excess iron in brain cells returns back to the ISF and is released into the CSF in the brain ventricles through bulk flow. The cells separating the ISF and the CSF are fenestrated allowing free exchange of iron between these compartments.

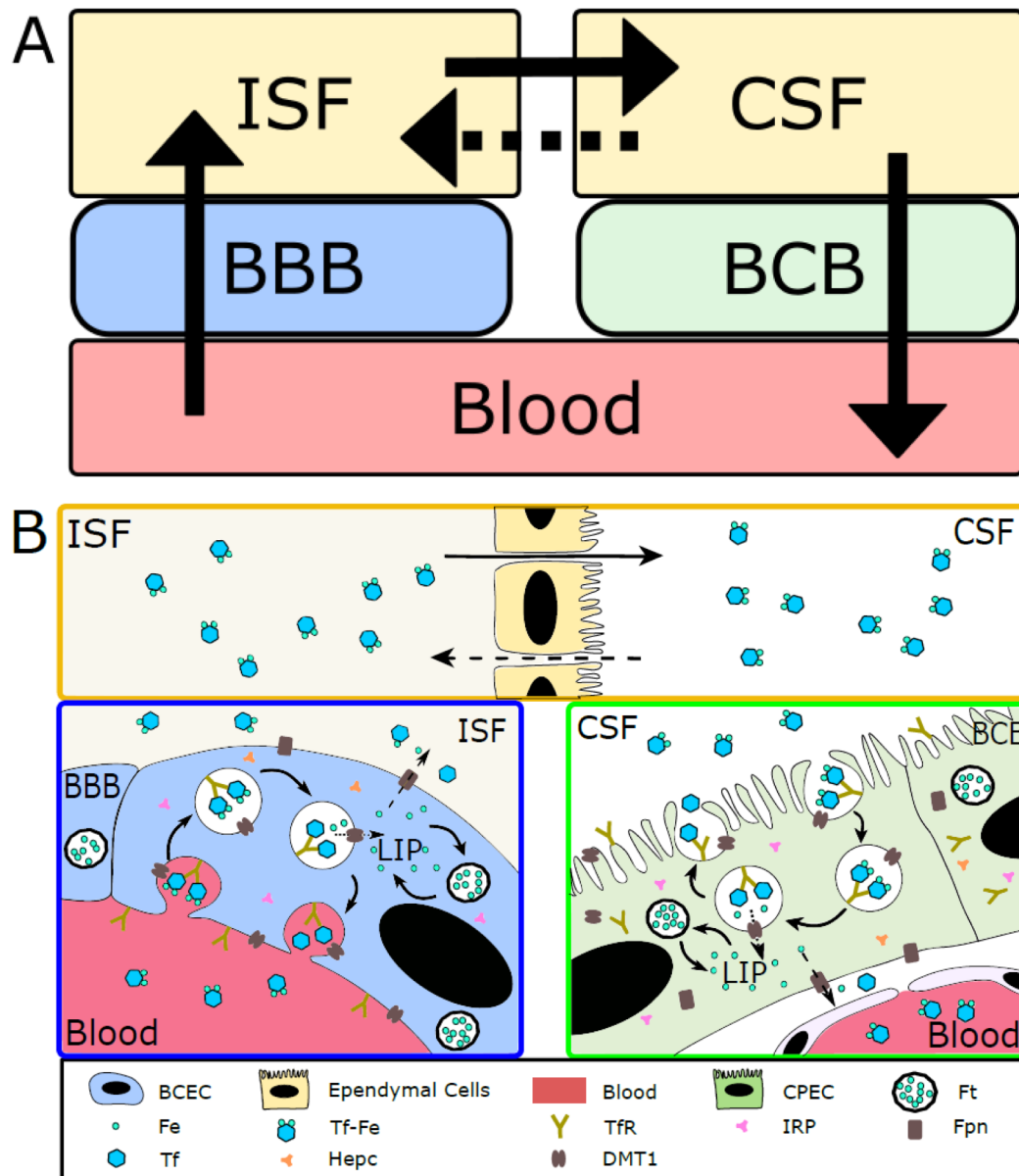


Figure 4.1 (A) Illustration of the flow of iron between the blood and the brain. The fenestrated cells between the ISF and the CSF allow free exchange of iron, but the direction of the fluid bulk flow is principally from the ISF into the CSF. The arrow represents the direction of the iron transport and the dotted arrow represents the weaker flow of Tf-Fe from ISF to CSF. (B) Conceptual biological diagram for iron uptake in the brain that the model in this chapter derived from. Abbreviations: BBB: blood brain barrier, BCB: blood cerebrospinal fluid, BCEC: brain capillary endothelial cell (comprises the BBB), CPEC: choroid plexus epithelial cell (comprises the BCB), CSF: cerebrospinal fluid, DMT1: divalent metal transporter 1, Fe: iron, Fpn: ferroportin, Ft: ferritin, Hepc: hepcidin, IRP: iron response protein, ISF: interstitial fluid, LIP: labile iron pool, Tf: transferrin, Tf-Fe: transferrin bound iron, TfR: transferrin receptor.

4.2 Materials and methods

The model is constructed, simulated and analysed using COPASI, a generic software package for biochemical system modelling [5]. The system biology graphical notation (SBGN) process diagram (figure 4.2) for the model was derived from figure 4.1 and created using Cell Designer [114]. Five compartments were constructed, representing the blood, the BBB, the interstitial fluid (ISF), the cerebrospinal fluid (CSF), and the BCB. The ISF surrounds the brain and provides iron for cells in the brain, so it represents the ‘brain’ compartment in this chapter. The volumes of these

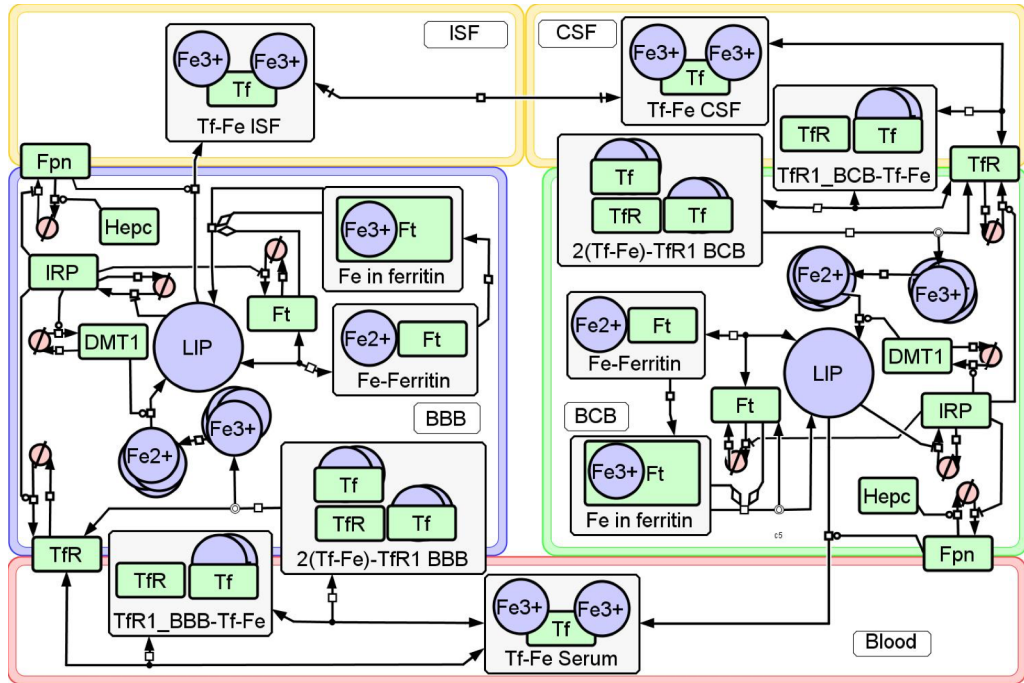


Figure 4.2 Systems Biology Graphical Notation (SBGN) process diagram of iron trafficking in the human brain barrier system model based on the mechanistic representation of the biological system shown in figure 4.1. Complexes are represented in boxes with component species. In the special case of the ferritin-iron complex symbol, the amounts of each species are not in stoichiometric amounts (there are thousands of iron ions per ferritin). Species overlaid on the compartment boundaries represent membrane-associated species. Abbreviation: BBB: blood brain barrier, BCB: blood cerebrospinal fluid, CSF: cerebrospinal fluid, DMT1: divalent metal transporter 1, Fe: iron, Fpn: ferroportin, Ft: ferritin, IRP: iron response protein, LIP: labile iron pool, Tf-Fe Serum: transferrin bound iron in the blood plasma, TfR: transferrin receptor.

compartments are listed in table 4-1. The corresponding volumes of the BBB and the BCB were derived by multiplying the total brain volume, 1400 ml, by the percentage of brain endothelial cells (BCECs) (0.2%) to give 2.8 ml [115, 116].

Table 4-1 Volume of model compartments

Compartment	Volume (l)	Source
Blood serum	0.15	human [115]
Blood brain barrier (BBB)	0.0028	human [115, 116]
Blood cerebrospinal fluid barrier (BCB)	0.0028	human [115, 116]
Interstitial fluid (ISF)	0.025	human [117]
Cerebrospinal fluid (CSF)	0.15	human [115]

Fe^{3+} binds strongly to Tf with an affinity constant, K_a , of 10^{22} M^{-1} [118], the K_{on} of the binding is $10^{20.2} \text{ M}^{-1} \text{ s}^{-1}$ [119]. The off rate for the reverse reaction ($K_a = K_{on}/K_{off}$) is very small, 0.0158 s^{-1} . Therefore, it was assumed that all iron arriving in the brain capillaries is of the form of Tf-Fe and the iron arriving at the ISF immediately binds to available empty Tf (apo-Tf) produced by neighbouring cells. The binding of iron to Apo-Tf was not considered in this model in order to avoid unnecessary complexity and also due to the high affinity of Apo-Tf to iron [39]. The concentration of Tf-Fe in the serum was fixed to represent the constant influx of iron from the liver. The concentration of hepcidin in both the BBB and the BCB was also fixed to represent hepcidin received from the liver. Hepcidin is mainly expressed in the liver and although this protein has been found in the brain, its translation in the brain is still not well established. It has been speculated that the hepcidin protein received in the brain is derived from the liver [73], thus the concentration of hepcidin is fixed in this model. The value of the concentration applied in this model was taken from the steady state simulation of hepcidin using the hepatocyte iron model built by Mitchell (2013) [120]. The initial concentrations of the metabolites were fixed to appropriate concentrations based on a literature survey, and for metabolites that go through a complex binding process, their initial concentrations were set to zero (table4-2).

Table 4-2 Initial concentration of all metabolites

Metabolites	Initial concentrations (M)	Source
Tf-Fe_Serum	5×10^{-6} (fixed)	human [121]
TfR_BBB	0	
TfR_BBB-Tf-Fe	0	
TfR_BBB-2(Tf-Fe)	0	
Endo_Fe ³⁺ _BBB	0	
Endo_Fe ²⁺ _BBB	0	
LIP_BBB	0	
IRP_BBB	0	
Fpn_BBB	0	
Fe-ferritin_BBB	0	
Ferritin_BBB	2×10^{-10}	<i>in silico</i> [94, 122]
Fe_within_ferritin_BBB	7×10^{-15}	
Hepcidin_BBB	5×10^{-9} (fixed)	<i>in silico</i> [120]
DMT1_BBB	0	
Tf-Fe_ISF	0	
TfR_BCB-Tf-Fe_CSF	0	
TfR_BCB-2(Tf-Fe)	0	
Tf-Fe_CSF	0	
TfR_BCB	0	
IRP_BCB	0	
Endo_Fe ³⁺ _BCB	0	
Endo_Fe ²⁺ _BCB	0	
LIP_BCB	0	
Hepcidin_BCB	5×10^{-9} (fixed)	<i>in silico</i> * [120]
Ferritin_BCB	2×10^{-10}	<i>in silico</i> * [94, 122]
Fe_within_ferritin_BCB	7×10^{-15}	
Fe-ferritin_BCB	0	
Fpn_BCB	0	
DMT1_BCB	0	

* *in silico model of human condition*

The model presented in this chapter was adapted from the human iron metabolism model developed by Mitchell et al. (2013) [94]. The model is built using ordinary differential equations (ODEs) to represent the rate of changes of each chemical

species. In cases where there is no evidence that the synthesis and degradation rate or binding rate of a certain metabolite is different in the brain than in the liver, they are therefore assumed to be the same. The equations applied to the computational model are explained in the following paragraphs, but reactions modelled using the same equation are not explained in detail. The full set of the reactions in the model are listed together with their corresponding functions and parameter values are listed in table 4-3. The full set of equations is given in Appendix A.

The degradation rates of the proteins were calculated using the following equation:

$$k_d = \frac{\ln 2}{T_{1/2}} \quad \text{Eq. 4.1}$$

where, k_d is the degradation rate constant and $T_{1/2}$ is the half-life of the relevant protein gathered from published literature. The degradation rate then can be used together with estimated steady-state concentration from the literature to compute the synthesis rate using the equation:

$$\frac{d[P]}{dt} = k_s - k_d[P] = 0 \quad \text{Eq. 4.2}$$

where, $[P]$ is the concentration of the protein, k_s is the synthesis rate and k_d is the degradation rate constant. The steady state concentration of the protein $[\hat{P}]$ is given by:

$$[\hat{P}] = \frac{k_s}{k_d} \quad \text{Eq. 4.3}$$

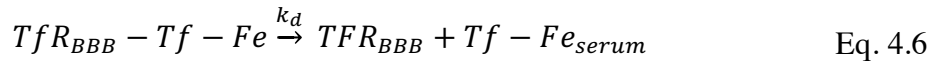
The half-life of transferrin receptor (TfR) was shown to be ~23 hours in [121] and the number of TfRs on the cell surfaces was shown to be 35000 TfRs per cell [123], which is 10 times lower than the number of TfRs in the liver cells [42, 124]. The degradation rate of TfRs in the BBB was calculated and the expression rate of the cell was adjusted to a value 10 times lower than the expression rate in the liver. The degradation and

expression rates of the remainder of the proteins were obtained using equations 4.1 and 4.2.

The reaction for the complex formations, such as the binding of two Tf-Fe serum molecules to TfR on the BBB and the BCB surfaces, was modelled using the on and off rate constants for the appropriate reversible mass action. The example below is the reaction for the binding of the first Tf-Fe serum to the TfR:



This reversible reaction was modelled using two irreversible mass action reactions:



where, k_a is the association rate and k_d is the dissociation rate. The ODEs corresponding to these kinetic reactions are given by:

$$\begin{aligned} \frac{d[TfR_{BBB}]}{dt} = & -k_a[TfR_{BBB}][Tf - Fe_{serum}] \\ & + k_d[TfR_{BBB} - Tf - Fe_{serum}] + \dots \end{aligned} \quad \text{Eq. 4.7}$$

$$\begin{aligned} \frac{d[Tf - Fe_{serum}]}{dt} = & -k_a[TfR_{BBB}][Tf - Fe_{serum}] \\ & + k_d[TfR_{BBB} - Tf - Fe_{serum}] + \dots \end{aligned} \quad \text{Eq. 4.8}$$

$$\begin{aligned} \frac{d[TfR_{BBB} - Tf - Fe_{serum}]}{dt} = & +k_a[TfR_{BBB}][Tf - Fe_{serum}] \\ & -k_d[TfR_{BBB} - Tf - Fe_{serum}] + \dots \end{aligned} \quad \text{Eq. 4.9}$$

Once the second Tf-Fe bound to TfR_{BBB}-Tf-Fe_{serum}, the complex TfR_{BBB}-2(Tf-Fe_{serum}) enters the endosome in the cytosol of the BBB and the BCB, the four iron molecules that were bound to Tf are released and reduced into Fe²⁺. Then the four reduced Fe²⁺

molecules are transported out of the endosome into the cytosol of the BBB by divalent metal transporter 1 (DMT1). Both iron reduction and iron endosomal export reactions follow Henri-Michaelis-Menten kinetics, namely:

$$v = V_{max} \left(\frac{[S]}{[S] + K_m} \right) \quad \text{Eq. 4.10}$$

where,

$$V_{max} = k_{cat} \times [M] \quad \text{Eq. 4.11}$$

and where, v is the reaction rate, $[S]$ is the concentration of the substrate, $[M]$ is the concentration of the modifier, V_{max} is the reaction's maximal rate, k_{cat} is the catalyst rate constant and K_m is the Michaelis constant, i.e. concentration of ligand producing half occupancy of the enzyme binding sites. In cases where K_m is not known, it has been estimated to be of the order of magnitude of the experimentally observed ligand concentration.

As mentioned in section 2.2.2, the binding of iron response protein (IRP) to the iron response element (IRE) at the 3' untranslated region (UTR) of the target mRNAs leads to stability and expression of the proteins, such as in TfR and DMT1. This reaction is represented by Hill kinetics in equation 3.11. The binding of IRP to the IRE at 5' UTR of the target mRNAs causes reduced translation rate, such as in the expression of ferritin and ferroportin. This is represented by equation 3.12, as follows.

$$v = [S] \times a \left(\frac{[M]^n}{K^n + [M]^n} \right) \quad \text{Eq. 4.12}$$

$$v = [S] \times a \left(1 - \frac{[M]^n}{K^n + [M]^n} \right) \quad \text{Eq. 4.13}$$

where, v is the reaction rate, S is the substrate, M is the modifier, K is the concentration of ligand producing half occupancy of the enzyme binding sites, a is the turnover number, and n is the Hill coefficient. When the value of n is equal to 1, the resulting response is equivalent to Henri-Michaelis-Menten kinetics. When n is larger than 1, it produces a positive cooperativity response, and when n is smaller than 1, it produces

a negative cooperativity response. The Hill coefficient was assumed to be 1 unless contradictory evidence was found. The degradation of ferroportin by hepcidin and the export of iron by ferroportin were also simulated using the Hill kinetics as per equation 3.11.

The binding of iron from the labile iron pool (LIP) to ferritin and its internalisation were modelled using mass action kinetics. The release of iron from ferritin was modelled using equations that Mitchell et al. (2013) [94] adapted from Salgado et al. (2010) [125]. There are two ways that iron internalised in ferritin can be released:

1. Ferritin releasing iron through its pores
2. Degradation of ferritin leading to the release of all the iron inside the ferritin.

The first iron release reaction is affected by the average amount of iron stored inside the ferritin. The equation for ferritin releasing iron through its pores is given by [94]:

$$v = [S] \times k_{loss} \left(1 + \frac{0.048 \frac{[FT1]}{[FT]}}{1 + \frac{[FT1]}{[FT]}} \right) \quad \text{Eq. 4.14}$$

where v is the reaction rate, S is the internalised iron, k_{loss} is the rate constant and $FT1/FT$ is the ratio of iron in the ferritin to the total ferritin protein available. The kinetics of iron release due to whole ferritin degradation is based on irreversible mass action, but the amount of iron released is an average of the ferritin levels and the total iron internalised in the ferritin. This gives the equation for [120]:

$$v = [S] \times k_d \times \frac{[FT1]}{[FT]} \quad \text{Eq. 4.15}$$

where v is the reaction rate, S is the internalised iron, k_d is the degradation rate constant and $FT1/FT$ is the ratio of iron in the ferritin to total ferritin protein available.

In order to analyse the sensitivity of the model metabolites to the reactions, the metabolic control analysis calculation was performed using COPASI, using equation [98, 99]:

$$C_{V_i}^A = \frac{\delta A}{\delta V_i} \frac{V_i}{A} \quad \text{Eq. 4.16}$$

where, A is the variable in the system, either concentrations or fluxes and V_i is the reaction rate.

Table 4-3 Reactions involved in the iron transport in the barriers and their parameters

Name	Reaction	Function	Parameters	Ref
TfR_BBB expression	\rightarrow TfR BBB; IRP BBB	Hill function \rightarrow	$a = 2 \times 10^{-12} \text{ s}^{-1}$, $n = 1$, $K = 1 \times 10^{-6} \text{ mol}$	[123, 124]
TfR_BBB degradation	TfR BBB \rightarrow	Mass action (irreversible)	$k = 8.37 \times 10^{-6} \text{ s}^{-1}$	[124]
TfR_BBB binding 1	$\text{TfR_BBB} + \text{Tf-Fe_serum} \rightarrow \text{TfR_BBB-Tf-Fe_serum}$	Mass action (irreversible)	$k = 837400 \text{ l}^*(\text{mol}^*\text{s})^{-1}$	[42]
TfR_BBB release 1	$\text{TfR_BBB-Tf-Fe_serum} \rightarrow \text{TfR_BBB} + \text{Tf-Fe_serum}$	Mass action (irreversible)	$k = 9.142 \times 10^{-4} \text{ s}^{-1}$	[42]
TfR_BBB binding 2	$\text{TfR_BBB-Tf-Fe_serum} + \text{Tf-Fe_serum} \rightarrow 2(\text{Tf-Fe})\text{-TfR_BBB}$	Mass action (irreversible)	$k = 121400 \text{ l}^*(\text{mol}^*\text{s})^{-1}$	[42]
TfR_BBB release 2	$2(\text{Tf-Fe})\text{-TfR_BBB} \rightarrow \text{TfR_BBB-Tf-Fe_serum} + \text{Tf-Fe_serum}$	Mass action (irreversible)	$k = 3.535 \times 10^{-3} \text{ s}^{-1}$	[42]
TfR_BBB iron internalisation	$2(\text{Tf-Fe})\text{-TfR_BBB} \xrightarrow{k_1} * \text{endoFe3_BBB} + \text{TfR_BBB}$	Mass action (reversible)	$k_1 = 0.8333 \text{ s}^{-1}$ $k_2 = 0.1 \text{ l}^5*(\text{mol}^4*\text{s})^{-1}$	[42]

Name	Reaction	Function	Parameters	Ref
Steap3_BBB iron reduction	endoFe3_BBB → endoFe2_BBB	Henri-Michealis-Menten	$K_m = 7.4 \times 10^{-5} \text{ mol} \cdot \text{l}^{-1}$ $V = 1.493 \times 10^{-4} \text{ mol} (\text{l} \cdot \text{s})^{-1}$ $a = 1.39 \times 10^{-10} \text{ s}^{-1}$	[94]
DMT1_BBB expression	→ DMT1_BBB; IRP_BBB	Hill function →	$n = 1$ $K = 2.5 \times 10^{-6} \text{ mol}$	[94]
DMT1_BBB degradation	DMT1_BBB →	Mass action (irreversible)	$k = 2.4 \times 10^{-5} \text{ s}^{-1}$	[94]
DMT1_BBB endosomal export	endoFe2_BBB → LIP_BBB; DMT1_BBB	Henri-Michealis-Menten	$k_{\text{cat}} = 258.6 \text{ s}^{-1}$ $K_m = 4.8 \times 10^{-6} \text{ mol} \cdot \text{l}^{-1}$ $a = 4 \times 10^{-11} \text{ mol} \cdot (\text{l} \cdot \text{s})^{-1}$	[94]
IRP_BBB expression	→ IRP_BBB; LIP_BBB	Hill Function -I	$n = 1$ $K = 1 \times 10^{-7} \text{ mol}$	[47]
IRP_BBB degradation	IRP_BBB →	Mass action (irreversible)	$k = 1.597 \times 10^{-5} \text{ s}^{-1}$	[126]

Name	Reaction	Function	Parameters	Ref
Fpn_BBB expression	$\rightarrow \text{Fpn_BBB}; \text{IRP_BBB}$	Hill function -I	$a = 1 \times 10^{-9} \text{ mol} \cdot (\text{l} \cdot \text{s})^{-1}$ $n = 1$ $K = 1 \times 10^{-7} \text{ mol}$	[94]
Fpn_BBB degradation	$\text{Fpn_BBB} \rightarrow; \text{Hepcidin_BBB}$	Biochemical hill function \rightarrow	$a = 2.315 \times 10^{-4} \text{ mol} \cdot (\text{l} \cdot \text{s})^{-1}$ $n = 5$ $K = 5 \times 10^{-9} \text{ mol}$	[94]
Fpn_BBB export	$2 * \text{LIP_BBB} \leftrightarrow \text{Tf-Fe_ISF}; \text{Fpn_BBB}$	Biochemical hill function \rightarrow	$a = 2 \text{ mol} \cdot (\text{l} \cdot \text{s})^{-1}$ $n = 1$ $K = 3 \times 10^{-6} \text{ mol}$	[127]
Temporary Tf- Fe_ISF use	$\text{Tf-Fe_ISF} \rightarrow$	Mass action (irreversible)	$k = 5 \times 10^{-5} \text{ s}^{-1}$	
Ferritin_BBB expression	$\rightarrow \text{Ferritin_BBB}; \text{IRP_BBB}$	Hill function -I	$a = 2.312 \times 10^{-13} \text{ mol} \cdot (\text{l} \cdot \text{s})^{-1}$ $n = 1$	[122]

Name	Reaction	Function	Parameters	Ref
Ferritin_BBB degradation	Ferritin_BBB \rightarrow	Mass action (irreversible)	$K = 1 \times 10^{-6} \text{ mol}$ $k = 1.203 \times 10^{-5} \text{ s}^{-1}$	[125]
Ferritin_BBB full degradation iron release	Fe_within_ferritin_BBB \rightarrow LIP_BBB; Fe_within_ferritin_BBB Ferritin_BBB	Mass action ferritin	$k = 1.203 \times 10^{-5} \text{ s}^{-1}$	[125]
Ferritin_BBB internalised iron release	Fe_within_ferritin_BBB \rightarrow LIP_BBB; Fe_within_ferritin_BBB Ferritin_BBB	Kloss Hill	$k_{\text{loss}} = 13.1251 \text{ s}^{-1}$	[125]
Ferritin_BBB iron binding	LIP_BBB + Ferritin_BBB \rightarrow Fe-ferritin_BBB	Mass action (irreversible)	$k = 4.71 \times 10^{10} \text{ l}^*(\text{mol}^*\text{s})^{-1}$	[125]
Ferritin_BBB iron internatlisation	Fe-ferritin_BBB \rightarrow Fe_within_ferritin_BBB + Ferritin_BBB	Mass action (irreversible)	$k = 108000 \text{ s}^{-1}$	[125]
Ferritin_BBB iron release	Fe-ferritin_BBB \rightarrow LIP_BBB + Ferritin_BBB	Mass action (irreversible)	$k = 22922 \text{ s}^{-1}$	[125]

Name	Reaction	Function	Parameters	Ref
Flow of Tf-Fe between ISF and CSF	$\text{Tf-Fe_ISF} \leftrightarrow \text{Tf-Fe_CSF}$	Mass action (reversible)	$k_1 = 100 \text{ s}^{-1}$ $k_2 = 100 \text{ s}^{-1}$	
TfR_BCB expression	$\rightarrow \text{TfR_BCB_apical}; \text{IRP_BCB}$	Hill Function \rightarrow	$a = 2 \times 10^{-12} \text{ s}^{-1}$ $n = 1$ $K = 1 \times 10^{-6} \text{ mol}$	[123, 124]
TfR_BCB degradation	$\text{TfR_BCB_apical} \rightarrow$	Mass action (irreversible)	$k = 8.37 \times 10^{-6} \text{ s}^{-1}$	[124]
TfR_BCB binding 1	$\text{TfR_BCB_apical} + \text{Tf-Fe_CSF} \rightarrow \text{TfR_BCB-Tf-Fe_CSF}$	Mass action (irreversible)	$k = 837400 \text{ l}^*(\text{mol}^*\text{s})^{-1}$	[42]
TfR_BCB release 1	$\text{TfR_BCB-Tf-Fe_CSF} \rightarrow \text{TfR_BCB_apical} + \text{Tf-Fe_CSF}$	Mass action (irreversible)	$k = 9.142 \times 10^{-4} \text{ s}^{-1}$	[42]
TfR_BCB binding 2	$\text{TfR_BCB-Tf-Fe_CSF} + \text{Tf-Fe_CSF} \rightarrow 2(\text{Tf-Fe})\text{-TfR_BCB}$	Mass action (irreversible)	$k = 121400 \text{ l}^*(\text{mol}^*\text{s})^{-1}$	[42]
TfR_BCB release 2	$2(\text{Tf-Fe})\text{-TfR_BCB} \rightarrow \text{TfR_BCB-Tf-Fe_CSF} + \text{Tf-Fe_CSF}$	Mass action (irreversible)	$k = 3.535 \times 10^{-3} \text{ s}^{-1}$	[42]
TfR_BCB iron internalisation	$2(\text{Tf-Fe})\text{-TfR_BCB} \leftrightarrow * \text{endoFe3_BCB} + \text{TfR_BCB_apical}$	Mass action (reversible)	$k_1 = 0.8333 \text{ s}^{-1}$ $k_2 = 0.1 \text{ l}^5*(\text{mol}^4*\text{s})^{-1}$	[42]

Name	Reaction	Function	Parameters	Ref
Steap3_BCB iron reduction	endoFe3_BCB → endoFe2_BCB	Henri-Michaelis-Menten	$K_m = 7.4 \times 10^{-5} \text{ mol} \cdot \text{l}^{-1}$ $V = 1.493 \times 10^{-4} \text{ mol} (\text{l} \cdot \text{s})^{-1}$ $a = 1.39 \times 10^{-10} \text{ s}^{-1}$	[94]
DMT1_BCB expression	→ DMT1_BCB; IRP_BCB	Hill function →	$n = 1$ $K = 2.5 \times 10^{-6} \text{ mol}$	[94]
DMT1_BCB degradation	DMT1_BCB →	Mass action (irreversible)	$k = 2.4 \times 10^{-5} \text{ s}^{-1}$	[94]
DMT1_BCB endosomal export	endoFe2_BCB → LIP_BCB; DMT1_BCB	Henri-Michealis-Menten	$k_{\text{cat}} = 258.6 \text{ s}^{-1}$ $K_m = 4.8 \times 10^{-6} \text{ mol} \cdot \text{l}^{-1}$ $a = 1 \times 10^{-9} \text{ mol} \cdot (\text{l} \cdot \text{s})^{-1}$	[94]
Fpn_BCB expression	→ Fpn_BCB; IRP_BCB	Hill function -l	$n = 1$ $K = 1 \times 10^{-7} \text{ mol}$	[94]
Fpn_BCB degradation	Fpn_BCB → ; Hecpidin_BCB	Biochemical hill function	$a = 2.315 \times 10^{-4} \text{ mol} \cdot (\text{l} \cdot \text{s})^{-1}$	[94]

Name	Reaction	Function	Parameters	Ref
Fpn_BCB export	$2 * \text{LIP_BCB} \xleftarrow{\text{Ff-Fe_serum}} \text{Fpn_BCB}$	Biochemical hill function	$n = 5$ $K = 5 \times 10^{-9} \text{ mol}$ $a = 2 \text{ mol} * (1 * s)^{-1}$ $n = 1$	[127]
IRP_BCB expression	$\rightarrow \text{IRP_BCB}; \text{LIP_BCB}$	Hill function -I	$K = 3 \times 10^{-6} \text{ mol}$ $a = 4 \times 10^{-11} \text{ mol} * (1 * s)^{-1}$ $n = 1$	[47]
IRP_BCB degradation	$\text{IRP_BCB} \rightarrow$	Mass action (irreversible)	$K = 1 \times 10^{-7} \text{ mol}$ $k = 1.597 \times 10^{-5} \text{ s}^{-1}$	[126]
Ferritin_BCB expression	$\rightarrow \text{Ferritin_BCB}; \text{IRP_BCB}$	Hill function -I	$a = 2.312 \times 10^{-13} \text{ mol} * (1 * s)^{-1}$ $n = 1$ $K = 1 \times 10^{-6} \text{ mol}$	[122]

Name	Reaction	Function	Parameters	Ref
Ferritin_BCB degradation	Ferritin_BCB \rightarrow	Mass action (irreversible)	$k = 1.203 \times 10^{-5} \text{ s}^{-1}$	[125]
Ferritin_BCB full degradation iron release	Fe_within_ferritin_BCB \rightarrow LIP_BCB; Fe_within_ferritin_BCB Ferritin_BCB	Mass action ferritin	$k = 1.203 \times 10^{-5} \text{ s}^{-1}$	[125]
Ferritin_BCB internalised iron release	Fe_within_ferritin_BCB \rightarrow LIP_BCB; Fe_within_ferritin_BCB Ferritin_BCB	Kloss Hill	$k_{\text{loss}} = 13.1251 \text{ s}^{-1}$	[125]
Ferritin_BCB iron binding	LIP_BCB + Ferritin_BCB \rightarrow Fe-ferritin_BCB	Mass action (irreversible)	$k = 4.71 \times 10^{10} \text{ l}^*(\text{mol}^*\text{s})^{-1}$	[125]
Ferritin_BCB iron internalisation	Fe-ferritin_BCB \rightarrow Fe_within_ferritin_BCB + Ferritin_BCB	Mass action (irreversible)	$k = 108000 \text{ s}^{-1}$	[125]
Ferritin_BCB iron release	Fe-ferritin_BCB \rightarrow LIP_BCB + Ferritin_BCB	Mass action (irreversible)	$k = 22922 \text{ s}^{-1}$	[125]

4.3 Model simulation results

A novel mathematical model of iron kinetics and transport between the blood and the brain across the brain barrier systems was presented in this chapter. To my knowledge, this is the first computational model of the iron transport across the brain barriers that incorporated the regulatory of the expression of TfR, DMT1, ferroportin and ferritin by IRP. The model in Systems Biology Markup Language (SBML) and COPASI format will be provided in the BioModels database in due course.

Figure 4.1 shows the biological diagram of brain iron trafficking that was adapted into the model and figure 4.2 depicts the process diagram of the model using the Systems Biology Graphical Notation (SBGN) standard [128]. The kinetics for each chemical species in the transport of iron in this model are characterised by nonlinear ordinary differential equations (listed in the appendix A)

Experimentally determined model parameter values for compartmental volumes, initial species concentrations, and rate constants for each species were extracted from the literature. Parameter estimation was not performed during model construction due to lack of available data. The accurate representation of the underlying protein dynamics allows the model to recreate qualitatively, rather than quantitatively, experimental observations. The accurate representation of the underlying protein dynamics allows the model to recreate experimental observation accurately. The work detailed here provides an extremely useful test bed for testing the dynamics of iron transport to and from the brain in response to various systemic serum iron levels.

4.3.1 Transferrin-transferrin receptor binding

Simulated transferrin receptor levels were found to be consistent with experimental concentrations. Serum iron in normal human blood exists primarily in the form of Fe^{3+} bound to Tf, so TfR is the primary importer of iron into the brain. The expression rate of TfR in the BBB is ten times lower than in the liver under normal conditions. The

model steady state simulation gives a prediction of 30050 TfRs per cell which is close to the value of 35000 previously published in Descamps (1996) [123]. This value is much lower than for other cell types [129].

To further confirm the appropriateness of the model, simulation results were compared to published experimental data. The transferrin receptor binding curve, shown in figure 4.3, was generated by plotting the steady state concentration of transferrin bound to its receptors as increasing doses of Tf-Fe are added into the serum compartment of the model. The values have been normalised by dividing all concentrations by the highest concentration value in the simulation and experimental

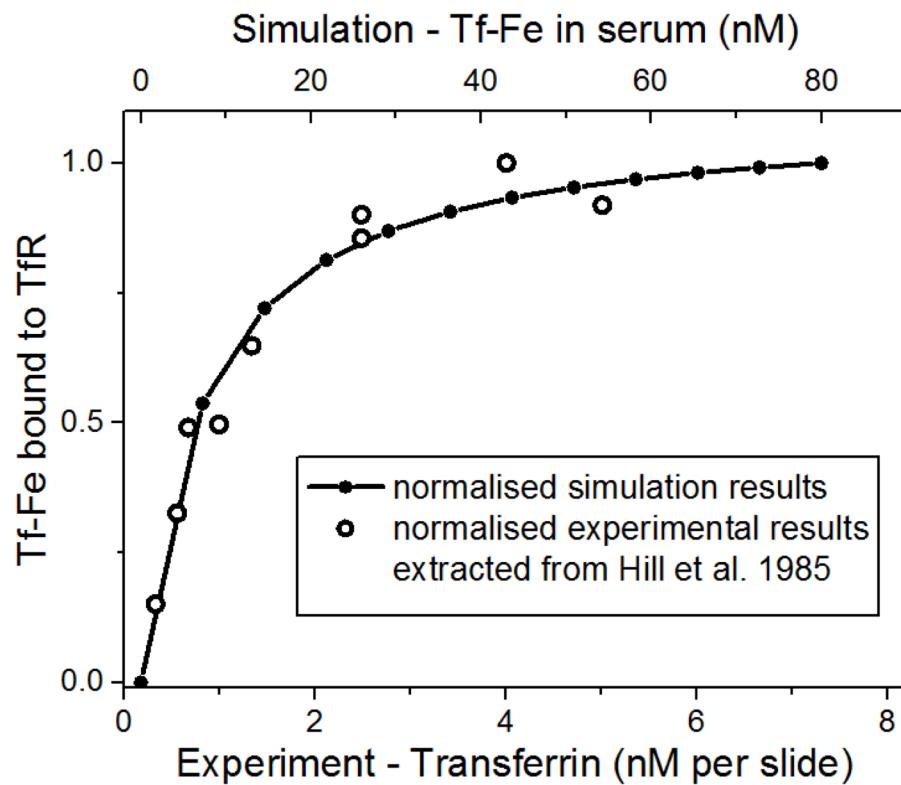


Figure 4.3 Transferrin – Transferrin Receptor binding curve, showing saturating of iron binding to BBB cells as seen in the experimental data with rat brain slices from Hill et al. (1985) [130]. Both simulation and experimental data share the same y-axis. The top axis is for the simulation data and the bottom axis is for the experimental data. The model was not fitted to these data.

results, respectively. This was done because the magnitude of the concentrations from the two different systems (simulated human brain and rat brain) are not expected to be similar. The simulated curve shows that the binding of transferrin-bound iron to the transferrin receptor does not depend linearly on the concentration of transferrin-bound iron available and that the process is saturable. The saturating kinetics resemble the experimentally derived binding curve for increasing concentration of ^{125}I -Tf to the TfR in rat brain slice performed on rat brains by Hill et al. (1985) as shown in figure 4.3 [130]. As the experimental results were acquired from a fraction of rat brains, the result is not comparable, quantitatively. However, the simulation result still shows a qualitative similarity to the dynamics of the experiment-derived binding curve.

4.3.2 Iron uptake across the blood brain barrier

Another comparison to experimental data performed was the simulation of the dynamics of the Tf-Fe concentration in the ISF following a virtual injection of Tf-Fe in the serum. The simulated curve shows a similar qualitative trend as that of the experimental result of Tf uptake performed by Taylor and Morgan (1990) [131] (figure 4.4). In the simulation, the addition of Tf-Fe to the serum in a virtually iron starved model results in an abrupt increase of Tf-Fe in the ISF. The concentration reaches a peak at around 1 hour and is then maintained until it decreases rapidly after ~ 7 hours. This trend is similar to that observed in the results of experimental studies [131] on the uptake of Tf by the rat brain after injection of ^{125}I - ^{59}Fe -Tf. The values in the graph have also been normalised such that the largest value is 1 and the smallest value is 0 for both the simulation and experimental results, respectively, to account for the different concentration magnitude that would be observed between the two systems (i.e. simulated human system and rat brain system). The value of chi squared value for the two qualitatively fitted data sets is approximately 0.04.

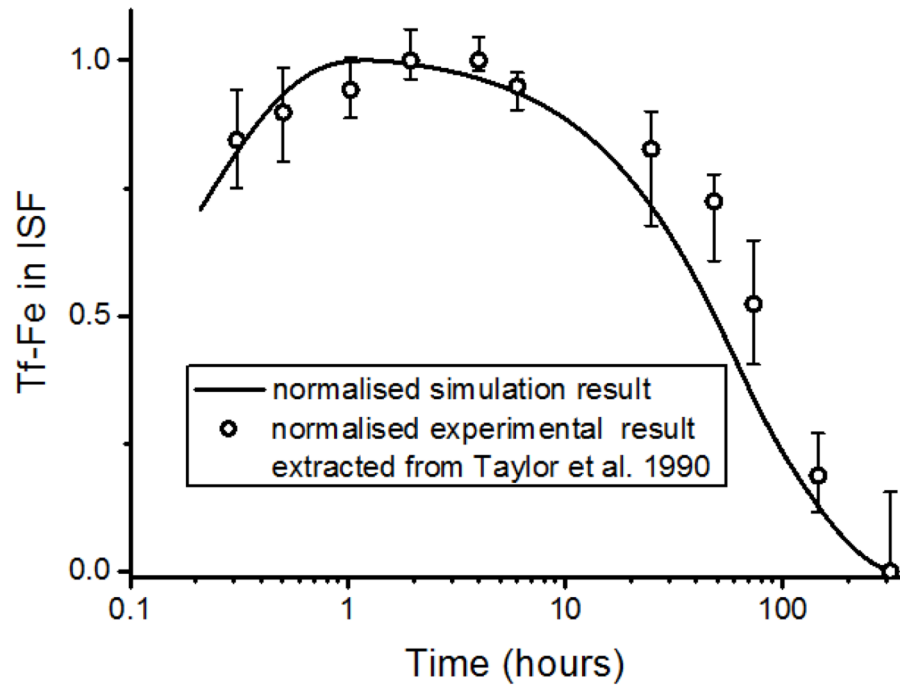


Figure 4.4 Semi-log plot of the time course of Tf-Fe Uptake across the BBB following an iron injection event. The simulation result shows similar dynamics for iron influx and subsequent outflow following radio-labelled iron injection compared to the study undertaken by Taylor and Morgan 1990 [131] on rat brains. The model was not fitted to these data. To confirm the model appropriateness we compared uptake dynamics with a simulation representing iron injection.

The model was used to examine the impact of constant high iron concentration, higher than $\sim 20 \mu\text{M}$ which is the normal serum iron concentration [14, 132], on the uptake of iron across the barriers, as shown in figure 4.5. The rate of iron uptake from the blood serum into the brain interstitial fluid quickly increases over the first couple of days, as shown in figure 4.5A. The higher the concentration of the serum iron the faster Tf-Fe uptake reaches its maximum rate. However the rate is tightly constrained to never exceed $0.12 \mu\text{M/s}$ even in extreme system iron loads. The concentration of LIP in the BBB and the BCB in response to iron overload is shown in figure 4.5B. The simulated LIP concentrations in both the BBB and the BCB reach steady state faster with increasing concentration of Tf-Fe in serum, however the steady state concentration of the LIP is unchanged ($\sim 0.13 \mu\text{M}$) when the Tf-Fe serum concentration is higher than

20 μM . Iron does not build-up in the LIP of the BBB and the BCB even for extreme iron loads. The concentration of the LIP ($<0.13\mu\text{M}$) is low (lower than the concentration that induces cell death in cultured pituitary cells) and this may indicate that the barrier cells are protected from free iron-related ROS damage and cell death that may compromise BBB/BCB integrity. Even for extreme system iron loads the BBB/BCB cells are not exposed to toxic levels of free iron.

As shown in figure 4.5C, the concentration of Tf-Fe in the ISF suddenly increases during the first day and reaches a maximum concentration, which is equal to the amount input to the serum. After several days, the concentration of Tf-Fe in the ISF drops to the steady state concentration ($\sim 23 \mu\text{M}$). This result shows that, in a shift to high system-iron concentrations, iron may transiently increase in the ISF/CSF, but iron is rapidly controlled and reduced within a couple of days. The model postulate that while brain cells may see temporary iron increases, the BBB/BCB functions as a buffer to minimise long-term exposure to iron resulting from system iron fluctuations. For Tf-Fe serum lower than 20 μM , the uptake flux and the steady state concentration of the LIP and Tf-Fe ISF are lower than for the other concentrations simulated. This may mean that, although excessive serum iron may not have much impact on the uptake and Tf-Fe ISF concentration, in the long run, the model predicts that serum iron deficiency may have a huge impact on brain iron concentration.

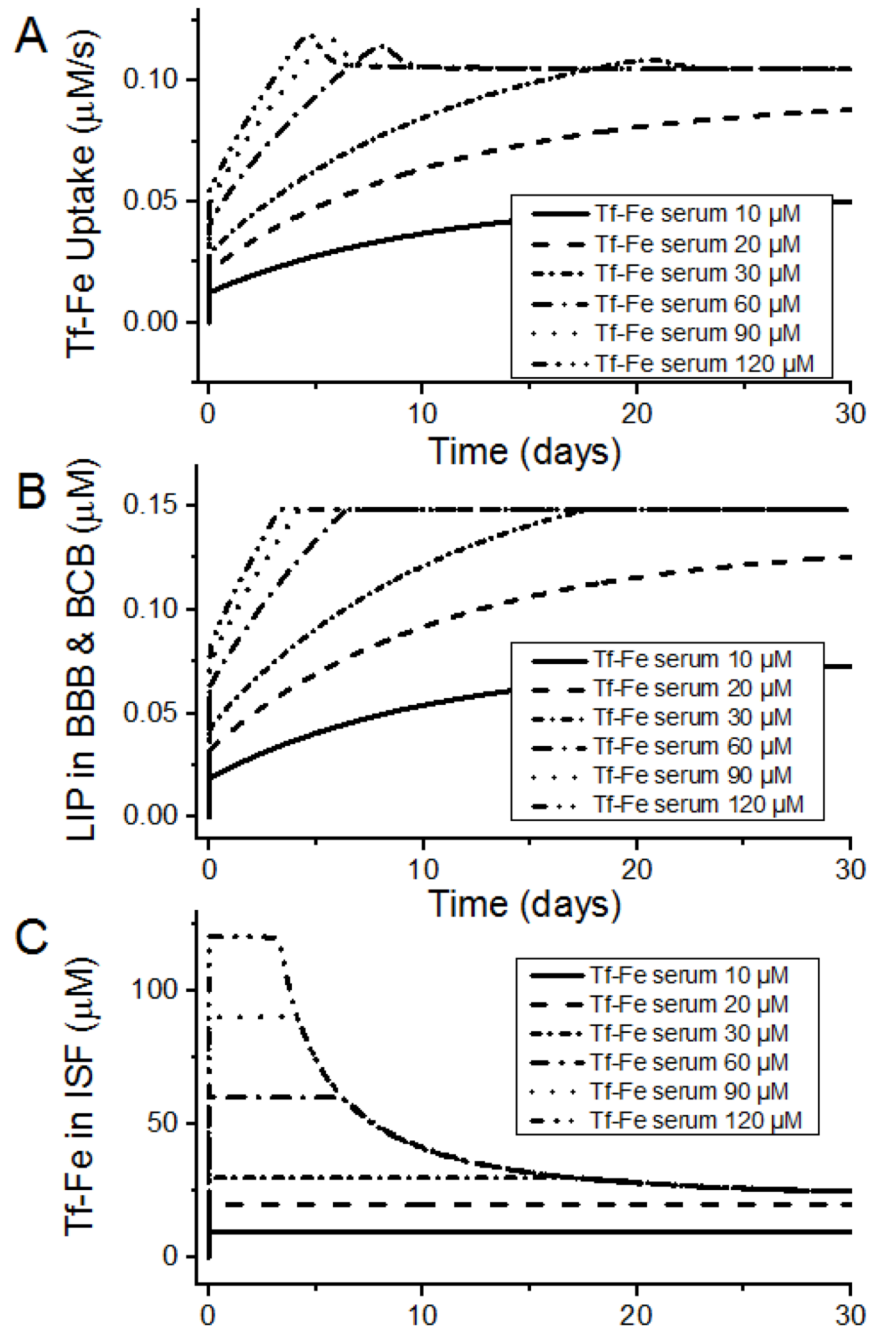


Figure 4.5 Metabolites in the model responding to various levels of increased iron load. (A) The rate of the iron uptake into the brain ISF. (B) The concentration of labile iron pool (LIP) in the BBB and BCB. (C) The concentration of Tf-Fe in the ISF.

4.3.3 Sensitivity analysis

Generic sensitivity analysis and metabolic control analysis (MCA) were performed to investigate which reactions in the model have the highest control over the concentration of iron in the BBB, BCB and ISF. The generic sensitivity analysis describes how sensitive the model is to the parameter value and the MCA relays how much the rates of the various reactions in the model affect the fluxes and concentrations at steady state. There are two methods of calculating MCA available in COPASI; the Reder algorithm and the Smallbone algorithm. Both algorithms were performed and the results are compared below. The result from MCA simulation, concentration control coefficient, could be interpreted as the percentage change of the metabolite given a one percent change in the reaction rate.

According to the literature, the smallbone method has overcome the limitation of the reder algorithm, however the MCA simulation using smallbone algorithm shows that the one percent changes in the IRP expression and degradation does not affect any metabolites, concentration control coefficient is 0. IRP is the main regulatory proteins in the system, so a one percent change in the expression and degradation of the protein was expected to affect the concentration of iron in the LIP in the BBB and the BCB, and in the ISF. The generic sensitivity analysis and MCA results for the concentration of the LIP in the BBB, the LIP in the BCB and the Tf-Fe in the ISF are listed in order of highest magnitude in tables 4-4, 4-5 and 4-6, respectively.

Table 4-4 Generic sensitivity analysis (sensitivity coefficient (SC)) and metabolic control analysis (concentration control coefficient (CCC)) for LIP in BBB

sensitivity		reder		smallbone	
reaction parameter	SC	reaction	CCC	reaction	CCC
k1 of binding of Tf-Fe to TfR BBB	0.766	TfR_BBB expression	0.767	Fpn_BBB export	-1.000
k1 of degradation of TfR BBB	-0.766	TfR_BBB –Tf-Fe binding	0.767	TfR_BBB-2Tf-Fe binding	0.841
a of export by Fpn BBB	-0.766	TfR_BBB degradation	-0.767	Fpn_BBB degradation	0.302
K of degradation of FPN BBB	-0.568	Fpn_BBB export	-0.767	Fpn_BBB expression	-0.302
k1 of degradation of IRP BBB	-0.409	IRP_BBB expression	0.409	TfR_BBB –Tf-Fe binding	0.122
K of expression of TfR BBB	-0.369	IRP_BBB degradation	-0.409	TfR_BBB iron internalisation	0.037
a of degradation of FPN BBB	0.227	Fpn_BBB degradation	0.227		
K of export by Fpn BBB	0.227	Fpn_BBB expression	-0.227		
a of expression of FPN BBB	-0.227				
n of export by Fpn BBB	-0.196				

Table 4-5 Generic sensitivity analysis (sensitivity coefficient (SC)) and metabolic control analysis (concentration control coefficient (CCC)) for LIP in BCB

sensitivity		reder		smallbone	
reaction parameter	SC	reaction	CCC	reaction	CCC
a of export by Fpn BCB	0.970	Fpn_BCB export	-0.974	Fpn_BCB export	-1.000
k1 of binding of Tf-Fe to TfR BBB	0.766	TfR_BBB degradation	-0.861	TfR_BBB-2Tf-Fe binding	0.841
k1 of degradation of TfR BBB	0.766	TfR_BBB expression	0.861	Fpn_BCB degradation	0.296
K of degradation of FPN BCB	0.720	TfR_BBB-Tf-Fe binding	0.861	Fpn_BCB expression	-0.296
K of expression of TfR BBB	0.369	IRP_BBB expression	0.319	TfR_BBB-Tf-Fe binding	0.122
k1 of degradation of IRP BBB	0.358	IRP_BBB degradation	-0.319	TfR_BBB iron internalisation	0.037
a of degradation of FPN BCB	0.288	Fpn_BCB degradation	0.307		
K of export by Fpn BCB	0.288	Fpn_BCB expression	-0.307		
a of expression of FPN BCB	0.288				
n of export by Fpn BCB	0.248				
K of expression of IRP BBB	0.204				
a of export by Fpn BBB	0.204				
K of degradation of FPN BBB	0.152				

Table 4-6 Generic sensitivity analysis (sensitivity coefficient (SC)) and metabolic control analysis (concentration control coefficient (CCC)) for Tf-Fe in ISF

local sensitivity		reder		smallbone	
reaction parameter	SC	reaction	CCC	reaction	CCC
k2 of flow of Tf-Fe between ISF and CSF	1.000	TfR_BBB expression	1.000	TfR_BBB-2Tf-Fe binding	0.873
k1 of binding of Tf-Fe to TfR BBB	1.000	TfR_BBB-Tf-Fe binding	1.000	TfR_BCB-2Tf-Fe binding	-0.873
k1 of degradation of TfR BCB	1.000	TfR_BBB degradation	-1.000	TfR_BBB-Tf-Fe binding	0.127
k1 of flow of Tf-Fe between ISF and CSF	-0.999	TfR_BCB expression	-1.000	TfR_BCB-Tf-Fe binding	-0.127
k1 of degradation of TfR BBB	-0.999	TfR_BCB degradation	1.000	TfR_BBB iron internalisation	0.039
k1 of binding of Tf-Fe to TfR BCB	-0.999	TfR_BCB-Tf-Fe binding	-1.000	TfR_BCB iron internalisation	-0.039
K of expression of TfR BCB	0.481	IRP_BBB degradation	-0.467		
K of expression of TfR BBB	-0.481	IRP_BBB expression	0.467		
k1 of degradation of IRP BCB	0.467	IRP_BCB expression	-0.467		
k1 of degradation of IRP BBB	-0.467	IRP_BCB degradation	0.467		
a of export by Fpn BBB	0.266	Fpn_BBB export	0.267		
K of expression of IRP BBB	0.266	Fpn_BCB export	-0.267		
a of export by Fpn BCB	-0.266				
K of expression of IRP BCB	-0.266				
K of degradation of FPN BBB	0.198				
K of degradation of FPN BCB	-0.198				

The control over the labile iron pools in the two barriers, the BBB and the BCB, were of interest because these iron pools are more prone to involvement in the generation of ROS by Fenton chemistry (table 4-4 and 4-5)[133]. According to the sensitivity coefficient, the reaction parameters that have highest control over the LIP in the BBB are the ' K_m ' parameter for TfR in the BBB binding to the first Tf-Fe, the ' K ' parameter of the degradation of the TfR BBB and a parameter of iron export out of the BBB by ferroportin. The ' k ' parameter for the degradation of ferroportin and the IRP in the BBB also has some degree of control over the concentration of the LIP in the BBB. The concentration control coefficient with the Reder MCA similarly shows that the binding of TfR in the BBB to the first Tf-Fe, the expression and degradation of TfR BBB and the exportation of iron out of the BBB have the highest control over the concentration of the LIP in the BBB. The expression and degradation of IRP and ferroportin in the BBB also have an effect on the concentration of LIP in the BBB, though to a lesser extent. The concentration control coefficient result with the Smallbone MCA algorithm indicated that the iron export reaction by ferroportin has the highest control over the LIP concentration in the BBB. The Smallbone result also shows that the reaction of the binding of the Tf-Fe to TfR in the BBB and the internalisation of the TfR Tf-Fe complex also have some degree of effect on the concentration of the LIP in the BBB. This result is different from the Reder algorithm results and generic sensitivity results which indicated that small changes in these two reactions are not significant.

The sensitivity analysis for the concentration of the LIP in the BCB shows that the ' a ' parameter of iron export out of the BCB by ferroportin has the most significant control over the concentration. This was followed by the ' k ' parameter of the binding of the first Tf-Fe onto TfR in the BBB, the ' k ' parameter of the degradation of BBB TfR, and the ' k ' parameter of the degradation of BCB ferroportin. The MCA result using the Reder algorithm showed a similar result with the iron export out of the BCB by ferroportin as the reaction most affecting the concentration of the LIP in the BCB. The expression and degradation of the BBB TfR and the binding of the first Tf-Fe to BBB

TfR also affects the concentration of LIP in the BCB according to Reder. The expression and degradation of the ferroportin protein have a lesser effect, although they are still significant. Like the two methods, the results with the Smallbone algorithm also demonstrate that the exportation of iron by ferroportin out of the BCB has the greatest effect on the concentration of LIP in the BCB. Unlike the other two methods, the next significant reactions that have control over BCB LIP according to the Smallbone algorithm are the binding of the second Tf-Fe on the TfR in the BBB and the internalisation of iron by TfR in the BBB.

The control over the concentration of Tf-Fe in the ISF is listed in table 4-6. The generic sensitivity coefficient implies the parameters for the two way flow between the ISF and CSF, the parameters for TfR degradation reaction in both the BBB and BCB, and the parameters for the binding of first iron to TfR in both the BBB and BCB have the highest control over the concentration of Tf-Fe in the ISF. Others reaction parameters that show some level of control are the expression of TfR in the BBB and BCB and the degradation of IRP in the BBB and BCB. The results from the Reder method show that the reactions involving TfR have the most significant effect on the concentration of Tf-Fe in the ISF. These reactions are: the expression and degradation of TfR in the BBB and BCB; and the binding of the first Tf-Fe onto the TfR in the BBB and BCB. The results of the Smallbone algorithm indicate that it is the binding reaction of the second Tf-Fe to TfR in the BBB and the BCB that have higher control over the concentration of ISF Tf-Fe rather than the binding of the first Tf-Fe onto the TfR in the BBB and BCB. The concentration of Tf-Fe in the brain ISF is controlled by the binding of Tf-Fe to TfR in the BBB and BCB and the internalisation of Tf-Fe in both barriers. A slight change in the rates of reaction for other proteins in the system appears to have less control over the concentration of Tf-Fe transported into the brain ISF.

4.3.4 Metabolite expression rates

The concentration control coefficient of the MCA results in the previous section predicts that TfR plays an important role in the transport of Tf-Fe into the brain.

Therefore in this section, the effect of changing the expression rate of either TfR or IRP in the BBB and BCB under different iron conditions is presented. The different conditions are: healthy serum iron condition ($20\ \mu\text{M}$ [14, 132]); serum iron deficiency condition ($2\ \mu\text{M}$ [132]); and serum iron overload condition ($200\ \mu\text{M}$). Figure 4.6 shows the concentration of Tf-Fe in the ISF and the LIP in the BBB and BCB when the expression rate of either TfR or IRP is 0.5x, 1x, 2x and 4x in both barriers simultaneously under the three conditions. Figure 4.6 shows that under normal iron conditions, the concentration of Tf-Fe in ISF decreases when the rate of TfR or IRP expression in both barriers is higher than the normal rate (1x). The concentration of the LIP in the BBB and BCB, increase with higher rate of TfR or IRP expression rate. Under iron deficiency condition, the steady state concentration of Tf-Fe in the brain ISF is unchanged but the concentration of LIP in both the BBB and BCB increases linearly with increasing expression rate of TfR and IRP. Under iron overload condition, the LIP in the BBB and BCB are unaffected by the TfR expression rate, while an increase in the rate of IRP expression slightly increases the concentrations. The concentration of Tf-Fe in the ISF, in contrast, decreases as the rate of TfR or IRP expression rate increases in both the BBB and the BCB.

Figures 4.7 and 4.8 show the effect of an imbalance in the expression of TfR and IRP between the BBB and BCB under the three different conditions. Figure 4.7 shows the concentration of Tf-Fe and LIP in the BBB and the BCB when the expression rate of TfR or IRP in the BBB is either increases or decreases, while the expression rate of TfR or IRP in the BCB is kept constant. The responses under the normal and iron deficiency conditions are again similar. Under these two conditions, higher expression rate of TfR/ IRP in the BBB increases the concentration of Tf-Fe in the ISF and the LIP in the BBB and BCB. Under iron overload condition, the concentration of Tf-Fe in the ISF and the LIP in the BBB and BCB stay constant as the expression rate of TfR

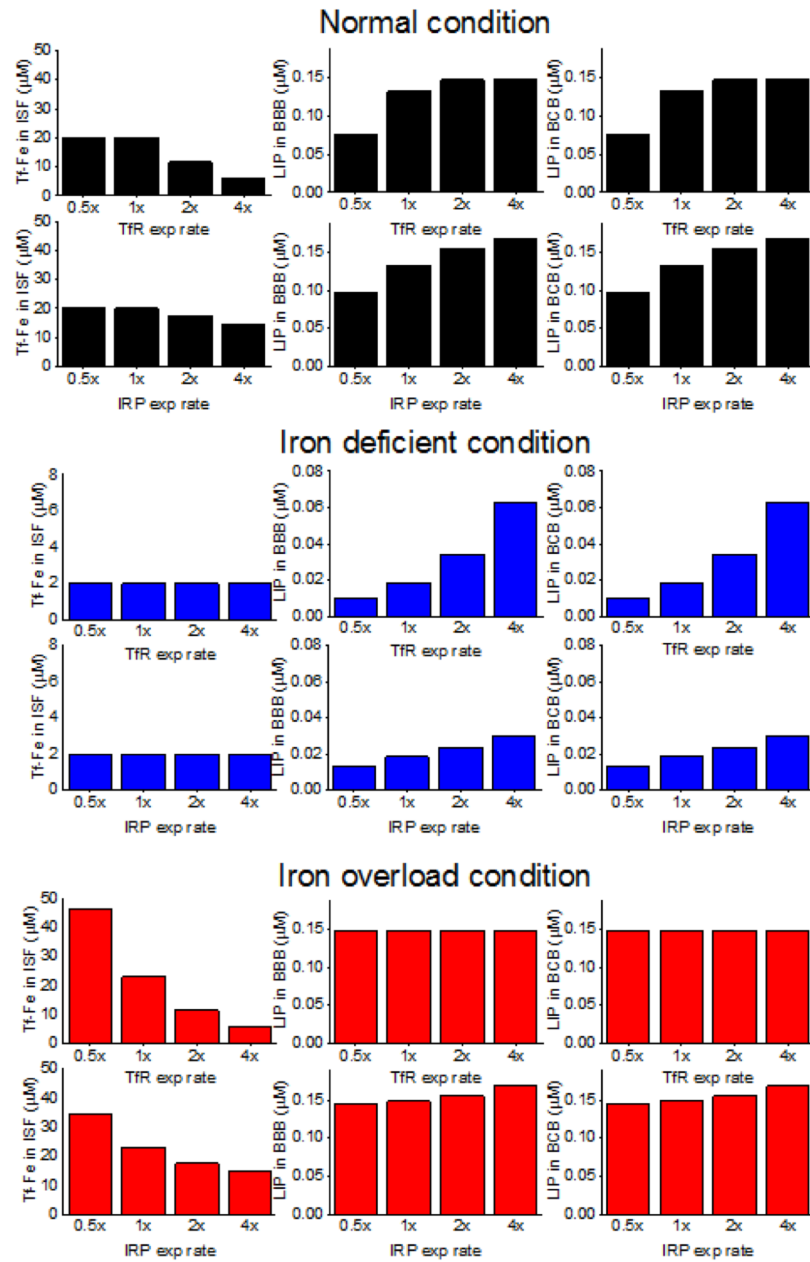


Figure 4.6 The effect of system-wide expression changes in TfR and IRP on the concentration of Tf-Fe in ISF and labile iron pool in both BBB and BCB under 3 conditions: normal iron serum 20 μM , iron deficiency 0.2 μM and iron overload 200 μM . This shows that system-wide changes in the expression rate of TfR and IRP decrease the concentration of iron in the brain ISF under normal and overload condition, but do not significantly change the amount of iron reaching the ISF under iron deficiency condition. There appears to be a shift on the effect of TfR or IRP expression with insufficient iron in the serum.

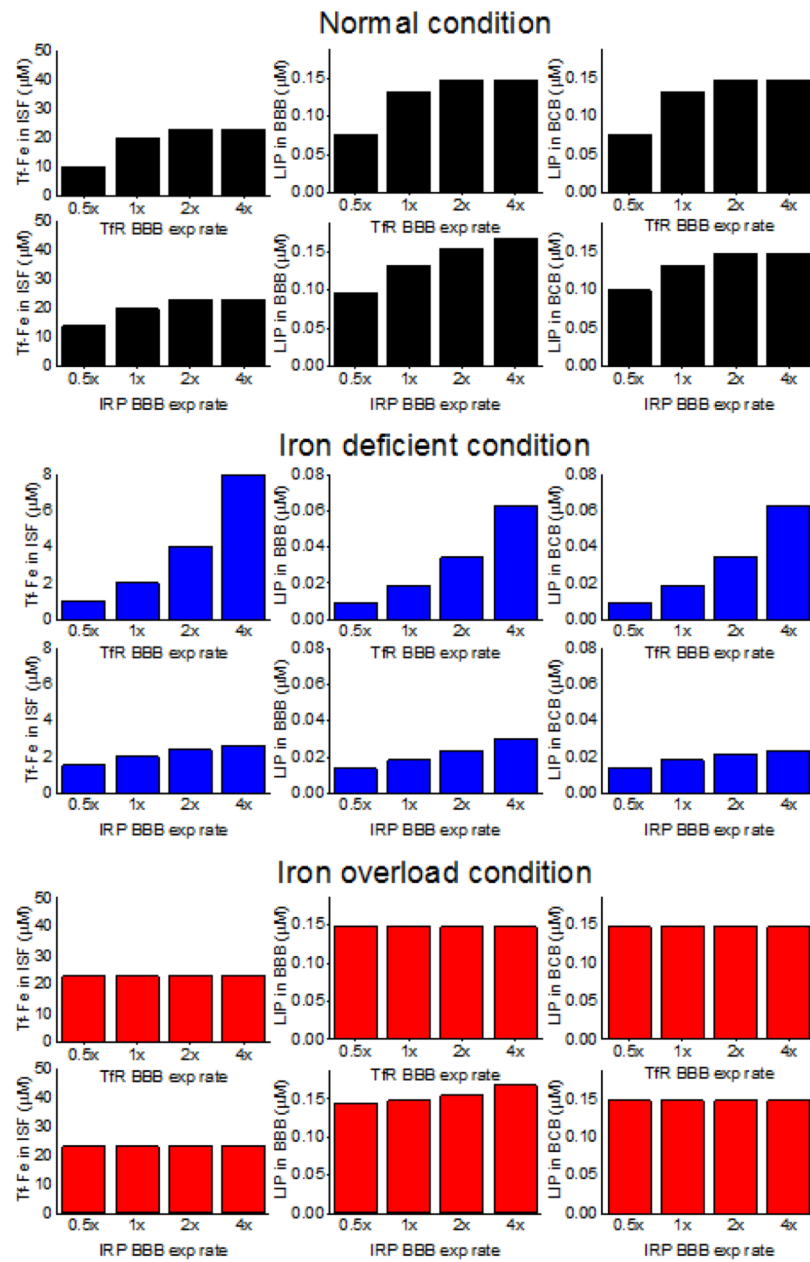


Figure 4.7 The consequences of perturbations of IRP and TfR expression only in BBB under 3 conditions: normal iron serum $20 \mu\text{M}$, iron deficiency $0.2 \mu\text{M}$ and iron overload $200 \mu\text{M}$. This shows that changes in BBB expression rate of TfR and IRP do not affect the concentration of iron in the brain ISF, as well as LIP in BBB and BCB, under normal and overload condition, but significantly change the amount of iron reaching the ISF and LIP under iron deficiency condition. There appears to be a shift on the effect of TfR or IRP expression with insufficient iron in the serum.

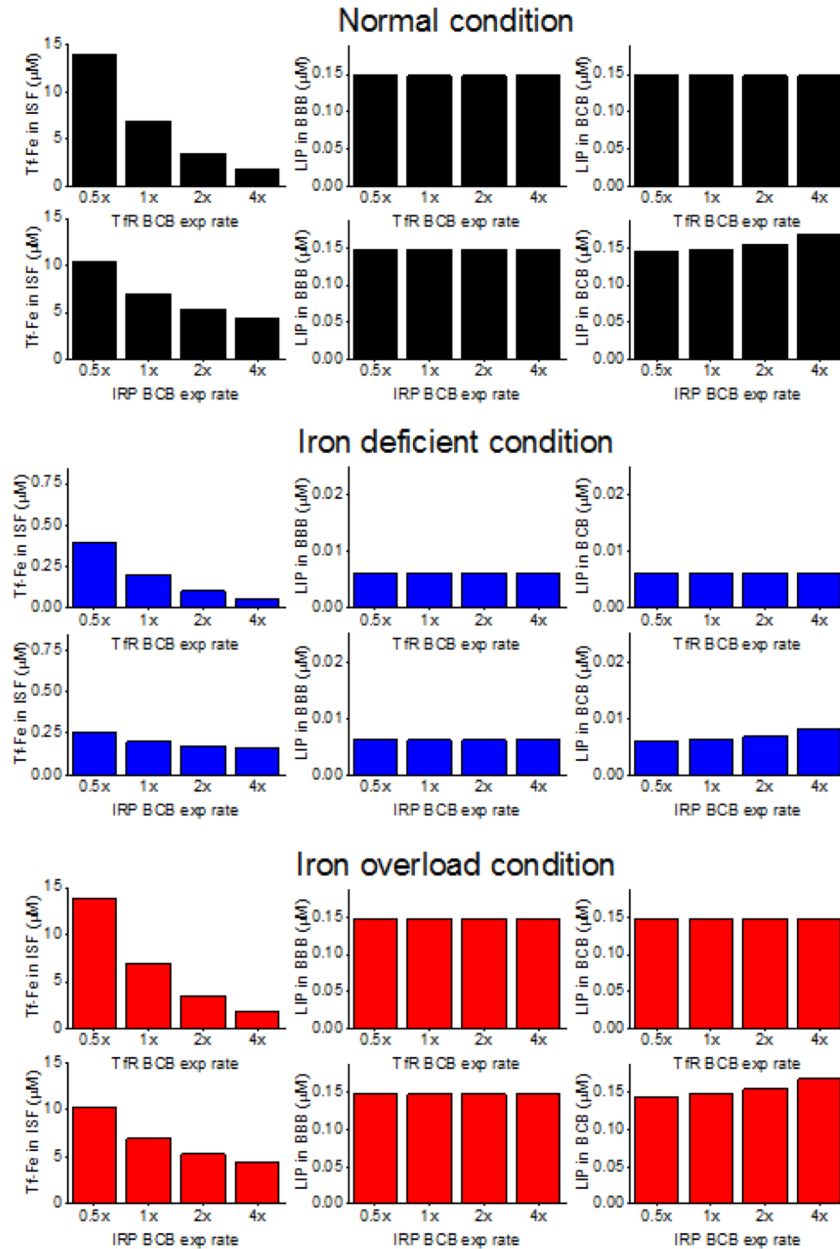


Figure 4.8 The consequences of perturbations of IRP and TfR expression only in BCB under 3 conditions: normal iron serum 20 μM , iron deficiency 0.2 μM and iron overload 200 μM . This shows that under all three conditions the changes in BBB expression rate of TfR and IRP decrease the concentration of iron in the brain ISF, but has no/ slight effect on the LIP in BBB and BCB.

or IRP in the BBB changes, except for the slight increases in the LIP in the BBB concentration when the IRP expression in the BBB increases.

Figure 4.8 shows the response of Tf-Fe in the ISF and the LIP in the BBB and BCB when the expression of TfR in the BCB is varied while in the BBB the TfR expression rate is kept at its normal level. Unlike the previous two simulations, the results determined by varying the expression of TfR or the IRP rate in the BCB appear to be similar across the three conditions. The concentration of Tf-Fe in the ISF decreases with an increasing expression rate for TfR or IRP in the BCB, while the steady state concentration of the LIP in the BBB stays constant. The concentration of LIP in BCB is affected by the increasing expression rate of IRP in the BCB, but not by the increasing rate of TfR in the BCB.

4.3.5 Iron uptake in response to varying iron usage in the brain

As previously mentioned, iron is involved in numerous metabolic reactions in the brain cells. A condition was simulated where the usage of iron in the brain ISF is (temporarily) increased to examine the resulting iron uptake across the barriers, especially the BBB. The result of the simulation (figure 4.9) shows that a spiked increase in the use of Tf-Fe in the ISF over a one day period affects the concentration of the ISF Tf-Fe, but does not perturb the concentration of LIP in BBB. Figure 4.9A shows that the rate of the temporary use of the Tf-Fe in the ISF was set to spike at $0.2 \mu\text{M/s}$ after a period of half a day before returning to the initial rate. The simulation result shows that the concentration of Tf-Fe in the ISF decreases as the rate of Tf-Fe usage increases, as shown in figure 4.9C. The concentration of Tf-Fe in the ISF reaches $0.364 \mu\text{M}$ when the usage rate reaches its peak. In comparison, the concentration of the LIP in the BBB (figure 4.9B) stays at the steady state value throughout the increased Tf-Fe usage in the ISF. This result shows that the BBB in this model does not compensate for the loss of Tf-Fe concentration in the ISF, which may not be the ideal response to a reduced brain iron concentration. The simulation over a longer period of time, over a year, of high iron consumption in the ISF shows the same result

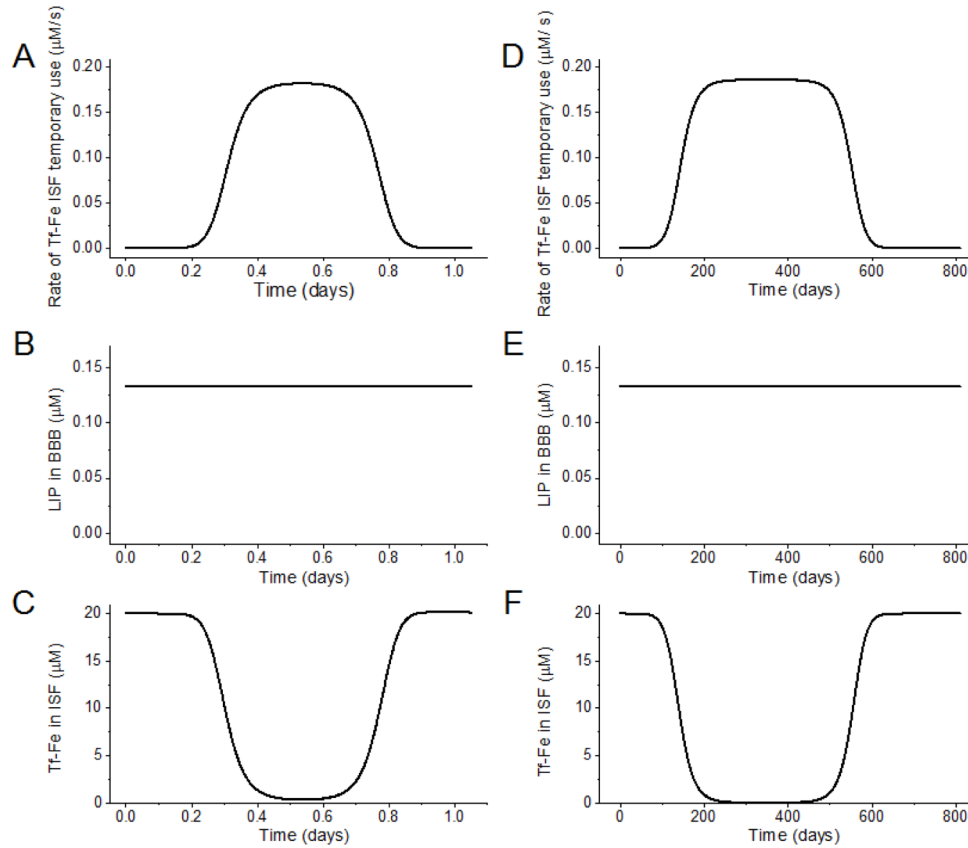


Figure 4.9 Iron uptake across the BBB in response to a temporary increase in the rate of Tf-Fe ISF usage. (A) The signal triggered to simulate an increase in Tf-Fe ISF usage for one day period. The set peak rate of Tf-Fe usage in the ISF is $0.20 \mu\text{M s}^{-1}$. (B) The concentration of the LIP in the BBB and (C) Tf-Fe in ISF in response to an increase in the ISF Tf-Fe consumption signal in A. (D) The signal triggered to simulate an increase in Tf-Fe ISF usage for a long period of time (more than 200 days). (E) The concentration of the LIP in the BBB and (C) Tf-Fe in the ISF in response to an increase in the ISF Tf-Fe consumption signal in D.

as the simulation over a day range, the concentration of the Tf-Fe is low during high iron usage in the ISF and the concentration of the LIP in the BBB stay constant, as shown in figure 4.9D – F. The LIP and ferritin (not shown) in the BBB in the model do not compensate for the loss of iron in the ISF. The concentration of the metabolites and the rates of the reactions in the BBB are unaffected by the increase in usage of Tf-Fe in the ISF.

4.4 Discussion

Iron is one of the essential metals in the brain and is involved in many metabolic reactions. The exact course of iron transport into the brain is still not fully understood; therefore, we have created a mathematical model of iron transport across the brain barrier systems. This new model provides an *in silico* resource to explore the brain iron transport system and the impact of brain iron dysregulation. The currently available iron uptake model in the brain by Simpson et al. (2014) [134] also recognised the BBB role in controlling the uptake of iron into the brain. However, they do not capture the system in complete detail because they have excluded the IRP, which regulates the expressions of the transport proteins (TfR, DMT1, ferroportin) and ferritin, from their model.

They have also hypothesised that TfRs are expressed on the abluminal side of the BBB, and it is TfRs that are responsible for sensing the iron saturation level [134]. This suggestion is still not yet backed up by sufficient experimental evidence, and there is also not enough evidence to prove the presence of abluminal TfR in the BBB. Therefore, this was not incorporated this into our model.

The brain barrier systems model simulations accurately replicate, in a qualitative sense, the form of the curves of the iron uptake kinetics across the BBB. This is evidenced in the quality of fit (chi squared value is approximately 0.04), obtained by fitting the simulated curves with independently-determined data from various experimental systems. The agreement is qualitative, not quantitative, because the absolute values are different even though there is good agreement in the form of the curves. In response to increasing Tf-Fe concentration in the serum, the concentration of Tf-Fe bound to TfR increases and saturates. The simulated kinetics appear to be comparable to experimental results obtained by Hill et al. (1985) [130]. The simulation and experimental TfRs reach maximum occupancy at a low concentration. It is suggested that serum iron levels towards iron overload would not cause a significant increase in the iron uptake rate into the BBB. We also studied the dynamics of brain

iron uptake in response to a serum Tf-Fe injection. The model shows similar dynamics to the time course study from rat brains by Taylor and Morgan (1990) [131]. The parameter values used in this model were derived from data from *in vitro* experiments and animal studies. The use of these parameters may raise doubts as to the validity of the model as often *in vitro* experiments do not perfectly mimic *in vivo* conditions and animal models are not equivalent to human models. Despite this limitation, the model is able to qualitatively replicate experimental observations that were not applied in the model calibration process (shown in figure 4.3 and 4.4).

The concentration of iron in the brain is more stable than in the liver. As the only barrier separating the two, it has been postulated in the literature that the BBB is mainly responsible for regulating the homeostasis of iron in the brain [7, 32, 134]. We simulated time courses of the model in response to an increasing constant concentration of Tf-Fe in the serum (figure 4.5). The model shows that increasing the concentration of serum Tf-Fe does not increase the rate of iron uptake into the brain. The barriers appear to limit the rate of uptake of iron into the ISF. As a result of the controlled iron uptake rates and intracellular iron buffering, the concentration of LIP in the barriers remains below $0.15\ \mu\text{M}$ even when challenged by high serum Tf-Fe level. Thus the model shows that the integrity of the barriers would be protected in an iron overload case. The concentration of iron in the ISF is also predicted to saturate at $\sim 23\ \mu\text{M}$, which is relatively low compared to the iron concentration inside the brain tissue. In the earlier part of the time course (figure 4.5C), the concentration of ISF iron increases sharply to a concentration similar to the input serum Tf-Fe before it declines to a steady state concentration after five days. This result supports the postulation that the BBB can regulate the homeostasis of iron in the brain. The model shows that the concentration of iron in the ISF is also quickly regulated to a safe level, even when the concentration of iron added into the model is six times the normal concentration ($\sim 20\ \mu\text{M}$) [14]. The regulation of iron is important with respect to the overall concentration of iron in the brain as the brain cells, neurones and glia are directly exposed to it. By

controlling the ISF and CSF iron level, the model shows that the BBB and BCB have a regulating capacity that agrees with previous hypotheses.

Sensitivity analyses were performed to evaluate how much changes in a specific parameter affect the metabolites in the model. Generic sensitivity measurements produced sensitivity coefficients in response to a small change in the specific parameters of a reaction. The MCA produced concentration control coefficients that describe how much a small change in the rate of a specific reaction affects the concentration of the metabolite of interest. Two different algorithms in COPASI were employed to perform the MCA: the Reder and Smallbone algorithm. The Reder algorithm is only valid under certain circumstances and the Smallbone algorithm is supposed to remove this limitation. However, our results show that using the Smallbone algorithm, the concentration control coefficient for all of the metabolites in respect to small changes in IRP expression and degradation in both the BBB and the BCB are zero. This is not the case with the Reder algorithm as well as generic sensitivity analysis which indicate that IRP expression and degradation have significant control over the concentration of the LIP in the BBB and the BCB and Tf-Fe in the ISF. Based on this result, we will rely more on the result from the Reder algorithm for the MCA to determine the reactions that affect the metabolites of interest.

The results from the sensitivity analysis show that the protein that has the most control over the concentration of the LIP in the BBB and the Tf-Fe in the ISF is TfR, followed by ferroportin and IRP. For the concentration of the LIP in the BCB, the protein that has most control is the ferroportin followed by TfR and IRP. The reactions involving the transport protein TfRs on the surface of both the BBB and the BCB have the highest control over iron transported into the brain. The IRPs in the BBB and the BCB also a significant effect on the concentration of the Tf-Fe in the ISF. Because the expression of the IRP is regulated by the concentration of the LIP in the BBB and the BCB, this may indicate that intracellular iron status in BBB/BCB epithelial cells could modulate iron concentrations available to cerebral tissue.

To investigate the effect of the abundance of the TfR and IRP, the concentration of the LIP in the BBB and the BCB and Tf-Fe in the ISF in response to different expression rates of the proteins. The results of the simulations are shown in figures 4.6, 4.7 and 4.8. Figure 4.6 shows that under normal and iron overload condition, when the expression rates of TfR in the BBB and BCB are varied simultaneously, the system-wide change of TfR on the barriers does have an impact on the amount of iron inside the BBB and the BCB and transported into the ISF. In this condition, higher than normal expression rate of TfR or IRP means reduced concentration of iron transported into the ISF, but higher LIP in both the BBB and the BCB. The result for iron deficiency condition shows that the system-wide change of TfR affects the iron in the BBB and BCB, but not the iron in the brain ISF. While in iron overload conditions, the system-wide change of TfR affects the iron in the brain ISF, but not the iron in the BBB and BCB. There appears to be a different regulation system for the iron uptake across the BBB and BCB in these three different conditions. This shift in regulation indicates the importance of experimental context when attempting to control iron metabolism with drugs and the potential for drug targets specific to iron deficiency that would avoid side effects when iron levels return to normal.

Simulations varying TfR or IRP expression rates in either the BBB independently (i.e. not in both the BBB and the BCB simultaneously) were performed and are shown in figure 4.7. In normal and overload conditions, the increase in TfR or IRP expression seems not to alter the concentration of iron transported into the brain and the barriers, whilst in iron deficiency, the concentration of Tf-Fe increases with increasing TfR in the BBB. From these results, it seems that, depending on whether there is sufficient concentration of the iron in the serum or not, the concentration of TfR may or may not have a notable effect on the transport of iron into the brain.

In all the conditions examined, the concentrations of LIP in the BBB and the BCB stay at $\sim 0.15\mu\text{M}$, which is below $1.2\mu\text{M}$, the concentration of iron that kills anterior pituitary cells [135]. The higher concentration of the LIP in the barrier increases the possibility of redox reaction occurring which may lead to cell death and loss of the

barrier integrity. According to the simulation, an increased expression rate of TfR or IRP in both barriers and only in the BBB or the BCB does not increase the probability of the BBB and the BCB losing their integrity due to a redox reaction.

Figure 4.5 shows how the model effectively responds to iron overload conditions in the serum. To investigate further how the BBB preserves iron homeostasis in the brain, a situation where there is a loss of iron in the brain ISF due to an increase in the uptake of iron into the nearby brain cells was simulated (figure 4.9). The result of this simulation shows that the BBB in the model does not maintain a steady state concentration of iron in the local ISF. The simulated high consumption reaction of the ISF Tf-Fe keeps the concentration of the Tf-Fe in the ISF relatively low over that period of time, while the concentration of all of the metabolites in the BBB stays at a steady state and the rate of the reactions in the BBB stay constant. The BBB model does not appear to balance the loss of the Tf-Fe in the nearby ISF. The probable reasons for this simulation result are: (1) the lack of feedback from the ISF compartment to the BBB and (2) the BBB stops providing more iron into the iron packed local cells.

One of the conclusions that can be taken from the simulation result shown in figure 4.9 is the suggestion that the presence of a positive feedback mechanism is required to ensure sufficient iron entering the brain. This function may be performed by hepcidin or a metabolite playing a role equivalent to hepcidin; there is very little evidence as yet for the presence of hepcidin in the BBB and this remains unconfirmed and a subject of debate. Hepcidin is mostly expressed in the liver and in this model, the concentration of hepcidin in both barriers is kept constant because of the theory that hepcidin protein found in the brain originates in the liver [73]. There are data showing that the hepcidin protein is widely distributed in the brain, however, its expression and presence in and in the vicinity of the BBB is not yet well established [73]. In recent years, there are research findings in human tissue and cells that show the presence of hepcidin mRNA and its expression in the astrocytes, cells that surround the brain capillaries, *ex vivo* and in cell culture [136, 137]. Another study found that an increase

in the concentration of iron in the astrocytes decreases the uptake of iron by the BBB, which further supports the feedback mechanism theory [134]. TfR2 and HFE protein that modulate the hepcidin levels in the liver are found in the brain [137], but have not yet been found in the abluminal side of the BBB. The mechanism by which the hepcidin acts as a regulator of iron export in the BBB is still under study.

In this chapter, an *in silico* model that represents the brain barrier systems in the human brain was developed and tested under different iron conditions and different expressions of important metabolites. The brain barrier systems model protected the brain from brain iron overload, which is consistent with the main predicted function of BBB and BCB in the human brain [21]. The model provides an *in silico* resource to begin exploring and predicting the impact of iron dysregulation in neurodegenerative diseases such as Alzheimer's disease and Parkinson's disease. Investigations that can only be undertaken by computational systems modelling, such as metabolic control analysis, provide new insights into the most critical function in the regulation of iron metabolism in health and disease. Important iron pathways in the disease may thereby be identified using this model, and these pathways could then be targeted in the model with simulated drug action. In the future, by adding a species to represent an iron modifying drug, as the therapeutic agent, the model could be integrated with a pharmacokinetic/pharmacodynamic model. This upgraded version of the model would be useful to improve understanding of the mechanism of action of existing therapeutics and to predict effective targets for novel therapeutics. Moreover, this model with the simulated drug action is a current priority as clinical trials of iron modifying drugs as protective agents are currently underway for PD and AD [20].

Chapter 5 Modelling iron metabolism in dopaminergic neurone of the Substantia nigra

In chapter 4, a computational model that describes the brain iron uptake was presented. The model described the tightly regulated iron uptake into the brain interstitial fluid (ISF), which was treated as the ‘brain’. This model does not include the transport of iron into the dopaminergic neurone (DA) neurone, which, as previously mentioned, is the cell that is highly involved in the progression of the Parkinson’s disease (PD). The disruption of brain iron homeostasis in PD is distinguished by an increase in iron concentration and increased cell death in certain areas in the brain, the DA neurone cells in the substantia nigra (SNpc) being the area that is most obviously affected in these respects. In order to explore the role of iron in the DA neurone, a completely original computational model that describes brain iron homeostasis in the DA neurones in health, and under conditions of iron overload, was developed for future application to PD using the same principles as the model in chapter 4. This new model is the subject of Chapter 5.

The main characteristic that differentiates the DA neurone in the SNpc from other types of neurone is the dark brown pigment called neuromelanin [138]. Neuromelanin binds to metal, primarily iron in the neurone. Neuromelanin has two different iron binding sites, high affinity binding sites with a disassociation constant K_D of ~ 10 nM and low affinity binding sites with a disassociation constant K_D of ~ 100 nM [139]. Iron bound to the neuromelanin high affinity binding sites is internalised into the neuromelanin core in a similar fashion to ferritin. By using Mossbauer spectroscopy,

Gerlach et al. (1995) showed that these binding sites appear to be similar to those in ferritin [140]. Iron sequestered by neuromelanin is redox inactive, but the iron bound to the low-affinity binding sites in neuromelanin has been linked to the formation of redox active complexes [15, 141]. The mechanism of iron binding to neuromelanin and its release is still under investigation [142]. The binding of iron to neuromelanin is included in the model presented in this chapter, to investigate the interaction of iron with neuromelanin in the health and PD.

Similar to iron uptake in the BBB and the BCB in chapter 4, in the DA neurone, two transferrin proteins bind to iron (Tf-Fe) in the ISF then bind to TfRs on the surface of the DA neurones. The binding initiates receptor-induced endocytosis of the 2 Tf-Fes. Inside the endosome, iron is chemically reduced and released into the labile iron pool (LIP) in the cytosol of the DA neurone, and TfR-Tf is recycled back to the surface of the neurone. Iron in the LIP may be involved in the production of dopamine and other processes [36]. Any excess iron is stored in neuromelanin or ferritin, or transported back out of the neurone by the ferroportin into the ISF. The expression of TfR, ferroportin, DMT1 and ferritin is monitored and governed by IRP [143].

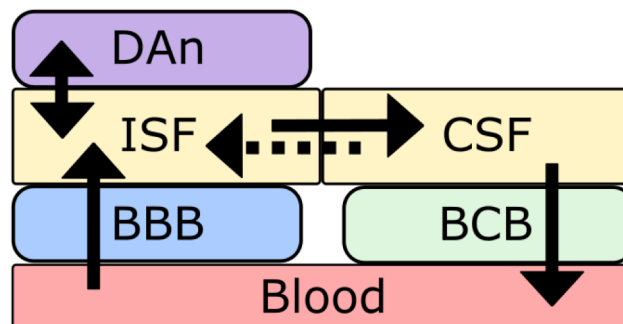


Figure 5.1 Illustration of the flow of iron between the blood and the brain including the DA neurone. The fenestrated cells between the ISF and the CSF allow free exchange of iron, but the direction of the fluid bulk flow is principally from the ISF into the CSF. The arrows represent the direction of the iron transport and the dotted arrow represents the weaker flow of Tf-Fe from ISF to CSF.

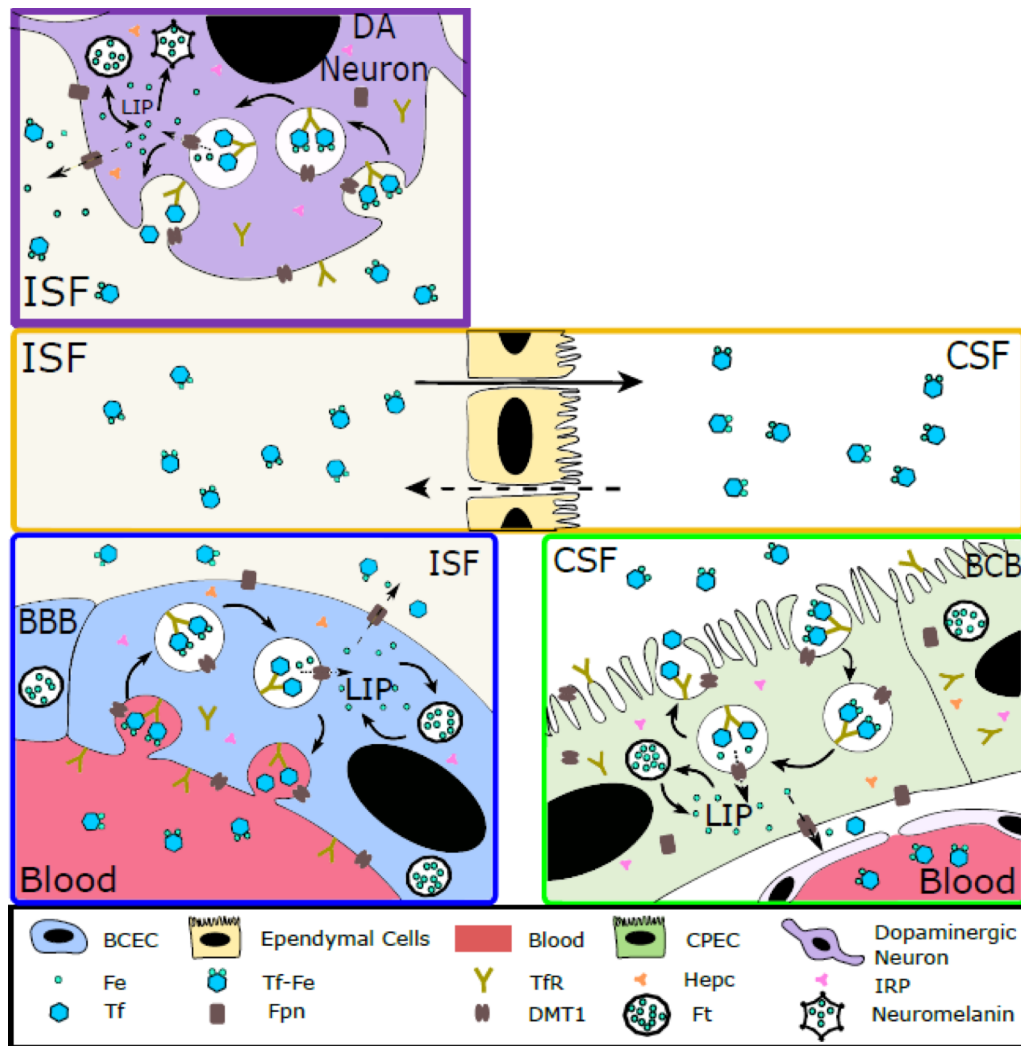


Figure 5.2 Conceptual biological diagram for iron uptake in the brain from which the model in this chapter derived. The direction of the flow of iron is shown in figure 5.1. Abbreviations: BBB: blood brain barrier, BCB: blood cerebrospinal fluid, BCEC: brain capillary endothelial cell (comprises the BBB), CPEC: choroid plexus epithelial cell (comprises the BCB), CSF: cerebrospinal fluid, DA neurone: dopaminergic neurone, DMT1: divalent metal transporter 1, Fe: iron, Fpn: ferroportin, Ft: ferritin, Hepc: hepcidin, IRP: iron response protein, ISF: interstitial fluid, LIP: labile iron pool, Tf: transferrin, Tf-Fe: transferrin bound iron, TfR: transferrin receptor.

In this chapter, a new compartment, representing the DA neurone, is added to the prior model presented in chapter 4 as shown in the illustration of the flow of iron in figure 5.1. The updated model describes a mechanistic computational model of iron transport

and regulation between the serum and the dopaminergic neurones. Using this computational model, the uptake of iron into the DA neurone will be explored.

5.1 Materials and methods

As in chapter 4, the multi-compartment *in silico* model of brain iron trafficking into the DA neurone has been created using COPASI. The model comprises nonlinear ordinary differential equations to characterise the kinetics of each chemical species incorporated. The methodology for modelling the combined iron metabolism in the BBB and BCB and the dopaminergic neurones was performed following the approaches described in chapter 4 section 4.2, unless stated below. A new compartment, describing the dopaminergic neurones, was added into the brain barrier system's iron metabolism. The schematics assumed the uptake of iron into the brain and the DA neurone included in the new model are shown in figure 5. 2. The process diagram for the model is depicted in System Biology Graphical Notations (SBGN) in figure 5. 3. The model consists of six compartments: blood serum, the BBB, the ISF, the CSF, the BCB, and the DA neurone in the SNpc. The volume of the DA neurone in this model is 5.5×10^3 l. This number was acquired by multiplying the volume of pigmented neurones, $17983 \mu\text{m}^3$, with the number of pigmented neurones, 3.045×10^8 [144]. The volume of the remaining compartments were kept unchanged. Also, all existing reactions incorporated in the original model and associated parameters were preserved.

In the DA neurone of the SNpc, the density of the TfR binding sites was estimated experimentally to be less than 4×10^{-12} mol/g tissue [87, 145]. By using the assumption that the density of brain cells is the same as water (~ 1000 g/l), the estimated concentration of TfR protein in the DA neurone is; $4 \times 10^{-12} \times 1000 = 4 \times 10^{-9}$ M, $4 \times 10^{-3} \mu\text{M}$ for TfR protein in the DA neurone. This value is ~ 100 x lower than the value of TfR concentration in the liver ($0.46 \mu\text{M}$) [124, 145]. The parameter for the expression rate of TfR in the DA neurone was set to be 100x lower than that in the

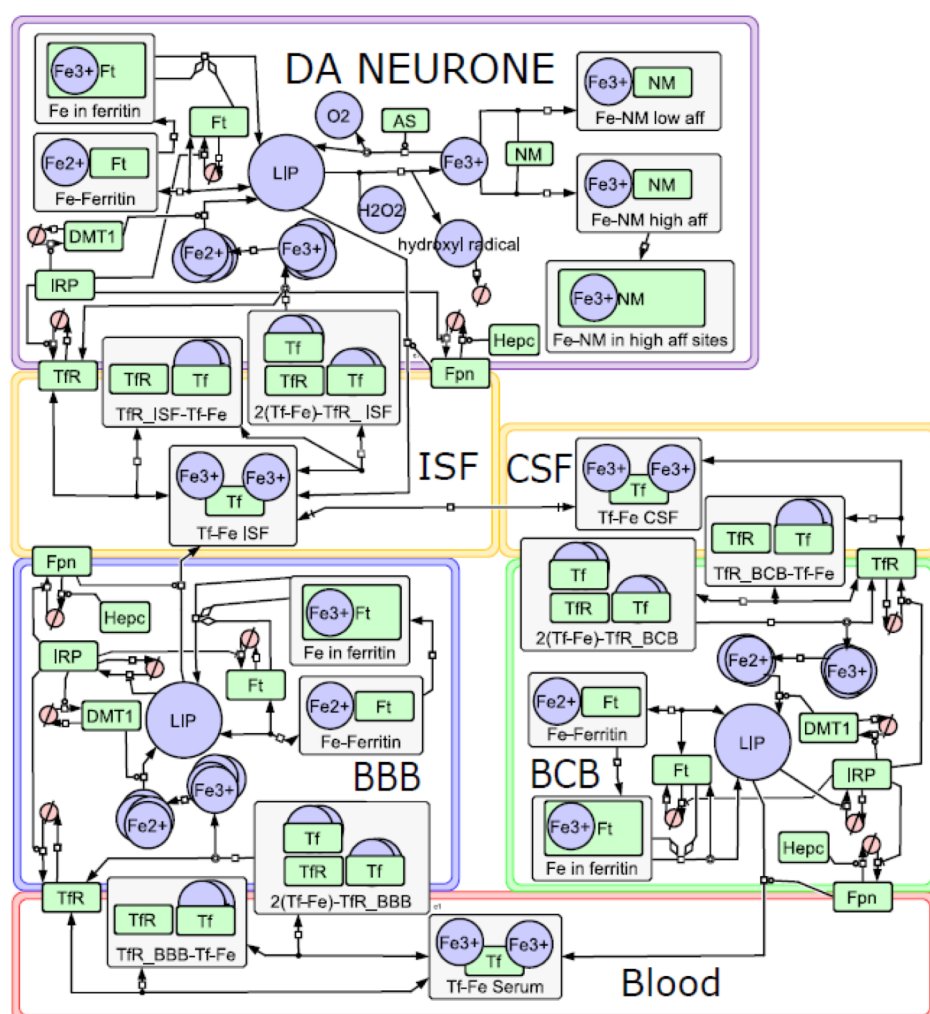


Figure 5.3 System Biology Graphical Notation (SBGN) process diagram of iron trafficking in the human brain barrier system and dopaminergic neurone model based on the mechanistic representation of the biological system shown in figure 5.2. Complexes are represented in boxes with component species. In the special case of the ferritin-iron complex, the amount for each species are not depicted in stoichiometric quantities (there are thousands or iron ions per ferritin). Species overlaid on the compartment boundaries represent membrane-associated species. Abbreviation: AS: ascorbate, BBB: blood brain barrier, BCB: blood cerebrospinal fluid, CSF: cerebrospinal fluid, DA neurone: dopaminergic neurone, DMT1: divalent metal transporter 1, Fe: iron, Fpn: ferroportin, Ft: ferritin, IRP: iron response protein, LIP: labile iron pool, NM: neuromelanin, Tf-Fe Serum: transferrin bound iron in the blood plasma, TfR: transferrin receptor.

liver, from $6 \times 10^{-12} \text{ s}^{-1}$ to $6 \times 10^{-14} \text{ s}^{-1}$ [94]. All other reactions involved in the iron endocytosis in the DA neurone were assumed to be identical those in the BBB and BCB. The reactions and parameters used are listed in table 5-1.

The concentration of the neuromelanin was derived by taking the average of the neuromelanin concentration shown in the figure in the paper by Zecca et al. (2001) [146]. The concentration of the neuromelanin was derived by multiplying the amount of available binding sites (6×10^{20} sites per g) [147] by the amount of neuromelanin available in the SNpc (2×10^{-3} g neuromelanin/ g wet tissue); $6 \times 10^{20} \times 2 \times 10^{-3} = 1.2 \times 10^{18}$ sites/ g wet tissue. Assuming that the density of brain cells is the same as water ($\sim 1000 \text{ g/l}$); $1.2 \times 10^{18} \times 1000 = 1.2 \times 10^{21}$ sites/ l wet tissue. Using the Avogadro's constant, the molar concentration is calculated; $1.2 \times 10^{21} / 6.023 \times 10^{23} = 2 \times 10^{-3} \text{ M}$, $2 \times 10^{-3} \text{ M} = 2 \times 10^3 \mu\text{M}$ of neuromelanin. Neuromelanin incorporates two different binding sites for iron; high ($KD = 7.18 \pm 1.08 \text{ nM}$) and low ($KD = 94.31 \pm 6.55 \text{ nM}$) affinity sites [139]. Neuromelanin binds to iron in the ferric form iron core similar to ferritin, thus neuromelanin was modelled in the same way as ferritin, using equations Eq. 4.14 and Eq. 4.15. The on and off binding rates for both the high and low affinity binding sites were adjusted with minimal changes from the ferritin kinetics, using the following equation:

$$KD_{NM} = \frac{K_{NM_{off}}}{K_{NM_{on}}} = \frac{K_{ferritin_{off}}/x}{x * K_{ferritin_{on}}} \quad \text{Eq. 5.1}$$

Unlike ferritin, neuromelanin does not appear to oxidise ferrous iron into ferric iron [148], so iron oxidation and reduction reaction are added. The LIP in the DA neurone is oxidised by H_2O_2 producing ferric iron and hydroxyl radical. The hydroxyl radical then is degraded. It has a half-life of 10^{-9} s [149], which was used to calculate the degradation rate using Eq. 4.1.

When simulating the neurodegenerative condition, some of the parameters in table 5-1 were adjusted according to data found in the published literature as follows. The

expression level of TfR was kept unchanged according to the result of post-mortem human brain studies comparing TfR level in healthy and PD subjects [87, 150]. The expression level of DMT1 and IRP in SN are increased by 11x and 3.5x, respectively, and the expression level of FPN in SN is decreased by 0.3x. These changes are according to the level of DMT1, IRP and ferroportin expression detected in Calcium-independent phospholipase A2 β (iPLA2 β)-KO mice [151]. iPLA2 β is encoded by the PLA2G6 gene. The mutation of this gene has been linked to PLA2G6-associated neurodegeneration (PLAN), which is the second most common type of neurodegeneration with brain accumulation (NBIA) [152]. In the experimental study, it has been shown that PLAN has some common iron accumulation pathways and degeneration in brain regions such as SN, so the result from this experiment in a mouse model was incorporated into the brain-iron-related simulation of a neurodegenerative condition [151]. In this thesis, this simulation will be called the PD/NBIA simulation.

Table 5-1 List of the reactions and their parameters for the DA neurone compartment in the extended model.

Name	Reaction	Function	Parameters	Ref
TfR_DAN expression	\rightarrow TfR DAN; IRP DAN	Hill function \rightarrow	$a = 6 \times 10^{-14} \text{ s}^{-1}$ $n = 1$ $K = 1 \times 10^{-6} \text{ mol}$	[123, 124]
TfR_DAN degradation	TfR DAN \rightarrow	Mass action (irreversible)	$k = 8.37 \times 10^{-6} \text{ s}^{-1}$	[124]
TfR_DAN binding 1	TfR_DAN + Tf-Fe_ISF \rightarrow TfR_DAN -Tf-Fe_ISF	Mass action (irreversible)	$k = 837400$ $l^*(\text{mol}^*\text{s})^{-1}$	[42]
TfR_DAN release 1	TfR_DAN -Tf-Fe_ISF \rightarrow TfR_DAN + Tf-Fe_ISF	Mass action (irreversible)	$k = 9.142 \times 10^{-4} \text{ s}^{-1}$	[42]
TfR_DAN binding 2	TfR_DAN -Tf-Fe_ISF + Tf-Fe_ISF \rightarrow 2(Tf-Fe)-TfR_DAN	Mass action (irreversible)	$k = 121400$ $l^*(\text{mol}^*\text{s})^{-1}$	[42]
TfR_DAN release 2	2(Tf-Fe)-TfR_DAN \rightarrow TfR_DAN -Tf-Fe_ISF + Tf-Fe_ISF	Mass action (irreversible)	$k = 3.535 \times 10^{-3} \text{ s}^{-1}$	[42]
TfR_DAN iron internalisation	2(Tf-Fe)-TfR_DAN \leftrightarrow * endoFe3_DAN + TfR_BBB	Mass action (reversible)	$k_1 = 0.8333 \text{ s}^{-1}$, $k_2 = 0.1 \text{ l}^5*(\text{mol}^4*\text{s})^{-1}$	[42]

Name	Reaction	Function	Parameters	Ref
Steap3_ DAN iron reduction	endoFe3_DAN → endoFe2_DAN	Henri-Michealis-Menten	$K_m = 7.4 \times 10^{-5} \text{ mol}^* \text{l}^{-1}$, $V = 1.493 \times 10^{-4} \text{ mol (l}^* \text{s)}^{-1}$	[94]
DMT1_ DAN expression	→ DMT1_DAN; IRP_DAN	Hill function →	$a = 1.39 \times 10^{-10} \text{ s}^{-1}$, $n = 1$, $K = 2.5 \times 10^{-6} \text{ mol}$	[94]
DMT1_ DAN degradation	DMT1_DAN →	Mass action (irreversible)	$k = 2.4 \times 10^{-5} \text{ s}^{-1}$	[94]
DMT1_ DAN endosomal export	endoFe2_DAN → LIP_DAN; DMT1_DAN	Henri-Michealis-Menten	$k_{\text{cat}} = 258.6 \text{ s}^{-1}$, $K_m = 4.8 \times 10^{-6} \text{ mol}^* \text{l}^{-1}$	[94]
IRP_ DAN expression	→ IRP_DAN; LIP_DAN	Hill Function -l	$a = 4 \times 10^{-11} \text{ mol}^* (\text{l}^* \text{s})^{-1}$, $n = 1$, $K = 1 \times 10^{-7} \text{ mol}$	[47]
IRP_ DAN degradation	IRP_DAN →	Mass action (irreversible)	$k = 1.597 \times 10^{-5} \text{ s}^{-1}$	[126]
Fpn_ DAN expression	→ Fpn_DAN; IRP_DAN	Hill function -l	$a = 1 \times 10^{-9} \text{ mol}^* (\text{l}^* \text{s})^{-1}$, $n = 1$, $K = 1 \times 10^{-7} \text{ mol}$	[94]
Fpn_ DAN degradation	Fpn_DAN →; Hecpidin_DAN	Biochemical hill function →	$a = 2.315 \times 10^{-4} \text{ mol}^* (\text{l}^* \text{s})^{-1}$, $n = 5$, $K = 5 \times 10^{-9} \text{ mol}$	[94]

Name	Reaction	Function	Parameters	Ref
Fpn_DAN export	$2 * \text{LIP_DAN} \leftarrow \text{Tf-Fe_ISF}; \text{Fpn_DAN}$	Biochemical hill function \rightarrow	$a = 2 \text{ mol}*(\text{l*s})^{-1}$, $n = 1$, $K = 3 \times 10^{-6} \text{ mol}$	[127]
Temporary Fe_DAN use	$\text{LIP_DAN} \rightarrow$	Mass action (irreversible)	$k = 5 \times 10^{-5} \text{ s}^{-1}$	
Ferritin_DAN expression	$\rightarrow \text{Ferritin_DAN}; \text{IRP_DAN}$	Hill function -l	$a = 2.312 \times 10^{-13} \text{ mol}*(\text{l*s})^{-1}$, $n = 1$, $K = 1 \times 10^{-6} \text{ mol}$	[122]
Ferritin_DAN degradation	$\text{Ferritin_DAN} \rightarrow$	Mass action (irreversible)	$k = 1.203 \times 10^{-5} \text{ s}^{-1}$	[125]
Ferritin_DAN full degradation iron release	$\text{Fe_within_ferritin_DAN} \rightarrow \text{LIP_DAN}; \text{Fe_within_ferritin_DAN}$ Ferritin_DAN	Mass action ferritin	$k = 1.203 \times 10^{-5} \text{ s}^{-1}$	[125]
Ferritin_DAN internalised iron release	$\text{Fe_within_ferritin_DAN} \rightarrow \text{LIP_DAN}; \text{Fe_within_ferritin_DAN}$ Ferritin_DAN	Kloss Hill	$k_{\text{loss}} = 13.1251 \text{ s}^{-1}$	[125]
Ferritin_DAN iron binding	$\text{LIP_DAN} + \text{Ferritin_DAN} \rightarrow \text{Fe-ferritin_DAN}$	Mass action (irreversible)	$k = 4.71 \times 10^{10} \text{ l}*(\text{mol*s})^{-1}$	[125]
Ferritin_DAN iron internatlisation	$\text{Fe-ferritin_DAN} \rightarrow \text{Fe_within_ferritin_DAN} + \text{Ferritin_DAN}$	Mass action (irreversible)	$k = 108000 \text{ s}^{-1}$	[125]
Ferritin_DAN iron release	$\text{Fe-ferritin_DAN} \rightarrow \text{LIP_DAN} + \text{Ferritin_DAN}$	Mass action (irreversible)	$k = 22922 \text{ s}^{-1}$	[125]

Name	Reaction	Function	Parameters	Ref
Fe2 oxidation by H2O2	LIP_SN + H2O2 -> Fe3 + hydroxylRadical	Mass action (irreversible)	$k = 2670 \text{ l}^*(\text{mol}^*\text{s})^{-1}$	[149]
hydroxyl Radical to water	hydroxylRadical ->	Mass action (irreversible)	$k = 6.9 \times 10^8 \text{ s}^{-1}$	
Fe3 reduction by AS and O2	Fe3 + O2 + AS -> LIP_SN	Mass action (irreversible)	$k1 = 1 \times 10^8 \text{ l}^*(\text{mol}^*\text{s})^{-1}$	[120]
Iron binding to high_affinity_neuromelanin	NM_SN + Fe3 = NM-Fe_SN_high_affinity	Mass action (reversible)	$k1 = 3.88 \times 10^{11} \text{ l}^*(\text{mol}^*\text{s})^{-1}, k2 = 2785.18 \text{ s}^{-1}$	[138]
Iron released from high_affinity_neuromelanin	Fe_in_NM_SN_high_affinity -> Fe3; Fe_in_NM_SN_high_affinity NM_SN	Mass action (irreversible)	$k = 12 \text{ s}^{-1}$	[138]
High_affinity_neuromelanin core formation	NM-Fe_SN_high_affinity -> Fe_in_NM_SN_high_affinity	Mass action (irreversible)	$k = 10098 \text{ s}^{-1}$	[138]
Iron binding to low_affinity_neuromelanin	NM_SN + Fe3 = NM-Fe_SN_low_affinity	Mass action (reversible)	$k1 = 1.07 \times 10^{11} \text{ l}^*(\text{mol}^*\text{s})^{-1}, k2 = 10098 \text{ s}^{-1}$	[138]

5.2 Results

5.2.1 Iron concentrations in the DA neurone

The result of a time course simulation performed at normal serum iron concentration, $20\ \mu\text{M}$, over a time period of 80 years is shown in figure 5.4. The simulated concentration of LIP in the DA neurone is $\sim 0.013\ \mu\text{M}$, which is around 10x lower compared to the concentration of LIP in the BBB and the BCB (shown in chapter 4,

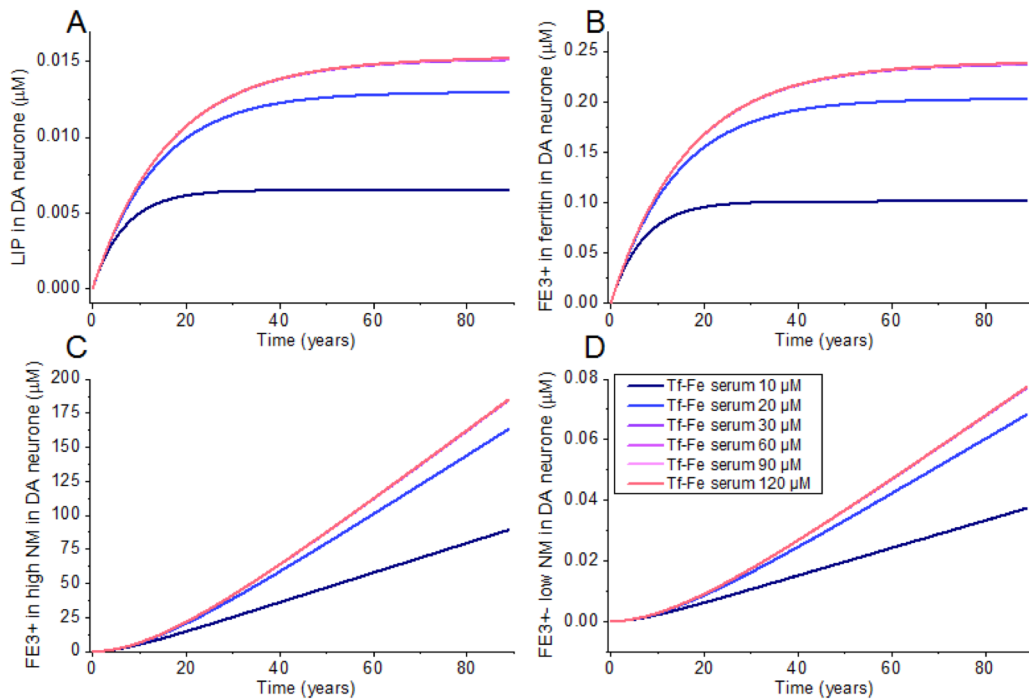


Figure 5.4 Time course simulations of the concentration of the metabolites in the DA neurone model responding to various levels of increased iron load. (A) The concentration of LIP in the DA neurone. (B) The concentration of iron in the ferritin in the DA neurone. (C) The concentration of iron at the high affinity binding sites of the neuromelanin in the DA neurone. (D) The concentration of iron at the low affinity binding sites of the neuromelanin in the DA neurone. The simulation was performed under normal conditions, Tf-Fe serum $20\ \mu\text{M}$, and is represented in bright blue. The curves representing Tf-Fe serum over than $30\ \mu\text{M}$ overlaps.

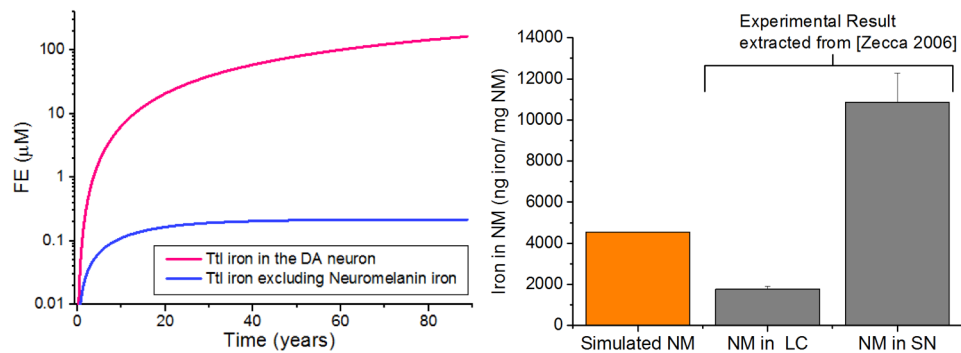


Figure 5.5 (A) Simulated time course of the accumulation of the total iron concentration in the DA neurone (red curve) and the total iron in the neurone without the iron in neuromelanin. Most of the iron in the DA neurone is sequestered to the neuromelanin. (B) The Simulated iron concentration in neuromelanin, ($\text{Fe}/\text{NM} = 4500 \text{ ng/mg neuromelanin}$), compared to the concentration determined experimentally in post-mortem LC (Locus Coeruleus) and SN (Substantia Nigra) tissue extracted from Zecca et al. (2006) [1].

figure 4.5). The time it takes to reach the steady state concentration is also much slower, 10 days vs 90 years. The concentration of the iron bound to the high affinity binding sites is $\sim 145 \mu\text{M}$ at 80 years and keeps increasing linearly. The concentration of iron at the low affinity binding sites also increases linearly over the time course, however the concentration is $\sim 0.06 \mu\text{M}$ around 2000 times lower than that at the high affinity binding sites. The total iron concentration in the neuromelanin at 80 years is estimated to be around 4530 ng iron/ mg neuromelanin, less than half of that compared to the concentration of iron in the SNpc neuromelanin experimental results of Zecca et al. (2006), shown in figure 5.5. In their paper, it was mentioned that the neuromelanin in the SNpc absorbed more iron during the isolation process, so the simulated concentration, which is between the concentration in the Locus Coeruleus and the SNpc, is within the range of possible *in vivo* concentration of iron in the neuromelanin. The concentration of iron in the ferritin is $\sim 0.20 \mu\text{M}$. This concentration is much lower than the iron concentration in the ferritin in the BBB and the BCB and the neuromelanin. The simulated concentration of ferritin protein in the DA neurone, 5.53 nM, is also lower than in the BBB and the BCB (9.26 nM).

Time course simulations for varying levels of Tf-Fe in the serum were performed using the model to predict the delivery of iron into the neurone under higher concentrations of iron, shown in figure 5.5. As shown in figure 5.5 in chapter 4, the concentration of iron in the ISF when serum iron is higher than $30\ \mu\text{M}$, staying at a steady state of $23.5\ \mu\text{M}$. Under this condition, the concentration of the metabolites in the DA neurone does not differ greatly from the concentration under normal iron conditions. The highest concentration of LIP in the DA neurone is $0.015\ \mu\text{M}$, which is still 10x lower than the normal concentration in the BBB or BCB. This value is also much lower than the concentration of labile iron that has been found to kill cells ($1.2\ \mu\text{M}$) [135]. The concentrations of iron at the low affinity binding sites in neuromelanin are $\sim 164\ \mu\text{M}$ and $\sim 0.07\ \mu\text{M}$, respectively. The concentration at the low affinity binding sites is much lower than the concentration at the high affinity binding sites. As the iron at low affinity sites has been linked to redox active complex [38], the model predicts that in normal condition, the concentration of this complex is low.

5.2.2 Iron concentration in DA neurone in the PD/NBIA simulation

The parameters for the expression rates for the proteins in the DA neurone were adjusted to the amount of protein found in the literature for NBIA and PD conditions, as described in materials and method section (section 5.1). The time course simulation was then performed under the same serum iron conditions for the control condition, shown in figure 5. 6. The concentration of the iron in the DA neurone is generally higher in the PD/NBIA simulation compared to the control. The concentration of LIP in the DA neurone at steady state is $\sim 0.38\ \mu\text{M}$ under normal serum iron conditions. This value is almost 30x higher than for the control condition and twice those in the LIP in the BBB and the BCB.

The concentration of iron in ferritin in the DA neurone reaches a steady state of $\sim 2.8\ \mu\text{M}$ at around ~ 80 years. This value is around 10x higher than for the control condition. The concentration of ferritin protein is $2.61\ \text{nM}$, half the concentration in the control condition. The concentration of the iron in the high affinity binding sites is $\sim 4300\ \mu\text{M}$

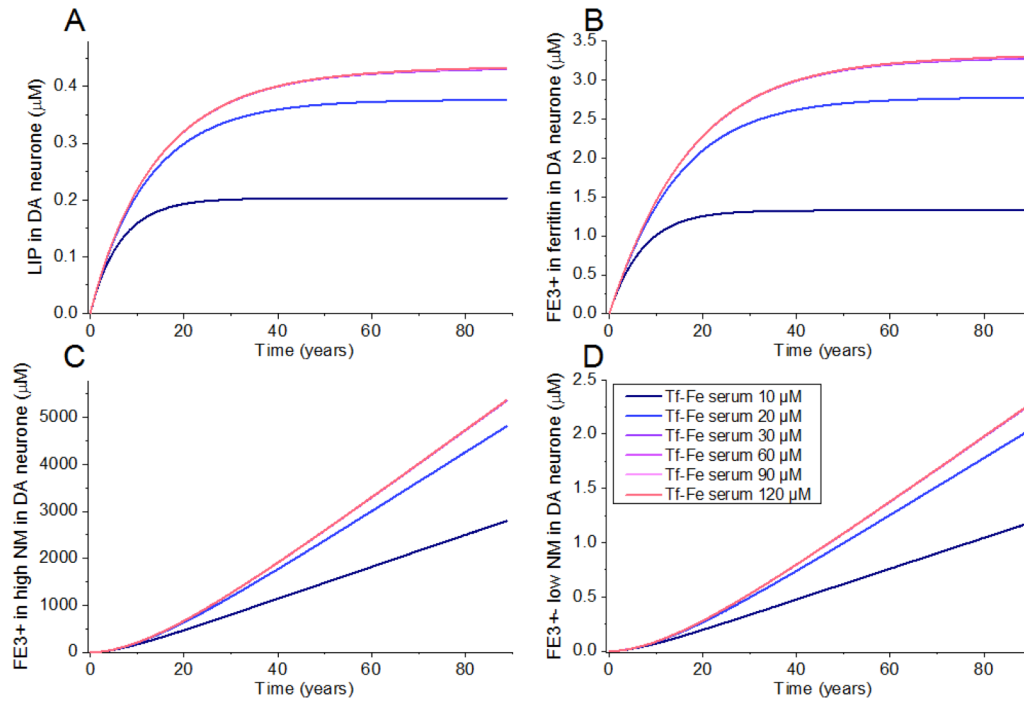


Figure 5.6 Time course simulations of the concentration of the metabolites in the DA neurone model responding to various levels of increased iron load in the PD/NBIA simulation. (A) The concentration of LIP in the DA neurone. (B) The concentration of iron in ferritin in the DA neurone. (C) The concentration of iron at the high affinity binding sites of neuromelanin in the DA neurone. (D) The concentration of iron at the low affinity binding sites of neuromelanin in the DA neurone. The simulations performed under normal conditions, where Tf-Fe serum of 20 μM , is represented in bright blue.

at 80 years and keeps increasing in a linear fashion. The concentration of iron at the low affinity binding sites also increases linearly over the time course, reaching a concentration of $\sim 1.8 \mu\text{M}$ at 80 years.

Time course simulations for varying levels of Tf-Fe in the serum were performed using the PD/NBIA model to predict the delivery of iron into the neurone under higher concentrations of iron, and are shown in figure 5.6. For a high serum iron concentration, the concentration of LIP in the DA neurone saturates at $0.43 \mu\text{M}$, which is higher than the normal concentration in the BBB or BCB. However, this value is still lower than the value at which redox damage in cells was observed ($1.2 \mu\text{M}$)[135].

The concentration of iron at the high and low affinity binding sites in neuromelanin reached $\sim 4800 \mu\text{M}$ and $\sim 2.0 \mu\text{M}$, respectively, at 80 years. The concentration of iron in the ferritin saturates at $3.3 \mu\text{M}$ with increasing serum iron. The time course simulations for varying serum iron concentrations predict that even under PD/NBIA condition the concentrations of the metabolites in the DA neurone do not differ greatly from the concentration for normal iron concentrations. The differences between the metabolite concentrations in the control condition and PD/NBIA simulation are much more significant than differences caused in the variation in the serum iron concentration, especially for iron in neuromelanin.

5.2.3 Metabolic control analysis

MCA was performed to investigate the reactions that have the greatest effect on the concentration of iron in the DA neurone. The Reder algorithm alone was used for this model, as the results in the previous chapter have shown that it is more suitable for this model. The result of the MCA calculations produced a concentration control coefficient for the metabolite of interest describing how much the rates of the various reactions in the model affect the metabolite's concentrations. The MCA results for the LIP in the DA neurone, iron at the high affinity binding sites of neuromelanin, and iron bound to the high and low affinity binding sites of neuromelanin are given in tables 5-2, 5-3, and 5-4, respectively.

The MCA results for the LIP show that the reactions that have the most control are the expression and degradation of TfR, the binding of Tf-Fe to the TfR in the BBB, BCB and the DA neurone. The export of iron out of the neurone by ferroportin also has similar effect as the TfR reactions on the LIP. The expression and degradation of ferroportin also have an impact on the LIP, but half the extent of the TfR and ferroportin. The expression and degradation of IRP in the BBB, the BCB and the DA neurone also have an influence on the LIP concentration. LIP is more prone to be involved in the radical generation than other types of iron in the neurone that are bound

to proteins, so the dysregulation in one of these reactions has a higher probability to cause cell damage by redox radicals.

Table 5-2 MCA concentration control coefficient (CCC) for LIP in the DA neurone

LIP in DA neurone	
reaction	CCC
(TfR1_BBB expression)	0.957
(TfR1_BBB binding 1)	0.957
(TfR1_BBB degradation)	-0.957
(TfR1_BCB_apical degradation)	0.957
(TfR1_BCB_apical expression)	-0.957
(TfR1_BCB binding 1)	-0.957
(TfR1_SN binding 1)	0.956
(TfR1_SN expression)	0.956
(Fpn_SN export)	-0.956
(TfR1_SN degradation)	-0.956
(IRP_BBB expression)	0.447
(IRP_BBB degradation)	-0.447
(IRP_BCB degradation)	0.447
(IRP_BCB expression)	-0.447
(IRP_SN expression)	0.395
(IRP_SN degradation)	-0.395
(Fpn_SN degradation)	0.320
(Fpn_SN expression)	-0.320
(Fpn_BBB export)	0.255
(Fpn_BCB export)	-0.255

The concentration control coefficient with the Reder MCA for the concentration of iron at the high and low affinity binding sites shows that oxidation and reduction of the LIP in the neurone have a great effect on the iron concentration at the neuromelanin

Table 5-3 MCA concentration control coefficient (CCC) for the concentration of iron at the high affinity binding sites of neuromelanin in the DA neurone.

Fe in the neuromelanin: High affinity binding sites	
reaction	CCC
(Fe2 oxidation by H2O2)	1.001
(Fe3 reduction by AS and O2)	-1.001
(iron released from high_affinity_neuromelanin)	-1.000
(TfR1_BBB binding 1)	0.958
(TfR1_BBB expression)	0.958
(TfR1_BBB degradation)	-0.958
(TfR1_BCB_apical degradation)	0.958
(TfR1_BCB_apical expression)	-0.958
(TfR1_BCB binding 1)	-0.958
(TfR1_SN binding 1)	0.958
(TfR1_SN expression)	0.958
(Fpn_SN export)	-0.958
(TfR1_SN degradation)	-0.958
(iron binding to high_affinity_neuromelanin)	0.784
(IRP_BBB expression)	0.448
(IRP_BBB degradation)	-0.448
(IRP_BCB degradation)	0.448
(IRP_BCB expression)	-0.448
(IRP_SN expression)	0.395
(IRP_SN degradation)	-0.395
(Fpn_SN degradation)	0.320
(Fpn_SN expression)	-0.320
(Fpn_BBB export)	0.255
(Fpn_BCB export)	-0.255
(high_affinity_neuromelanin core formation)	0.216

Table 5-4 MCA concentration control coefficient (CCC) for the concentration of iron at the low affinity binding sites of neuromelanin in the DA neurone.

Fe bound to the neuromelanin: Low affinity binding sites	
reaction	CCC
(Fe2 oxidation by H2O2)	1.001
(Fe3 reduction by AS and O2)	-1.001
(TfR1_BBB binding 1)	0.958
(TfR1_BBB expression)	0.958
(TfR1_BCB_apical degradation)	0.958
(TfR1_BCB_apical expression)	-0.958
(TfR1_BCB binding 1)	-0.958
(TfR1_SN binding 1)	0.958
(TfR1_SN expression)	0.958
(Fpn_SN export)	-0.958
(TfR1_SN degradation)	-0.958
(IRP_BBB expression)	0.448
(IRP_BBB degradation)	-0.448
(IRP_BCB degradation)	0.448
(IRP_BCB expression)	-0.448
(IRP_SN expression)	0.395
(IRP_SN degradation)	-0.395
(Fpn_SN degradation)	0.320
(Fpn_SN expression)	-0.320
(Fpn_BBB export)	0.255
(Fpn_BCB export)	-0.255

high binding sites. The expression and degradation of TfR, the binding of Tf-Fe to the TfR in the BBB, BCB and the DA neurone have a great impact on the concentration of iron in neuromelanin. The expression and degradation of IRP and ferroportin in the BBB, the BCB and the neurone also have an effect on the concentration of iron in the neurone, though to a lesser extent.

5.3 Discussion

An increase in iron in the SNpc is a marker of PD, but the role of iron in the progression of the disease is not completely understood. The novel computational model introduced in this chapter was created to investigate the uptake of iron into the DA neurone in the SNpc. The parameters used in the model were derived from multiple published experimental studies. PD and a NBIA phenotype that shows similar iron deposition in SNpc as is observed in PD, were reproduced by simulating a modified expression of proteins involved in iron regulation in the neurone.

Time course simulations of the model were performed under normal iron concentration conditions. The concentration of labile iron in the DA neurone is quite low, around 10x lower than the concentration of iron in the BBB and the BCB. Even after saturation, the steady state concentration of the labile iron is still low, less than the value found to induce cell death in the pituitary cells in published experiments [135]. In comparison, the concentration of iron in neuromelanin is almost 1000 times higher, illustrating that neuromelanin is the iron sequesterer in the neurone. This is also shown by the huge difference in concentration between the total iron concentration in the DA neurone and the total iron concentration with iron in the neuromelanin excluded in figure 5.5 (A). The concentration of iron in ferritin in the neurone is very low compared to neuromelanin. The model thus predicts that ferritin does not play a huge role in iron regulation in this neurone.

The simulated concentration of iron in neuromelanin was compared to the experimental concentration measured by Zecca et al. (2006) [1] in figure 5.5. The

simulated concentration at 80 years lies between the concentration of iron in the neuromelanin in the Locus Coeruleus and the SNpc. Although the simulated value is not close to the experimental value, it was discussed in the paper that neuromelanin may sequestered additional iron during isolation from the SNpc tissue due to the high iron concentration in the region.

The results from the MCA simulations show that the protein that has the most control over the concentration of LIP in the DA neurone and iron in neuromelanin is TfR, followed by FPN and IRP. FPN and IRP were two of the proteins which expression were changed for the PD/NBIA simulation. The model simulated PD/NBIA condition, based on an estimated increase in proteins found in the published literature [151]. The total iron concentration in the DA neurone in PD/NBIA simulation is higher than for the control, as has been shown in the published literature [17]. The concentration of labile iron in the neurone remains relatively low. Most of the iron is sequestered in the neuromelanin, as in the control case. However, the simulated concentration of iron in neuromelanin under PD/NBIA condition is 10 times the concentration of iron in the neuromelanin in a healthy SNpc, from Zecca et al. (2001) [146]. At this concentration, neuromelanin may have become pro-oxidant and cause cell damage.

Time course simulations with different serum iron were performed under normal and PD/NBIA condition, as shown in figure 5.4 and 5.6. The graphs illustrate that the different concentrations of serum iron in both conditions do not have a strong effect on the concentration of labile iron in the DA neurone or iron in the neuromelanin. While the dysregulation in the protein expression has a much greater impact on iron uptake and iron concentration in the DA neurone, as can be concluded by comparing the concentration of iron in the DA neurone in health and PD/NBIA simulation, under the same serum iron concentration. If cell death in DA neurones in PD is caused by the generation of free radicals by iron, then dysregulation of the proteins, such as shown in the PD/NBIA simulation, could be the likely cause.

Chapter 6 Conclusions and future work

The thesis work is about developing new models that could be used to explore the iron regulation in the brain and how it changes, and might be treated, in Parkinson's disease (PD). The synchrotron work, particularly the scanning transmission X-ray microscopy (STXM) measurement of organic and inorganic materials, offer new dataset to inform the model. The results from the synchrotron work and computational modelling show how each method has its own advantages for looking at this problem from a different direction and how they complement each other.

6.1 Cell to neuropil iron concentration ratio determined by SXRF

In this study, synchrotron X-ray fluorescence (SXRF) maps of the SNpc region taken prior to this project for control and PD cases were processed and analysed. The aim was to produce a ratio of the concentration of iron in the individual dopaminergic (DA) neurones and the surrounding neuropil in both cases. This quantification is of interest because the DA neurone is one of the cells affected in PD and also the compartment modelled in chapter 5. The ratio could be used to validate the model or to adjust the model parameters to reproduce the concentration ratio. However, the small sample size was not conducive for producing a statistically robust ratio of the iron

concentration in the cells and neuropil, and the work included here simply serves as an illustration of how this method might be used in more quantitative work in future.

SXRF allows high spatial resolution mapping of the region of interest, better than 100 nm at some beamlines [88]. In the future, with a complementary optical image of the map area, the dopaminergic neurones can be differentiated and segmented from the neuropil. Then, the intensity of the iron signal in and out of the cell can be calculated and compared. Absolute concentration, not relative concentration, can also be calculated by using the photon flux from a reference material of known iron concentration. This flux can be used to convert the peak areas to concentration. The calculated concentrations from the SXRF measurement could be used to validate the computational model or for parameter estimation to improve the model. Therefore, the results from future work using SXRF would present an effective quantitative technique for post-mortem tissue to calculate the concentration of iron in the cells and the surrounding area.

6.2 Neuromelanin in the DA neurone

In the collaborative STXM analysis described in chapter 3, it is the first time STXM energy spectra have been obtained from neuromelanin. The result shows a feature in the energy spectrum at 286 eV that may be specific to neuromelanin. It is also the first time this energy has been linked to neuromelanin. This energy was chosen because the map at this energy shows only the distinct granular structures and not the surrounding tissue (off-peak energy for the tissue). The comparison of this granular structure to the visible neuromelanin granule in the optical image of the resin-embedded tissue section revealed that they are analogous to each other. This finding is still at an early stage, more imaging and comparison have to be made to determine if this energy peak is specific to neuromelanin structure. The next step would be to compare the structure map using STXM to the adjacent stained section, to determine if the structure seen at 286 eV match the neuromelanin structure.

When an X-ray absorption energy has been determined to be specific to neuromelanin structure, then together with the iron map, a composite map showing the iron inside the neuromelanin can be produced. This method will allow an accurate diagnosis of the presence of iron and its redox state in the neuromelanin in the tissue at high spatial resolution. The result from this observation can be applied to the computational modelling of neuromelanin in the DA neurone. The neuromelanin in the current model stores Fe^{3+} and this complex is assumed not redox active. However, should Fe^{2+} be found in the neuromelanin in control or PD, the way the neuromelanin is modelled should also change. Following further investigation, a reaction for the reduction of iron in the neuromelanin, for example, may be added.

6.3 Ferrous and zero valent iron in the SNpc in PD

One of the aims of this project was to study the compartmentalisation of iron deposition in the SNpc tissue. In chapter 3, STXM was applied to investigate this in both a control and PD case. This study was pilot work for a new analytical approach implementing STXM to study human tissue, and in this project, to do so in the context of PD. STXM allows images of a biological sample in its natural (unstained) state to be taken, and because it can be conducted non-destructively, it permits measurements of multiple organic and inorganic compounds in a single tissue section.

The STXM result shows that iron found in the control tissue is exclusively in Fe^{3+} form and the iron found in the PD tissue includes Fe^{2+} and zero valent iron (Fe^0). Non-heme iron in human is mostly ferric, and bound to transferrin or stored in ferritin. Iron in these forms is not likely to be involved in a redox reaction that produces reactive oxygen species (ROS), so the finding of Fe^{3+} in control tissue is expected. Fe^{2+} is low in abundance and highly reactive, it is associated with the labile iron pool, and its presence in tissue has been implicated in the occurrence of redox reactions that generate ROS and cause subsequent cell damage and death. Thus, the observation of

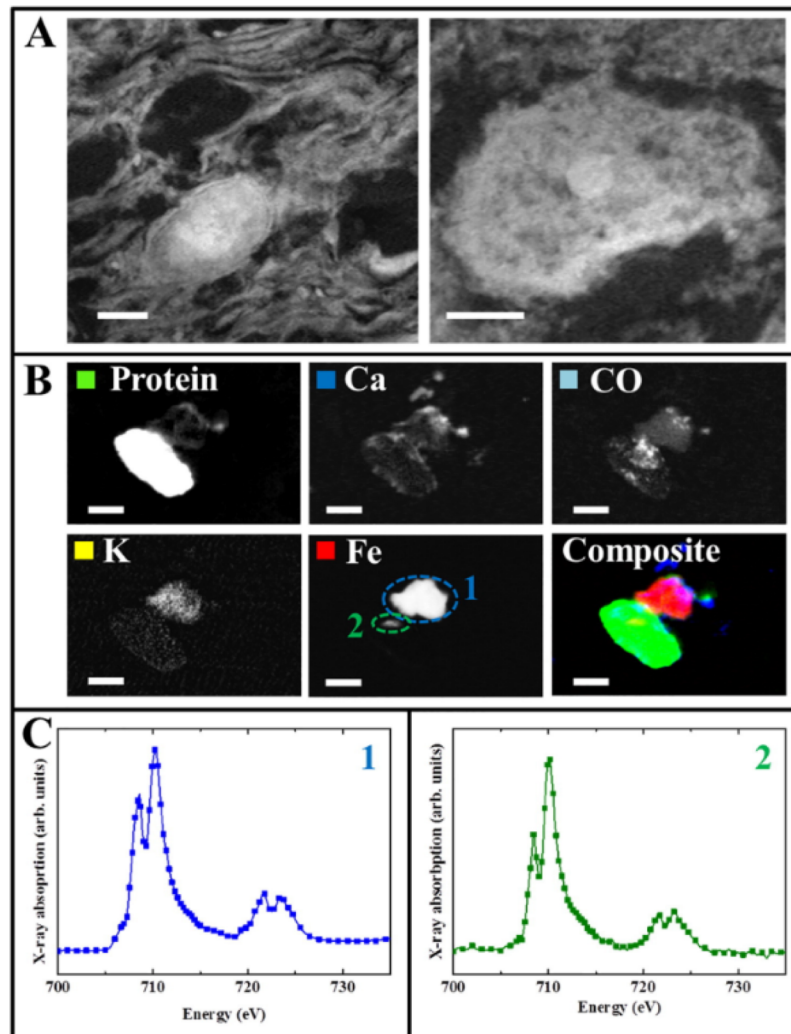


Figure 6.1 (A) Tissue structures of human putamen (left) and amygdala (right) taken at oxygen K-edge energy 532.1 eV. (B) Speciation maps of a protein deposit in human amygdala tissue with Alzheimer's disease. Acquisition energies: carbon K-edge (285.2 eV; protein), calcium L-edge (352.6 eV), oxygen K-edge (533.8 eV; carbonate (CO)), potassium L-edge (300 eV) and iron L-edge (710 eV). Composite image created using colours indicated in the individual map panels. Scale bars 2 μ m. (C) Iron L-edge X-ray absorption spectra of the two iron deposits identified in the iron panel map in (B). [151]

Fe^{2+} in PD tissue supports the hypothesis that iron-induced redox stress is a contributing factor to cell death in SNpc in PD.

The study here involved only one control and one PD case. This study was designed to determine the feasibility of analysing these fragile, chemically unfixed post-mortem human brain tissue samples using STXM. The result shows that both control and PD samples are feasible; both can withstand the tissue processing and STXM analysis, so that in the future, with more samples, statistical comparisons between groups can be obtained. We have already started to showcase the method in our demonstration of human brain amygdala tissue analysis by STXM, which is to our knowledge the first application of STXM to intact human brain tissue, as shown in figure 6.1 [153]. Zero valent iron spectra were also detected from the PD tissue, and to the best of our knowledge this is the first observation in PD tissue. Recently, we reported evidence of zero valent iron in human amyloid plaque cores using STXM [105]. This shows the high sensitivity of the technique and that with the original protocol development work done for this thesis, and the subsequent application, STXM is emerging as a powerful technique to study the organic and inorganic content of human brain samples.

6.4 Synchrotron imaging: challenges faced and future opportunities

For the samples as shown in figure 3.9 for the STXM, the tissue architecture is very fragile following traditional frozen archiving of the bulk samples at brain banks, and some of the iron detected is not directly associated with well-defined tissue structures. This complication should not affect the observation of the redox state of iron found in the region, but the location of this iron cannot reliably be related to structures within the tissue when the tissue architecture is damaged. In addition to freeze-thaw damage, the possible reasons the tissue is in this condition are due to the nature of the tissue itself caused by the disease or damage arising during sample embedding.

The condition of the PD case tissue sample, figure 3.11, prepared during the same time is not as damaged as the control tissue presented in figure 3.9. As cell death is not expected to the same extent in the control tissue, the damage is most likely caused by

the tissue preservation so a better tissue preservation method is recommended in the future. An example is the plunge freezing method to preserve the tissue. Plunge freezing method relies on the theory that crystallisation of ice does not occur under the cooling rates of $10^3 - 10^4$ °C/s [154], this would mean minimal damage to the tissue caused by freezing.

Optimising the detection limits of the experiment is the most important factor in being able to analyse the iron. However, another challenge is that labile or weakly-bound iron might not be retained in the tissue. The possible cause for any loss of the iron is that some fraction of the iron has been washed away during the sample preparation process. To preserve all forms of iron during the sample preparation/ embedding in the future, the proposed plan is to use cryo ultra-microtome sectioning [155]. By using this sectioning method, the samples do not have to be dehydrated and embedded in the resin. The tissue can be sectioned in a frozen state. This sectioning has been used to prepare samples for transmission electron microscopy. The samples to be sectioned have to be fixed with a sucrose solution to avoid the samples from breaking during sectioning. However, the sucrose solution may change the chemical state of the iron in the sample, so this method is not currently viable to be applied to the sample preparation in this thesis. Another Ph.D. student in the group is currently developing a cryo-ultramicrotomy method that will not require the usage of fixative so that it will be compatible with the purpose of the STXM measurement.

6.5 Evaluating the computational model of brain iron metabolism in health

The blood brain barrier (BBB) model is presented in this thesis because BBB is the iron point of entry into the brain and it has been shown in the literature that it regulates the iron homeostasis in the brain [39]. To investigate the dysregulation of iron in PD, it is essential to understand how iron is taken into the brain. This thesis presents the most comprehensive computational model of the iron transport in the brain barrier

systems (the BBB and the brain cerebrospinal fluid barrier (BCB)) metabolism to date. The only existing model on the iron transport into the brain was developed by Simpson et al. (2014) [134], and their model mainly focused on the transport of iron from blood into the brain. Although it was mentioned in the experimental part of their paper that the regulation of transferrin receptor in the BBB takes place, the model does not include the regulations of TfR and other proteins expressions by iron regulatory protein (IRP) [134]. The barrier model in this thesis includes the regulatory reactions by IRP and an improved iron binding and internalisation into the ferritin. It also has more realistic compartments and transport flux (blood – BBB – interstitial fluid (ISF) – cerebrospinal fluid - BCB – blood).

In the construction of the brain barrier systems model, parameter estimation was not performed to obtain the parameters of individual reactions. Parameter estimation is usually used to derive the most highly optimised kinetic parameters to fit the experimental data. The consequence of not executing parameter estimation is that the confidence of the parameter fit may be unknown because the authors would have performed their curve fitting and may not have mentioned the confidence level. Even without performing parameter estimation, the current brain barrier systems model performs well as the barriers protect the brain compartment against iron overload, as reflected in experimental data. Doing parameter estimation in the future, when experimental data for the kinetics of the metabolites in the BBB and BCB are published, may enable refinement of the model. Performing parameter estimation for all kinetic parameters may be redundant because the model may not be sensitive to some of the parameters, and it may only be necessary to do this for TfR expression and degradation, as discussed below.

The model presented here has not been through extensive quantitative validation due to the limited availability of published data, but it has replicated the binding curve of transferrin bound iron (Tf-Fe) to TfR and captures the dynamics of the concentration of iron in the ISF in response to iron injection described in the literature [130, 131]. The metabolic control analysis (MCA) of the model indicates that the TfR controls the

uptake of the iron into the ISF, in agreement with the convention that TfR regulates the iron uptake in the BBB. When experimental data for TfR expression and degradation in BBB and BCB by IRP become available, performing parameter estimation on these may improve the performance of the model.

An iron overload simulation shows that the *in silico* BBB model is able to regulate the iron concentration in the ISF to a safe level. The simulation result reveals that in health the BBB and the BCB are able to maintain their labile iron pool (LIP) concentration at a level that does not cause redox-induced cell death in different conditions of systemic iron overload. The model postulates that the BBB and BCB are capable of maintaining intracellular iron homeostasis, even under conditions of systemic iron overload, and thereby protecting the brain and the barriers from iron mediated oxidative stress. This supports the concept of the function of the BBB and the BCB as the brain's protective barrier systems, specifically in terms of preventing brain iron overload in healthy human [21].

A simulation of iron deficiency in brain ISF, arising from an increase in iron uptake by nearby neuronal cells, is shown in figure 4.9. The purpose of the simulation was to investigate how the brain barrier systems model would behave when the concentration of iron in the ISF was reduced because of an increase in iron uptake by nearby neuronal cells. The simulation results show that the brain barrier systems model does not increase the iron uptake into the ISF to regulate this potential iron deficiency condition. The simulated concentration of iron in the BBB stays at the steady-state level. The barrier systems model does not transport more iron out of the barriers into the ISF to compensate for the reduced concentration of iron in the ISF.

The human brain barrier systems are postulated to perform a major role in regulating brain iron levels, so feasible explanations for why the barrier systems model does not compensate for lowered iron in the ISF, by exporting more iron from inside the barriers into the ISF, are as follows:

(1) To prevent even more iron being taken up into neuronal cells. In this scenario, the brain barrier systems are doing their proposed job as the brain iron regulatory system.

(2) Because a regulatory protein or mechanism that is responsible for detecting and regulating the iron deficiency condition was not accounted for in this model; this may be a protein or mechanism that is as yet unknown. Hepcidin is the only known enzyme to have this regulatory role in systemic iron uptake because it is the enzyme that controls the degradation of the only known iron exporter, ferroportin. However, the presence of hepcidin in, or in the vicinity of the BBB, is still debated because the evidence for hepcidin mRNA in the brain is scarce [136].

The model allows for a more extensive investigation of the iron uptake into the brain across the BBB and BCB under different conditions of systemic iron availability. This makes it possible to evaluate the effects of varying concentrations for proteins that are responsible for iron regulation, the effect this has on the concentration of iron transported into the ISF and, thereby, the effect on iron concentration reaching the tissues of the brain. The model has also predicted the presence of a new metabolite that has a vital role in sensing the brain iron concentration and regulating iron transport into the brain, a prediction which could be studied in future experimentally.

6.6 Evaluating the computational model of SNpc DA neurone iron metabolism in health and neurodegenerative condition

To investigate the role of iron in PD, the barrier model was expanded to include a compartment that represents the DA neurone in the SNpc. The DA neurone simulation in this thesis is the first quantitative model of iron trafficking into the neurone. The model allows the user to explore how iron in the brain is transported into, and stored in, the DA neurone.

One of the main features of the DA neurone is the dark pigment called neuromelanin. Among its many roles, Neuromelanin is understood to be protective by sequestering potentially toxic metals, such as iron [156]. The DA neurone model simulation, figure 5.4, shows that most of the iron concentration in the neurone is bound to the neuromelanin, resulting in a low LIP in the neurone. This simulation result is in conceptual agreement with the experimental observations that led to the hypothesis that neuromelanin has a protective role [157] .

The simulated iron concentration in the neuromelanin in the DA neurone, 4500 ng/mg NM, lies between the concentration of iron in the isolated Locus coeruleus (~2000 ng/mg NM) and isolated SNpc (~11000 ng/mg NM) measured by Zucca et al. (2006) [1]. While the simulated concentration does not match the experimental concentration, it was mentioned in the paper by Zucca et al. (2006) [1], that the higher concentration measured in the SNpc was caused by the neuromelanin absorbing more iron during the isolation process. Since the iron concentration in the Locus coeruleus is lower than the SNpc, the simulated concentration lies in the possible range of neuromelanin iron concentration *in vivo*.

Iron bound to the low affinity binding sites of the neuromelanin has been proposed to remain redox active [59]. In the simulated healthy condition, increasing the concentration of serum iron doubled the concentration of iron in the low affinity binding sites of the neuromelanin. By comparison, in the PD / neurodegeneration with brain iron accumulation (NBIA) simulation, the concentration of the iron in the low affinity sites of the neuromelanin is approximately 33% higher than the concentration of iron in the simulated healthy condition. Therefore, the increase of potentially redox active iron in the neuromelanin (the iron associated with the low affinity binding sites) is substantially higher in the NBIA condition, where the expression of several proteins responsible for iron homeostasis were dysregulated to be consistent with results obtained in independent experiments with an A2 β (iPLA2 β)-KO animal model of a general form of NBIA [151]. The results from this simulation are consistent with protein dysregulation playing a more significant role than an increase in serum blood

iron concentration in ROS-induced cell death in brain iron accumulation disorders [158].

According to the MCA, the TfR expression and degradation in the BBB, BCB and DA neurone is one of the key regulators for the concentration of LIP in the DA neurone and for iron in the neuromelanin. When experimental data for TfR expression and degradation in BBB and BCB by IRP become available in the future, performing parameter estimation on these may improve the performance of the DA neurone model. From the MCA result, it can be deduced that the integrity of the BBB and the BCB, especially the TfR level, may directly affect the exposure of the DA neurone to iron-induced redox stress.

One of the aims of this project was to build a computational model of the iron transport into the DA neurone of the SNpc that allows for investigation of iron dysregulation in health and PD, and to create simulations to test theories about why DA neurone cells in the SNpc are affected in the PD. This aim was nearly fulfilled because in this study the model was used to computationally recreate the condition found in both PD and NBIA. The NBIA experimental data incorporated to inform the development of the model were taken from an animal model with prominent iron deposition in the SNpc, and a similar iron accumulation pathway as evidenced in PD. The results from the simulation of the iron accumulation condition led to the hypothesis presented in this thesis that DA neurons in PD are vulnerable to ROS induced cell death as a result of the dysregulation of metabolite expression and degradation.

6.7 Computational model limitations and future opportunities

There are limited quantitative human data available for model parameterisation. The model used data from multiple other sources such as the animal experiment data and *in vitro* data. In cases where no human brain data were available, the model incorporated data from other human cell types. The quality of these data place limits on the efficacy of the model.

Another limiting factor is the scope of the model presented here. The model only includes a part of the iron transport mechanism in the body. It does not include:

- Other cell types that surround the DA neurone – these cells, such as glia cells that are rich in iron, may have an impact on the iron transport into the DA neurone. The model compartment of such cells would be connected directly to the ISF compartment, so they could acquire iron via the BBB independently of the neurones, and should not have great effect on the iron uptake into the DA neurone.
- Specific cell populations from other regions of the brain - the accumulation of iron in certain areas of the brain is associated with neurodegenerative diseases, such as iron accumulation in the substantia nigra in PD and in the putamen in Alzheimer's disease (AD) [159]. The reason why iron accumulates only in these regions is still under investigation. The current model is not capable of investigating this problem. An extended version of the model that contains specific mechanisms of iron loading in other regions of the brain may reveal how the heterogeneous distribution of iron in the brain arises in health and disease, including factors causing regional accumulation.
- Other proteins or reactions that may be important in the uptake of iron in these compartments – alpha-synuclein is not included in the model. The aggregation of alpha-synuclein in the presence of iron has been shown repeatedly, however, the role of iron in this aggregation is not fully understood [160]. Once the interaction is better understood, the addition of alpha-synuclein to the model should allow the impact of alpha synuclein on iron regulation in PD to be modelled.
- The complexity of some of the reactions – the ferritin has two subunits and the ratio of these subunits is affected by the cell types and iron status. In the model, the ferritin is modelled as a single protein, therefore, the model could not predict the ferritin subunit ratios and the cell-specific ferritin type could not be simulated using the model. Neuromelanin was modelled in this study in a

similar way to how ferritin was modelled because the iron binding structure in neuromelanin is similar to ferritin [58]. This might place a limit on how well the model replicates the dynamic of iron binding to neuromelanin. A better understanding of the binding mechanism of iron to neuromelanin may improve the current model.

- Metabolism of other metals that may affect the iron uptake process - Copper uptake in to the brain shares similar transporter as the iron uptake, such as DMT1 and the caeruloplasmin, and its dysregulation in the brain has been implicated in neurodegenerative diseases. In the BBB and the BCB, DMT1 has been shown to also mediate the transport of copper and may inhibit the transport of iron by DMT1 [7]. The ferrireductase caeruloplasmin that oxidises newly released Fe^{2+} from the BBB to Fe^{3+} , is also a copper carrier. Care should be taken when interpreting the results of iron metabolism that may be impacted by other metabolic process. An extended model that includes the copper metabolism would be able to investigate the role of copper in the diseases that also exhibit altered iron handling, such as Wilson's disease and aceruloplasminemia [161]. The concentration of copper has been found to decrease in the SNpc in PD [162]. The extended version of the model that includes the copper uptake into the DA neurone may be useful in the investigation of this finding.

Metabolic control analysis (MCA) is applied in the computational analysis to determine the key reactions that affect the concentration of iron in the different compartments in the model. In COPASI, there are two algorithms available, the Reder algorithm and the Smallbone algorithm. According to the literature [163], the Smallbone algorithm has overcome the Reder algorithm's limitation, which is that the algorithm is only valid if the matrix in the equation is of full rank. The Smallbone method directly chooses the linearly independent rows of the matrix so that the matrix is of full rank. However, the calculation of the metabolic control analysis using the Smallbone algorithm shows the control coefficient of the expression of the IRP in the

BBB and the BCB to be zero for all metabolites, which does not fit the role of IRP as the protein that regulates many of the transport proteins in the model. Therefore, in this thesis, the Reder algorithm were used to interpret the key factors of the brain iron metabolism. The results from the Reder algorithm calculation was compared to the result of generic sensitivity analysis and they reveal results leading to a similar conclusion.

6.7.1 Future modelling experiment opportunities

The models presented have a great potential for expansion in size and detail. This section presents opportunities to develop the model in the future, developments that were not undertaken here due to time constraints.

The clinical study using iron chelator for PD patient, done by Devos et al. (2014) [20] shows great potential to be an effective therapy to remove iron from the SNpc in PD. Deferiprone (DFP), the drug used in the study, was shown to be able to cross the BBB and affect the SNpc [164]. An extended version of the model that includes a metabolite that mimics the function of DFP would be a powerful tool to investigate the possible mechanism of action of DFP that is not yet demonstrated in the literature, as well as its effect on the iron uptake mechanisms in the BBB and DA neurone. The extended version may also be useful in improving treatment design with DFP, or in the development of an improved iron chelating drug for PD.

The modelling of the hypoxia – inducible factor-2 α (HIF – 2) into the existing compartments in the model would create a more extensive model that would include the iron uptake into the brain in response to hypoxia. The HIF – 2 responds to the hypoxic condition and the iron level in the cells by modulating the expressions of proteins such as TfR and DMT1 in the body [165, 166]. Dr Tracey Rouault² has suggested that although the roles of HIF-2 in the BBB has not been experimentally studied, it is logical to assume it plays similar role in the barrier because it is highly

² Private communication received on March 2018

expressed in the brain capillaries [167] and is responsive to the iron and oxygen level. The addition of reactive oxygen species (ROS) to this extended model will assist the study of the possible role of ROS in the regulation of HIF-2. Moreover, the ROS modelling will improve the understanding of the formation of toxic radicals that produce oxidative stress and the possible discovery of targets for reducing the damage caused by oxidative stress in PD and other neurodegenerative diseases.

Another area where the modelling of ROS, HIF and iron transport will be useful is for brain tumours. The increase in ROS, HIF and TfR are implicated in the development or survival of neoplastic cells [168]. Recent studies have also suggested that these cells became more malignant, they increase the production of hepcidin to decrease the concentration of iron exporter, ferroportin, so that they can retain more iron [169]. A similar model to the current model, but tailored to the transport in the neoplastic cells, would provide a tool to investigate further the flux or concentrations of the metabolites of interest with lower cost and time consumed than an animal or *in vitro* model. Potential therapeutic solutions can be tested before application to animal models to increase the successful chance of the experiment and minimize the use of the laboratory animals.

A further point made by Dr Tracey Rouault² is the possibility that the basal ganglia function is analogous to that of the liver, storing iron and releasing hormones that control the transport of iron in the brain. Once the metabolites present in the basal ganglia are better identified, an initial model could be developed to assess the regulatory contribution from the basal ganglia. The current model shows a good regulatory mechanism in response to iron overload, but does not appear to respond to an iron drop in the ISF. The addition of the basal ganglia compartment may overcome this problem.

In summary, this thesis presents the most complete model of the computational model of the iron transport in the brain barrier systems (the BBB and the BCB) metabolism to date and a novel model of the computational model of the iron transport in the DA

neurone. The method development work to perform the STXM analysis of SNpc tissue has shown strong potential for subcellular redox state analysis and label-free imaging of the organic material. This includes a spectral feature that may be specific to neuromelanin. In combination, the advances in computational modelling and analytical measurement create an opportunity to improve understanding of iron dysregulation in the human brain.

References

- [1] F. A. Zucca, C. Bellei, S. Giannelli, M. R. Terreni, M. Gallorini, E. Rizzio, *et al.*, "Neuromelanin and iron in human locus coeruleus and substantia nigra during aging: consequences for neuronal vulnerability," *J Neural Transm (Vienna)*, vol. 113, pp. 757-67, Jun 2006.
- [2] R. R. Crichton and R. J. Ward, "Parkinson's Disease," in *Metal-based Neurodegeneration*, ed: John Wiley & Sons, Ltd, 2006, pp. 53-76.
- [3] O.-B. Tysnes and A. J. J. o. N. T. Storstein, "Epidemiology of Parkinson's disease," vol. 124, pp. 901-905, August 01 2017.
- [4] J. Blesa and S. Przedborski, "Parkinson's disease: animal models and dopaminergic cell vulnerability," *Frontiers in Neuroanatomy*, vol. 8, p. 155, 2014.
- [5] J. Everett, E. Céspedes, N. D. Telling, L. R. Shelford, C. Exley, J. F. Collingwood, *et al.*, "Ferrous iron formation following the co-aggregation of ferric iron and the Alzheimer's disease peptide β -amyloid (1-42)," *Journal of the Royal Society Interface*, vol. 11, 06 / 06 / 2014.
- [6] J. Dobson, J. F. Collingwood, R. K. K. Chong, T. Kasama, L. Cervera-Gontard, R. E. Dunin-Borkowski, *et al.*, "Three-dimensional tomographic imaging and characterization of iron compounds within Alzheimer's plaque core material," *Journal of Alzheimer's Disease*, vol. 14, pp. 235-245, 01 / 01 / 2008.
- [7] W. Zheng and A. D. Monnot, "Regulation of brain iron and copper homeostasis by brain barrier systems: implication in neurodegenerative diseases," *Pharmacol Ther*, vol. 133, pp. 177-88, Feb 2012.
- [8] P. Jenner and C. W. Olanow, "Oxidative stress and the pathogenesis of Parkinson's disease," *Neurology*, vol. 47, pp. S161-70, Dec 1996.
- [9] P. s. UK. (2018, 23/09/2018). *The incidence and prevalence of Parkinson's in the UK: Summary of findings*. Available: https://www.parkinsons.org.uk/sites/default/files/2018-01/CS2960_Incidence_and_prevalence_report_branding_summary_report.pdf

- [10] C. C. Winterbourn, "Toxicity of iron and hydrogen peroxide: the Fenton reaction," *Toxicol Lett*, vol. 82-83, pp. 969-74, Dec 1995.
- [11] R. Crichton, "The Importance of Iron for Biological Systems," in *Iron Metabolism*, ed: John Wiley & Sons, Ltd, 2009, pp. 17-58.
- [12] M. W. Hentze, M. U. Muckenthaler, B. Galy, and C. Camaschella, "Two to tango: regulation of Mammalian iron metabolism," *Cell*, vol. 142, pp. 24-38, Jul 9 2010.
- [13] R. R. Crichton and R. J. Ward, "Oxidative Stress and Redox-Active Metal Ions," in *Metal-based Neurodegeneration*, ed: John Wiley & Sons, Ltd, 2006, pp. 21-52.
- [14] E. Mills, X. P. Dong, F. Wang, and H. Xu, "Mechanisms of brain iron transport: insight into neurodegeneration and CNS disorders," *Future Med Chem*, vol. 2, pp. 51-64, Jan 2010.
- [15] D. T. Dexter, A. Carayon, F. Javoy-Agid, Y. Agid, F. R. Wells, S. E. Daniel, *et al.*, "Alterations in the levels of iron, ferritin and other trace metals in Parkinson's disease and other neurodegenerative diseases affecting the basal ganglia," *Brain*, vol. 114 (Pt 4), pp. 1953-75, Aug 1991.
- [16] M. E. Gotz, K. Double, M. Gerlach, M. B. Youdim, and P. Riederer, "The relevance of iron in the pathogenesis of Parkinson's disease," *Ann N Y Acad Sci*, vol. 1012, pp. 193-208, Mar 2004.
- [17] N. P. Visanji, J. F. Collingwood, M. E. Finnegan, A. Tandon, E. House, and L. N. Hazrati, "Iron deficiency in parkinsonism: region-specific iron dysregulation in Parkinson's disease and multiple system atrophy," *J Parkinsons Dis*, vol. 3, pp. 523-37, 2013.
- [18] C. M. Hershko, G. M. Link, A. M. Konijn, and Z. I. Cabantchik, "Iron chelation therapy," *Curr Hematol Rep*, vol. 4, pp. 110-6, Mar 2005.
- [19] D. S. Kalinowski and D. R. Richardson, "The evolution of iron chelators for the treatment of iron overload disease and cancer," *Pharmacol Rev*, vol. 57, pp. 547-83, Dec 2005.
- [20] D. Devos, C. Moreau, J. C. Devedjian, J. Kluza, M. Petrault, C. Laloux, *et al.*, "Targeting chelatable iron as a therapeutic modality in Parkinson's disease," *Antioxid Redox Signal*, vol. 21, pp. 195-210, Jul 10 2014.
- [21] R. Crichton, D. Dexter, and R. Ward, "Brain iron metabolism and its perturbation in neurological diseases," in *Metal Ions in Neurological Systems*, W. Linert and H. Kozlowski, Eds., ed: Springer Vienna, 2012, pp. 1-15.
- [22] N. C. Andrews, "The iron transporter DMT1," *Int J Biochem Cell Biol*, vol. 31, pp. 991-4, Oct 1999.
- [23] N. C. Andrews, "Metal transporters and disease," *Curr Opin Chem Biol*, vol. 6, pp. 181-6, Apr 2002.

- [24] J. L. Beard, J. A. Wiesinger, N. Li, and J. R. Connor, "Brain iron uptake in hypotransferrinemic mice: influence of systemic iron status," *J Neurosci Res*, vol. 79, pp. 254-61, Jan 1-15 2005.
- [25] D. B. Kell and E. Pretorius, "Serum ferritin is an important inflammatory disease marker, as it is mainly a leakage product from damaged cells," *Metallomics*, vol. 6, pp. 748-73, Apr 2014.
- [26] P. Arosio, R. Ingrassia, and P. Cavadini, "Ferritins: a family of molecules for iron storage, antioxidation and more," *Biochim Biophys Acta*, vol. 1790, pp. 589-99, Jul 2009.
- [27] T. A. Rouault and S. Cooperman, "Brain Iron Metabolism," *Seminars in Pediatric Neurology*, vol. 13, pp. 142-148, 9// 2006.
- [28] T. Moos, T. Skjoerringe, S. Gosk, and E. H. Morgan, "Brain capillary endothelial cells mediate iron transport into the brain by segregating iron from transferrin without the involvement of divalent metal transporter 1," *J Neurochem*, vol. 98, pp. 1946-58, Sep 2006.
- [29] T. Moos and T. Rosengren Nielsen, "Ferroportin in the postnatal rat brain: implications for axonal transport and neuronal export of iron," *Semin Pediatr Neurol*, vol. 13, pp. 149-57, Sep 2006.
- [30] J. R. Burdo, S. L. Menzies, I. A. Simpson, L. M. Garrick, M. D. Garrick, K. G. Dolan, *et al.*, "Distribution of divalent metal transporter 1 and metal transport protein 1 in the normal and Belgrade rat," *J Neurosci Res*, vol. 66, pp. 1198-207, Dec 15 2001.
- [31] M. Knutson, S. Menzies, J. Connor, and M. Wessling-Resnick, "Developmental, regional, and cellular expression of SFT/UbcH5A and DMT1 mRNA in brain," *J Neurosci Res*, vol. 76, pp. 633-41, Jun 1 2004.
- [32] M. W. Bradbury, "Transport of iron in the blood-brain-cerebrospinal fluid system," *J Neurochem*, vol. 69, pp. 443-54, Aug 1997.
- [33] D.-L. Zhang, M. C. Ghosh, and T. A. Rouault, "The physiological functions of iron regulatory proteins in iron homeostasis - an update," *Frontiers in Pharmacology*, vol. 5, 2014-June-13 2014.
- [34] N. Wilkinson and K. Pantopoulos, "The IRP/IRE system in vivo: insights from mouse models," *Frontiers in Pharmacology*, vol. 5, 2014-July-28 2014.
- [35] W. Zheng, S. Ren, and J. H. Graziano, "Manganese inhibits mitochondrial aconitase: a mechanism of manganese neurotoxicity," *Brain Res*, vol. 799, pp. 334-42, Jul 20 1998.
- [36] T. A. Rouault, "Systemic iron metabolism: a review and implications for brain iron metabolism," *Pediatr Neurol*, vol. 25, pp. 130-7, Aug 2001.
- [37] P. Piccinelli and T. Samuelsson, "Evolution of the iron-responsive element," *RNA*, vol. 13, pp. 952-66, Jul 2007.

- [38] L. Zecca, M. B. Youdim, P. Riederer, J. R. Connor, and R. R. Crichton, "Iron, brain ageing and neurodegenerative disorders," *Nat Rev Neurosci*, vol. 5, pp. 863-73, Nov 2004.
- [39] T. Moos and E. Morgan, "Transferrin and Transferrin Receptor Function in Brain Barrier Systems," *Cellular and Molecular Neurobiology*, vol. 20, pp. 77-95, 2000/02/01 2000.
- [40] C. A. Enns and H. H. Sussman, "Physical characterization of the transferrin receptor in human placenta," *J Biol Chem*, vol. 256, pp. 9820-3, Oct 10 1981.
- [41] D. R. Richardson and P. Ponka, "The molecular mechanisms of the metabolism and transport of iron in normal and neoplastic cells," *Biochim Biophys Acta*, vol. 1331, pp. 1-40, Mar 14 1997.
- [42] A. P. West, Jr., M. J. Bennett, V. M. Sellers, N. C. Andrews, C. A. Enns, and P. J. Bjorkman, "Comparison of the interactions of transferrin receptor and transferrin receptor 2 with transferrin and the hereditary hemochromatosis protein HFE," *J Biol Chem*, vol. 275, pp. 38135-8, Dec 8 2000.
- [43] H. Gunshin, B. Mackenzie, U. V. Berger, Y. Gunshin, M. F. Romero, W. F. Boron, *et al.*, "Cloning and characterization of a mammalian proton-coupled metal-ion transporter," *Nature*, vol. 388, pp. 482-8, Jul 31 1997.
- [44] M. Arredondo, P. Munoz, C. V. Mura, and M. T. Nunez, "DMT1, a physiologically relevant apical Cu¹⁺ transporter of intestinal cells," *Am J Physiol Cell Physiol*, vol. 284, pp. C1525-30, Jun 2003.
- [45] M. D. Fleming and N. C. Andrews, "Mammalian iron transport: an unexpected link between metal homeostasis and host defense," *J Lab Clin Med*, vol. 132, pp. 464-8, Dec 1998.
- [46] G. J. Anderson and C. D. Vulpe, "Mammalian iron transport," *Cell Mol Life Sci*, vol. 66, pp. 3241-61, Oct 2009.
- [47] T. A. Rouault, "Iron metabolism in the CNS: implications for neurodegenerative diseases," *Nat Rev Neurosci*, vol. 14, pp. 551-64, Aug 2013.
- [48] N. Hubert and M. W. Hentze, "Previously uncharacterized isoforms of divalent metal transporter (DMT)-1: implications for regulation and cellular function," *Proc Natl Acad Sci U S A*, vol. 99, pp. 12345-50, Sep 17 2002.
- [49] T. Skjorringe, A. Burkhart, K. B. Johnsen, and T. Moos, "Divalent metal transporter 1 (DMT1) in the brain: implications for a role in iron transport at the blood-brain barrier, and neuronal and glial pathology," *Front Mol Neurosci*, vol. 8, p. 19, 2015.
- [50] B. Mackenzie, H. Takanaga, N. Hubert, A. Rolfs, and M. A. Hediger, "Functional properties of multiple isoforms of human divalent metal-ion transporter 1 (DMT1)," *Biochem J*, vol. 403, pp. 59-69, Apr 1 2007.

- [51] P. M. Harrison and P. Arosio, "The ferritins: molecular properties, iron storage function and cellular regulation," *Biochim Biophys Acta*, vol. 1275, pp. 161-203, Jul 31 1996.
- [52] D. J. Pinero, N. Q. Li, J. R. Connor, and J. L. Beard, "Variations in dietary iron alter brain iron metabolism in developing rats," *J Nutr*, vol. 130, pp. 254-63, Feb 2000.
- [53] S. Levi, S. J. Yewdall, P. M. Harrison, P. Santambrogio, A. Cozzi, E. Rovida, *et al.*, "Evidence of H- and L-chains have co-operative roles in the iron-uptake mechanism of human ferritin," *Biochem J*, vol. 288 (Pt 2), pp. 591-6, Dec 1 1992.
- [54] F. M. Torti and S. V. Torti, "Regulation of ferritin genes and protein," *Blood*, vol. 99, pp. 3505-16, May 15 2002.
- [55] F. A. Zucca, E. Basso, F. A. Cupaioli, E. Ferrari, D. Sulzer, L. Casella, *et al.*, "Neuromelanin of the human substantia nigra: an update," *Neurotox Res*, vol. 25, pp. 13-23, Jan 2014.
- [56] F. A. Zucca, J. Segura-Aguilar, E. Ferrari, P. Munoz, I. Paris, D. Sulzer, *et al.*, "Interactions of iron, dopamine and neuromelanin pathways in brain aging and Parkinson's disease," *Prog Neurobiol*, Oct 9 2015.
- [57] A. Biesemeier, O. Eibl, S. Eswara, J. N. Audinot, T. Wirtz, G. Pezzoli, *et al.*, "Elemental mapping of Neuromelanin organelles of human Substantia Nigra: correlative ultrastructural and chemical analysis by analytical transmission electron microscopy and nano-secondary ion mass spectrometry," *J Neurochem*, vol. 138, pp. 339-53, Jul 2016.
- [58] F. Tribl, E. Asan, T. Arzberger, T. Tatschner, E. Langenfeld, H. E. Meyer, *et al.*, "Identification of L-ferritin in neuromelanin granules of the human substantia nigra: a targeted proteomics approach," *Mol Cell Proteomics*, vol. 8, pp. 1832-8, Aug 2009.
- [59] B. A. Faucheux, M. E. Martin, C. Beaumont, J. J. Hauw, Y. Agid, and E. C. Hirsch, "Neuromelanin associated redox-active iron is increased in the substantia nigra of patients with Parkinson's disease," *J Neurochem*, vol. 86, pp. 1142-8, Sep 2003.
- [60] R. G. Perez and T. G. Hastings, "Could a loss of alpha-synuclein function put dopaminergic neurons at risk?," *J Neurochem*, vol. 89, pp. 1318-24, Jun 2004.
- [61] J. L. Eriksen, T. M. Dawson, D. W. Dickson, and L. Petrucelli, "Caught in the act: alpha-synuclein is the culprit in Parkinson's disease," *Neuron*, vol. 40, pp. 453-6, Oct 30 2003.
- [62] Y. Peng, C. Wang, H. H. Xu, Y. N. Liu, and F. Zhou, "Binding of alpha-synuclein with Fe(III) and with Fe(II) and biological implications of the resultant complexes," *J Inorg Biochem*, vol. 104, pp. 365-70, Apr 2010.

- [63] N. Golts, H. Snyder, M. Frasier, C. Theisler, P. Choi, and B. Wolozin, "Magnesium inhibits spontaneous and iron-induced aggregation of alpha-synuclein," *J Biol Chem*, vol. 277, pp. 16116-23, May 3 2002.
- [64] T. Hasegawa, M. Matsuzaki, A. Takeda, A. Kikuchi, H. Akita, G. Perry, *et al.*, "Accelerated alpha-synuclein aggregation after differentiation of SH-SY5Y neuroblastoma cells," *Brain Res*, vol. 1013, pp. 51-9, Jul 2 2004.
- [65] S. Turnbull, B. J. Tabner, O. M. El-Agnaf, S. Moore, Y. Davies, and D. Allsop, "alpha-Synuclein implicated in Parkinson's disease catalyses the formation of hydrogen peroxide in vitro," *Free Radic Biol Med*, vol. 30, pp. 1163-70, May 15 2001.
- [66] S. Abboud and D. J. Haile, "A novel mammalian iron-regulated protein involved in intracellular iron metabolism," *J Biol Chem*, vol. 275, pp. 19906-12, Jun 30 2000.
- [67] A. Burkhart, L. B. Thomsen, M. S. Thomsen, J. Lichota, C. Fazakas, I. Krizbai, *et al.*, "Transfection of brain capillary endothelial cells in primary culture with defined blood-brain barrier properties," *Fluids Barriers CNS*, vol. 12, p. 19, 2015.
- [68] R. C. McCarthy and D. J. Kosman, "Mechanisms and regulation of iron trafficking across the capillary endothelial cells of the blood-brain barrier," *Front Mol Neurosci*, vol. 8, p. 31, 2015.
- [69] L. J. Wu, A. G. Leenders, S. Cooperman, E. Meyron-Holtz, S. Smith, W. Land, *et al.*, "Expression of the iron transporter ferroportin in synaptic vesicles and the blood-brain barrier," *Brain Res*, vol. 1001, pp. 108-17, Mar 19 2004.
- [70] E. Nemeth, M. S. Tuttle, J. Powelson, M. B. Vaughn, A. Donovan, D. M. Ward, *et al.*, "Hepcidin regulates cellular iron efflux by binding to ferroportin and inducing its internalization," *Science*, vol. 306, pp. 2090-3, Dec 17 2004.
- [71] S. M. Wang, L. J. Fu, X. L. Duan, D. R. Crooks, P. Yu, Z. M. Qian, *et al.*, "Role of hepcidin in murine brain iron metabolism," *Cell Mol Life Sci*, vol. 67, pp. 123-33, Jan 2010.
- [72] M. Hadziahmetovic, Y. Song, P. Ponnuru, J. Iacovelli, A. Hunter, N. Haddad, *et al.*, "Age-dependent retinal iron accumulation and degeneration in hepcidin knockout mice," *Invest Ophthalmol Vis Sci*, vol. 52, pp. 109-18, Jan 2011.
- [73] A. Raha, R. Vaishnav, R. Friedland, A. Bomford, and R. Raha-Chowdhury, "The systemic iron-regulatory proteins hepcidin and ferroportin are reduced in the brain in Alzheimer's disease," *Acta Neuropathologica Communications*, vol. 1, p. 55, 2013.
- [74] R. Raha-Chowdhury, A. A. Raha, S. Forostyak, J. W. Zhao, S. R. Stott, and A. Bomford, "Expression and cellular localization of hepcidin mRNA and protein in normal rat brain," *BMC Neurosci*, vol. 16, p. 24, Apr 21 2015.

- [75] M. W. Bradbury, "The blood-brain barrier," *Exp Physiol*, vol. 78, pp. 453-72, Jul 1993.
- [76] R. Daneman and A. Prat, "The blood-brain barrier," *Cold Spring Harb Perspect Biol*, vol. 7, p. a020412, Jan 5 2015.
- [77] N. J. Abbott, A. A. Patabendige, D. E. Dolman, S. R. Yusof, and D. J. Begley, "Structure and function of the blood-brain barrier," *Neurobiol Dis*, vol. 37, pp. 13-25, Jan 2010.
- [78] K. B. Johnsen and T. Moos, "Revisiting nanoparticle technology for blood-brain barrier transport: Unfolding at the endothelial gate improves the fate of transferrin receptor-targeted liposomes," *J Control Release*, vol. 222, pp. 32-46, Jan 28 2016.
- [79] R. N. Kalaria and S. N. Kroon, "Expression of leukocyte antigen CD34 by brain capillaries in Alzheimer's disease and neurologically normal subjects," *Acta Neuropathol*, vol. 84, pp. 606-12, 1992.
- [80] C. E. Johanson, E. G. Stopa, and P. N. McMillan, "The blood-cerebrospinal fluid barrier: structure and functional significance," *Methods Mol Biol*, vol. 686, pp. 101-31, 2011.
- [81] B. Engelhardt and L. Sorokin, "The blood-brain and the blood-cerebrospinal fluid barriers: function and dysfunction," *Seminars in Immunopathology*, vol. 31, pp. 497-511, 2009/11/01 2009.
- [82] X. Wang, G. J. Li, and W. Zheng, "Upregulation of DMT1 expression in choroidal epithelia of the blood-CSF barrier following manganese exposure in vitro," *Brain Res*, vol. 1097, pp. 1-10, Jun 30 2006.
- [83] G. J. Li, B. S. Choi, X. Wang, J. Liu, M. P. Waalkes, and W. Zheng, "Molecular mechanism of distorted iron regulation in the blood-CSF barrier and regional blood-brain barrier following in vivo subchronic manganese exposure," *Neurotoxicology*, vol. 27, pp. 737-44, Sep 2006.
- [84] A. E. Oakley, J. F. Collingwood, J. Dobson, G. Love, H. R. Perrott, J. A. Edwardson, *et al.*, "Individual dopaminergic neurons show raised iron levels in Parkinson disease," *Neurology*, vol. 68, pp. 1820-5, May 22 2007.
- [85] J. Salazar, N. Mena, S. Hunot, A. Prigent, D. Alvarez-Fischer, M. Arredondo, *et al.*, "Divalent metal transporter 1 (DMT1) contributes to neurodegeneration in animal models of Parkinson's disease," *Proc Natl Acad Sci U S A*, vol. 105, pp. 18578-83, Nov 25 2008.
- [86] C. M. Morris, J. M. Candy, S. Omar, C. A. Bloxham, and J. A. Edwardson, "Transferrin receptors in the parkinsonian midbrain," *Neuropathol Appl Neurobiol*, vol. 20, pp. 468-72, Oct 1994.
- [87] B. A. Faucheux, E. C. Hirsch, J. Villares, F. Selimi, A. Mouatt-Prigent, F. Javoy-Agid, *et al.*, "Distribution of ¹²⁵I-ferrotransferrin binding sites in the

- mesencephalon of control subjects and patients with Parkinson's disease," *J Neurochem*, vol. 60, pp. 2338-41, Jun 1993.
- [88] J. F. Collingwood and M. R. Davidson, "The role of iron in neurodegenerative disorders: insights and opportunities with synchrotron light," *Front Pharmacol*, vol. 5, p. 191, 2014.
 - [89] P. M. Bertsch and D. B. Hunter, "Applications of synchrotron-based X-ray microprobes," *Chem Rev*, vol. 101, pp. 1809-42, Jun 2001.
 - [90] J. Everett, "The aggregation and reduction of iron minerals by the Alzheimer's disease peptide β -amyloid (1-42): an X-ray absorption study," Keele University, 2015.
 - [91] G. Van der Laan, "Applications of soft x-ray magnetic dichroism," in *Journal of Physics: Conference Series*, 2013, p. 012127.
 - [92] P. Mendes, S. Hoops, S. Sahle, R. Gauges, J. Dada, and U. Kummer, "Computational modeling of biochemical networks using COPASI," *Methods Mol Biol*, vol. 500, pp. 17-59, 2009.
 - [93] A. Diercks and A. Aderem, "Systems Approaches to Dissecting Immunity," in *Systems Biology*. vol. 363, M. G. Katze, Ed., ed: Springer Berlin Heidelberg, 2013, pp. 1-19.
 - [94] S. Mitchell and P. Mendes, "A Computational Model of Liver Iron Metabolism," *PLoS Comput Biol*, vol. 9, p. e1003299, 2013.
 - [95] T. Wajima, G. K. Isbister, and S. B. Duffull, "A comprehensive model for the humoral coagulation network in humans," *Clin Pharmacol Ther*, vol. 86, pp. 290-8, Sep 2009.
 - [96] F. Ortega, J. L. Garces, F. Mas, B. N. Kholodenko, and M. Cascante, "Bistability from double phosphorylation in signal transduction. Kinetic and structural requirements," *FEBS J*, vol. 273, pp. 3915-26, Sep 2006.
 - [97] S. Hoops, S. Sahle, R. Gauges, C. Lee, J. Pahle, N. Simus, *et al.*, "COPASI--a COMplex PATHway SIMulator," *Bioinformatics*, vol. 22, pp. 3067-74, Dec 15 2006.
 - [98] H. Kacser and J. A. Burns, "The control of flux," *Symp Soc Exp Biol*, vol. 27, pp. 65-104, 1973.
 - [99] R. Heinrich and T. A. Rapoport, "A linear steady-state treatment of enzymatic chains. General properties, control and effector strength," *Eur J Biochem*, vol. 42, pp. 89-95, Feb 15 1974.
 - [100] M. E. Finnegan, "Investigation of the relationship between iron and high field MRI in healthy and Alzheimer's disease tissue," University of Warwick, 2013.
 - [101] V. Antharam, J. F. Collingwood, J. P. Bullivant, M. R. Davidson, S. Chandra, A. Mikhaylova, *et al.*, "High field magnetic resonance microscopy of the human hippocampus in Alzheimer's disease: quantitative imaging and correlation with iron," *Neuroimage*, vol. 59, pp. 1249-60, Jan 16 2012.

- [102] J. Li, A. P. Hitchcock, H. D. H. Stöver, and I. Shirley, "A New Approach to Studying Microcapsule Wall Growth Mechanisms," *Macromolecules*, vol. 42, pp. 2428-2432, 2009/04/14 2009.
- [103] N. D. Telling, J. Everett, J. F. Collingwood, J. Dobson, G. van der Laan, J. J. Gallagher, *et al.*, "Iron Biochemistry is Correlated with Amyloid Plaque Morphology in an Established Mouse Model of Alzheimer's Disease," *Cell Chem Biol*, vol. 24, pp. 1205-1215 e3, Oct 19 2017.
- [104] A. J. M. U. Hitchcock, Hamilton ON Canada Google Scholar, "Axis Version 21q (09-June-04)," 2004.
- [105] J. Everett, J. F. Collingwood, V. Tjendana-Tjhin, J. Brooks, F. Lermyte, G. Plascencia-Villa, *et al.*, "Nanoscale synchrotron X-ray speciation of iron and calcium compounds in amyloid plaque cores from Alzheimer's disease subjects," *Nanoscale*, vol. 10, pp. 11782-11796, 2018.
- [106] A. D. Surowka, P. Wrobel, D. Adamek, E. Radwanska, and M. Szczerbowska-Boruchowska, "Synchrotron radiation based X-ray fluorescence shows changes in the elemental composition of the human substantia nigra in aged brains," *Metallomics*, vol. 7, pp. 1522-31, Nov 2015.
- [107] E. Carboni, J. D. Nicolas, M. Topperwien, C. Stadelmann-Nessler, P. Lingor, and T. Salditt, "Imaging of neuronal tissues by x-ray diffraction and x-ray fluorescence microscopy: evaluation of contrast and biomarkers for neurodegenerative diseases," *Biomed Opt Express*, vol. 8, pp. 4331-4347, Oct 1 2017.
- [108] J. Everett, E. Cespedes, L. R. Shelford, C. Exley, J. F. Collingwood, J. Dobson, *et al.*, "Evidence of redox-active iron formation following aggregation of ferrihydrite and the Alzheimer's disease peptide beta-amyloid," *Inorg Chem*, vol. 53, pp. 2803-9, Mar 17 2014.
- [109] J. K. Andersen, "Iron dysregulation and Parkinson's disease," *J Alzheimers Dis*, vol. 6, pp. S47-52, Dec 2004.
- [110] J. Sian-Hulsmann, S. Mandel, M. B. Youdim, and P. Riederer, "The relevance of iron in the pathogenesis of Parkinson's disease," *J Neurochem*, vol. 118, pp. 939-57, Sep 2011.
- [111] M. S. Medeiros, A. Schumacher-Schuh, A. M. Cardoso, G. V. Bochi, J. Baldissarelli, A. Kegler, *et al.*, "Iron and Oxidative Stress in Parkinson's Disease: An Observational Study of Injury Biomarkers," *PLoS One*, vol. 11, p. e0146129, 2016.
- [112] V. Tjendana-Tjhin, S. Mitchell, E. Milward, M. Chappell, and J. J. M. D. Collingwood, "a computational model of iron transport between the blood circulation and the brain: 1851," vol. 31, pp. S608-S609, 2016.
- [113] R. C. McCarthy and D. J. Kosman, "Iron transport across the blood-brain barrier: development, neurovascular regulation and cerebral amyloid angiopathy," *Cell Mol Life Sci*, Oct 30 2014.

- [114] A. Funahashi, M. Morohashi, H. Kitano, and N. Tanimura, "CellDesigner: a process diagram editor for gene-regulatory and biochemical networks," *BIOSILICO*, vol. 1, pp. 159-162, 11/05/ 2003.
- [115] S. S. Rengachary and R. G. Ellenbogen, *Principles of Neurosurgery*: Elsevier Mosby, 2005.
- [116] W. M. Pardridge, "Blood-brain barrier biology and methodology," *J Neurovirol*, vol. 5, pp. 556-69, Dec 1999.
- [117] L. Sakka, G. Coll, and J. Chazal, "Anatomy and physiology of cerebrospinal fluid," *European Annals of Otorhinolaryngology, Head and Neck Diseases*, vol. 128, pp. 309-316, 12// 2011.
- [118] R. Martin, J. Savory, S. Brown, R. Bertholf, and M. J. C. c. Wills, "Transferrin binding of Al^{3+} and Fe^{3+} ," vol. 33, pp. 405-407, 1987.
- [119] K. Thorstensen and I. Romslo, "The role of transferrin in the mechanism of cellular iron uptake," *Biochem J*, vol. 271, pp. 1-9, Oct 1 1990.
- [120] S. Mitchell, P. Pedrosa Mendes, and M. University of. (2013). *A computational model of human iron metabolism*. Available: <http://www.manchester.ac.uk/escholar/uk-ac-man-scw:214181>
- [121] M. B. Johnson and C. A. Enns, "Diferic transferrin regulates transferrin receptor 2 protein stability," *Blood*, vol. 104, pp. 4287-93, Dec 15 2004.
- [122] A. Cozzi, S. Levi, B. Corsi, P. Santambrogio, A. Campanella, G. Gerardi, *et al.*, "Role of iron and ferritin in TNF α -induced apoptosis in HeLa cells," *FEBS Lett*, vol. 537, pp. 187-92, Feb 27 2003.
- [123] L. Descamps, M. P. Dehouck, G. Torpier, and R. Cecchelli, "Receptor-mediated transcytosis of transferrin through blood-brain barrier endothelial cells," *The American Journal Of Physiology*, vol. 270, pp. H1149-H1158, 1996.
- [124] M. Chloupkova, A. S. Zhang, and C. A. Enns, "Stoichiometries of transferrin receptors 1 and 2 in human liver," *Blood Cells Mol Dis*, vol. 44, pp. 28-33, Jan 15 2010.
- [125] J. C. Salgado, A. Olivera-Nappa, Z. P. Gerdtzen, V. Tapia, E. C. Theil, C. Conca, *et al.*, "Mathematical modeling of the dynamic storage of iron in ferritin," *BMC Syst Biol*, vol. 4, p. 147, 2010.
- [126] K. Pantopoulos, N. K. Gray, and M. W. Hentze, "Differential regulation of two related RNA-binding proteins, iron regulatory protein (IRP) and IRPB," *RNA*, vol. 1, pp. 155-63, Apr 1995.
- [127] J. Sarkar, V. Seshadri, N. A. Tripoulas, M. E. Ketterer, and P. L. Fox, "Role of ceruloplasmin in macrophage iron efflux during hypoxia," *J Biol Chem*, vol. 278, pp. 44018-24, Nov 07 2003.
- [128] A. Funahashi, A. Jouraku, Y. Matsuoka, and H. Kitano, "Integration of CellDesigner and SABIO-RK," *In Silico Biol*, vol. 7, pp. S81-90, 2007.

- [129] L. Salter-Cid, A. Brunmark, Y. Li, D. Leturcq, P. A. Peterson, M. R. Jackson, *et al.*, "Transferrin receptor is negatively modulated by the hemochromatosis protein HFE: Implications for cellular iron homeostasis," *Proceedings of the National Academy of Sciences*, vol. 96, pp. 5434-5439, May 11, 1999 1999.
- [130] J. M. Hill, M. R. Ruff, R. J. Weber, and C. B. Pert, "Transferrin receptors in rat brain: neuropeptide-like pattern and relationship to iron distribution," *Proceedings of the National Academy of Sciences*, vol. 82, pp. 4553-4557, July 1, 1985 1985.
- [131] E. M. Taylor and E. H. Morgan, "Developmental changes in transferrin and iron uptake by the brain in the rat," *Developmental Brain Research*, vol. 55, pp. 35-42, 8/1/ 1990.
- [132] M. R. Beamish, G. M. Addison, P. Llewellyn, M. Hodgkins, C. N. Hales, and A. Jacobs, "Ferritin estimation by a radioimmunoassay technique: serum levels in normal subjects and patients with blood disorders," *Br J Haematol*, vol. 22, p. 637, May 1972.
- [133] Z. I. Cabantchik, "LABILE IRON IN CELLS AND BODY FLUIDS . Physiology, Pathology and Pharmacology," *Frontiers in Pharmacology*, vol. 5, 2014-March-13 2014.
- [134] I. A. Simpson, P. Ponnuru, M. E. Klinger, R. L. Myers, K. Devraj, C. L. Coe, *et al.*, "A novel model for brain iron uptake: introducing the concept of regulation," *J Cereb Blood Flow Metab*, Oct 15 2014.
- [135] E. D. Weinberg, "Iron withholding: a defense against infection and neoplasia," *Physiol Rev*, vol. 64, pp. 65-102, Jan 1984.
- [136] R. C. McCarthy and D. J. Kosman, "Glial cell ceruloplasmin and hepcidin differentially regulate iron efflux from brain microvascular endothelial cells," *PLoS One*, vol. 9, p. e89003, 2014.
- [137] M. M. Hanninen, J. Haapasalo, H. Haapasalo, R. E. Fleming, R. S. Britton, B. R. Bacon, *et al.*, "Expression of iron-related genes in human brain and brain tumors," *BMC Neurosci*, vol. 10, p. 36, 2009.
- [138] K. L. Double, M. Gerlach, V. Schunemann, A. X. Trautwein, L. Zecca, M. Gallorini, *et al.*, "Iron-binding characteristics of neuromelanin of the human substantia nigra," *Biochem Pharmacol*, vol. 66, pp. 489-94, Aug 1 2003.
- [139] M. Gerlach, K. L. Double, D. Ben-Shachar, L. Zecca, M. B. Youdim, and P. Riederer, "Neuromelanin and its interaction with iron as a potential risk factor for dopaminergic neurodegeneration underlying Parkinson's disease," *Neurotox Res*, vol. 5, pp. 35-44, 2003.
- [140] M. Gerlach, A. X. Trautwein, L. Zecca, M. B. Youdim, and P. Riederer, "Mossbauer spectroscopic studies of purified human neuromelanin isolated from the substantia nigra," *J Neurochem*, vol. 65, pp. 923-6, Aug 1995.

- [141] L. Zecca, L. Casella, A. Albertini, C. Bellei, F. A. Zucca, M. Engelen, *et al.*, "Neuromelanin can protect against iron-mediated oxidative damage in system modeling iron overload of brain aging and Parkinson's disease," *J Neurochem*, vol. 106, pp. 1866-75, Aug 2008.
- [142] D. Olivares, X. Huang, L. Branden, N. H. Greig, and J. T. Rogers, "Physiological and pathological role of alpha-synuclein in Parkinson's disease through iron mediated oxidative stress; the role of a putative iron-responsive element," *Int J Mol Sci*, vol. 10, pp. 1226-60, Mar 2009.
- [143] A. D. Monnot, G. Zheng, and W. Zheng, "Mechanism of copper transport at the blood-cerebrospinal fluid barrier: influence of iron deficiency in an in vitro model," *Exp Biol Med (Maywood)*, vol. 237, pp. 327-33, Mar 2012.
- [144] G. Rudow, R. O'Brien, A. V. Savonenko, S. M. Resnick, A. B. Zonderman, O. Pletnikova, *et al.*, "Morphometry of the human substantia nigra in ageing and Parkinson's disease," *Acta Neuropathol*, vol. 115, pp. 461-70, Apr 2008.
- [145] D. C. Mash, J. Pablo, D. D. Flynn, S. M. Eface, and W. J. Weiner, "Characterization and distribution of transferrin receptors in the rat brain," *J Neurochem*, vol. 55, pp. 1972-9, Dec 1990.
- [146] L. Zecca, M. Gallorini, V. Schunemann, A. X. Trautwein, M. Gerlach, P. Riederer, *et al.*, "Iron, neuromelanin and ferritin content in the substantia nigra of normal subjects at different ages: consequences for iron storage and neurodegenerative processes," *J Neurochem*, vol. 76, pp. 1766-73, Mar 2001.
- [147] W. S. Enochs, P. Petherick, A. Bogdanova, U. Mohr, and R. Weissleder, "Paramagnetic metal scavenging by melanin: MR imaging," *Radiology*, vol. 204, pp. 417-23, Aug 1997.
- [148] D. Sulzer, C. Cassidy, G. Horga, U. J. Kang, S. Fahn, L. Casella, *et al.*, "Neuromelanin detection by magnetic resonance imaging (MRI) and its promise as a biomarker for Parkinson's disease," *NPJ Parkinsons Dis*, vol. 4, p. 11, 2018.
- [149] G. Bacic and M. Mojovic, "EPR spin trapping of oxygen radicals in plants: a methodological overview," *Ann N Y Acad Sci*, vol. 1048, pp. 230-43, Jun 2005.
- [150] N. P. Visanji, J. F. Collingwood, M. E. Finnegan, A. Tandon, E. House, and L.-N. Hazrati, "Iron deficiency in parkinsonism: region-specific iron dysregulation in Parkinson's disease and multiple system atrophy," *Journal Of Parkinson's Disease*, vol. 3, pp. 523-537, 2013.
- [151] G. Beck, K. Shinzawa, H. Hayakawa, K. Baba, T. Yasuda, H. Sumi-Akamaru, *et al.*, "Deficiency of Calcium-Independent Phospholipase A2 Beta Induces Brain Iron Accumulation through Upregulation of Divalent Metal Transporter 1," *PLoS One*, vol. 10, p. e0141629, 2015.
- [152] A. Gregory and S. Hayflick, "Neurodegeneration with brain iron accumulation disorders overview," 2014.

- [153] J. F. Collingwood and F. Adams, "Chemical imaging analysis of the brain with X-ray methods," *Spectrochimica Acta Part B: Atomic Spectroscopy*, vol. 130, pp. 101-118, 2017/04/01/ 2017.
- [154] D. Cheng, D. Mitchell, D. Shieh, F. J. C. M. C. t. A. i. S. Braet, and e. F. Technology. A. Mendez-Vilas, Badajoz, Spain, "Practical considerations in the successful preparation of specimens for thin-film cryo-transmission electron microscopy," pp. 880-890, 2012.
- [155] R. A. Steinbrecht and K. Zierold, *Cryotechniques in biological electron microscopy*: Springer Science & Business Media, 2012.
- [156] L. Zecca, C. Bellei, P. Costi, A. Albertini, E. Monzani, L. Casella, *et al.*, "New melanic pigments in the human brain that accumulate in aging and block environmental toxic metals," *Proc Natl Acad Sci U S A*, vol. 105, pp. 17567-72, Nov 11 2008.
- [157] H. Fedorow, F. Tribl, G. Halliday, M. Gerlach, P. Riederer, and K. L. Double, "Neuromelanin in human dopamine neurons: comparison with peripheral melanins and relevance to Parkinson's disease," *Prog Neurobiol*, vol. 75, pp. 109-24, Feb 2005.
- [158] D. Kaur and J. Andersen, "Does cellular iron dysregulation play a causative role in Parkinson's disease?," *Ageing Research Reviews*, vol. 3, pp. 327-343, 2004/07/01/ 2004.
- [159] Y. Tao, Y. Wang, J. T. Rogers, and F. Wang, "Perturbed iron distribution in Alzheimer's disease serum, cerebrospinal fluid, and selected brain regions: a systematic review and meta-analysis," *J Alzheimers Dis*, vol. 42, pp. 679-90, 2014.
- [160] R. Ortega, A. Carmona, S. Roudeau, L. Perrin, T. Ducic, E. Carboni, *et al.*, "alpha-Synuclein Over-Expression Induces Increased Iron Accumulation and Redistribution in Iron-Exposed Neurons," *Mol Neurobiol*, vol. 53, pp. 1925-34, Apr 2016.
- [161] P. Dusek, T. Litwin, and A. Czlonkowska, "Wilson Disease and Other Neurodegenerations with Metal Accumulations," *Neurol Clin*, vol. 33, pp. 175-204, Feb 2015.
- [162] H. Kozlowski, M. Luczkowski, M. Remelli, and D. Valensin, "Copper, zinc and iron in neurodegenerative diseases (Alzheimer's, Parkinson's and prion diseases)," *Coordination Chemistry Reviews*, vol. 256, pp. 2129-2141, 10// 2012.
- [163] K. Smallbone, *Metabolic Control Analysis: Rereading Reder*, 2013.
- [164] R. C. Hider, S. Roy, Y. M. Ma, X. Le Kong, and J. Preston, "The potential application of iron chelators for the treatment of neurodegenerative diseases," *Metallomics*, vol. 3, pp. 239-49, Mar 2011.

- [165] P. J. Ratcliffe, "HIF-1 and HIF-2: working alone or together in hypoxia?," *J Clin Invest*, vol. 117, pp. 862-5, Apr 2007.
- [166] M. Mastrogiannaki, P. Matak, B. Keith, M. C. Simon, S. Vaulont, and C. Peyssonnaud, "HIF-2alpha, but not HIF-1alpha, promotes iron absorption in mice," *J Clin Invest*, vol. 119, pp. 1159-66, May 2009.
- [167] C. P. Bracken, A. O. Fedele, S. Linke, W. Balrak, K. Lisy, M. L. Whitelaw, *et al.*, "Cell-specific regulation of hypoxia-inducible factor (HIF)-1alpha and HIF-2alpha stabilization and transactivation in a graded oxygen environment," *J Biol Chem*, vol. 281, pp. 22575-85, Aug 11 2006.
- [168] J. L. Steegmann-Olmedillas, "The role of iron in tumour cell proliferation," *Clin Transl Oncol*, vol. 13, pp. 71-6, Feb 2011.
- [169] H. Drakesmith, E. Nemeth, and T. Ganz, "Ironing out Ferroportin," *Cell Metab*, vol. 22, pp. 777-87, Nov 03 2015.

Appendix A

List of Equations

$$\begin{aligned}
\frac{d([TfR1_BBB])}{dt} = & -k1("TfR1_BBB \text{ degradation}") \cdot [TfR1_BBB] \\
& + \frac{a("TfR1_BBB;expression") \cdot [IRP_BBB]^{n("TfR1_BBB \text{ expression}")}}{K^{n("TfR1_BBB;expression")} + [IRP_BBB]^{n("TfR1_BBB \text{ expression}")}} \\
& - k1("TfR1_BBB \text{ binding } 1") \cdot [^nTfR1_BBB] \cdot [^nTf - Fe_serum] \\
& + k1("TfR1_BBB \text{ release } 1") \cdot [^nTfR1_BBB - Tf - Fe_serum] \\
& + \{k1("TfR1_BBB \text{ iron internalisation}") \cdot [^n2(Tf - Fe) - TfR1_BBB] \\
& - (k2("TfR1_BBB \text{ iron internalisation"}) \cdot [endoFe3_BBB] \cdot [endoFe3_BBB] \\
& \cdot [endoFe3_BBB] \cdot [TfR1_BBB])\}
\end{aligned} \tag{1}$$

$$\begin{aligned}
\frac{d([^nTfR1_BBB - Tf - Fe_serum])}{dt} = & + k1("TfR1_BBB \text{ binding } 1") \cdot [TfR1_BBB] \cdot [^nTf - Fe_serum] \\
& - k1("TfR1_BBB \text{ release } 1") \cdot [^nTfR1_BBB - Tf - Fe_serum] \\
& - k1("TfR1_BBB \text{ binding } 2") \cdot [^nTfR1_BBB - Tf - Fe_serum] \cdot [^nTf - Fe_serum] \\
& + k1("TfR1_BBB \text{ release } 2") \cdot [^n2(Tf - Fe) - TfR1_BBB]
\end{aligned} \tag{2}$$

$$\begin{aligned}
\frac{d([^n2(Tf - Fe) - TfR1_BBB])}{dt} = & + k1("TfR1_BBB \text{ binding } 2") \cdot [Tf - Fe_serum] \cdot [^nTfR1_BBB - Tf - Fe_serum] \\
& - k1("TfR1_BBB \text{ release } 2") \cdot [^n2(Tf - Fe) - TfR1_BBB] \\
& - k1("TfR1_BBB \text{ iron internalisation}") \cdot [^n2(Tf - Fe) - TfR1_BBB] \\
& + \{k2("TfR1_BBB \text{ iron internalisation"}) \cdot [endoFe3_BBB] \cdot [endoFe3_BBB] \\
& \cdot [endoFe3_BBB] \cdot [TfR1_BBB]\}
\end{aligned} \tag{3}$$

$$\begin{aligned}
\frac{d([endoFe3_BBB])}{dt} = & + 4 \cdot \{k1("TfR1_BBB \text{ iron internalisation}") \cdot [^n2(Tf - Fe) - TfR1_BBB] \\
& - (k2("TfR1_BBB \text{ iron internalisation"}) \cdot [endoFe3_BBB] \cdot [endoFe3_BBB] \\
& \cdot [endoFe3_BBB] \cdot [TfR1_BBB])\} \\
& - \frac{V("Steap3_BBB \text{ iron reduction"}) \cdot [endoFe3_BBB]}{Km("Steap3_BBB \text{ iron reduction"}) + [endoFe3_BBB]}
\end{aligned} \tag{4}$$

$$\begin{aligned}
\frac{d([endoFe2_BBB])}{dt} = & + \frac{V("Steap3_BBB \text{ iron reduction"}) \cdot [endoFe3_BBB]}{Km("Steap3_BBB \text{ iron reduction"}) + [endoFe3_BBB]} \\
& - \left(kcat("DMT1_BBB \text{ iron export"}) \cdot [DMT1_BBB] \right. \\
& \cdot \left. \frac{([endoFe2_BBB])}{Km("DMT1_BBB \text{ endosomal export"}) + [endoFe3_BBB]} \right)
\end{aligned} \tag{5}$$

$$\begin{aligned}
\frac{d([LIP_BBB])}{dt} = & + (K(\text{"Ferritin_BBB full degradation iron release"}) \cdot \frac{[Fe_in_ferritin_BBB]}{[Ferritin_BBB]} \\
& \cdot [Ferritin_BBB]) \\
& + [Fe_within_ferritin_BBB] \cdot kloss(\text{"Ferritin_BBB internalised iron release"}) \\
& \cdot \left(1 + \frac{0.048 \cdot \frac{[Fe_within_ferritin_BBB]}{[Ferritin_BBB]}}{1 + \frac{[Fe_within_ferritin_BBB]}{[Ferritin_BBB]}} \right) \\
& - 2 \cdot \left(a(\text{"Fpn_BBB export"}) \cdot \frac{[Fpn_BBB]^{\eta(\text{"Fpn_BBB export"})}}{K^{\eta(\text{"Fpn_BBB export"})} + [Fpn_BBB]^{\eta(\text{"Fpn_BBB export"})}} \right. \\
& \cdot [LIP_BBB] \left. \right) \\
& - k1(\text{"Ferritin_BBB iron binding"}) \cdot [LIP_BBB] \cdot [Ferritin_BBB] \\
& + k1(\text{"Ferritin_BBB iron release"}) \cdot [^55Fe - ferritin_BBB] \\
& + \left(kcat(\text{"DMT1_BBB iron export"}) \cdot [DMT1_BBB] \right. \\
& \cdot \frac{([endoFe2_BBB])}{Km(\text{"DMT1_BBB endosomal export"}) + [endoFe3_BBB]} \left. \right)
\end{aligned} \tag{6}$$

$$\begin{aligned}
\frac{d([IRP_BBB])}{dt} = & + a(\text{"IRP_BBB expression"}) \cdot \left(1 - \frac{[LIP_BBB]^{\eta(\text{"IRP_BBB expression"})}}{K^{\eta(\text{"IRP_BBB expression"})} + [LIP_BBB]^{\eta(\text{"IRP_BBB expression"})}} \right) \\
& - k1(\text{"IRP_BBB degradation"}) \cdot [IRP_BBB]
\end{aligned} \tag{7}$$

$$\begin{aligned}
\frac{d([Fpn_BBB])}{dt} = & + a(\text{"Fpn_BBB expression"}) \cdot \left(1 - \frac{[IRP_BBB]^{\eta(\text{"Fpn_BBB expression"})}}{K^{\eta(\text{"Fpn_BBB expression"})} + [IRP_BBB]^{\eta(\text{"Fpn_BBB expression"})}} \right) \\
& - \left(a(\text{"Fpn_BBB degradation"}) \cdot \frac{[Hepcidin_BBB]^{\eta(\text{"Fpn_BBB degradation"})}}{K^{\eta(\text{"Fpn_BBB degradation"})} + [Hepcidin_BBB]^{\eta(\text{"Fpn_BBB degradation"})}} \right. \\
& \cdot [Fpn_BBB] \left. \right)
\end{aligned} \tag{8}$$

$$\begin{aligned}
\frac{d([^55Fe - ferritin_BBB])}{dt} = & + k1(\text{"Ferritin_BBB iron binding"}) \cdot [LIP_BBB] \cdot [Ferritin_BBB] \\
& - k1(\text{"Ferritin_BBB iron internalisation"}) \cdot [^55Fe - ferritin_BBB] \\
& - k1(\text{"Ferritin_BBB iron release"}) \cdot [^55Fe - ferritin_BBB]
\end{aligned} \tag{9}$$

$$\begin{aligned}
\frac{d([Ferritin_BBB])}{dt} = & -k1("Ferritin_BBB \text{ degradation}") \cdot [Ferritin_BBB] \\
& + a("Ferritin_BBB \text{ expression}") \\
& \cdot \left(1 - \frac{[IRP_BBB]^{n("Ferritin_BBB \text{ expression}")}}{K^{n("Ferritin_BBB \text{ expression}")} + [IRP_BBB]^{n("Ferritin_BBB \text{ expression}")}} \right) \\
& - k1("Ferritin_BBB \text{ iron binding}") \cdot [LIP_BBB] \cdot [Ferritin_BBB] \\
& + k1("Ferritin_BBB \text{ iron internalisation}") \cdot [^nFe - ferritin_BBB^n] \\
& + k1("Ferritin_BBB \text{ iron release}") \cdot [^nFe - ferritin_BBB^n]
\end{aligned} \tag{10}$$

$$\begin{aligned}
\frac{d([Fe_within_ferritin_BBB])}{dt} = & k1("Ferritin_BBB \text{ iron internalisation}") \cdot [^nFe - ferritin_BBB^n] \\
& - \left([Ferritin_BBB] \cdot kloss("Ferritin_BBB \text{ internalised iron release"}) \cdot \left(1 + \frac{0.048 \cdot \frac{[Fe_within_ferritin_BBB]}{[Ferritin_BBB]}}{1 + \frac{[Fe_within_ferritin_BBB]}{[Ferritin_BBB]}} \right) \right) \\
& - K("Ferritin_BBB \text{ full degradation iron release"}) \\
& \cdot \frac{[Fe_within_ferritin_BBB][Ferritin_BBB]}{[Ferritin_BBB]}
\end{aligned} \tag{11}$$

$$\begin{aligned}
\frac{d([DMT1_BBB])}{dt} = & -k1("DMT1_BBB \text{ degradation}") \cdot [DMT1_BBB] \\
& + \frac{a("DMT1_BBB \text{ expression"}) \cdot [IRP_BBB]^{n("DMT1_BBB \text{ expression}")}}{K^{n("DMT1_BBB \text{ expression}")} + [IRP_BBB]^{n("DMT1_BBB \text{ expression}")}}
\end{aligned} \tag{12}$$

$$\begin{aligned}
\frac{d([^nTf - Fe_ISF^n])}{dt} = & \left(a("Fpn_BBB \text{ export"}) \cdot \frac{[Fpn_BBB]^{n("Fpn_BBB \text{ export}")}}{K^{n("Fpn_BBB \text{ export}")} + [Fpn_BBB]^{n("Fpn_BBB \text{ export}")}} \right. \\
& \cdot [LIP_BBB] \Big) \\
& - \{ k1("Flow of Tf-Fe between ISF \& CSF^n") \cdot [^nTf - Fe_ISF^n] \\
& + k2("Flow of Tf-Fe between ISF \& CSF^n") \cdot [^nTf - Fe_CSF^n] \} \\
& + \left(a("Fpn_SN \text{ export"}) \cdot \frac{[Fpn_SN]^{n("Fpn_SN \text{ export}")}}{K^{n("Fpn_SN \text{ export}")} + [Fpn_SN]^{n("Fpn_SN \text{ export}")}} \right. \\
& \cdot [LIP_SN] \Big) \\
& - k1("TfR1_SN \text{ binding 1^n}") \cdot [TfR1_SN] \cdot [^nTf - Fe_ISF^n] \\
& - k1("TfR1_SN \text{ binding 2^n}") \cdot [^nTfR1_SN - Tf - Fe_SN^n] \cdot [^nTf - Fe_ISF^n] \\
& + k1("TfR1_SN \text{ release 1^n}") \cdot [^nTfR1_SN - Tf - Fe_SN^n] \\
& + k1("TfR1_SN \text{ release 2^n}") \cdot [^n2(Tf - Fe) - TfR1_SN^n]
\end{aligned} \tag{13}$$

$$\begin{aligned}
\frac{d([{}^n\text{TfR1_BCB} - \text{Tf} - \text{Fe_CSF}])}{dt} = & \\
& + k1({}^n\text{TfR1_BCB binding 1}^n) \cdot [\text{TfR1_BCB}] \cdot [{}^n\text{Tf} - \text{Fe_CSF}] \\
& - k1({}^n\text{TfR1_BCB release 1}^n) \cdot [{}^n\text{TfR1_BCB} - \text{Tf} - \text{Fe_CSF}] \\
& - k1({}^n\text{TfR1_BCB binding 2}^n) \cdot [{}^n\text{TfR1_BCB} - \text{Tf} - \text{Fe_CSF}] \cdot [{}^n\text{Tf} - \text{Fe_CSF}] \\
& + k1({}^n\text{TfR1_BCB release 2}^n) \cdot [{}^n2(\text{Tf} - \text{Fe}) - \text{TfR1_BCB}]
\end{aligned} \tag{14}$$

$$\begin{aligned}
\frac{d([{}^n2(\text{Tf} - \text{Fe}) - \text{TfR1_BCB}])}{dt} = & \\
& + k1({}^n\text{TfR1_BCB binding 2}^n) \cdot [{}^n\text{Tf} - \text{Fe_CSF}] \cdot [{}^n\text{TfR1_BCB} - \text{Tf} - \text{Fe_CSF}] \\
& - k1({}^n\text{TfR1_BCB release 2}^n) \cdot [{}^n2(\text{Tf} - \text{Fe}) - \text{TfR1_BCB}] \\
& - k1({}^n\text{TfR1_BCB iron internalisation}^n) \cdot [{}^n2(\text{Tf} - \text{Fe}) - \text{TfR1_BCB}] \\
& + (k2({}^n\text{TfR1_BCB iron internalisation}^n) \cdot [\text{endoFe3_BCB}] \cdot [\text{endoFe3_BCB}] \\
& \quad \cdot [\text{endoFe3_BCB}] \cdot [\text{TfR1_BCB}])
\end{aligned} \tag{15}$$

$$\begin{aligned}
\frac{d([{}^n\text{Tf} - \text{Fe_CSF}])}{dt} = & + \{k1({}^n\text{Flow of Tf-Fe between ISF \& CSF}^n) \cdot [{}^n\text{Tf} - \text{Fe_ISF}] \\
& - k2({}^n\text{Flow of Tf-Fe between ISF \& CSF}^n) \cdot [{}^n\text{Tf} - \text{Fe_CSF}]\} \\
& - k1({}^n\text{TfR1_BCB binding 1}^n) \cdot [{}^n\text{TfR1_BCB}] \cdot [{}^n\text{Tf} - \text{Fe_CSF}] \\
& - k1({}^n\text{TfR1_BCB binding 2}^n) \cdot [{}^n\text{TfR1_BCB} - \text{Tf} - \text{Fe_CSF}] \cdot [{}^n\text{Tf} - \text{Fe_CSF}] \\
& + k1({}^n\text{TfR1_BCB release 1}^n) \cdot [{}^n\text{TfR1_BCB} - \text{Tf} - \text{Fe_CSF}] \\
& + k1({}^n\text{TfR1_BCB release 2}^n) \cdot [{}^n2(\text{Tf} - \text{Fe}) - \text{TfR1_BCB}]
\end{aligned} \tag{16}$$

$$\begin{aligned}
\frac{d([\text{TfR1_BCB}])}{dt} = & -k1({}^n\text{TfR1_BCB degradation}^n) \cdot [\text{TfR1_BCB}] \\
& + \frac{a({}^n\text{TfR1_BCB;expression}^n) \cdot [\text{IRP_BCB}]^{n({}^n\text{TfR1_BCB expression}^n)}}{K({}^n\text{TfR1_BCB expression}^n) + [\text{IRP_BCB}]^{n({}^n\text{TfR1_BCB expression}^n)}} \\
& - k1({}^n\text{TfR1_BCB binding 1}^n) \cdot [{}^n\text{TfR1_BCB}] \cdot [{}^n\text{Tf} - \text{Fe_CSF}] \\
& + k1({}^n\text{TfR1_BCB release 1}^n) \cdot [{}^n\text{TfR1_BCB} - \text{Tf} - \text{Fe_CSF}] \\
& + \{k1({}^n\text{TfR1_BCB iron internalisation}^n) \cdot [{}^n2(\text{Tf} - \text{Fe}) - \text{TfR1_BCB}] \\
& - (k2({}^n\text{TfR1_BCB iron internalisation}^n) \cdot [\text{endoFe3_BCB}] \cdot [\text{endoFe3_BCB}] \\
& \quad \cdot [\text{endoFe3_BCB}] \cdot [\text{TfR1_BCB}])\}
\end{aligned} \tag{17}$$

$$\begin{aligned}
\frac{d([\text{IRP_BCB}])}{dt} = & \\
& + a({}^n\text{IRP_BCB expression}^n) \cdot \left(1 - \frac{[\text{LIP_BCB}]^{n({}^n\text{IRP_BCB expression}^n)}}{K({}^n\text{IRP_BCB expression}^n) + [\text{LIP_BCB}]^{n({}^n\text{IRP_BCB expression}^n)}}\right) \\
& - k1({}^n\text{IRP_BCB degradation}^n) \cdot [\text{IRP_BCB}]
\end{aligned} \tag{18}$$

$$\begin{aligned}
\frac{d([endoFe3_BCB])}{dt} = & +4 \cdot \{k1("TfR1_BCB \text{ iron internalisation}") \cdot [^2(Tf - Fe) - TfR1_BCB"] \\
& - (k2("TfR1_BCB \text{ iron internalisation}") \cdot [endoFe3_BCB] \cdot [endoFe3_BCB] \\
& \cdot [endoFe3_BCB] \cdot [TfR1_BCB])\} \\
& - \frac{V("Steap3_BCB \text{ iron reduction}") \cdot [endoFe3_BCB]}{Km("Steap3_BCB \text{ iron reduction}") + [endoFe3_BCB]}
\end{aligned} \tag{19}$$

$$\begin{aligned}
\frac{d([endoFe2_BCB])}{dt} = & + \frac{V("Steap3_BCB \text{ iron reduction}") \cdot [endoFe3_BCB]}{Km("Steap3_BCB \text{ iron reduction}") + [endoFe3_BCB]} \\
& - \left(kcat("DMT1_BCB \text{ iron export}") \cdot [DMT1_BCB] \right. \\
& \left. \cdot \frac{([endoFe2_BCB])}{Km("DMT1_BCB \text{ endosomal export}") + [endoFe3_BCB]} \right)
\end{aligned} \tag{20}$$

$$\begin{aligned}
\frac{d([LIP_BCB])}{dt} = & + (K("Ferritin_BCB \text{ full degradation iron release}") \cdot \frac{[Fe_in_ferritin_BCB]}{[Ferritin_BCB]} \\
& \cdot [Ferritin_BCB]) \\
& + [Fe_within_ferritin_BCB] \cdot kloss("Ferritin_BCB \text{ internalised iron release}") \\
& \cdot \left(1 + \frac{0.048 \cdot \frac{[Fe_within_ferritin_BCB]}{[Ferritin_BCB]}}{1 + \frac{[Fe_within_ferritin_BCB]}{[Ferritin_BCB]}} \right) \\
& - 2 \cdot \left(a("Fpn_BCB \text{ export}") \cdot \frac{[Fpn_BCB]^{\eta("Fpn_BCB \text{ export}")}}{K("Fpn_BCB \text{ export}") + [Fpn_BCB]^{\eta("Fpn_BCB \text{ export}")}} \right. \\
& \left. \cdot [LIP_BCB] \right) \\
& - k1("Ferritin_BCB \text{ iron binding}") \cdot [LIP_BCB] \cdot [Ferritin_BCB] \\
& + k1("Ferritin_BCB \text{ iron release}") \cdot [^2Fe - ferritin_BCB"] \\
& + \left(kcat("DMT1_BCB \text{ iron export}") \cdot [DMT1_BCB] \right. \\
& \left. \cdot \frac{([endoFe2_BCB])}{Km("DMT1_BCB \text{ endosomal export}") + [endoFe3_BCB]} \right)
\end{aligned} \tag{21}$$

$$\begin{aligned}
\frac{d([Fpn_BCB])}{dt} = & + a("Fpn_BCB \text{ expression}") \cdot \left(1 - \frac{[IRP_BCB]^{\eta("Fpn_BCB \text{ expression}")}}{K("Fpn_BCB \text{ expression}") + [IRP_BCB]^{\eta("Fpn_BCB \text{ expression}")}} \right) \\
& - \left(a("Fpn_BCB \text{ degradation}") \cdot \frac{[Hepcidin_BCB]^{\eta("Fpn_BCB \text{ degradation}")}}{K("Fpn_BCB \text{ degradation}") + [Hepcidin_BCB]^{\eta("Fpn_BCB \text{ degradation}")}} \right. \\
& \left. \cdot [Fpn_BCB] \right)
\end{aligned} \tag{22}$$

$$\begin{aligned}
\frac{d([{}^5\text{Fe} - \text{ferritin_BCB}])}{dt} = & +k1(\text{"Ferritin_BCB iron binding"}) \cdot [\text{LIP_BCB}] \cdot [\text{Ferritin_BCB}] \\
& - k1(\text{"Ferritin_BCB iron internalisation"}) \cdot [{}^5\text{Fe} - \text{ferritin_BCB}] \\
& - k1(\text{"Ferritin_BCB iron release"}) \cdot [{}^5\text{Fe} - \text{ferritin_BCB}]
\end{aligned} \tag{23}$$

$$\begin{aligned}
\frac{d([\text{Ferritin_BCB}])}{dt} = & -k1(\text{"Ferritin_BCB degradation"}) \cdot [\text{Ferritin_BCB}] \\
& + a(\text{"Ferritin_BCB expression"}) \\
& \cdot \left(1 - \frac{[\text{IRP_BCB}]^{n(\text{"Ferritin_BCB expression"})}}{K^{n(\text{"Ferritin_BCB expression"})} + [\text{IRP_BCB}]^{n(\text{"Ferritin_BCB expression"})}} \right) \\
& - k1(\text{"Ferritin_BCB iron binding"}) \cdot [\text{LIP_BCB}] \cdot [\text{Ferritin_BCB}] \\
& + k1(\text{"Ferritin_BCB iron internalisation"}) \cdot [{}^5\text{Fe} - \text{ferritin_BCB}] \\
& + k1(\text{"Ferritin_BCB iron release"}) \cdot [{}^5\text{Fe} - \text{ferritin_BCB}]
\end{aligned} \tag{24}$$

$$\begin{aligned}
\frac{d([\text{Fe_within_ferritin_BCB}])}{dt} = & k1(\text{"Ferritin_BCB iron internalisation"}) \cdot [{}^5\text{Fe} - \text{ferritin_BCB}] \\
& - \left([\text{Ferritin_BCB}] \cdot k\text{loss}(\text{"Ferritin_BCB internalised iron release"}) \cdot \left(1 + \frac{0.048 \cdot \frac{[\text{Fe_within_ferritin_BCB}]}{[\text{Ferritin_BCB}]}}{1 + \frac{[\text{Fe_within_ferritin_BCB}]}{[\text{Ferritin_BCB}]}} \right) \right) \\
& - K(\text{"Ferritin_BCB full degradation iron release"}) \\
& \cdot \frac{[\text{Fe_within_ferritin_BCB}][\text{Ferritin_BCB}]}{[\text{Ferritin_BCB}]}
\end{aligned} \tag{25}$$

$$\begin{aligned}
\frac{d([\text{DMT1_BCB}])}{dt} = & -k1(\text{"DMT1_BCB degradation"}) \cdot [\text{DMT1_BCB}] \\
& + \frac{a(\text{"DMT1_BCB expression"}) \cdot [\text{IRP_BCB}]^{n(\text{"DMT1_BCB expression"})}}{K^{n(\text{"DMT1_BCB expression"})} + [\text{IRP_BCB}]^{n(\text{"DMT1_BCB expression"})}}
\end{aligned} \tag{26}$$

$$\begin{aligned}
\frac{d([\text{DMT1_DAN}])}{dt} = & -k1(\text{"DMT1_DAN degradation"}) \cdot [\text{DMT1_DAN}] \\
& + \frac{a(\text{"DMT1_DAN expression"}) \cdot [\text{IRP_DAN}]^{n(\text{"DMT1_DAN expression"})}}{K^{n(\text{"DMT1_DAN expression"})} + [\text{IRP_DAN}]^{n(\text{"DMT1_DAN expression"})}}
\end{aligned} \tag{27}$$

$$\begin{aligned}
\frac{d([LIP_DAN])}{dt} = & + (K_{("Ferritin_DAN \text{ full degradation iron release"})} \cdot \frac{[Fe_in_ferritin_DAN]}{[Ferritin_DAN]} \\
& \cdot [Ferritin_DAN]) \\
& + [Fe_within_ferritin_DAN] \cdot kloss_{("Ferritin_DAN \text{ internalised iron release"})} \\
& \cdot \left(1 + \frac{0.048 \cdot \frac{[Fe_within_ferritin_DAN]}{[Ferritin_DAN]}}{1 + \frac{[Fe_within_ferritin_DAN]}{[Ferritin_DAN]}} \right) \\
& - 2 \cdot \left(a_{("Fpn_DAN \text{ export"})} \cdot \frac{[Fpn_DAN]^{n_{("Fpn_DAN \text{ export"})}}}}{K_{("Fpn_DAN \text{ export"})}^{n_{("Fpn_DAN \text{ export"})}}} + [Fpn_DAN]^{n_{("Fpn_DAN \text{ export"})}}} \right. \\
& \cdot [LIP_DAN] \left. \right) \\
& - k1_{("Ferritin_DAN \text{ iron binding"})} \cdot [LIP_DAN] \cdot [Ferritin_DAN] \\
& + k1_{("Ferritin_DAN \text{ iron release"})} \cdot [^55Fe - ferritin_DAN] \\
& + \left(kcat_{("DMT1_DAN \text{ iron export"})} \cdot [DMT1_DAN] \right. \\
& \cdot \frac{([endoFe2_DAN])}{Km_{("DMT1_DAN \text{ endosomal export"})} + [endoFe3_DAN]} \left. \right) \\
& - k1_{("Fe2 \text{ oxidation by H2O2"})} \cdot [LIP_DAN] \cdot [H2O2] \\
& + k1_{("Fe3 \text{ reduction by AS \& O2"})} \cdot [Fe3] \cdot [O2] \cdot [AS] \\
& + k1_{(iron_use_SN)} \cdot [LIP_SN]
\end{aligned} \tag{28}$$

$$\begin{aligned}
\frac{d([Fpn_DAN])}{dt} = & + a_{("Fpn_DAN \text{ expression"})} \cdot \left(1 - \frac{[IRP_DAN]^{n_{("Fpn_DAN \text{ expression"})}}}}{K_{("Fpn_DAN \text{ expression"})}^{n_{("Fpn_DAN \text{ expression"})}}} + [IRP_DAN]^{n_{("Fpn_DAN \text{ expression"})}}} \right) \\
& - \left(a_{("Fpn_DAN \text{ degradation"})} \cdot \frac{[Hepcidin_DAN]^{n_{("Fpn_DAN \text{ degradation"})}}}}{K_{("Fpn_DAN \text{ degradation"})}^{n_{("Fpn_DAN \text{ degradation")}}} + [Hepcidin_DAN]^{n_{("Fpn_DAN \text{ degradation")}}}} \right. \\
& \cdot [Fpn_DAN] \left. \right)
\end{aligned} \tag{29}$$

$$\begin{aligned}
\frac{d([endoFe2_DAN])}{dt} = & + \frac{V_{("Steap3_DAN \text{ iron reduction"})} \cdot [endoFe3_DAN]}{Km_{("Steap3_DAN \text{ iron reduction"})} + [endoFe3_DAN]} \\
& - \left(kcat_{("DMT1_DAN \text{ iron export"})} \cdot [DMT1_DAN] \right. \\
& \cdot \frac{([endoFe2_DAN])}{Km_{("DMT1_DAN \text{ endosomal export"})} + [endoFe3_DAN]} \left. \right)
\end{aligned} \tag{30}$$

$$\begin{aligned}
\frac{d([TfR1_DAN])}{dt} = & -k1("TfR1_DAN \text{ degradation}") \cdot [TfR1_DAN] \\
& + \frac{a("TfR1_DAN;expression") \cdot [IRP_DAN]^{n("TfR1_DAN \text{ expression}")}}{K^{n("TfR1_DAN;expression")} + [IRP_DAN]^{n("TfR1_DAN \text{ expression}")}} \\
& - k1("TfR1_DAN \text{ binding } 1") \cdot [^nTfR1_DAN^n] \cdot [^nTf - Fe_ISF^n] \\
& + k1("TfR1_DAN \text{ release } 1") \cdot [^nTfR1_DAN - Tf - Fe_ISF^n] \\
& + \{k1("TfR1_DAN \text{ iron internalisation}") \cdot [^n2(Tf - Fe) - TfR1_DAN^n] \\
& - (k2("TfR1_DAN \text{ iron internalisation}") \cdot [endoFe3_DAN] \cdot [endoFe3_DAN] \\
& \cdot [endoFe3_DAN] \cdot [TfR1_DAN])\}
\end{aligned} \tag{31}$$

$$\begin{aligned}
\frac{d([^nTfR1_DAN - Tf - Fe_ISF^n])}{dt} = & + k1("TfR1_DAN \text{ binding } 1") \cdot [TfR1_DAN] \cdot [^nTf - Fe_ISF^n] \\
& - k1("TfR1_DAN \text{ release } 1") \cdot [^nTfR1_DAN - Tf - Fe_ISF^n] \\
& - k1("TfR1_DAN \text{ binding } 2") \cdot [^nTfR1_DAN - Tf - Fe_ISF^n] \cdot [^nTf - Fe_ISF^n] \\
& + k1("TfR1_DAN \text{ release } 2") \cdot [^n2(Tf - Fe) - TfR1_DAN^n]
\end{aligned} \tag{32}$$

$$\begin{aligned}
\frac{d([^n2(Tf - Fe) - TfR1_DAN^n])}{dt} = & + k1("TfR1_DAN \text{ binding } 2") \cdot [^nTf - Fe_ISF^n] \cdot [^nTfR1_DAN - Tf - Fe_ISF^n] \\
& - k1("TfR1_DAN \text{ release } 2") \cdot [^n2(Tf - Fe) - TfR1_DAN^n] \\
& - k1("TfR1_DAN \text{ iron internalisation}") \cdot [^n2(Tf - Fe) - TfR1_DAN^n] \\
& + (k2("TfR1_DAN \text{ iron internalisation}") \cdot [endoFe3_DAN] \cdot [endoFe3_DAN] \\
& \cdot [endoFe3_DAN] \cdot [TfR1_DAN])
\end{aligned} \tag{33}$$

$$\begin{aligned}
\frac{d([IRP_DAN])}{dt} = & + a("IRP_DAN \text{ expression}") \cdot \left(1 - \frac{[LIP_DAN]^{n("IRP_DAN \text{ expression}")}}{K^{n("IRP_DAN;expression")} + [LIP_DAN]^{n("IRP_DAN \text{ expression}")}} \right) \\
& - k1("IRP_DAN \text{ degradation}") \cdot [IRP_DAN]
\end{aligned} \tag{34}$$

$$\begin{aligned}
\frac{d([endoFe3_DAN])}{dt} = & + 4 \cdot \{k1("TfR1_DAN \text{ iron internalisation}") \cdot [^n2(Tf - Fe) - TfR1_DAN^n] \\
& - (k2("TfR1_DAN \text{ iron internalisation}") \cdot [endoFe3_DAN] \cdot [endoFe3_DAN] \\
& \cdot [endoFe3_DAN] \cdot [TfR1_DAN])\} \\
& - \frac{V("Steap3_DAN \text{ iron reduction"}) \cdot [endoFe3_DAN]}{Km("Steap3_DAN \text{ iron reduction"}) + [endoFe3_DAN]}
\end{aligned} \tag{35}$$

$$\begin{aligned}
\frac{d([^nFe - ferritin_DAN^n])}{dt} = & + k1("Ferritin_DAN \text{ iron binding}") \cdot [LIP_DAN] \cdot [Ferritin_DAN] \\
& - k1("Ferritin_DAN \text{ iron internalisation}") \cdot [^nFe - ferritin_DAN^n] \\
& - k1("Ferritin_DAN \text{ iron release}") \cdot [^nFe - ferritin_DAN^n]
\end{aligned} \tag{36}$$

$$\begin{aligned}
\frac{d([Ferritin_DAN])}{dt} = & -k1("Ferritin_DAN\ degradation") \cdot [Ferritin_DAN] \\
& + a("Ferritin_DAN\ expression") \\
& \cdot \left(1 - \frac{[IRP_DAN]^{n("Ferritin_DAN\ expression")}}{K^{n("Ferritin_DAN\ expression")}} + [IRP_DAN]^{n("Ferritin_DAN\ expression")} \right) \\
& - k1("Ferritin_DAN\ iron\ binding") \cdot [LIP_DAN] \cdot [Ferritin_DAN] \\
& + k1("Ferritin_DAN\ iron\ internalisation") \cdot [^55Fe - ferritin_DAN] \\
& + k1("Ferritin_DAN\ iron\ release") \cdot [^55Fe - ferritin_DAN]
\end{aligned} \tag{37}$$

$$\begin{aligned}
\frac{d([Fe_within_ferritin_DAN])}{dt} = & k1("Ferritin_DAN\ iron\ internalisation") \cdot [^55Fe - ferritin_DAN] \\
& - \left([Ferritin_DAN] \cdot kloss("Ferritin_DAN\ internalised\ iron\ release") \cdot \left(1 + \frac{0.048 \cdot \frac{[Fe_within_ferritin_DAN]}{[Ferritin_DAN]}}{1 + \frac{[Fe_within_ferritin_DAN]}{[Ferritin_DAN]}} \right) \right) \\
& - K("Ferritin_DAN\ full\ degradation\ iron\ release") \\
& \cdot \frac{[Fe_within_ferritin_DAN][Ferritin_DAN]}{[Ferritin_DAN]}
\end{aligned} \tag{38}$$

$$\begin{aligned}
\frac{d([Fe3])}{dt} = & -k1("Fe3\ reduction\ by\ AS\ \&\ O2") \cdot [Fe3] \cdot [O2] \cdot [AS] \\
& + k1("Fe2\ oxidation\ by\ H2O2") \cdot [LIP_DAN] \cdot [H2O2] \\
& + \{k1("High_affinity_NM-Fe.binding") \cdot [NM_SN] \cdot [Fe3] \\
& \quad - k2("High_affinity_NM-Fe.binding") \cdot [^55NM - Fe_SN_high_affinity]\} \\
& + k1("iron_release_from_NM_high_affinity") \cdot [Fe_in_NM_SN_high_affinity] \\
& - \{k1("Low_affinity_NM-Fe.binding") \cdot [NM_SN] \\
& \quad - k2("Low_affinity_NM-Fe.binding") \cdot [^55NM - Fe_SN_low_affinity]\}
\end{aligned} \tag{39}$$

$$\begin{aligned}
\frac{d([hydroxylRadical])}{dt} = & +k1("Fe2\ oxidation\ by\ H2O2") \cdot [LIP_SN] \cdot [H2O2] \\
& - k1("hydroxylRadical\ to\ water") \cdot [hydroxylRadical]
\end{aligned} \tag{40}$$

$$\begin{aligned}
\frac{d([^55NM - Fe_SN_high_affinity])}{dt} = & +\{k1("High_affinity_NM-Fe.binding") \cdot [NM_SN] \cdot [Fe3] \\
& \quad - k2("High_affinity_NM-Fe.binding") \cdot [^55NM - Fe_SN_high_affinity]\} \\
& - k1(NM_mineral_core_formation_high_affinity) \cdot [^55NM - Fe_SN_high_affinity]
\end{aligned} \tag{41}$$

$$\begin{aligned}
\frac{d([Fe_in_NM_SN_high_affinity])}{dt} = & -k1("iron_release_from_NM_high_affinity") \cdot [Fe_in_NM_SN_high_affinity] \\
& + k1(NM_mineral_core_formation_high_affinity) \cdot [^55NM - Fe_SN_high_affinity]
\end{aligned} \tag{42}$$

$$\begin{aligned} \frac{d(["\text{NM} - \text{Fe_SN_low_affinity}"])}{dt} = & + \{k1["\text{NM} - \text{Fe_SN_low_affinity}] \cdot [\text{NM_SN}] \cdot [\text{Fe3}] \\ & - k2["\text{Low_affinity_NM} - \text{Fe_binding}] \cdot ["\text{NM} - \text{Fe_SN_low_affinity}"]\} \end{aligned} \quad (43)$$

Appendix B

Ethical approval letter



PRIVATE
Miss Vindy Tjendana
Engineering
University of Warwick
Coventry
CV4 7AL

28 June 2018

Dear Miss Tjendana,

Study Title and BSREC Reference: *Iron Metabolism in the brain* REGO-2018-2222

Thank you for submitting the above-named project to the University of Warwick Biomedical and Scientific Research Ethics Committee for research ethical review.

I am pleased to advise that research ethical approval is granted.

In undertaking your study, you are required to comply with the University of Warwick's *Research Data Management Policy*, details of which may be found on the Research and Impact Services' webpages, under "Codes of Practice & Policies" » "Research Code of Practice" » "Data & Records" » "Research Data Management Policy", at:
http://www2.warwick.ac.uk/services/ris/research_integrity/code_of_practice_and_policies/research_code_of_practice/datacollection_retention/research_data_mgt_policy

You are also required to comply with the University of Warwick's *Information Classification and Handling Procedure*, details of which may be found on the University's Governance webpages, under "Governance" » "Information Security" » "Information Classification and Handling Procedure", at:
<http://www2.warwick.ac.uk/services/gov/informationsecurity/handling>.

Investigators should familiarise themselves with the classifications of information defined therein, and the requirements for the storage and transportation of information within the different classifications:

Information Classifications:

<http://www2.warwick.ac.uk/services/gov/informationsecurity/handling/classifications>

Handling Electronic Information:

<http://www2.warwick.ac.uk/services/gov/informationsecurity/handling/electronic/>

Handling Paper or other media

<http://www2.warwick.ac.uk/services/gov/informationsecurity/handling/paper/>.

Please also be aware that BSREC grants **ethical approval** for studies. **The seeking and obtaining of all other necessary approvals is the responsibility of the investigator**

www.warwick.ac.uk



These other approvals may include, but are not limited to:

1. Any necessary agreements, approvals, or permissions required in order to comply with the University of Warwick's Financial Regulations and Procedures.
2. Any necessary approval or permission required in order to comply with the University of Warwick's Quality Management System and Standard Operating Procedures for the governance, acquisition, storage, use, and disposal of human samples for research.
3. All relevant University, Faculty, and Divisional/Departmental approvals, if an employee or student of the University of Warwick.
4. Approval from the applicant's academic supervisor and course/module leader (as appropriate), if a student of the University of Warwick.
5. Health Research Authority (HRA) approval for research studies undertaken in NHS Trusts (previously NHS R+D approval).
6. NHS Trust Clinical Audit Approval, for clinical audit studies undertaken in NHS Trusts.
7. Approval from Departmental or Divisional Heads, as required under local procedures, within Health and Social Care organisations hosting the study.
8. Local ethical approval for studies undertaken overseas, or in other HE institutions in the UK.
9. Approval from Heads (or delegates thereof) of UK Medical Schools, for studies involving medical students as participants.
10. Permission from Warwick Medical School to access medical students or medical student data for research or evaluation purposes.
11. NHS Trust Caldicott Guardian Approval, for studies where identifiable data is being transferred outside of the direct clinical care team. Individual NHS Trust procedures vary in their implementation of Caldicott guidance, and local guidance must be sought.
12. Any other approval required by the institution hosting the study, or by the applicant's employer.

There is no requirement to supply documentary evidence of any of the above to BSREC, but applicants should hold such evidence in their Study Master File for University of Warwick auditing and monitoring purposes. You may be required to supply evidence of any necessary approvals to other University functions, e.g. The Finance Office, Research & Impact Services (RIS), or your Department/School.

May I take this opportunity to wish you success with your study, and to remind you that any Substantial Amendments to your study require approval from BSREC before they may be implemented.

Yours sincerely

pp.

Dr David Ellard
Chair
Biomedical and Scientific
Research Ethics Sub-Committee

**Biomedical and Scientific
Research Ethics Sub-Committee**
Research & Impact Services
University of Warwick
Coventry, CV4 8UW.
E: BSREC@Warwick.ac.uk

[http://www2.warwick.ac.uk/services/
ris/research_integrity/researchethics
committees/biomed](http://www2.warwick.ac.uk/services/ris/research_integrity/researchethicscommittees/biomed)

Appendix C

Conference abstract – Movement Disorder congress 2016

A computational model of iron transport between the blood circulation and the brain

V. Tjendana-Tjhin, S. Mitchell, E.A. Milward, M.J. Chappell, J.F. Collingwood (Coventry, United Kingdom)

Meeting: 20th International Congress

Abstract Number: 1851

Keywords: Brain iron accumulation, Dopaminergic neurons, Neuroprotective agents, Parkinsonism

Session Information

Date: Thursday, June 23, 2016

Session Time: 12:00pm-1:30pm

Session Title: Neuropharmacology

Location: Exhibit Hall located in Hall B, Level 2

Objective: To create a mechanistic computational model of iron transport between the circulation and brain, permitting *in silico* investigation of homeostatic regulation of iron at the human blood-brain barrier (BBB) and blood-cerebrospinal fluid barrier (BCB).

Background: The human brain utilizes iron in numerous essential processes. Iron trafficking is tightly regulated to minimize damage from iron-mediated excess free radical generation. Iron uptake across the BBB utilizes the iron transport protein transferrin, and is dependent on transferrin receptor expression (TfR) at the BBB (C. Morris, Brain 2011 v134 p924). Disruption of brain iron homeostasis is evident in certain neurodegenerative disorders, and elevated iron in the dopaminergic neurons of the substantia nigra (SN) is a particular feature of Parkinson's disease (PD). Dysregulation of iron in PD is not fully understood. Treatment with oral chelators that appear to modify iron levels in the SN can delay progression of early-stage PD (D. Devos et. al., Antioxid. Redox Signal. 2014 v21 p195). A computational model that describes brain iron homeostasis at a level that replicates experimental observations, and predicts the impact of perturbations (e.g. with chelating drugs) is highly desirable.

Methods: A mechanistic, multi-compartment *in silico* model of brain iron trafficking has been created using COPASI: Biochemical System Simulator software. The model comprises nonlinear ordinary differential equations to characterize the kinetics of each chemical species incorporated. Experimentally determined model parameter values for compartmental volumes, and initial concentrations and rate constants for each species, were derived from the literature.

Results: Model simulations accurately replicate the kinetics of iron uptake across the BBB with independently determined experimental data. In response to simulated iron overload in the blood circulation the model predicts that regulatory activity at the BBB/BCB, utilizing intracellular-scale control circuits, protects against excessive iron loading in the brain.

Conclusions: This new model provides an *in silico* resource to explore the impact of iron dysregulation and iron modifying drugs on the primary compartments of the human brain, and to better understand mechanisms of action of existing therapeutics.

To cite this abstract in AMA style:

V. Tjendana-Tjhin, S. Mitchell, E.A. Milward, M.J. Chappell, J.F. Collingwood. A computational model of iron transport between the blood circulation and the brain [abstract]. *Mov Disord.* 2016; 31 (suppl 2).

<http://www.mdsabstracts.org/abstract/a-computational-model-of-iron-transport-between-the-blood-circulation-and-the-brain/>. Accessed September 29, 2018.

Appendix D

Conference abstract – BioIron conference 2017

Poster #34

COMPUTATIONAL MODELLING OF IRON TRANSPORT BETWEEN BLOOD CIRCULATION, BRAIN, AND DOPAMINERGIC NEURONS OF THE SUBSTANTIA NIGRA

Vindy Tjendana Tjhin, MSc¹, Simon Mitchell, PhD², Elizabeth A. Milward, PhD³, Charles E. Hutchinson, MD¹, Michael J. Chappell, PhD¹ and Joanna F. Collingwood, PhD¹

¹University of Warwick; ²UCLA; ³University of Newcastle

Presented By: Vindy Tjendana Tjhin, MSc

Objective: to create a mechanistic computational model of iron transport between the blood circulation and the brain, permitting *in silico* investigation of homeostatic regulation of iron at the human blood-brain barrier (BBB) and blood-cerebrospinal fluid barrier (BCB), and to extend this with compartments that facilitate analysis of altered iron loading in neurodegenerative disorders.

Introduction: Iron trafficking in the human brain is tightly regulated, helping to minimize damage catalyzed by redox-active iron. Uptake of iron across the BBB utilizes the iron transport protein transferrin, and is demonstrably dependent on transferrin receptor (TfR) expression at the BBB. Iron uptake and efflux from neurons is also tightly regulated, with uptake primarily dependent on TfRs. In healthy dopaminergic neurons of the substantia nigra (SN), the expression level of TfRs is lower than for many other brain regions, and average tissue iron concentration in the SN exceeds other regions excepting globus pallidus and red nucleus. Within dopaminergic neurons of the SN, ferritin concentration is atypically low compared to other neurons; much of the intracellular iron is complexed with neuromelanin which may serve as an intracellular iron store and perform a protective function in isolating iron from the cytosol. Disrupted brain iron homeostasis is evidenced in certain neurodegenerative disorders; elevated iron in dopaminergic neurons of the SN pars compacta is a particular feature of Parkinson's disease (PD). Iron dysregulation in PD is not fully understood, and while treatment of early-stage PD patients with deferiprone appeared to delay deterioration and modify iron levels in the SN, the mechanism is not confirmed. A computational model that accurately describes brain iron homeostasis at a level that replicates experimental observations, and allows prediction of the impact of perturbations (e.g. with iron-modifying drugs) is therefore highly desirable.

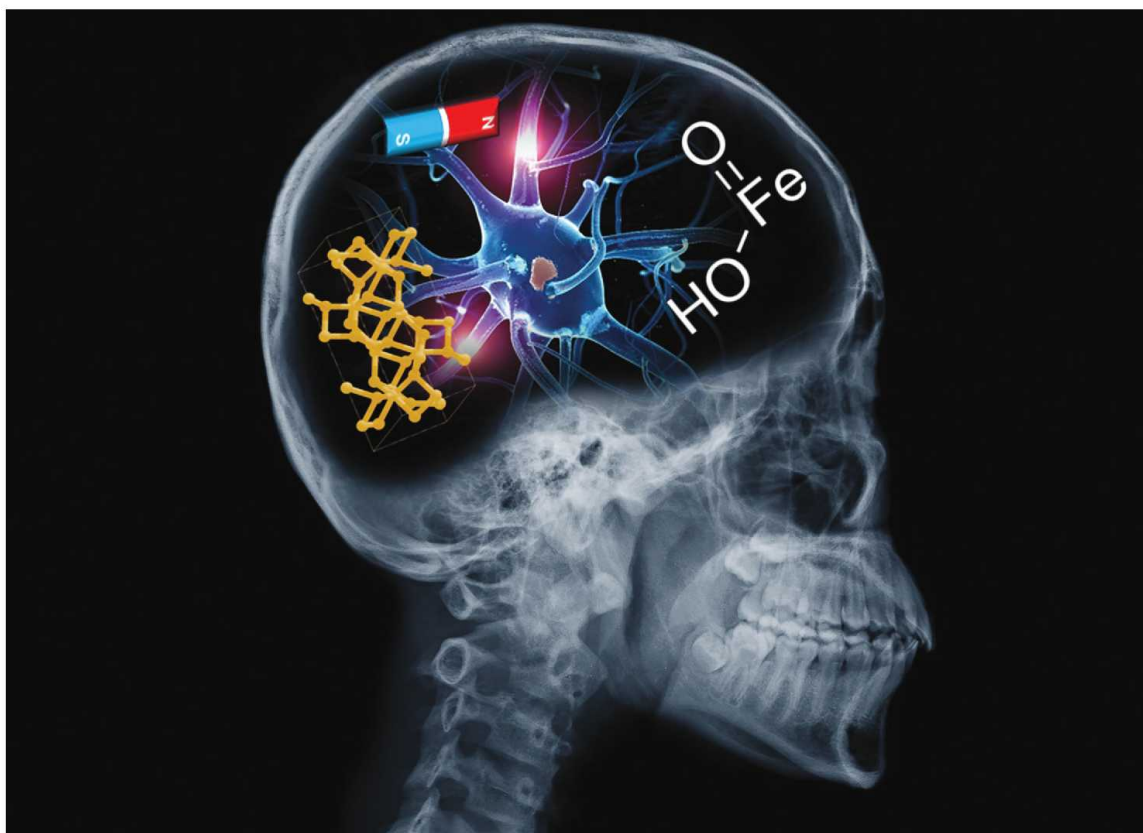
Methods: A compartmental *in silico* model of brain iron trafficking between the blood and the brain, and between the interstitial fluid (ISF) and the dopaminergic neurons, has been created using COPASI: Biochemical System Simulator software. Nonlinear ordinary differential equations characterized the kinetics of each chemical species involved in the transport of iron between the compartments. Experimentally determined model parameter values for compartmental volumes, initial species concentrations, and rate constants for each species, were derived from the literature.

Results: Model simulations accurately replicate the kinetics of iron uptake across the BBB with independently determined data from various experimental systems. In response to simulated iron overload, the model predicts that regulatory activity at the BBB/BCB protects against excessive iron loading in the brain, evidenced in the response of the ISF iron levels to varying blood iron levels. Within the dopaminergic neurons, steady state simulations of iron concentration (including ferritin- and neuromelanin-bound iron), and concentrations of iron response proteins and TfRs compare well with independently determined experimental data from the literature.

Conclusions: This new model provides an *in silico* resource to explore the impact of iron dysregulation and iron modifying drugs on the primary compartments of the human brain, to improve understanding of the mechanism of action of existing therapeutics, and to predict effective targets for novel therapeutics.

Appendix E

Publications - 2018

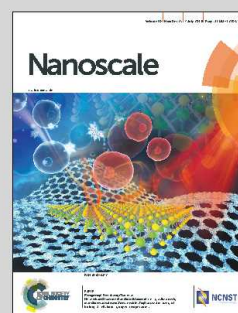


Showcasing research from Keele University and University of Warwick, UK, and University of Florida and the University of Texas at San Antonio, USA, featuring data from the Diamond and Advanced Light Source synchrotrons.

Nanoscale synchrotron X-ray speciation of iron and calcium compounds in amyloid plaque cores from Alzheimer's disease subjects

Could X-rays be used to expose the complex biochemistry, biomineralisation and magnetic oxide phases forming in neurodegenerative diseases? Everett *et al.* demonstrate the use of synchrotron X-rays to probe iron and calcium biochemistry in plaques isolated from the brains of individuals with Alzheimer's disease. Their results suggest links between disease pathology and the presence of chemically-reduced iron in the brain.

As featured in:



See Joanna F. Collingwood *et al.*, *Nanoscale*, 2018, 10, 11782.



rsc.li/nanoscale

Registered charity number: 207890



Cite this: *Nanoscale*, 2018, **10**, 11782

Nanoscale synchrotron X-ray speciation of iron and calcium compounds in amyloid plaque cores from Alzheimer's disease subjects†

James Everett,^{a,b} Joanna F. Collingwood,^{a,b,*c} Vindy Tjendana-Tjhin,^b Jake Brooks,^b Frederik Lermyte,^b Germán Plascencia-Villa,^d Ian Hands-Portman,^e Jon Dobson,^{b,c,f} George Perry^{b,g} and Neil D. Telling^{b,a}

Altered metabolism of biometals in the brain is a key feature of Alzheimer's disease, and biometal interactions with amyloid- β are linked to amyloid plaque formation. Iron-rich aggregates, including evidence for the mixed-valence iron oxide magnetite, are associated with amyloid plaques. To test the hypothesis that increased chemical reduction of iron, as observed *in vitro* in the presence of aggregating amyloid- β , may occur at sites of amyloid plaque formation in the human brain, the nanoscale distribution and physicochemical states of biometals, particularly iron, were characterised in isolated amyloid plaque cores from human Alzheimer's disease cases using synchrotron X-ray spectromicroscopy. *In situ* X-ray magnetic circular dichroism revealed the presence of magnetite: a finding supported by ptychographic observation of an iron oxide crystal with the morphology of biogenic magnetite. The exceptional sensitivity and specificity of X-ray spectromicroscopy, combining chemical and magnetic probes, allowed enhanced differentiation of the iron oxides phases present. This facilitated the discovery and speciation of ferrous-rich phases and lower oxidation state phases resembling zero-valent iron as well as magnetite. Sequestered calcium was discovered in two distinct mineral forms suggesting a dynamic process of amyloid plaque calcification *in vivo*. The range of iron oxidation states present and the direct observation of biogenic magnetite provide unparalleled support for the hypothesis that chemical reduction of iron arises in conjunction with the formation of amyloid plaques. These new findings raise challenging questions about the relative impacts of amyloid- β aggregation, plaque formation, and disrupted metal homeostasis on the oxidative burden observed in Alzheimer's disease.

Received 12th September 2017,
Accepted 19th March 2018
DOI: 10.1039/c7nr06794a
rsc.li/nanoscale

Introduction

Disrupted metal ion homeostasis has been linked to the development and progression of Alzheimer's disease (AD). Calcium

is the most abundant metal element in the human brain, and disturbed calcium signalling pathways and elevated intracellular calcium levels have been reported in conjunction with AD pathogenesis.^{1–3} Transition metals are present at trace levels in comparison to calcium, but they still play many essential roles in normal brain metabolism. Of the transition metals associated with AD pathology, iron is the most abundant in the healthy brain and is critical for normal brain function.

In the AD brain, iron concentration is significantly elevated in several tissue regions including the putamen.⁴ Locally elevated concentrations of atypical iron oxide aggregates and evidence of neurotoxic redox-active iron phases correlate with pathological hallmarks of AD throughout the brain. Sophisticated regulatory processes are required to maintain homeostasis, trafficking and storage for the many biometals essential to neuronal function.⁵ For example, iron is essential in energy production, nerve impulse transduction and neurotransmitter synthesis;^{5,6} these roles are enabled through controlled iron valence state changes *in vivo*, with both ferric

^aInstitute for Science and Technology in Medicine, Thornburrow Drive, Keele University, Staffordshire, ST4 7QB, UK

^bWarwick Engineering in Biomedicine, School of Engineering, Library Road, University of Warwick, Coventry, CV4 7AL, UK. E-mail: J.F.Collingwood@warwick.ac.uk

^cDepartment of Materials Science and Engineering, University of Florida, Gainesville, FL 32611, USA

^dDepartment of Physics and Astronomy, The University of Texas at San Antonio (UTSA), San Antonio, TX, 78249, USA

^eSchool of Life Sciences, Gibbet Hill Campus, University of Warwick, Coventry, CV4 7AL, UK

^fJ. Crayton Pruitt Family Department of Biomedical Engineering, Institute for Cell and Tissue Science & Engineering, University of Florida, Gainesville, FL 32611, USA

^gDepartment of Biology and UTSA Neurosciences Institute, The University of Texas at San Antonio (UTSA), San Antonio, TX, 78249, USA

†Electronic supplementary information (ESI) available. See DOI: 10.1039/c7nr06794a. Raw images and spectral data for this paper will be accessible via the Keele Research Repository at <http://dx.doi.org/10.21252/KEELE-0000027>.

(Fe³⁺) and ferrous (Fe²⁺) iron normally present in the brain. Non-heme iron is stored as a comparatively *redox-inactive* ferrihydrite-like mineral typically of the form (5Fe₂O₃·9H₂O), a ferric oxyhydroxide phase within the 12 nm protein cage ferritin.^{5,7} Iron binding is protective against iron partaking in redox reactions (e.g. Fenton chemistry) which may overwhelm antioxidant defences with the excess generation of reactive oxygen species (ROS).⁸ The most chemically available 'labile' and *redox-active* form is ferrous iron which may comprise ~5% of total intracellular iron.⁹ Redox-active iron levels are understood to be tightly regulated by oxidation–reduction (redox) processes such as the ferroxidase function of ferritin.^{5,10} Likewise, calcium (Ca) is vital for brain function and it plays fundamental roles in the development and plasticity of the nervous system. A large gradient exists between extracellular (10^{−3} M) and intracellular Ca²⁺ (10^{−7} M) pools, maintained by active pumping of Ca²⁺ through channels in the cell membrane.¹¹ Maintaining these gradients enables cells to use transient increases in intracellular calcium concentrations as an initiation event for a variety of cellular responses, including: neurotransmitter release, metabolic regulation, cell growth, synaptic efficiency and long-term potentiation. Therefore the maintenance of both calcium and iron homeostasis in brain is fundamental to its normal function, with metal dysregulation being shown to have catastrophic effects.^{11–14}

Iron dysregulation has been implicated in the development of AD, an age-related neurodegenerative condition which is the most common cause of dementia amongst the elderly.¹⁵ The underlying causes of the disease are not fully understood, and no effective treatments or cure exist. Evidence of significant cell damage, in conjunction with markers of oxidative stress, has resulted in oxidative damage being investigated as a major effector of neurodegeneration.^{16–18} Increased levels of material incorporating ferrous iron, potentially capable of catalysing redox chemistry have been reported post-mortem in AD subjects compared to age-matched disease-free controls.^{19–22} It is therefore possible that increased redox-active iron loading in AD provides a source of oxidative stress. As iron accumulation and oxidative stress have been shown as early events in AD,²³ the presence of inappropriate levels of redox-active iron could be a key event in triggering Aβ aggregation and free radical damage in AD.

Although the origin of the ferrous iron associated with AD is unclear, evidence implicates amyloid-β (Aβ) in this phenomenon.^{17,24–28} Aβ is the major constituent of amyloid plaque cores (APC),²⁹ a hallmark lesion of AD that is understood to convey neurotoxicity directly through its ability to produce reactive species including ROS,^{30,31} and indirectly by inducing the formation of neurofibrillary tangles (NFTs, comprised of hyper-phosphorylated tau protein).^{32,33} There are numerous reports of iron-containing Aβ plaques, including some reports that plaques incorporate ferrous-rich phases (such as the magnetic iron oxide, magnetite [Fe₃O₄]), as evidenced by histochemical staining,²¹ microscopic particle-induced X-ray emission analysis (microPIXE),³⁴ MRI,³⁵ HR-TEM and 3D electron tomography.³⁶ Furthermore, Aβ

plaques have been shown to be associated with ferritin in AD,³⁷ and ferritin isolated from AD post-mortem brain was reported to contain increased levels of ferrous iron compared to controls.³⁸ These observations indicate that Aβ is associated with the formation of phases incorporating ferrous iron by altering the way iron is handled. Indeed, the ability of Aβ to directly alter iron chemistry has been demonstrated previously. *In vitro* studies showed that Aβ can induce the redox-cycling of iron precipitates,²⁶ while our previous X-ray absorption studies showed that Aβ chemically reduces a variety of ferric iron phases (including ferrihydrite) into pure ferrous forms.^{24,25} The conversion of redox-inactive iron into redox-active phases has the potential to cause significant oxidative damage to neuronal populations; therefore, targeting amyloid/iron interaction in AD may prove an effective means to lower overall oxidative stress and delay disease progression.

Another factor indicated in the development of AD is disrupted calcium signalling.^{1,39,40} Perturbed intracellular calcium homeostasis induced signal-transduction cascades associated with AD, mutations in genes associated with familial AD showed a direct effect on calcium homeostasis, and calcium was implicated as a co-factor in the formation of Aβ plaques and NFTs,¹ suggesting that Aβ may be directly involved in disrupted calcium handling. Transgenic mice displaying amyloid deposition displayed impaired calcium homeostasis,³⁹ whilst *in vitro* studies showed that addition of Aβ to cell cultures induced an influx of calcium across the cell membrane.⁴¹ Levels of Ca²⁺ are higher in aged neurons, which may reflect compromised management of calcium gradients across the cell membranes.⁴² Calcium has been observed in amyloid deposits isolated from the thalamus of transgenic APP mice and the hippocampus of human AD cases,⁴³ whilst increased calcium levels have also been observed in human tissues displaying amyloid pathology.^{44,45} Some forms of calcium dysregulation may be a compensatory process in AD to modulate neuronal excitability and slow pathology.⁴²

In our most recent investigation we provided *ex vivo* evidence demonstrating both ferrous iron and magnetite to be directly correlated with the presence of APC in cortical tissue from a transgenic mouse model of AD.⁴⁶ However, the ability of Aβ to induce chemical reduction and biomineralisation of iron within human AD tissues is unproven, and the species of calcium and ferrous-rich iron phases associated with APC are not precisely described. Following the suggestion that the source of Aβ, the amyloid precursor protein APP, has a fundamental role in normal brain iron trafficking,⁴⁷ it is even more critical that Aβ aggregates are considered in the context of brain metal ion (dys)metabolism. Understanding the chemical speciation of metals associated with AD pathology is crucial in the development of therapies intended to diagnose, monitor and treat the disorder. Identifying iron species and mineral phases disproportionately associated with AD could support clinical diagnosis using non-invasive iron-sensitive techniques such as MRI. Better understanding of iron species associated with AD may also facilitate the development of novel therapies intended to alleviate iron-associated toxicity.⁴⁸ There are chal-



allenges to overcome if iron is to be selectively chelated for therapeutic purposes without compromising iron trafficking required for healthy brain function.

The aim of the present study was to investigate the distribution and physicochemical properties of iron-rich deposits in human APC, using a non-destructive spectromicroscopy technique that has not previously been applied to studies of human APC, Scanning Transmission X-ray Microscopy (STXM). This method has unique potential for precise determination of the nanoscale distribution and speciation of trace levels of organic and inorganic material in APC.

Experimental methods

This study used spectromicroscopy with high spatial and energy resolution to determine the physicochemical characteristics of iron deposits in human APC. The technique of choice was STXM, a synchrotron-based X-ray technique which offers outstanding sensitivity to probe and subsequently map chemical speciation at spatial resolutions routinely approaching 20 nm. Further to this, STXM X-ray Circular Magnetic Dichroism (XMCD) was performed to elucidate the magnetic state of iron inclusions identified within APC.

Isolation of amyloid plaque core (APC) material

Human brain tissue was obtained with the informed written consent of relatives, from autopsy AD patients. The protocols used to obtain, isolate and identify the APCs were approved by the Bioethics Committee (Department of Pathology, Case Western Reserve University), and this study was performed under UK ethical approval 07/MRE08/12 and USA IRB 03-00-26.

Brains from two AD cases (Braak stage VI) were removed at autopsy (5 h post-mortem) divided in half, cut into one cm slices and stored at -70°C . Frozen tissue sections were thawed and grey matter from the frontal and temporal lobes was isolated by removing blood vessels, meninges and white matter. Grey matter was then homogenized by heating to 95°C in the presence of 2% SDS and 50 mM Tris-buffer, before being filtered (110 μm pore size) to remove large tissue debris. The resulting material was pelleted through centrifugation at 800 rpm. AD tissues were further homogenized through the addition of 0.1% SDS, 150 mM NaCl and 0.02% NaN_3 before being filtered (35 μm pore size) and pelleted at 1000 rpm for 15–30 min. APC were isolated from the 35 μm filtrate through ultracentrifugation at 20 000 rpm in a sucrose gradient (1.8–1.2 M sucrose, in a 0.1% SDS, 150 mM NaCl and 0.02% NaN_3 solution). The resulting interfaces were collected and recovered for a final time with 0.1% SDS, 150 mM NaCl and 0.02% NaN_3 , before being concentrated through centrifugation at 1200 rpm.

Embedding and Sectioning of APC

Approximately 40 μL of pelleted APC was transferred into a centrifugal concentrator (Corning® Spin-X® UF; 40 kDa cut-off) and was spun at 6690 rpm for 10 minutes. APC were de-

hydrated through an ethanol series (100 μL ; 40%–100% dry), with waste ethanol being removed through centrifugation (6690 rpm for 10 minutes). Other chemical fixatives were not introduced, to limit metal ion leaching or transformation of mineral compounds. Once dehydrated, APC were embedded in a STXM compatible aliphatic resin comprised of a 1:1 molar mixture of trimethylolpropane triglycidyl ether:4,4'-methylenebis(2-methylcyclohexylamine). This resin contains no carbonyl or aromatic groups, making it an ideal embedding substrate when examining protein-based structures, due the lack of strong spectral features at the carbon K-absorption edge that overlap with protein peaks. Resin was polymerized over 24 h at 60°C .

Semi-thin sections containing APC were cut to a thickness of either 500 nm or 200 nm using a Reichert-Jung Ultra-cut microtome. A 500 nm thickness was cut to maximise the probability of observing APC, whereas a 200 nm thickness was cut to allow carbon spectroscopy using STXM. Non-metallic blades were used throughout the sectioning process to prevent metal contamination in the sample material.

Congo red staining

Sections 500 nm in thickness from both AD cases were stained for amyloid structures using a 1% Congo red solution. Sections were stained for approximately 30 minutes, and excess stain was removed with deionized H_2O . Stained sections were examined for birefringence under cross-polarized light using an Olympus IX51 microscope (60 \times objective lens).

Scanning transmission X-ray microscopy

X-ray spectromicroscopy experiments were performed at the Advanced Light Source (Lawrence Berkeley National Laboratory, Berkeley CA, USA), on beamline 11.0.2 using the STXM end-station, and Diamond Light Source, (Oxfordshire, UK) on beamline I08, with a focused X-ray spot size of ca. 25 nm (25 nm zone plate) in both instances. Energy-specific images were created by raster scanning the sample across the focussed beam and recording transmitted X-ray intensity. Exposure times were kept to a minimum (≤ 5 ms per point) to prevent X-ray induced photo-reduction of APC constituents, based on our previous experiments using various iron standard samples.⁴⁶

To map distributions of chemical species associated with APC, paired images were taken at the energy corresponding to the spectral feature of interest and an off-peak energy a few eV below the feature. The off-peak image was then subtracted to create a difference map, revealing the chemical speciation image over the region of interest for the selected spectral feature.

X-ray absorption spectra were obtained from a series of images (a 'stack') taken at energies spanning a desired absorption edge. The signal intensity recorded in the stack was converted to optical density using background regions that did not contain any sample material. For carbon K-edge absorption spectra, the background signal from the resin was subtracted as described in Telling *et al.*⁴⁶ This method of spectro-



microscopy allows X-ray absorption spectra to be generated from each pixel of an image, enabling spectral analysis of highly localised regions of interest. For stack measurements, the dark count (background noise attributable to the beam-line) was subtracted prior to the generation of the X-ray absorption spectra.

XMCD experiments were performed at Diamond Light source on beamline 108 using circularly polarised light. XMCD measurements were obtained by attaching NdFeB permanent ring magnets (allowing X-ray transmission) to the back face of the sample probe, with a sample section being mounted to the front face. The magnetic field at the sample position was ~ 150 mT, which is below the saturation field for magnetite, but sufficient to allow a degree of magnetic polarization. XMCD spectra were obtained by performing stacks over the iron L_3 -absorption edge (700–716 eV) using both right and left circularly polarised X-rays, with an exposure time of 5 ms per pixel. XMCD spectra were created by subtracting X-ray absorption spectra obtained under right circularly polarised (RCP) light from equivalent spectra obtained under left circularly polarised light (LCP). In addition to the APC material, an embedded synthetic magnetite nanopowder reference sample was created using the same embedding series as for the APC. APC and magnetite samples were prepared in separate laboratories so no cross contamination of samples could occur.

STXM data were processed using the aXis 2000 software package (<http://unicom.mcmaster.ca/aXis2000.html>). For iron L_3 -edge X-ray absorption spectra collected for XMCD analysis, a 3-point smoothing filter was applied to the raw data. ImageJ software was used to adjust the brightness and contrast of X-ray microscopy images. Pseudo-coloured composite images were created by converting grey scale X-ray microscopy images to false colour before recombining the images as overlays. Twelve plaque cores were examined using X-ray spectromicroscopy.

Analysis of X-ray absorption spectra

To obtain an estimate of the relative proportion of different iron phases within iron inclusions, reference X-ray absorption spectra from standards of Fe^{3+} , Fe^{2+} , Fe_3O_4 and Fe^0 were used to fit the measured iron $L_{2,3}$ -edge X-ray absorption spectra from each area, using a non-linear least-squares fitting procedure. A precise quantitative determination of the phase proportions would require the accurate scaling of the X-ray absorption spectra from these reference samples. However, the required scaling factors are not easy to determine when comparing iron phases with oxidation states that vary from pure metal to Fe^{3+} , due to the widely varying spectral shape and post-edge absorption intensities. Approximate scaling was instead determined by normalising the X-ray absorption intensity for each reference material (after background subtraction) to the integrated intensity over the $L_{2,3}$ absorption edges (Fig. S1†), following a method similar to that discussed in Regan *et al.*⁴⁹ However, we note here that the reference spectra we have used have only a limited post L_2 range, and so the scaling is less accurate than would be obtained using more

extended spectra. Despite this limitation, the estimated iron phase proportions derived in this way give a reliable indication of the relative differences between the individual iron-rich regions measured in the different inclusions.

We note that no evidence of chemical reduction was observed in ferric iron standards prepared using the same embedding series as for the APC, as described in the ESI† of our previously published work from the APP/PS1 mouse model of Alzheimer's disease (see Telling *et al.*⁴⁶).

Ptychography

Ptychography images of resin-embedded APC (500 nm thickness) were collected at the ALS beamline 11.0.2 using the STXM end-station. Paired images of the APC were taken at a peak iron L_3 -edge absorption energy (710 eV) and an off peak energy (705 eV) allowing an iron ptychography contrast map to be created.

Results

Identification of amyloid plaque cores (APC)

To confirm the presence and structural arrangement of APC in resin-embedded sections, Congo red staining was performed on 500 nm thick sections obtained from both AD cases. These were examined for birefringence using cross-polarizing optical microscopy. In both cases abundant areas with “apple-green” birefringence were observed (Fig. 1), confirming the presence and, importantly, the preservation of the fibrillar arrangement of APC. Radially symmetric birefringence, characteristic of spherulite amyloid structures⁵⁰ (see Fig. 1c) was also observed throughout all sections examined, further verifying the presence of amyloid material.

Iron and calcium loading of APC

The spatial distribution and chemical composition of APC in unstained 200 nm and 500 nm thick sections were determined using STXM. All resin-embedded sections in this study utilised a specialist aliphatic embedding resin that does not contain strong spectral features at the C, N or O absorption K-edges, differentiating it from commonly-used electron microscopy epoxy resins.⁵¹ We have elsewhere demonstrated how the con-

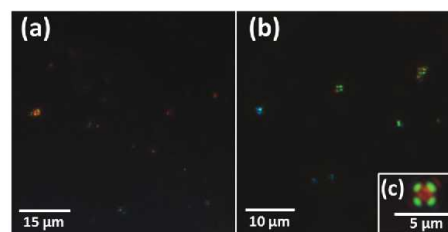


Fig. 1 Congo red stained sections containing APC exhibiting birefringence under cross-polarized light. Sections (a) and (b) were obtained from case X, whilst section (c) was taken from case Y.



tribution to the X-ray absorption from the resin can be subtracted from images obtained at the carbon absorption K-edge, in order to map a specific protein or peptide distribution in embedded sections of mouse brain tissue.⁴⁶ The analytical procedure from the tissue analysis was applied to the isolated APC in the present study. Additionally, in the thicker 500 nm sections (which impede X-ray transmission at the principal carbon K-edge absorption energy of 288.5 eV for proteins), the oxygen K-edge was used to identify peptide (here amyloid) content from APC, as well as to identify other oxygenated compounds. Validation for the use of the oxygen K-edge in these thicker sections is demonstrated in ESI Fig. S2,[†] where near-equivalent peptide maps were obtained using protein X-ray absorption features at the carbon K-edge (285.0 eV) and the oxygen K-edge (532.1 eV).

The oxygen K-edge was ultimately chosen over the carbon K-edge for peptide mapping in 500 nm thick sections, as this absorption edge was far less susceptible to X-ray saturation effects.

For the 500 nm thick sections, an X-ray beam energy of 530 eV (which is near the oxygen K-edge, but not associated with any spectral features) was used to observe the entire APC. Images obtained at this energy showed the APC to be dense granular structures ranging from 5 to 25 μm in size (see ESI Fig. S3[†]). To determine precisely the energies of the spectral features observed near the oxygen K-edge, an image stack was collected over the 525 eV–545 eV energy range from a typical APC (ca. 3.5 μm in diameter) as shown in Fig. 2a. The resulting X-ray absorption spectrum (Fig. 2g, lowest trace) included four main features: (1) a sharp peak at 532.1 eV, corresponding to 1 s to π^* transitions from protein carbonyl groups;⁵² (2) a shallow peak at 533.8 eV, characteristic of 1 s to π^* transitions from the carbonyl groups of carbonates;⁵³ (3) a peak at 537.6 eV, attributed to calcium oxide (CaO) bonds;⁵³ and finally (4) a 1 s to π^* carbonyl group carbonate peak at 540 eV (ref. 53) (although there was insufficient information in this energy region to define the exact position of this particular peak).

By examining localised regions of interest within this APC (highlighted as coloured boxes in Fig. 2a; top left), its heterogeneous nature was revealed with different constituents dominating the oxygen spectra in these selected regions (Fig. 2g; top). For example, the area labelled G1 (Fig. 2a) showed a single spectral feature at the oxygen K-edge at 532.1 eV (Fig. 2g) which was attributed to peptides. The map obtained from this spectral feature (Fig. 2b) showed strong intensity in the region of G1, which did not appear in the other maps (Fig. 2c–e). Of particular note, area G2 showed a strong feature at 533.8 eV attributed to carbonates (Fig. 2g, peak 2), and the corresponding map obtained using this feature (Fig. 2d) revealed the presence of small dense clusters. These carbonate-containing clusters were associated with the spectral feature from calcium oxide bonds (CaO) at 537.6 eV, and they can also be observed in the Ca map (Fig. 2c), suggesting them to be calcium carbonate. Interestingly, further areas of the APC demonstrating CaO absorption features (Fig. 2g, area G3) did not also show carbonate X-ray absorption features, indicating

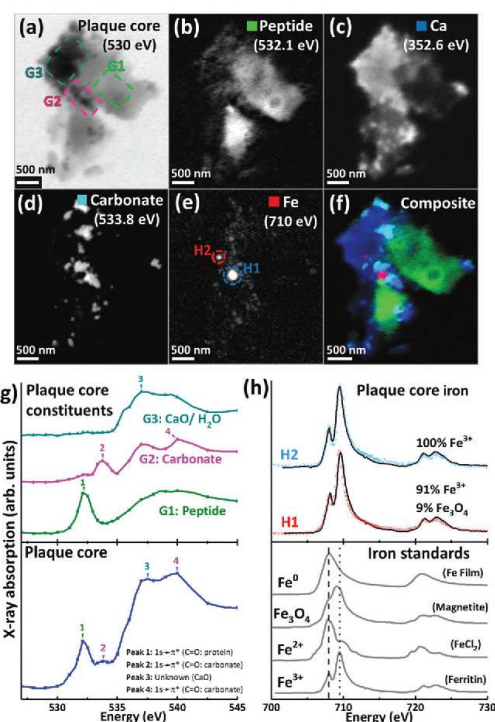


Fig. 2 X-ray spectromicroscopy images and speciation dependent contrast maps, oxygen K-edge X-ray absorption spectra, and iron $L_{2,3}$ -edge X-ray absorption spectra, from an amyloid plaque core of case Y. (a) Off resonance 530 eV image. (b) Oxygen K-edge peptide map. (c) Calcium L-edge map. (d) Oxygen K-edge carbonate map. (e) Iron L-edge map. (f) Composite image displaying peptide (green), calcium (blue), carbonate (sky blue) and iron (red) content of the plaque core. (g) Oxygen K-edge X-ray absorption spectra from the whole sectioned plaque core (bottom), and localised plaque core regions (top) as identified in the 530 eV microscopy image (a). (h) Iron $L_{2,3}$ -edge X-ray absorption spectra from reference Fe^{3+} [ferritin], Fe^{2+} [FeCl_2] and magnetite [Fe_3O_4] and iron zero [Fe^0] standards (bottom), and two amyloid plaque core iron deposits (top) as labelled in the iron contrast map (e). The dashed line at 708 eV and dotted line at 709.5 eV in the iron reference spectra show the peak absorption energies for Fe^{2+} and Fe^{3+} cations respectively.

diversity in the calcium species present, beyond calcium carbonate. It should also be noted that water could contribute to the absorption feature at 537.6 eV (ref. 54) (peak 3 in Fig. 2g), which would be consistent with the presence of a hydrous calcium phase such as hydroxyapatite.

The APC displayed an inhomogeneous peptide distribution as evidenced by dense peptide spots and striations (Fig. 2b). A high level of calcium loading was observed throughout the APC (Fig. 2c), with some smaller (100–500 nm) localised regions of carbonate and iron deposition also present (Fig. 2d). Importantly, while carbonate was only found in APC regions containing calcium, there were calcium-rich regions



that did not contain carbonate, indicating that not all calcium in APC was present as a carbonate phase. Alternative forms might be calcium divalent ions and calcium phosphate phases such as the aforementioned hydroxyapatite.

Iron $L_{2,3}$ -edge mapping showed iron to be present as well-defined dense clusters, and also distributed throughout the whole APC at a lower concentration (Fig. 2e). The two dense iron-containing regions (labelled H1 and H2 in Fig. 2e) were examined at a series of energies across the iron $L_{2,3}$ absorption edge (700 eV–740 eV) to provide X-ray absorption spectra allowing the oxidation state of the iron to be elucidated. In order to provide an estimate of the relative proportions of the iron phases contributing to each iron $L_{2,3}$ -edge X-ray absorption spectrum measured in the APC, a non-linear least-squares fitting procedure was employed. Equivalent iron $L_{2,3}$ -edge X-ray absorption spectra from iron reference standards exhibiting different known oxidation states are presented in Fig. 2h (bottom), and scaled iron references used for fitting are shown in Fig. S1,† to facilitate accurate characterization of iron-rich inclusions in the APC. From the fits shown in Fig. 2h, both areas H1 and H2 contained predominantly ferric (Fe^{3+}) iron, with H2 being a pure ferric phase (Fig. 2h, top).

For 200 nm thick sections, with an example shown in Fig. 3, an energy near the calcium L-edges (350 eV) was used to

identify APC features (a) and the carbon K-edge was used to determine the spatial distribution of the peptide (Fig. 3b). In this example the calcium L-edge (as opposed to the carbon K-edge) was preferred for initial identification of APC, as a weaker contrast was obtained at the carbon edge due to carbon background signal in the embedding resin. As before, serial images were collected over the entire carbon K-edge (280–320 eV) to establish the exact position of carbon-based absorption features in the energy spectrum. The carbon K-edge X-ray absorption spectrum from the APC (shown in Fig. 3h) was comprised of a 3-peak structure, with two sharp peaks at (1) 285 eV and (2) 288.5 eV, corresponding to the $1s$ to π^* transitions of peptide aromatic and amide groups respectively, and a further peak (3) at 290.5 eV corresponding to the $1s$ to π^* transition of carbonate.⁵⁵ The peak (1) at 285 eV was chosen for chemical mapping of peptide content, owing to its sharp energy resolution, and its lower absorption intensity compared to the high intensity peak (2) at 288.5 eV; with this higher energy peak being particularly vulnerable to X-ray saturation effects due to the strong absorption of 288.5 eV photons by both the resin and peptide.

Using these characteristic spectral features, species-specific spatial distribution maps within APC were generated as shown in Fig. 3, including peptide (285 eV, Fig. 3b), iron (710 eV, Fig. 3c), calcium (352.6 eV, Fig. 3d) and carbonate (290.5 and 533.8 eV, Fig. 3e and f respectively). As in Fig. 2, the APC is seen to be comprised of peptides varying in thickness/density resulting in intense protein spots, although these features were less apparent than in the 500 nm sections where more APC material was present (see ESI Fig. S4† for comparisons of peptide maps from 200 nm and 500 nm thick sections).

As in our first observations, the APC was heavily loaded with calcium (Fig. 3d). To confirm that large areas of carbonate were present throughout the plaque, corresponding maps were taken at carbonate spectral features using both the carbon K-edge (290.5 eV, Fig. 3e) and oxygen K-edge (533.8 eV, Fig. 3f) showing consistent contrast features, thus confirming the presence of carbonate. The carbonate distribution was confined to areas also containing calcium whilst the calcium content extends beyond this, indicating multiple calcium forms to be present. Further deposits of iron (ca. 200–500 nm diameter) were identified throughout this core (Fig. 3c), the oxidation states of which are considered in the following section. Additional examples of APC examined from both AD patient cases (labelled as case X and case Y) are shown in Fig. 4, confirming that the same pattern of concurrent calcium and iron loading was observed within the peptide rich amyloid cores. This pattern was repeated for *all* APC examined (see also ESI Fig. S5†). Furthermore, the identification of overlapping yet distinct calcium and calcium carbonate content was consistently observed throughout APC from both AD cases.

Nanoscale iron distribution, oxidation and magnetic state

Scanning transmission X-ray microscopy (STXM) images and speciation-dependent contrast maps of APC from case Y are displayed in Fig. 5(a–e). As with the previously described

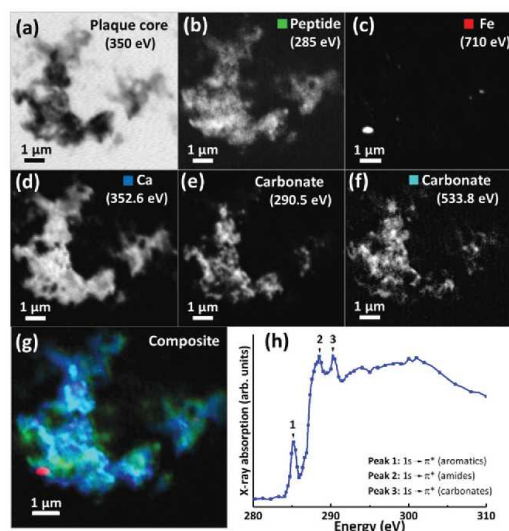


Fig. 3 (a–g) X-ray microscopy images and speciation dependent contrast maps of an amyloid plaque core from case X (scale bar = 1 μm). (a) Off resonance calcium L-edge (350 eV) image. (b) Carbon K-edge protein map. (c) Iron L-edge map. (d) Calcium L-edge map. (e) Carbon K-edge carbonate map. (f) Oxygen K-edge carbonate map. (g) Composite image showing: protein (green), calcium (blue), oxygen K-edge carbonate (sky blue), and iron (red) content of the plaque core. (h) Amyloid plaque core carbon K-edge X-ray absorption spectrum. Energy positions for $1s$ to π^* transitions for aromatics, amides and carbonates are labelled 1, 2 and 3 respectively.



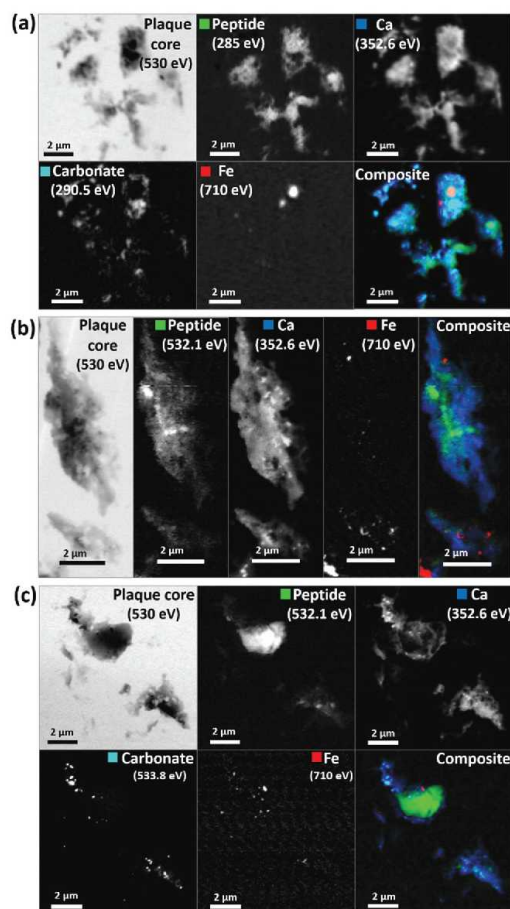


Fig. 4 STXM images and speciation dependent contrast maps of amyloid plaque cores from case X (a), and case Y (b and c). The maps show the off-resonance (530 eV) image, oxygen K-edge peptide map (532 eV), calcium L-edge map (352 eV), oxygen K-edge carbonate map (533 eV), iron L-edge map (710 eV), and composite image displaying peptide (green), calcium (blue), carbonate (sky blue) and iron (red) content of the plaque core.

plaques, the APC was comprised of dense areas of peptides (Fig. 5b), exhibiting regions of carbonate (Fig. 5c) and iron deposition (Fig. 5d). This structure was too dense for calcium mapping at 352.6 eV. Examination of the iron deposits (highlighted in Fig. 5d) across the iron $L_{2,3}$ absorption edge revealed iron to be present in ferric and ferrous-rich states (Fig. 5f). Area F1 appeared as a pure Fe^{3+} material with a principal iron L_3 peak at 709.5 eV and a separate low energy feature at 708 eV, both arising from Fe^{3+} cations (as also seen in the Fe^{3+} spectra in Fig. 2h). Area F2 displayed features consistent with an increase of the ferrous iron containing phases Fe^{2+} and Fe_3O_4 , as evidenced by the enhancement of the feature at 708 eV in

relation to the principal Fe^{3+} peak at 709.5 eV. As the principal Fe^{2+} peak resides at 708 eV (see for example the ferrous chloride standard in Fig. 2h), this suggests a slight increase in Fe^{2+} content. The presence of Fe_3O_4 (ca. 10%) in area F2 was determined through the relative intensities of the iron L_2 -edge Fe^{2+} and Fe^{3+} absorption features (found at 721 eV and 723 eV respectively), which were approximately equal in intensity. Fitting showed that an increase in 708 eV peak intensity arising solely through the presence of Fe^{2+} resulted in a poor L_2 edge fit, with the peak feature at 721 eV dominating the peak at 723 eV. By including both Fe_3O_4 and Fe^{2+} , a more accurate L_2 -edge fit was created, whilst maintaining the fit at the L_3 -edge. However, calculating a precise fit and percentage value for the phases contributing to the F2 spectrum was difficult, as the spectrum displayed signs of saturation, manifesting as an enhanced post-edge absorption intensity when compared to the fitted data.

The spectrum from F3 showed subtle changes in L_3 -edge features, with the low energy 708 eV peak becoming less discernible (in comparison to the ferric standard) appearing as a shoulder on the 709.5 eV peak feature. A shoulder feature on the principal Fe^{3+} cation feature is characteristic of the mixed-valence mineral magnetite (a magnetite reference spectrum can be seen in Fig. 2h). The F3 spectrum fit showed this iron inclusion to be comprised primarily of magnetite (ca. 60%) with a minor contribution from Fe^{3+} cations. The iron $L_{2,3}$ absorption edge spectrum from the small dense iron deposit labelled F4 in Fig. 5d is shown as the uppermost spectrum in Fig. 5f. This deposit was shown to be in a chemically reduced state as the low energy peak feature at 708 eV was not discernible, appearing as a shoulder on the 709.5 eV peak feature, again consistent with the redox-active mixed-valence mineral magnetite. The fit of the F4 spectrum showed this area to be principally comprised of magnetite (ca. 81%), with minor contributions from Fe^{3+} and Fe^{2+} (see ESI Fig. S6† for the calculated iron components used for fitting). The observation of magnetite in APC is consistent with observations by other techniques.^{36,56,57}

Evidence of chemically reduced, redox-active iron phases was also observed in case X from the APC displayed in Fig. 3 (see also Fig. 5g). From the iron $L_{2,3}$ -edge X-ray absorption spectra shown in Fig. 5h, the two iron deposits observed in this plaque core were heavily reduced, resembling a ferrous mineral phase, whilst also displaying features consistent with zero valence (Fe^0) iron.^{58,59} Whilst the principal iron L_3 -edge absorption feature for both Fe^{2+} and Fe^0 resides at 708 eV, these two phases are easily distinguishable by the broader line-shape of the spectrum for Fe^0 which lacks the multiplet fine structure seen in the oxide spectra, as well as the more prominent L_2 peak and post- L_2 edge absorption intensity for Fe^0 (see for example Fig. S7†).

The fit for region H1 determined this area to be ca. 60% comprised of a spectrum resembling Fe^0 with further contributions from Fe^{2+} and Fe^{3+} cations (see ESI Fig. S7† for the calculated components used for fitting). The evidence for the presence of Fe^0 is particularly convincing at the iron L_2 -absorp-

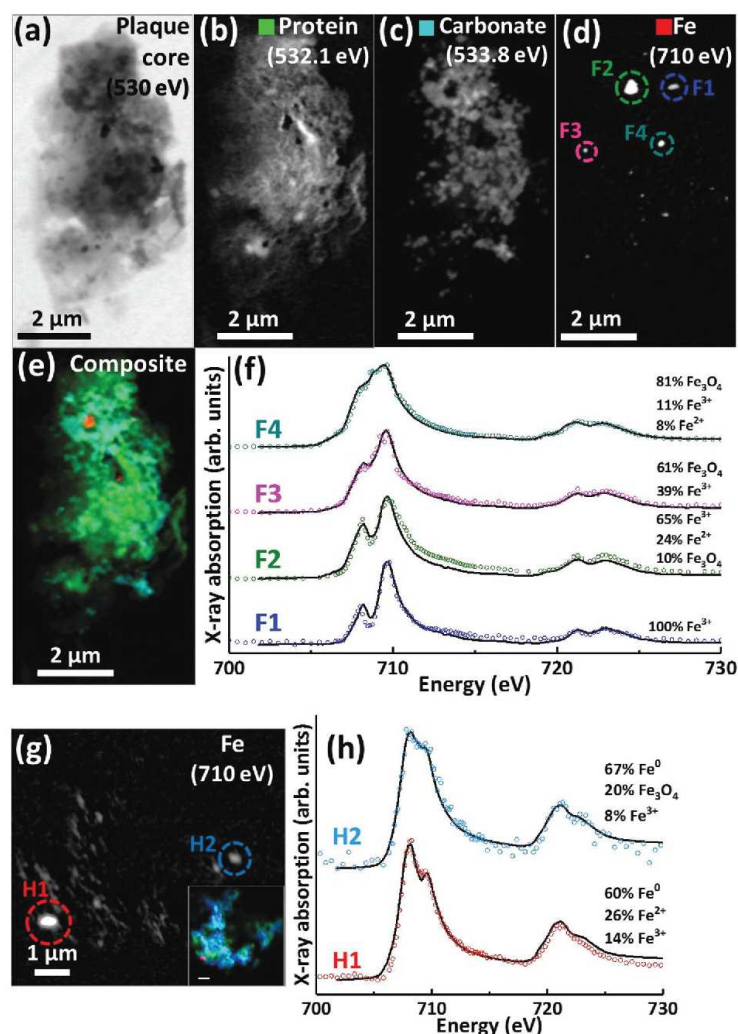


Fig. 5 STXM images, speciation dependent contrast maps and iron $L_{2,3}$ -edge absorption spectra from an amyloid plaque from case Y (a–f) and case X (g–h). (a) Off resonance 530 eV image. (b) Oxygen K-edge protein map. (c) Oxygen K-edge carbonate map. (d) Iron L-edge map. (e) Composite image showing: protein (green), carbonate (sky blue) and iron (red). Scale bars = 2 μ m. (f) Iron $L_{2,3}$ -edge absorption spectra from the iron deposits labelled in the iron map (d). (g) Iron L-edge map and composite (inset) of the amyloid plaque core shown in Fig. 3 (scale bar = 1 μ m). (h) Iron $L_{2,3}$ -edge absorption spectra from the iron deposits labelled in the iron map (g). The solid lines for the spectra correspond to best fit curves created by superposition of suitably scaled iron reference X-ray absorption spectra see Fig. S1†

tion edge where this area strongly resembles the Fe^0 reference. Likewise, fitting of region H2 indicated a spectrum resembling Fe^0 to be the predominant phase. The presence of iron in such low oxidation states was unexpected; this is the first time evidence consistent with Fe^0 has been reported in human APC to our knowledge, confirming the sensitivity of X-ray spectro-microscopy as a tool to probe chemical species within complex material of biological origin.

A further APC from case Y is presented in Fig. 6. Speciation dependent mapping showed this plaque similarly comprised of peptides (Fig. 6b) and carbonate (Fig. 6c), with iron content primarily confined to a sub-micron region in the centre of the plaque (Fig. 6d). A high magnification iron oxidation state difference map was created for this region to specifically differentiate iron species by subtracting the image acquired at the prominent Fe^{2+} peak (708 eV) from the image taken at the pro-

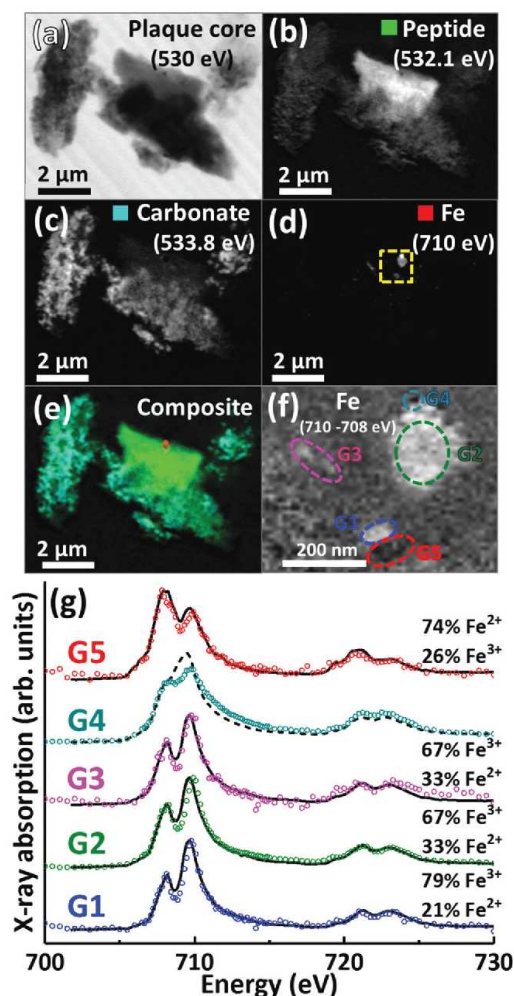


Fig. 6 STXM images, speciation dependent contrast maps and iron $L_{2,3}$ -edge absorption spectra from an amyloid plaque core from case Y. (a) Off resonance 530 eV image. (b) Oxygen K-edge protein map. (c) Oxygen K-edge carbonate map. (d) Iron L-edge map. (e) Composite image showing: protein (green), carbonate (sky blue) and iron (red) content. Scale bars = 2 μm . (f) High magnification iron oxidation state difference map of the inset area (yellow dashed line) in (d) showing Fe^{3+} (white), and Fe^{2+} (black) content of the iron deposits. Scale bar = 200 nm. (g) Iron $L_{2,3}$ -edge absorption spectra from the iron regions labelled in the iron oxidation state difference map (f). The solid and dashed black lines for the spectra correspond to best fit curves created by superposition of suitably scaled iron reference X-ray absorption spectra, see Fig. S1.†

minent Fe^{3+} peak (710 eV), resulting in Fe^{3+} deposits showing a bright contrast and Fe^{2+} a dark contrast. This oxidation state difference map revealed localised variation in Fe^{3+} and Fe^{2+}

content even within single nanoscale iron deposits (Fig. 6f). Examination of specific X-ray absorption across the iron $L_{2,3}$ -edge (Fig. 6g) revealed significant variation in the oxidation state across this area containing particulate iron (Fig. 6f), with evidence of primarily ferric iron (areas G1, G2 and G3) and a Fe^{2+} dominated spectrum (area G5) consistent with a largely ferrous material (*ca.* 74%) as determined by the fitting of the spectra. Area G4 shows evidence of saturation effects at the L_{3} -edge, resulting in an artificially high shoulder feature on the peak feature at 709.5 eV, giving the false impression of a high Fe^{2+} content. An attempted fit for this spectrum is provided as a dashed black line in Fig. 6g; however, due to the saturation effects, a quantitative analysis of the constituent iron phases in this area was not possible.

Iron L_{3} -edge X-ray microscopy images, speciation maps, circular polarization-dependent X-ray absorption and XMCD spectra from case X APC sections (adjacent to those shown in Fig. 3 and 5(g, h)), measured under an applied magnetic field are displayed in Fig. 7. Iron L_{3} -edge X-ray absorption and XMCD spectra from a reference magnetite standard (labelled Fe_3O_4) examined on the same beamline are shown in Fig. 7c and d. The magnetite XMCD spectrum displays a characteristic 3-point negative-positive-negative peak structure corresponding to magnetic iron cations present in Fe^{2+} octahedral, Fe^{3+} tetrahedral and Fe^{3+} octahedral sites respectively (see Telling *et al.*, 2017⁴⁶). Thus the appearance of these features in XMCD spectra obtained from APC would indicate the presence of ordered magnetite. Conversely, the absence of XMCD peak features (*i.e.* where the spectra obtained under RCP and LCP are identical) would indicate the presence of a non-magnetic iron phase.

XMCD spectra obtained from three iron-rich inclusions highlighted in Fig. 7b are displayed in Fig. 7d. By examining these spectra, a clear difference in magnetic ordering can be observed across the areas. Area C1 shows a weak XMCD effect, with a single poorly defined negative peak, whereas areas C2 and C3 display XMCD features consistent with magnetite. In particular, the XMCD spectra from area C3 displays a 3-point negative-positive-negative peak structure consistent with the magnetite reference in terms of both shape and relative peak intensities. Likewise, the examination of an iron inclusion from a further case X APC shown in Fig. 7(e–h), provided an XMCD spectrum consistent with a magnetite-like phase. However, in this case the relative positive and negative peak intensities in the XMCD spectrum (Fig. 7h), as well as the shape of the X-ray absorption spectra (Fig. 7g) suggest a more oxidised form similar to maghemite (see Telling *et al.*⁴⁶). Taken together these data strongly indicate the presence of varying oxidation states of the mineral magnetite within APC from human AD tissue.

To examine the morphology of iron deposits in APC in even greater detail, high-resolution ptychographic imaging was employed. Ptychography involves scanning a sample and simultaneously collecting scattered X-rays in addition to transmitted X-rays, thereby allowing a much greater spatial resolution to be resolved (*ca.* 2 nm) compared to traditional STXM

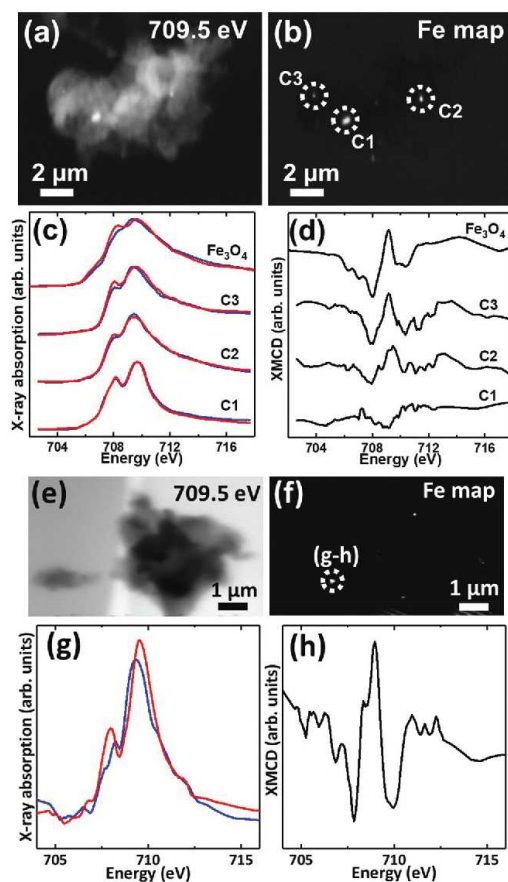


Fig. 7 (a, e) X-ray microscopy images (b, f) iron $L_{2,3}$ edge speciation maps (c, g) X-ray absorption spectra and (d, h) XMCD spectra from an APC of case X. Panels (c) and (g) show X-ray absorption spectra obtained using LCP (blue spectra) and RCP (red spectra). Panels (d) and (h) show the corresponding XMCD spectra created by subtracting the RCP spectra from the LCP spectra. All spectra were obtained in a magnetic field of ~ 150 mT applied parallel to the incident X-ray beam.

techniques (20–30 nm in spatial resolution).⁶⁰ Fig. 8 shows a ptychography image and iron content map from iron region 2 of the APC shown in Fig. 5(a–e). A dense triangular shaped object *ca.* 300 nm in diameter can be seen in the left field of the 710 eV image. Iron mapping showed the entirety of the triangular deposit to contain iron, with the structure strongly resembling the morphology of magnetite biominerals previously observed in magnetotactic microorganisms⁶¹ and extracted from human brain tissue.^{62,63} A single crystal of magnetite this large would be magnetically blocked. Altering the intensity threshold in the iron contrast image (see Fig. 8, inset) revealed a lower-concentration background of iron distributed beyond the triangular deposit, indicating the presence

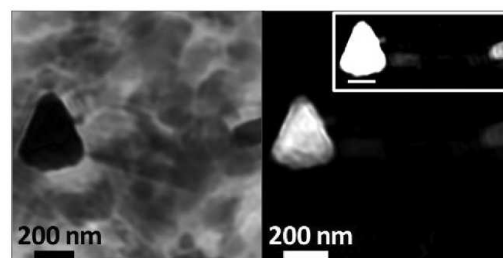


Fig. 8 Ptychography image (710 eV; left) and iron contrast map (right) of iron deposit 2 located in the amyloid plaque core of Fig. 5(a–e). High contrast iron map (right; inset) shows additional iron detail in this region.

of iron throughout the APC in addition to the dense iron deposits. Elongated (rod-like) structures are also observed in the 710 eV image (Fig. 8a), but not in the iron map, that are consistent with the size/morphology of nanocrystalline calcium-based minerals such as calcite⁶⁴ or hydroxyapatite,⁶⁵ supporting the earlier interpretation of the calcium and carbonate maps seen in all the APC.

Discussion

The precise analysis achieved here with X-ray spectromicroscopy and X-ray magnetic circular dichroism revealed APC associated with diffuse iron, and dense iron deposits incorporating ferrous iron, as well as the mixed-valence iron oxide magnetite. In addition, evidence consistent with zero-valent iron was observed in these structures for the first time. Calcium deposits were also observed within APC, including novel evidence of plaque calcification and calcium carbonate deposition. The presence of these iron and calcium features was observed consistently in multiple plaques isolated from the two independent AD cases.

The incorporation of iron into APC is in agreement with previous examination of human AD tissues, for example by histology,²¹ micro particle-induced X-ray emission analysis,³⁴ and MRI.³⁵ The present spectromicroscopy observations in human APC are supported by our recent *in vitro* A β /iron^{24,25} and *ex vivo* transgenic APP/PS1 mouse X-ray spectromicroscopy studies.^{46,66} In the APC presented here, iron was principally evident as sub-micron dense deposits, with no direct correlation between peptide and iron morphology being observed. These findings are consistent with observations of iron particulates in regions of dense amyloid pathology with an apparently amorphous structure.⁴⁶ For both AD cases investigated, iron $L_{2,3}$ -edge X-ray absorption spectra from APC demonstrated iron to be present in multiple different oxidation states. These ranged from pure ferric phases (Fe^{3+}), to the mixed-valence ($\text{Fe}^{2+}/\text{Fe}^{3+}$) magnetic phase magnetite, predominantly ferrous (Fe^{2+}) and, outstandingly, spectra consistent with zero-valent (Fe^0) materials. Importantly, this variation in Fe oxidation state

occurred across individual APC, and within single nanoscale deposits, a result in keeping with our STXM examination of transgenic mouse APP/PS1 tissue.⁴⁶

Our recent *in vitro* studies used X-ray spectromicroscopy to demonstrate that aggregation of synthetic A β (1–42) is accompanied by chemical reduction of ferric iron into a pure ferrous form.^{24,25} Earlier studies indicated redox cycling of iron in the presence of A β ,^{26,28} further supported by evidence for mixed valence iron oxide in an APP/PS1 mouse model of AD.⁶⁶ These new findings in human APC support the hypothesis of a dynamic processes occurring *in vitro* and *in vivo*, and strongly implicate A β in the formation of elevated levels of potentially redox-active ferrous and zero-valent iron phases in human brain. Interactions of A β with Fe ions can occur by coordination through His residues in the N-terminal region, as observed by Raman scattering.⁶⁷ In prior work it was suggested that A β becomes oxidized in the process of reducing iron by residue Met-35 of A β (1–42).^{68,69} Recently, however, it has been shown that Met-35 is inaccessible once amyloid fibres have formed, since this residue is buried in a hydrophobic interface region.⁷⁰ The X-ray spectromicroscopy measurements performed here permitted unambiguous identification of the redox state of a variety of iron species, but did not provide information about the oxidation state of the A β in the APC. In the context of our prior *in vitro* analysis, this evidence for a ferrous and zero-valent iron fraction also occurring in the APC is noteworthy because it indicates the stability of the analyte during sample handling. These APC were necessarily resin-embedded and sectioned prior to analysis, which was not required for synchrotron X-ray analysis of the aggregates formed *in vitro* that also evidenced chemical reduction of iron in the presence of aggregating A β .^{24,25}

The ability of A β to cycle iron throughout the ferrihydrite–magnetite–wüstite and potentially even zero-valent iron phase paradigm *in vivo*, implicates aggregating A β in the sustained generation of free-radical-producing iron species. The catalytic behaviour of iron in Fenton chemistry and related processes means that the free radical burden is likely to be more influenced by local iron chemistry than by absolute iron concentration. In the AD brain with evidence for disrupted iron metabolism and localised iron accumulation, there would be no shortage of fuel for these reactions; the localised nature of redox-active iron formation would have the potential to catalyse generation of free radical burdens inducing neuronal damage/death over time. Indeed, increased levels of oxidative stress have previously been reported in tissues with a high density of A β deposition,⁶⁹ although the capacity of amyloid to directly generate free radicals has often been debated.^{71,72} From our observations we suggest that A β is acting *indirectly* rather than *directly* in this regard, with free radicals generated through A β conversion of redox-inactive iron phases into redox-active forms.

Gaining a better understanding of the impacts on iron biochemistry of aggregating A β *versus* established APC remains a pressing issue, emphasized in recent work showing that A β immunization increased iron deposition in the choroid

plexus.⁷³ The debate continues as to whether APC formation has a protective effect through lowering the availability of unbound redox-active metal ions, and whether this protective effect may offset free radical damage arising indirectly from A β fibril formation. One explanation is that the aggregating mono- or oligomeric A β is a driver of free radical generation through its chemical reduction of iron,²⁴ and that subsequent formation of dense insoluble aggregates may serve a protective role in having sequestered (effectively chelated) the redox-active iron species typical of those reported here in the APC. This is consistent with the hypothesis that A β plaques may be a physiological response rather than a pathological process in their own right.⁷⁴ However, the nanoscale X-ray spectromicroscopy analysis presented here indicates that iron is present in a range of oxidation states, which could indicate the dynamic redox-cycling occurring within APC upon metal overload; in this scenario, dissolution of plaques may create local sources of toxic reactive iron species in the brain.

Ptychography obtained at the iron L₃-edge enabled the morphology of iron deposits within APC to be resolved at a remarkably high spatial resolution of *ca.* 2 nm. Through this approach we identified an iron deposit with a strong resemblance to a single magnetite/maghemite crystal. Further magnetic characterization of iron inclusions within APC using XMCD confirmed the presence of magnetite in multiple plaque cores. This supports prior work suggesting a role for A β in the biosynthesis of magnetite in human brain,³⁶ where evidence for magnetite has previously been reported in inorganic materials extracted from brain tissue homogenates,^{62,63} in isolated ferritin,³⁸ in ferritin-core-sized iron oxide deposits located within APC by electron beam methods,³⁶ and in plaque-rich human tissue from AD cases.⁵⁷

The precise source(s) of the iron integrated into APC *in vivo* is not yet known. Multiple sources of iron may be relevant to amyloid–iron interaction in AD such as: ferritin-bound ferrihydrite, transferrin, labile iron pools (including jettisoned ferritin iron content⁷⁵), hemosiderin formed at sites of microbleeds and haemorrhage in the brain, from disrupted neuronal mitochondria, and/or potential external sources of iron such as airborne particulate matter which have been suggested to enter the brain *via* the olfactory bulb.⁷⁶ Furthermore, the influence of the initial iron phase upon amyloid's reductant properties *in vivo* has not previously been characterised. Closer examination of the location and characteristics of amyloid/iron structures within intact AD tissues may provide clearer indications as to the source of amyloid-associated iron.

In all APC examined here, extensive accumulation of calcium was observed. By characterizing both calcium carbonate and total calcium content we demonstrated that calcium within APC was present in more than one form. Although the non-carbonate calcium phases observed could not be fully characterised, oxygen K-edge X-ray absorption features indicated this material was comprised of a hydrous calcium phase. Apatite, a calcium phosphate mineral (Ca₅(PO₄)₃), is produced in biological systems and readily associates with water to form hydroxyapatite (Ca₅(PO₄)₃(OH)). It is therefore possible that



hydroxyapatite is the crystalline form adopted by the non-carbonate calcium phase observed. Subsequent analysis of the phosphorus content of APC would be required to confirm this. Ptychographic images of APC revealed the presence of rod-like features with size and morphology matching calcium-based crystalline phases such as calcite or hydroxyapatite,^{64,65} which indicated that calcium biomineralization may be occurring during the formation of amyloid plaques in AD. Importantly, the confirmed presence of multiple calcium phases suggests that a dynamic process of plaque calcification may occur *in vivo*.

From the present experiments it was not possible to determine the origin of the calcium, or the effect of calcium on amyloid/iron interactions (such as competitive calcium/iron binding to amyloid). Examples of potential sources for the calcium observed in APC include: transferrin, in which carbonates are used for iron binding; calmodulin or other calcium binding proteins such as lithostathine (an inflammatory protein shown to accumulate in APC); or pools of extracellular Ca^{2+} used in processes such as neurotransmitter release.^{11,14} It is not yet determined if the forms of calcium observed in the APC are representative of the original source(s) of calcium, or if a biomineralization pathway (to be determined) produces carbonate in conjunction with APC formation.

The accumulation of calcium within APC may drive, or arise from, disrupted calcium trafficking and homeostasis in AD patients. Calcium triggers numerous signalling pathways in both excitable and non-excitable brain cells, whilst also regulating synaptic connections.^{11,14} In prior work, A β impacted calcium signalling pathways to the detriment of neuronal health and function.¹ Maintaining equilibrium in the extracellular Ca pool is vital to sustain these calcium signalling pathways, so the binding of calcium by A β as evidenced in this present study may have a detrimental effect upon Ca-dependent cellular signalling arising from the propensity of A β to act as a metal-binding protein.

Concurrent deposition of iron and calcium has previously been observed at significantly lower spatial resolution in tissue exhibiting amyloid aggregates (in the thalamus of APP mice^{43,77}), and in APC from the hippocampus.^{43,44} The results presented here are unique in obtaining the iron and calcium distribution, and the chemical speciation and mineral phase of iron and calcium inclusions with nanoscale resolution in human APC from confirmed AD cases. In particular, the appearance of dense calcium carbonate regions, co-located with another calcium phase (potentially based on apatite), was an unprecedented result. One interpretation of the distribution variation of the two calcium phases observed in these APC is that the transformation from apatite-like phases to calcium carbonate may occur over time. Detailed investigation of such processes, to predict age-dependent characteristics of calcifications *in vivo*, will help determine if features such as calcifications have utility as markers of disease progression to aid with clinical staging. Notably, “ferro-calcic” amyloid plaques have been evidenced in magnetic resonance imaging (MRI) contrast in the thalamus of transgenic APP/PS1 mice,⁷⁷

where the MRI properties of dense iron and calcium-rich deposits are sufficiently different from the surrounding tissue that they provide endogenous contrast. It will be important to distinguish calcium from iron deposition if the impact of iron modifying treatments is to be evaluated clinically by MRI.

The roles of iron and calcium cannot be fully explored without consideration of the wider range of metal and metalloid elements detected in human APC, including other transition metals (e.g. copper, zinc, manganese), aluminium (non-essential, and which facilitates iron-mediated oxidative reactions as well as affecting A β aggregation), and silicon, amongst others.^{34,36,44,78} In semi-quantitative synchrotron XRF analysis of the transition metal burden in human APC, copper concentration was elevated to the greatest extent (relative to copper concentration in the surrounding tissue) and linked with elevated production of H_2O_2 , a key component of Fenton chemistry. The proportionate increase in iron and calcium was comparatively modest for these more abundant elements.⁴⁴ To provide effective neuroprotection against toxicity arising from amyloid-metal reactions, a better understanding of the many competing interactions and influence of co-factors on reaction rates, including the chemically bound and unbound forms of each species, is required. For example, labile iron is more chemically available to partake in redox chemistry than complexed iron species (e.g. Fe^{2+} and Fe^{3+} of haemoglobin), and would be readily reduced in the presence of oxidants such as the H_2O_2 associated with copper loading in AD plaques, fueling the catalytic production of ROS by iron.^{44,79}

With iron being essential to healthy brain function, especially for energy production in mitochondria, it is of paramount importance to determine how to distinguish normally-metabolized iron from any iron species that elevates neuronal stress. To date, therapies that target iron metabolism in AD have been unsuccessful. One reason may be the lack of specificity resulting in depletion of iron stores and other essential metal cations required to sustain neuronal health (Cu, Zn, Mg, among others).^{8,80} This study represents a significant advance in the spatial resolution and precise speciation with which various iron phases are described in APC from AD cases. As different iron phases have distinct physicochemical properties, these findings may prove vital in the tailoring of AD diagnostics and therapies that discriminate detrimental forms of iron from those that are essential to normal function.

Conclusions

The X-ray spectromicroscopy methodology developed in this study enabled characterization of the distribution of organic materials (proteins), and precise nanoscale imaging and speciation of inorganic materials (iron and calcium compounds) in APC. The STXM methods enabled this to be done without the need for chemical fixation or contrast agents that significantly affect metal chemistry, and with significantly lower beam dose than required for equivalent electron-beam analyses. The unique concurrent characterization of iron and



calcium within human amyloid plaques is a finding that will enable progress in understanding the implications of interactions between amyloid- β , calcium, and iron, where disrupted calcium signalling pathways and elevated intracellular calcium have previously been observed in Alzheimer's disease. These iron and calcium species observed within the APC are assumed to be the products of metal-amyloid interactions *in vivo*, where wider evidence points to these interactions playing a role in the progression of AD.

The results support the hypothesis that iron is chemically reduced in the presence of aggregating A β and implicate this process as source of excess free radical generation. Whereas it has previously been assumed that these chemically reduced iron phases are rich in ferrous iron (Fe²⁺), we have now found evidence consistent with the presence of both zero-valent (Fe⁰) as well as ferrous-rich iron phases within pathological A β structures. These observations do not completely exclude the possibility of other phases such as iron sulphide.⁸¹ In addition, through detailed magnetic characterization, we demonstrate the mixed valence magnetic iron phase magnetite to be present within APC. Furthermore, we provide direct evidence that APC have the capacity to bind large quantities of calcium-rich species; this may be a significant sign of disrupted calcium homeostasis and cellular signalling, resulting in neuronal deterioration over time. The new observation that multiple calcium phases are present in APC suggests that a dynamic process of plaque calcification may occur *in vivo*.

Importantly, this unique application of X-ray spectromicroscopy has enabled concurrent *in situ* nanoscale characterization of iron and calcium minerals in human APC. These new observations support the hypothesis that A β plays a major role in disrupted iron and calcium biochemistry, and raise questions about whether A β binding enhances or counteracts the increased oxidative burden and disrupted neuronal signalling evidenced in AD. Determining the key mechanisms governing the formation of APC and neuronal responses to these metal-amyloid phases has scope to facilitate improved diagnosis of AD, as iron and calcium minerals affect magnetic resonance imaging signals. It also offers new perspectives for the development of therapies that successfully target iron toxicity in Alzheimer's disease patients.

Conflicts of interest

There are no conflicts to declare.

Acknowledgements

This work was supported by EPSRC grants EP/K035193/1 (JFC), EP/N033191/1-EP/N033140/1 (JFC-NDT), the Alzheimer's Association (AARFD-17-529742), University of Warwick alumni donations (VTT, JE), the RCM1 Program from NIH at UTSA (5G12RR013646, G12MD007591), San Antonio Life Sciences Institute (SALSI)-Clusters in Research Excellence Program, and

Semmes Foundation. The amyloid plaque cores were isolated from tissues obtained with informed consent, and were analysed in accordance with the Declaration of Helsinki under the remit of ethical approval 07/MRE08/12 from the UK National Research Ethics Service. We thank Tolek Tyliczszak (Advanced Light Source, Lawrence Berkeley National Laboratory, CA, USA) for specialist technical assistance with data collection at beamline 11.0.2. The Advanced Light Source is supported by the Director, Office of Science, Office of Basic Energy Sciences, of the U.S. Department of Energy under Contract No. DE-AC02-05CH11231. We thank Diamond Light Source for access to beamline 108 (proposal SP15247 and SP15854-3) that contributed to the results presented here, and thank Tooru Araki, Majid Kazemian Abyaneh and Burkhard Kaulich for technical assistance at the beamline. We thank Sandra Siedlak (Case Western Reserve University, Cleveland OH, USA) for technical assistance in isolation of the amyloid plaque cores.

References

- 1 F. M. LaFerla, *Nat. Rev. Neurosci.*, 2002, **3**, 862–872.
- 2 I. Bezprozvanny and M. P. Mattson, *Trends Neurosci.*, 2008, **31**, 454–463.
- 3 C. Supnet and I. Bezprozvanny, *J. Alzheimers Dis.*, 2010, **20**(Suppl 2), S487–S498.
- 4 Y. Tao, Y. Wang, J. T. Rogers and F. Wang, *J. Alzheimers Dis.*, 2014, **42**, 679–690.
- 5 J. R. Connor, S. L. Menzies, J. R. Burdo and P. J. Boyer, *Pediatr. Neurol.*, 2001, **25**, 118–129.
- 6 L. Zecca, M. B. H. Youdim, P. Riederer, J. R. Connor and R. R. Crichton, *Nat. Rev. Neurosci.*, 2004, **5**, 863–873.
- 7 J. F. Collingwood and N. D. Telling, in *Iron Oxides: From Nature to Applications*, ed. D. Faivre, Wiley-VCH Verlag GmbH & Co. KGaA, Weinheim, Germany, 2016, ch. 7, DOI: 10.1002/9783527691395.ch7.
- 8 D. Kell, *Nature*, 2009, **460**, 669.
- 9 Z. I. Cabantchik, *Front. Pharmacol.*, 2014, **5**, 45.
- 10 D. M. Lawson, A. Treffry, P. J. Artymuk, P. M. Harrison, S. J. Yewdall, A. Luzzago, G. Cesareni, S. Levi and P. Arosio, *FEBS Lett.*, 1989, **254**, 207–210.
- 11 T. B. Simons, *Neurosurg. Rev.*, 1988, **11**, 119–129.
- 12 Y. Ke and Z. M. Qian, *Lancet Neurol.*, 2003, **2**, 246–253.
- 13 P. Munoz and A. Hummer, *Biomaterials*, 2012, **25**, 825–835.
- 14 A. Ghosh and M. Greenberg, *Science*, 1995, **268**, 239–247.
- 15 A. S. Association, *Alzheimers Dement.*, 2012, **8**, 131–168.
- 16 D. Pratico, *Drug Dev. Res.*, 2002, **56**, 446–451.
- 17 M. A. Smith, C. A. Rottkamp, A. Nunomura, A. K. Raina and G. Perry, *Biochim. Biophys. Acta, Mol. Basis Dis.*, 2000, **1502**, 139–144.
- 18 C. C. Conrad, P. L. Marshall, J. M. Talent, C. A. Malakowsky, J. Choi and R. W. Gracy, *Biochem. Biophys. Res. Commun.*, 2000, **275**, 678–681.
- 19 J. Dobson, *Exp. Brain Res.*, 2002, **144**, 122–126.
- 20 D. Hautot, Q. A. Pankhurst, N. Khan and J. Dobson, *Proc. R. Soc. B*, 2003, **270**, S62–S64.



- 21 M. A. Smith, P. L. R. Harris, L. M. Sayre and G. Perry, *Proc. Natl. Acad. Sci. U. S. A.*, 1997, **94**, 9866–9868.
- 22 C. Quintana and L. Gutierrez, *Biochim. Biophys. Acta*, 2010, **1800**, 770–782.
- 23 A. Nunomura, G. Perry, G. Aliev, K. Hirai, A. Takeda, E. K. Balraj, P. K. Jones, H. Ghanbari, T. Wataya, S. Shimohama, S. Chiba, C. S. Atwood, R. B. Petersen and M. A. Smith, *J. Neuropathol. Exp. Neurol.*, 2001, **60**, 759–767.
- 24 J. Everett, E. Cespedes, L. R. Shelford, C. Exley, J. F. Collingwood, J. Dobson, G. van der Laan, C. A. Jenkins, E. Arenholz and N. D. Telling, *J. R. Soc., Interface*, 2014a, **11**, 20140165.
- 25 J. Everett, E. Cespedes, L. R. Shelford, C. Exley, J. F. Collingwood, J. Dobson, G. van der Laan, C. A. Jenkins, E. Arenholz and N. D. Telling, *Inorg. Chem.*, 2014b, **53**, 2803–2809.
- 26 A. Khan, J. P. Dobson and C. Exley, *Free Radicals Biol. Med.*, 2006, **40**, 557–569.
- 27 X. D. Huang, C. S. Atwood, M. A. Hartshorn, G. Multhaup, L. E. Goldstein, R. C. Scarpa, M. P. Cuajungco, D. N. Gray, J. Lim, R. D. Moir, R. E. Tanzi and A. I. Bush, *Biochemistry*, 1999, **38**, 7609–7616.
- 28 T. Rival, R. M. Page, D. S. Chandraratna, T. J. Sendall, E. Ryder, B. Liu, H. Lewis, T. Rosahl, R. Hider, L. M. Camargo, M. S. Shearman, D. C. Crowther and D. A. Lomas, *Eur. J. Neurosci.*, 2009, **29**, 1335–1347.
- 29 C. L. Masters, G. Multhaup, G. Simms, J. Pottgiesser, R. N. Martins and K. Beyreuther, *EMBO J.*, 1985, **4**, 2757–2763.
- 30 M. A. Smith, K. Hirai, K. Hsiao, M. A. Pappolla, P. L. R. Harris, S. L. Siedlak, M. Tabaton and G. Perry, *J. Neurochem.*, 1998, **70**, 2212–2215.
- 31 A. Monji, H. Utsumi, T. Ueda, T. Imoto, I. Yoshida, S. Hashioka, K. Tashiro and N. Tashiro, *Life Sci.*, 2002, **70**, 833–841.
- 32 J. Gotz, F. Chen, J. van Dorpe and R. M. Nitsch, *Science*, 2001, **293**, 1491–1495.
- 33 A. Yamamoto, R. W. Shin, K. Hasegawa, H. Naiki, H. Sato, F. Yoshimasu and T. Kitamoto, *J. Neurochem.*, 2002, **82**, 1137–1147.
- 34 M. A. Lovell, J. D. Robertson, W. J. Teesdale, J. L. Campbell and W. R. Markesbery, *J. Neurol. Sci.*, 1998, **158**, 47–52.
- 35 M. D. Meadowcroft, D. G. Peters, R. P. Dewal, J. R. Connor and Q. X. Yang, *NMR Biomed.*, 2015, **28**, 297–305.
- 36 J. F. Collingwood, R. K. K. Chong, T. Kasama, L. Cervera-Gontard, R. E. Dunin-Borkowski, G. Perry, M. Posfai, S. L. Siedlak, E. T. Simpson, M. A. Smith and J. Dobson, *J. Alzheimers Dis.*, 2008, **14**, 235–245.
- 37 I. Grundkeiqbal, J. Fleming, Y. C. Tung, H. Lassmann, K. Iqbal and J. G. Joshi, *Acta Neuropathol.*, 1990, **81**, 105–110.
- 38 C. Quintana, J. M. Cowley and C. Marhic, *J. Struct. Biol.*, 2004, **147**, 166–178.
- 39 K. V. Kuchibhotla, S. T. Goldman, C. R. Lattarulo, H.-Y. Wu, B. T. Hyman and B. J. Backsai, *Neuron*, 2008, **59**, 214–225.
- 40 M. Kawahara, *Curr. Alzheimer Res.*, 2004, **1**, 87–95.
- 41 H. Lin, R. Bhatia and R. Lal, *FASEB J.*, 2001, **15**, 2433–2444.
- 42 C. Supnet and I. Bezprozvanny, *Cell Calcium*, 2010, **47**, 183–189.
- 43 C. Quintana, T.-D. Wu, B. Delatour, M. Dhenain, J. L. Guerquin-Kern and A. Croisy, *Microsc. Res. Tech.*, 2007, **70**, 281–295.
- 44 L. M. Miller, Q. Wang, T. P. Telivala, R. J. Smith, A. Lanzirrotti and J. Miklossy, *J. Struct. Biol.*, 2006, **155**, 30–37.
- 45 F. Watt, *Cell. Mol. Biol.*, 1996, **42**, 17–26.
- 46 N. D. Telling, J. Everett, J. F. Collingwood, J. Dobson, G. van der Laan, J. J. Gallagher, J. Wang and A. P. Hitchcock, *Cell Chem. Biol.*, 2017, **24**, 1205–1215.
- 47 D. G. Peters, J. R. Connor and M. D. Meadowcroft, *Neurobiol. Dis.*, 2015, **81**, 49–65.
- 48 S. Ayton, P. Lei and A. I. Bush, *Neurotherapeutics*, 2015, **12**, 109–120.
- 49 T. J. Regan, H. Ohlag, C. Stamm, F. Nolting, J. Luning, J. Stohr and R. L. White, *Phys. Rev. B: Condens. Matter Mater. Phys.*, 2001, **64**, 2124422.
- 50 C. Exley, E. House, J. F. Collingwood, M. R. Davidson, D. Cannon and A. M. Donald, *J. Alzheimers Dis.*, 2010, **20**, 1159–1165.
- 51 J. Li, A. P. Hitchcock, H. D. H. Stöver and I. Shirley, *Macromolecules*, 2009, **42**, 2428–2432.
- 52 T. Weidner, N. Samuel, K. McCrea, L. Gamble, R. Ward and D. Castner, *Biointerphases*, 2010, **5**, 9–16.
- 53 R. T. DeVos, R. A. Metzler, L. Kabalah-Amitai, B. Pokroy, Y. Politi, A. Gal, L. Addadi, S. Weiner, A. Fernandez-Martinez, R. Demichelis, J. D. Gale, J. Ihli, F. C. Meldrum, A. Z. Blonsky, C. E. Killian, C. B. Salling, A. T. Young, M. A. Marcus, A. Scholl, A. Doran, C. Jenkins, H. A. Bechtel and P. Gilbert, *J. Phys. Chem. B*, 2014, **118**, 8449–8457.
- 54 J. D. Smith, C. D. Cappa, K. R. Wilson, B. M. Messer, R. C. Cohen and R. J. Saykally, *Science*, 2004, **306**, 851–853.
- 55 J. Cosmidis, K. Benzerara, N. Nassif, T. Tyliczszak and F. Bourdelle, *Acta Biomater.*, 2015, **12**, 260–269.
- 56 G. Plascencia-Villa, A. Ponce, J. F. Collingwood, M. J. Arellano-Jimenez, X. Zhu, J. T. Rogers, I. Betancourt, M. Jose-Yacamán and G. Perry, *Sci. Rep.*, 2016, **6**, 24873.
- 57 J. F. Collingwood, A. Mikhaylova, M. Davidson, C. Batich, W. J. Streit, J. Terry and J. Dobson, *J. Alzheimers Dis.*, 2005, **7**, 267–272.
- 58 A. Michelin, E. Drouet, E. Foy, J. J. Dynes, D. Neff and P. Dillmann, *J. Anal. At. Spectrom.*, 2013, **28**, 59–66.
- 59 J. Leveneur, G. I. N. Waterhouse, J. Kennedy, J. B. Metson and D. R. G. Mitchell, *J. Phys. Chem. C*, 2011, **115**, 20978–20985.
- 60 D. A. Shapiro, Y.-S. Yu, T. Tyliczszak, J. Cabana, R. Celestre, W. Chao, K. Kaznatcheev, A. L. D. Kilcoyne, F. Maia, S. Marchesini, Y. S. Meng, T. Warwick, L. L. Yang and H. A. Padmore, *Nat. Photonics*, 2014, **8**, 765–769.
- 61 W. Lin, K. Benzerara, D. Faivre and Y. Pan, *Front. Microbiol.*, 2014, **5**, 293.



- 62 J. L. Kirschvink, A. Kobayashi-Kirschvink and B. J. Woodford, *Proc. Natl. Acad. Sci. U. S. A.*, 1992, **89**, 7683–7687.
- 63 P. P. Schultheiss-Grassi, R. Wessiken and J. Dobson, *Biochim. Biophys. Acta*, 1999, **1426**, 212–216.
- 64 K. Benzerara, N. Menguy, F. Guyot, C. Dominici and P. Gillet, *Proc. Natl. Acad. Sci. U. S. A.*, 2003, **100**, 7438–7442.
- 65 P. Gentile, C. Wilcock, C. Miller, R. Moorehead and P. Hatton, *Materials*, 2015, **8**, 2297.
- 66 J. J. Gallagher, M. E. Finnegan, B. Grehan, J. Dobson, J. F. Collingwood and M. A. Lynch, *J. Alzheimers Dis.*, 2012, **28**, 147–161.
- 67 J. Dong, C. S. Atwood, V. E. Anderson, S. L. Siedlak, M. A. Smith, G. Perry and P. R. Carey, *Biochemistry*, 2003, **42**, 2768–2773.
- 68 X. D. Huang, R. D. Moir, R. E. Tanzi, A. I. Bush and J. T. Rogers, *Redox-Active Metals. Neurol. Disord.*, 2004, **1012**, 153–163.
- 69 D. A. Butterfield, A. M. Swomley and R. Sultana, *Antioxid. Redox Signaling*, 2013, **19**, 823–835.
- 70 M. A. Walti, F. Ravotti, H. Arai, C. G. Glabe, J. S. Wall, A. Bockmann, P. Guntert, B. H. Meier and R. Riek, *Proc. Natl. Acad. Sci. U. S. A.*, 2016, **113**, E4976–E4984.
- 71 S. I. Dikalov, M. P. Vitek, K. R. Maples and R. P. Mason, *J. Biol. Chem.*, 1999, **274**, 9392–9399.
- 72 Z. Y. Cai, B. Zhao and A. Ratka, *NeuroMol. Med.*, 2011, **13**, 223–250.
- 73 N. Joseph-Mathurin, O. Dorieux, S. G. Trouche, A. Boutajangout, A. Kraska, P. Fontes, J. M. Verdier, E. M. Sigurdsson, N. Mestre-Frances and M. Dhenain, *Neurobiol. Aging*, 2013, **34**, 2613–2622.
- 74 R. J. Castellani and G. Perry, *Biochem. Pharmacol.*, 2014, **88**, 671–676.
- 75 D. B. Kell and E. Pretorius, *Metallomics*, 2014, **6**, 748–773.
- 76 B. A. Maher, I. A. Ahmed, V. Karloukovski, D. A. MacLaren, P. G. Foulds, D. Allsop, D. M. Mann, R. Torres-Jardon and L. Calderon-Garciduenas, *Proc. Natl. Acad. Sci. U. S. A.*, 2016, **113**, 10797–10801.
- 77 M. Dhenain, N. El Tannir El Tayara, T.-D. Wu, M. Guégan, A. Volk, C. Quintana and B. Delatour, *Neurobiol. Aging*, 2009, **30**, 41–53.
- 78 C. Exley and E. R. House, *Monatsh. Chem.*, 2011, **142**, 357–363.
- 79 H. Wu, J.-J. Yin, W. G. Wamer, M. Zeng and Y. M. Lo, *J. Food Drug Anal.*, 2014, **22**, 86–94.
- 80 X. Li, J. Jankovic and W. Le, *J. Neural Transm.*, 2011, **118**, 473–477.
- 81 J. Kowalska, B. Nayyar, J. Kowalska, B. Nayyar, J. Rees, C. Schiewer, S. Lee, J. Kovacs, F. Meyer, T. Weyhermüller, E. Otero and S. DeBeer, *Inorg. Chem.*, 2017, **56**, 8147–8158.



Appendix F

Publications - 2018

Nanoscale Examination of Biological Tissues Using X-ray Spectromicroscopy

James Everett^{1,2*}, Vindy Tjendana Tjhin², Jake Brooks², Frederik Lermyte², Ian Hands-Portman³, Jon Dobson^{4,5}, Joanna Collingwood² and Neil Telling¹

¹ Institute for Science and Technology in Medicine, Keele University, Stoke-on-Trent, UK

² Warwick Engineering in Biomedicine, School of Engineering, University of Warwick, Coventry, UK

³ School of Life Sciences, Gibbet Hill Campus, University of Warwick, Coventry, UK

⁴ Department of Materials Science and Engineering, University of Florida, Gainesville, USA

⁵ J. Crayton Pruitt Family Department of Biomedical Engineering, Institute for Cell and Tissue Science & Engineering, University of Florida, Gainesville, USA

* Corresponding author, email: j.everett@keele.ac.uk

Establishing the composition and distribution of chemical compounds within biological materials is fundamental to understanding the chemistry that drives life. Additionally, region-specific changes in chemical homeostasis have been linked to disease states [1]. Traditional techniques used to explore these relationships rely on the use of fixatives and dyes, which can significantly alter the native chemistry of the sample material [2]. Here we describe methodology for the preparation and examination of biological sample materials, including human tissues, using the X-ray Spectromicroscopy technique Scanning Transmission X-ray Microscopy (STXM). Through STXM we show the distribution and speciation of organic and inorganic materials within biological samples at a nanoscale resolution. Importantly this approach does not require the use of dyes, aldehyde fixatives or contrast agents and therefore offers an unprecedented insight into the native chemistry of biological samples.

Human brain tissues were ethanol dehydrated and embedded in a resin comprised of equimolar trimethylolpropane triglycidyl ether: 4,4'-methylenebis (2-methylcyclohexylamine). Semi-thin (typically 200-500 nm) sections from embedded samples were cut using a non-metallic blade, before being mounted onto a support. STXM was performed at the carbon *K*-edge, oxygen *K*-edge, calcium *L*-edge and iron *L*-edge. To map distributions of chemical species, paired images were taken at the energy corresponding to a peak feature of interest and an off-peak energy a few eV away from this feature. The off-peak image is then subtracted from the peak image to give a difference map. This process is demonstrated in Figure 1, for a 200 nm thick section of human substantia nigra tissue imaged at the carbon *K*-edge. Here the peak image (288.3 eV; left) corresponds to the 1s to π^* transition for amide groups (proteins), whereas the off-peak image (290 eV; middle) corresponds to the principal carbon *K*-edge absorption feature for the resin (see also [1]). This image processing allows artifacts and background resin absorption features to be removed, revealing the true tissue structure. From these difference maps, tissue structure is shown to be well preserved over the 160 μm^2 area presented. The high resolution map taken at ca. 40 nm resolution (right; inset) shows cellular structures, also displaying subcellular organelles.

Further speciation maps and a carbon *K*-edge absorption spectrum from a 200 nm thick section of human amygdala tissue are shown in Figure 2. X-ray absorption spectra were obtained from a series of images taken at energies spanning the carbon *K*-edge edge. The resulting spectrum from tissue area A1 (Figure 2f; green spectrum) was consistent with a synthetic peptide standard (Figure 2f; black spectrum), indicating the tissue to have been preserved through the embedding process. Further dense areas of tissue (as evidenced by enhanced contrast in Figure 2a) were found to be loaded with calcium (Figure 2b), carbonates (Figure 2c) and iron (Figure 2d). This demonstrates STXM to be sensitive to altered chemical

compositions throughout tissue sections. These findings validate the use of X-ray spectromicroscopy for the examination of biological materials, including tissues of human origin, demonstrating these techniques to be suitable for determining (nanoscale) regional differences in chemical composition.

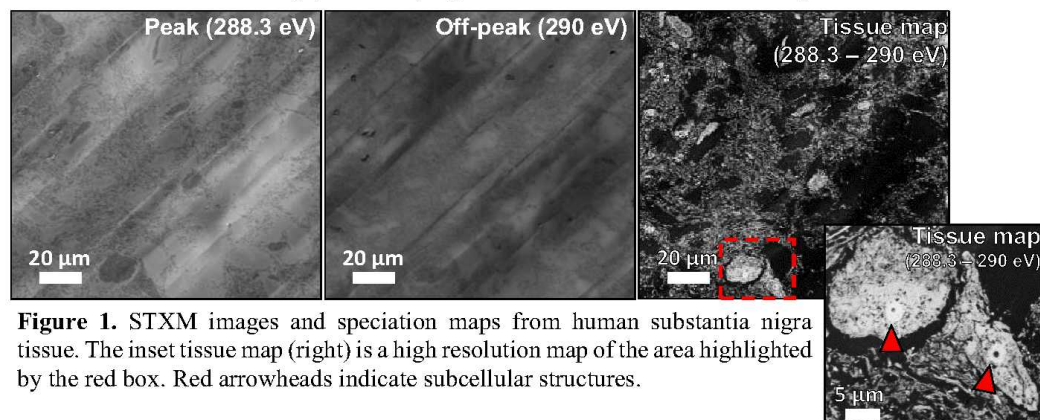


Figure 1. STXM images and speciation maps from human substantia nigra tissue. The inset tissue map (right) is a high resolution map of the area highlighted by the red box. Red arrowheads indicate subcellular structures.

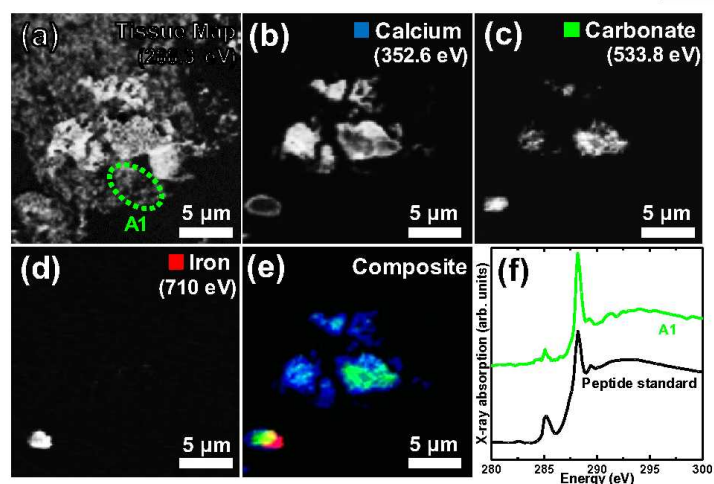


Figure 2. (a)–(e) STXM speciation maps, (f) carbon *K*-edge absorption spectrum from amygdala tissue.

References:

- [1] N D Telling *et al.* Cell Chem. Biol. **24** (2017), 1205–1215
- [2] J A Kiernan “Histological and Histochemical Methods” ed. 5 (Scion Publishing, Banbury, UK)
- [3] This work was supported by EPSRC grants EP/K035193/1, EP/N033191/1 - EP/N033140/1 and University of Warwick alumni donations. Tissues were obtained with informed consent, and analyzed in accordance with the Declaration of Helsinki under the remit of ethical approval 07/MRE08/12 from the UK National Research Ethics Service. We thank staff at the Advanced Light Source beamline 11.0.2 and Diamond Light Source beamline I08 for assistance with data collection.